UNIVERSITÀ DEGLI STUDI DI CAMERINO

School of Advanced Studies

DOCTORAL COURSE IN

Physical and Chemical Processes in Earth Systems

XXXIII cycle

MULTISCALE GEOLOGICAL MODELLING FOR FLUID FLOW EVALUATION ON DEFORMED CARBONATES

PhD Student
Tiziano Volatili

Supervisor
Prof. Emanuele Tondi

Table of Contents

INTRODUCTION **4**

1. FROM FRACTURE ANALYSIS TO FLOW SIMULATIONS IN FRACTURED CARBONATES: THE CASE STUDY OF THE ROMAN VALLEY QUARRY (MAJELLA MOUNTAIN, ITALY) **13**

1.1. Introduction **14**

1.2. Geological framework **16**

1.2.1. The study area 17

1.3. Methodology **24**

1.3.1. Fracture data acquisition and processing 24

1.3.2. DFN modelling 27

1.3.3. Porosity and permeability laboratory analysis 29

1.3.4. Static model construction 29

1.3.5. Fluid flow simulations 31

1.4. Results **35**

1.4.1 Matrix porosity and permeability 35

1.4.2. Fracture geometry and reservoir properties 36

1.4.3. Fluid Flow Simulations 40

1.5. Discussion **44**

1.6. Conclusions **48**

2. ANALYSIS OF FRACTURE ROUGHNESS CONTROL ON PERMEABILITY USING SFM AND FLUID FLOW SIMULATIONS: IMPLICATIONS FOR CARBONATE RESERVOIR CHARACTERIZATION **56**

2.1. Introduction **57**

2.2. Methodology **62**

2.2.1. Sample Collection 62

2.2.2. Mapping surface topography 65

2.2.3. Fracture Surface Processing and Analysis 67

2.2.4. Single Fracture Modeling 69

2.2.5. Lattice-Boltzmann method and permeability computation 71

2.3. Results **75**

2.3.1. Fracture surface properties 75

2.3.2. Permeability results 76

2.4. Discussion **84**

2.4.1. SfM photogrammetry surface scanning 84

2.4.2. Fracture Roughness Characterization 84

2.4.3. Permeability in function of fracture properties 85

2.4.4. Consequences to reservoir modeling 86

2.5. Conclusions **87**

3. PORE-SCALE DUAL-POROSITY AND DUAL-PERMEABILITY MODELING IN AN EXPOSED MULTI-FACIES POROUS CARBONATE RESERVOIR 94
3.1. Introduction 96
3.2. Geological settings 98
3.3. Methods 103
3.3.1. Sample preparation 103
3.3.2. Synchrotron radiation computed microtomography (SR micro-CT) 103
3.3.3. Structure from Motion (SfM) imaging and dual-porosity modeling 105
3.3.4. Quantitative image analysis 108
3.3.5. Computational Fluid Dynamics (CFD) simulations 109
3.4. Results 110
3.4.1. Matrix pore-network petrophysical properties 110
3.4.2. Petrophysical properties of the DP/P models 114
3.5. Discussion 123
3.5.1. Hydrocarbon distribution according to pore-scale observations 123
3.5.2. Effect of macrofractures in fluid storage and migrations 125
3.5.3. Effect of fracture roughness on porosity and permeability of the DP/P models 126
3.5.4. Considerations for modeling and upscaling 128
3.6. Conclusion 129

4. OUTCROP-SCALE FRACTURE ANALYSIS AND SEISMIC MODELLING OF A BASIN-BOUNDING NORMAL FAULT IN PLATFORM CARBONATES, CENTRAL ITALY 142
4.1. Introduction 143
4.2. Structural setting of the Fucino Basin 145
4.3. Methods 148
4.3.1. Structural analysis 148
4.3.2. Petrophysical and acoustic properties 153
4.3.3. Seismic modelling 155
4.4. Results 160
4.4.1. Fracture properties 160
4.4.2. Petrophysical properties 165
4.4.3. Petrophysical and seismic velocity model 167
4.4.4. Seismic models 169
4.4.4.2. Effect of geophysical conditions 171
4.5. Discussion 173
4.5.1. Fault damage zone architecture 173
4.5.2. Petrophysical properties 173
4.5.3. Seismic modelling 175
4.5. Conclusions 176

5. GENERAL CONCLUSIONS 186

INTRODUCTION

Porous and tight deformed carbonate rocks represent important geofluid reservoirs for natural resources exploitation (e.g., groundwater, hydrocarbons, geothermal energy). Carbonate reservoirs are characterized by a wide range of different permeability structures and petrophysical properties associated to the fault and fracture networks and lithological/ diagenetical variations (Billi et al., 2003; Antonellini et al., 2008; Faulkner et al., 2010; Bigi et al., 2013; Maffucci et al., 2015; Ferraro et al., 2020; Smeraglia et al., 2021). Specifically, in tight carbonates, where the matrix porosity and permeability are negligible, these petrophysical properties mainly depend on two factors, the geometrical parameters of the fracture network (i.e., fracture length distribution, orientation, intensity) and the hydraulic aperture. These parameters affect the connectivity and determine the preferential pathways for fluid migration and/or storage (Aydin, 2000; Graham-Wall et al., 2006; Agosta et al., 2010; Romano et al., 2020). Whereas, in deformed porous carbonates, the petrophysical properties are driven by the interplay between matrix properties, related to their sedimentological and diagenetical history and the fracture network properties. In porous rocks, the strain localization in deformation features, represented by deformation bands, may strongly affect the fluid flow, causing a drastic reduction of porosity and permeability due to grain reorganization, grain crushing, pressure dissolution and cementation (Fossen and Bale, 2007; Tondi, 2007; Tondi et al., 2016; Cilona et al., 2012; Antonellini et al., 2014; Zambrano et al., 2018).

The fluid storage and migration in deformed carbonates is strongly affected by the fault zone architecture. The fault zone architecture is composed by two main structural domains: the damage zone and the fault core (Fig. 1). The fault core includes the main slip surfaces, which accommodate most of the fault displacement and cohesive and/or un-cohesive fault rocks. The damage zone commonly encompasses the fault core and includes a thick zone of fractured and faulted host rocks. Both damage zone and fault core, especially their geometrical and petrophysical characteristics, play an important role in hydraulic behavior of fault zones (Caine et al., 1996; Sagy et al., 2001; Rotevatn et al., 2007). The fault core generally behaves as a fluid barrier/baffle depending on its degree of fault rock comminution and cementation (Sibson, 2000; Billi et al., 2003; Ferraro et al., 2020). Contrarily, due to the presence of fault related fractures and subsidiary faults, the damage zone is commonly assessed as a

localized/distributed conduit to fluid flow especially in tight carbonates (Aydin, 2000; Gudmundsson et al., 2001; Panza et al., 2016; Zambrano et al 2016; Smeraglia et al., 2021).

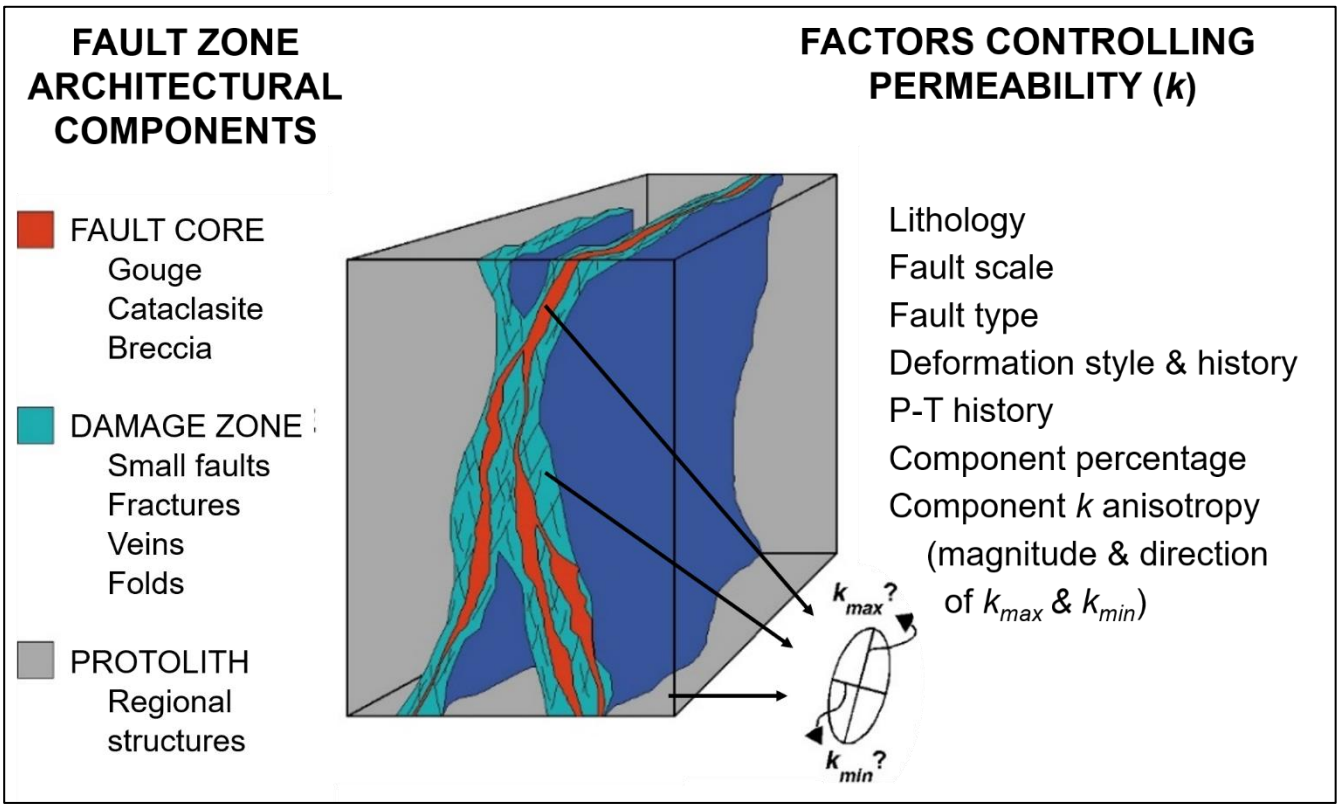

Fig. 1. Conceptual model of fault zone and its structural domains (from Caine et al., 1996). Ellipse represents permeability (k) anisotropy that might be associated with each distinct architectural component of fault zone.

The geometrical and petrophysical properties of sub-seismic structures, such as small faults (throw < 20 m) or clusters of narrowly spaced fractures, known as fracture corridors, may relevantly affect the fluid flow without being detected in seismic prospection (e.g., Antonellini and Aydin, 1995; Walsh et al., 1998; Sternlof et al. 2004). Although fractures are not detected by conventional seismic reflection data, their cumulative effect can be imaged as a seismic disturbance zone (Chopra & Marfurt, 2009; Li et al., 2015; Iacopini et al., 2016). Through seismic modelling and attribute-based interpretation, it is possible to investigate the seismic signature of outcrop-based

geological models and determine at which geological and petrophysical conditions the internal fault architecture can be imaged in seismic. Therefore, it is fundamental to quantitatively characterize the fracture distribution of fault damage zones and their related hydraulic properties to simulate the fluid flow in deformed carbonate reservoirs (Healy et al., 2015; Bigi et al., 2015; Zambrano et al., 2016; Cooke et al., 2018; Romano et al., 2020).

In order to reduce the uncertainties related to reservoir characterization, studies encompassing fluid flow simulations should consider complex geological models, including both lithological and structural heterogeneities, applying a dual-porosity/permeability (DP/P) modelling approach at different scales. The use of DP/P models including the hydraulic properties of both matrix and fracture pore systems is largely applied in reservoir assessment workflow, however the interplay between fractures and matrix porosity at the microscale is poorly understood.

In this Ph.D. thesis, the effect of both lithological and structural heterogeneities on fluid flow was investigated, in both porous and tight carbonates, by means of multiscale geological models and fluid flow simulations. The petrophysical properties (i.e., porosity, permeability) of the analyzed multiscale fault zones have been investigated by the implementation of 3D models based on different stochastic and deterministic approaches such as the Discrete Fracture Network modelling (DFN), Structure from Motion photogrammetry (SfM), X-ray computed microtomography (micro-CT) and Lattice-Boltzmann Method (LBM). Furthermore, a 2D elastic-petrophysical model of a seismic scale fault zone in tight carbonates was investigated through the seismic modelling pre-stack depth migration (PSDM) technique, performing a sensitivity analysis of different geophysical and geological conditions to test the seismic signature of a seismic scale fault zone internal architecture.

The bulk of this doctoral thesis consists of four scientific papers:

Chapter 1. From fracture analysis to flow simulations in fractured carbonates: the case study of the Roman Valley quarry (Majella Mountain, Italy), published in Marine and Petroleum Geology 100 (2019) 95–110.

Chapter 2. Analysis of fracture roughness control on permeability using SfM and fluid flow simulations: implications for carbonate reservoir characterization, published in Geofluids, Volume 2019, Article ID 4132386.

Chapter 3. Pore-scale dual-porosity and dual-permeability modeling in an exposed multi-facies porous carbonate reservoir, published in Marine and Petroleum Geology 128 (2021) 105004.

Chapter 4. Outcrop-scale fracture analysis and seismic modelling of a basin-bounding normal fault in platform carbonates, central Italy, submitted in Journal of Structural Geology.

The studies related to the first three papers have been carried out within the same study area, the inactive Roman Valley quarry (Majella Mountain, central Italy), well-known for its historical bitumen extraction. This site facilitates the study of a well-exposed analogue of a porous deformed carbonate reservoir and allows gaining information about matrix, fracture and fault characteristics that influenced hydrocarbon migration. Furthermore, the bitumen shows distribution within the quarry helps to further discuss and validate the obtained results.

In the first chapter, the main objective was to assess the impact of both stratigraphic and structural heterogeneities on fluid flow at the outcrop scale. This was possible by creating a large-scale DP/P model of the study area, which includes the petrophysical properties (i.e., porosity and permeability) of the matrix and fracture pore systems associated with the different studied lithofacies and fault zones. The studied rocks consist of ramp carbonates belonging to the lower member of the Bolognano Formation (Oligocene-Miocene in age) composed of grainstones, packstones and wackestones. These rocks are crosscut by two high-angle oblique-slip faults WNW-ESE oriented with up to 40 m of throw. The petrophysical properties of matrix and fractures were derived from laboratory measurements and field-based Discrete Fracture Network (DFN) modelling, respectively. Finally, the DP/P model was used to run fluid flow simulation, testing different scenarios of well locations. The fluid distribution in the matrix, resulting from these flow simulations, is consistent with field observations where

bitumen localizes within the most pervious lithofacies (grainstones). In the fault zones, the fracture network gains a relevant fluid flow anisotropy, enhancing the fluid flow along the faults, whereas the across fault fluid flow is controlled by type and lateral continuity of fault rocks, where fault breccias represent conduits and cataclasites localized barriers.

Although the use of DFN models is an acceptable representation of the macroscopy heterogeneities associated with sub-seismic resolution faults in a reservoir characterization, at the pore-scale the fluid flow is controlled by the matrix and fracture pore morphology. Therefore, the scale of investigation was changed in the second and third chapters focusing on the effect of pore scale heterogeneities on permeability. Specifically, the second chapter focuses on the analysis of the so-called fracture hydraulic aperture, which differs from the mechanical aperture due to a friction factor related to the roughness of the fracture walls. Samples of fracture surface have been collected from the different lithofacies outcropping within the Roman Valley quarry and digitalized using SfM photogrammetry in a highly controlled laboratory setting, applying a fracture surface micro-topography. This study incorporates fluid flow simulations, using the Lattice-Boltzmann method, and the use of synthetic computer-generated fractures for estimation of the fracture roughness. The quantitative analysis of fault surface roughness was achieved by implementing the power spectral density (PSD), which provides an objective description of the roughness, based on the frequency distribution of the surface asperities in the Fourier domain. This work evaluates the respective controls on permeability exerted by the fracture displacement (perpendicular and parallel to the fracture walls), surface roughness, and surface pair mismatch. The results may contribute to defining a more accurate equation of hydraulic aperture and permeability of single fractures. The third chapter aims to investigate the interaction between the fracture and matrix pore systems at the microscale. To do so, microscale DP/P models were generated by incorporating two different methods of 3D imaging such as, high resolution synchrotron X-ray microtomography (micro-CT) and SfM photogrammetry. Quantitative analyses of pristine rock and DP/P models were performed to evaluate the contribution of macrofracture segments to the porosity and connectivity of the pore network. These results were integrated with fluid flow simulations by applying a sensitivity analysis to evaluate the control exerted by fracture roughness parameters (i.e., asperity height distribution and fractal dimension) on porosity and permeability in various lithofacies. The results of this study demonstrate the utility of obtaining

microscale DP/P models as complementary approach to explain the geofluids distribution in fractured multi-facies porous carbonates.

Finally, the fourth chapter focuses on an integrated outcrop-based characterization and seismic modelling of the internal architecture of a seismic scale fault zone hosted in tight carbonates. This was possible in a key outcrop represented by an active quarry, located at the southeastern boundary of the Fucino Basin (Abruzzo region, central Italy). Here, the footwall damage zone of a seismic scale fault (throw ≈ 300 m), known as Venere Fault (VF), is well-exposed in a 3D view and crosscut by many subsidiary structures. This study presents a workflow to investigate the across strike distribution of petrophysical properties within the VF damage zone, through quantitative fracture analysis and in-situ permeability measurements. A large-scale 2D petrophysical-elastic base model of the VF zone was constrained incorporating results from field analyses and digital outcrop models (DOM) from SfM photogrammetry technique. This base model was tested in ray-based seismic modelling (PSDM; Lecomte et al., 2008), performing a sensitivity analysis of geological and geophysical parameters to investigate the seismic signature of the VF zone. The present contribution hence highlights the great importance of high-resolution structural analysis of fault damage zones for seismic modelling, and subsurface fault characterization.

References

Agosta, F., Alessandroni, M., Antonellini, M., Tondi, E., Giorgioni, M., 2010. From fractures to flow: a field-based quantitative analysis of an outcropping carbonate reservoir. Tectonophysics 490, 197e213.

Antonellini, M.A., Aydin, A., 1995. Effect of faulting on fluid flow in porous sandstones: geometry and spatial distribution. AAPG Bull. 79, 642-671.

Antonellini, M., Tondi, E., Agosta, F., Aydin, A., Cello, G., 2008. Failure modes in deepwater carbonates and their impact for fault development: Majella Mountain, Central Apennines, Italy. Mar. Petrol. Geol. 25, 1074–1096.

Antonellini M., Cilona A., Tondi E., Zambrano M. & Agosta F. (2014). Fluid-flow numerical experiments of faulted porous carbonates, Northwest Sicily (Italy). Marine and Petroleum Geology, 55, 186-201.

Aydin, A., 2000. Fractures, faults, and hydrocarbon entrapment, migration and flow. Mar. Petrol. Geol. 17, 797–814.

Bigi, S., Battaglia, M., Alemanni, A., Lombardi, S., Campana, A., Borisova, E., & Loizzo, M. (2013). CO2 flow through a fractured rock volume: Insights from field data, 3D fractures representation and fluid flow modeling. International Journal of Greenhouse Gas Control, 18, 183-199.

Bigi, S., Marchese, M., Meda, M., Nardon, S., & Franceschi, M. (2015). Discrete fracture network of the Latemar carbonate platform. Italian Journal of Geosciences, 134(3), 474-494.

Billi, A., Salvini, F., Storti, F., 2003. The damage zone-fault core transition in carbonate rocks: implications for fault growth, structure and permeability. J. Struct. Geol. 25, 1779–1794.

Caine, J.S., Evans, J.P., Forster, C.B., 1996. Fault zone architecture and permeability structure. Geology 24, 1025–1028.

Chopra, S., & Marfurt, K. J. (2009). Interpreting fractures through 3D seismic discontinuity attributes and their visualization. CSEG Recorder, 34(8), 5–14.

Cilona, A., Baud, P., Tondi, E., Agosta, F., Vinciguerra, S., Rustichelli, A., Spiers, C.J., 2012. Deformation bands in porous carbonate grainstones: field and laboratory observations. J. Struct. Geol. 45, 137-157.

Cooke, A.P., Fisher, Q.J., Michie, E.A.H., Yielding, G., 2018. Investigating the controls on fault rock distribution in normal faulted shallow burial limestones, Malta, and the implications for fluid flow. J. Struct. Geol. 114, 22–42. https://doi.org/10.1016/j.jsg.2018.05.024.

Faulkner, D.R., Jackson, C.A.L., Lunn, R.J., Schlische, R.W., Shipton, Z.K., Wibberley, C.A.J., Withjack, M.O., 2010. A review of recent developments concerning the structure, mechanics and fluid flow properties of fault zones. J. Struct. Geol. 32, 1557e1575.

Ferraro, F., Agosta, F., Prasad, M., Vinciguerra, S., Violay, M., & Giorgioni, M. (2020). Pore space properties in carbonate fault rocks of peninsular Italy. Journal of Structural Geology. https://doi.org/10.1016/j.jsg.2019.103913.

Fossen, H., Bale, A., 2007. Deformation bands and their influence on fluid flow. AAPG Bull. 91, 1685-1700.

Graham-Wall, B., Girgacea, R., Mesonjesi, A., Aydin, A., 2006. Evolution of fluid pathways through fracture controlled faults in carbonates of the Albanides fold-thrust belt. AAPG (Am. Assoc. Pet. Geol.) Bull. 90, 1227–1249.

Gudmundsson, A., Berg, S. S., Lyslo, K. B., & Skurtveit, E. (2001). Fracture networks and fluid transport in active fault zones. Journal of Structural Geology. https://doi.org/10.1016/S0191-8141(00)00100-0.

Healy, D., Rizzo, R.E., Cornwell, D.G., Farrell, N.J.C., Watkins, H., Timms, N.E., Gomez-Rivas, E., Smith, M., 2017. FracPaQ: a MATLABTM toolbox for the quantification of fracture patterns. J. Struct. Geol. 95, 1–16. https://doi.org/10.1016/j.jsg.2016.12.003.

Iacopini, D., Butler, R. W. H., Purves, S., McArdle, N., & De Freslon, N. (2016). Exploring the seismic expression of fault zones in 3D seismic volumes. Journal of Structural Geology. https://doi.org/10.1016/j.jsg.2016.05.005.

Lecomte, I. (2008). Resolution and illumination analyses in PSDM: A ray-based approach. Leading Edge (Tulsa, OK). https://doi.org/10.1190/1.2919584.

Li, F., Zhao, T., Lin, T., & Marfurt, K. J. (2015). Fracture characterization based on attenuation estimation from seismic reflection data using well-log-based localized spectral correction. Society of Petroleum Engineers - Unconventional Resources Technology Conference, URTeC 2015. https://doi.org/10.2118/178529-ms.

Maffucci, R., Bigi, S., Corrado, S., Chiodi, A., Di Paolo, L., Giordano, G., & Invernizzi, C. (2015). Quality assessment of reservoirs by means of outcrop data and "discrete fracture network" models: The case history of Rosario de La Frontera (NW Argentina) geothermal system. Tectonophysics, 647, 112-131.

Panza, E., Agosta, F., Rustichelli, A., Zambrano, M., Tondi, E., Prosser, G., ... & Janiseck, J. M. (2016). Fracture stratigraphy and fluid flow properties of shallow-water, tight carbonates: the case study of the Murge Plateau (southern Italy). Marine and Petroleum Geology, 73, 350-370.

Romano, V., Bigi, S., Carnevale, F., Hyman, J.D., Karra, S., Valocchi, A.J., Tartarello, M.C., Battaglia, M., 2020. Hydraulic characterization of a fault zone from fracture distribution. Journal of Structural Geology 104036.

Rotevatn, A., Fossen, H., Hesthammer, J., Aas, T. E., & Howell, J. A. (2007). Are relay ramps conduits for fluid flow? Structural analysis of a relay ramp in Arches National Park, Utah. Geological Society Special Publication. https://doi.org/10.1144/GSL.SP.2007.270.01.04

Sagy, A., Reches, Z. E., & Roman, I. (2001). Dynamic fracturing: Field and experimental observations. Journal of Structural Geology, 23(8), 1223-1239.

Sibson, R. H. (2000). Tectonic controls on maximum sustainable overpressure: fluid redistribution from stress transitions. Journal of Geochemical Exploration, 69, 471-475.

Smeraglia, L., Mercuri, M., Tavani, S., Pignalosa, A., Kettermann, M., Billi, A., & Carminati, E. (2021). 3D Discrete Fracture Network (DFN) models of damage zone fluid corridors within a reservoir-scale normal fault in carbonates: Multiscale approach using field data and UAV imagery. Marine and Petroleum Geology, 126, 104902.

Sternlof, K., Chapin, J., Pollard, D., Durlofsky, L., (2004). Permeability effects of deformation band arrays in sandstone. AAPG Bull. 88, 1315–1329.

Tondi, E., Antonellini, M., Aydin, A., Marchegiani, L., Cello, G., (2006). Interaction between deformation bands and pressure solution seams in fault development in carbonate grainstones of Majella Mountain, Italy. J. Struct. Geol. 28, 376–391.

Tondi, E., Rustichelli, A., Cilona, A., Balsamo, F., Storti, F., Napoli, G., Renda, P., Giorgioni, M., (2016). Hydraulic properties of fault zones in porous carbonates, examples from central and southern Italy. Italian J. Geosci. 135, 68e79. https://doi.org/10.3301/IJG.2015.08 f.1.

Zambrano, M., Tondi, E., Korneva, I., Panza, E., Agosta, F., Janiseck, J. M., & Giorgioni, M. (2016). Fracture properties analysis and discrete fracture network modelling of faulted tight limestones, Murge Plateau, Italy. Italian Journal of Geosciences, 135(1), 55-67.

Zambrano, M., Tondi, E., Mancini, L., Lanzafame, G., Trias, F.X., Arzilli, F., Materazzi, M., Torrieri, S., 2018. Fluid flow simulation and permeability computation in deformed porous carbonate grainstones. Adv. Water Resour. 115. https://doi.org/10.1016/j.advwatres.2018.02.016.

CHAPTER

1

FROM FRACTURE ANALYSIS TO FLOW SIMULATIONS IN FRACTURED CARBONATES: THE CASE STUDY OF THE ROMAN VALLEY QUARRY (MAJELLA MOUNTAIN, ITALY)

The present chapter has been published in Marine and Petroleum Geology 100 (2019) 95–110.

1. FROM FRACTURE ANALYSIS TO FLOW SIMULATIONS IN FRACTURED CARBONATES: THE CASE STUDY OF THE ROMAN VALLEY QUARRY (MAJELLA MOUNTAIN, ITALY)

T. Volatili[1,2], M. Zambrano[1,2], A. Cilona[3], B.A.H. Huisman[3], A. Rustichelli[2], M. Giorgioni[4], S. Vittori[1], E. Tondi[1,2]

[1]*School of Science and Technology, University of Camerino, Italy*
[2]*Reservoir Characterization Project (www.rechproject.com)*
[3]*Shell Global Solutions International B.V., The Netherlands*
[4]*Shell Italia Exploration and Production S.p.A., Rome, Italy*

Abstract

This work assesses the impact of the stratigraphic and structural heterogeneities on the fluid distribution and migration within a deformed carbonate reservoir analogue. The study was carried out in the abandoned Roman Valley quarry (Majella Mountain, central Italy), well-known for its historical bitumen extraction. The studied rocks consist of ramp carbonates of the lower member of the Bolognano Formation (Oligocene-Miocene in age) mainly composed of grainstones, and secondary packstones and wackestones. In the quarry, the exposed rocks are crosscut by two high-angle oblique-slip faults striking WNW-ESE with up to 40 meters of throw.

With the aim of deciphering the contribution of both matrix and fracture pore space on the fluid storage and migration, both laboratory measurements and field-based Discrete Fracture Network (DFN) models (cubes with 4-meters per side) have been carried out. The obtained dual-porosity/permeability model, which includes the lithological and the structural heterogeneities observed at the location, was used to run flow simulations under different scenarios of well locations.

The fluid distribution in the matrix, resulting from these flow simulations, is consistent with field observations where bitumen localizes within the most permeable lithofacies (grainstones). In the fault zones, the fracture network causes an important fluid flow anisotropy, enhancing the flow in a direction subparallel to the faults. The flow orthogonal to the fault zones is controlled by type and lateral continuity of fault rocks, where fault breccias represent conduits and cataclasites localized barriers.

Keywords: D*eformed Carbonates, Geological Model, Dual-Porosity/Permeability, Fault Sealing.*

1.1. Introduction

More than 60% of the world's oil, and about 40% of the world's gas reserves are held in carbonate rocks (Garland et al., 2012). For this reason, the assessment of stratigraphic, sedimentological, petrographic, petrophysical, and mechanical properties of carbonates has increasingly drawn an interest in the recent past. Indeed, all these properties strongly affect the deformation mechanisms in carbonate rocks resulting in a broad range of mechanical responses associated with the same stress field (Billi et al., 2003; Graham et al., 2003; Agosta and Aydin, 2006; Micarelli et al., 2005, 2006a; Antonellini et al., 2008; Rustichelli et al., 2013a; Fossen, 2016; Giorgioni et al., 2016).

Particularly, in tight carbonates, fracture networks can represent preferential pathways for fluid flow and/or accumulation (Caine et al., 1996; Aydin, 2000; Graham-Wall et al., 2006; Agosta et al., 2009, 2010; Solano et al., 2011) depending on their nature, connectivity and evolutionary stage (Cello et al., 2001; Rawling, 2001; Agosta & Kirschner, 2003; Billi, 2005). Conversely, in porous carbonate rocks these discontinuities can represent either buffers that inhibit fluid flow (Tondi 2007; Tondi et al., 2016; Micarelli et al. 2006b; Faulkner et al., 2010; Zambrano et al., 2017, 2018) or pathways for fluid circulation (Aydin et al., 2006; Agosta et al., 2010). Therefore, characterizing and quantifying type and distribution of discontinuities is fundamental to enable an optimal development of carbonate reservoirs (Aydin, 2000; Bense et al., 2013).

The reservoir properties of deformed carbonates are mainly the result of interplay between matrix properties (a combination of sedimentological and diagenetic history), which depends mostly on rock texture, and properties of the fracture network. The fracture network properties include individual fracture orientation, dimension, intensity, connectivity, aperture and roughness (Caine & Forster, 1999; Billi et al., 2003; Micarelli et al. 2006b; Agosta et al., 2010).

Several literature studies have used flow simulation with complex reservoir properties to investigate the effect of fault zones on fluid flow and reservoir production (Forster & Evans, 1991; Matthai et al., 1998; Ferrill et al., 1999; Flodin et al., 2001; Micarelli et al., 2006b; Fisher & Jolley, 2007; Al-Hinai et al., 2008; Nieto & Jensen, 2012; Antonellini et al., 2014, Zambrano et al., 2016; Panza et al., 2018; Romano et al., 2017). With this study,

we aim to test a workflow based on a multi-disciplinary characterization of carbonates by modelling both lithological and structural heterogeneities and assessing their control on fluid flow.

The modelled rocks are fractured carbonates, which are invaded by bitumen and crop out at the inactive Roman Valley Quarry, located in the northern termination of the Majella Mountain (Italy). Agosta et al. (2009) demonstrated that most of this hydrocarbon postdates the faulting activity and took place at a time when the faults were already exposed at the surface (Middle-Upper Pleistocene). The distribution of hydrocarbons in this outcrop therefore represents the remnants of paleo fluid flow paths (Agosta et al., 2010), and can be used to validate the results of computed fluid flow simulations.

In particular, the aims of this work are the following: 1) characterize the fracture networks within distinct carbonate lithofacies by means of a field-based quantitative fracture analysis; 2) derive porosity and permeability of the matrix in various lithofacies through conventional laboratory measurements, and of the fractures by means of DFN modelling (Wei et al., 1995; Wilson et al., 2011, Korneva et al., 2014; Zambrano et al., 2016; Panza et al., 2018); 3) investigate reservoir-scale, fluid flow properties by modelling fault zones comprising of sealing and conductive fault segments in dual-porosity/permeability flow simulations; and 4) evaluate the control exerted by lithological and structural heterogeneities on fluid flow.

The results of the static and dynamic modelling performed in this study can help reduce the uncertainty related to the modelling of flow across and along seismic and sub-seismic fault zones in carbonate reservoirs (Zhang and Sanderson, 1997; Micarelli et al. 2006b; Faulkner et al. 2010; Antonellini et al., 2014).

1.2. Geological framework

The Majella Mountain is an east-verging thrust-bound, asymmetric, box-shaped anticline (Fig. 1.1) which is made of a ≈2 km-thick Jurassic to Miocene carbonate succession. The Mesozoic platform carbonates are exposed at a relatively small portion of the Majella central-eastern sector, whereas their correlative slope-to-basin limestones and the overlying Late Cretaceous to Miocene ramp limestones and marls are widespread over the whole mountain.

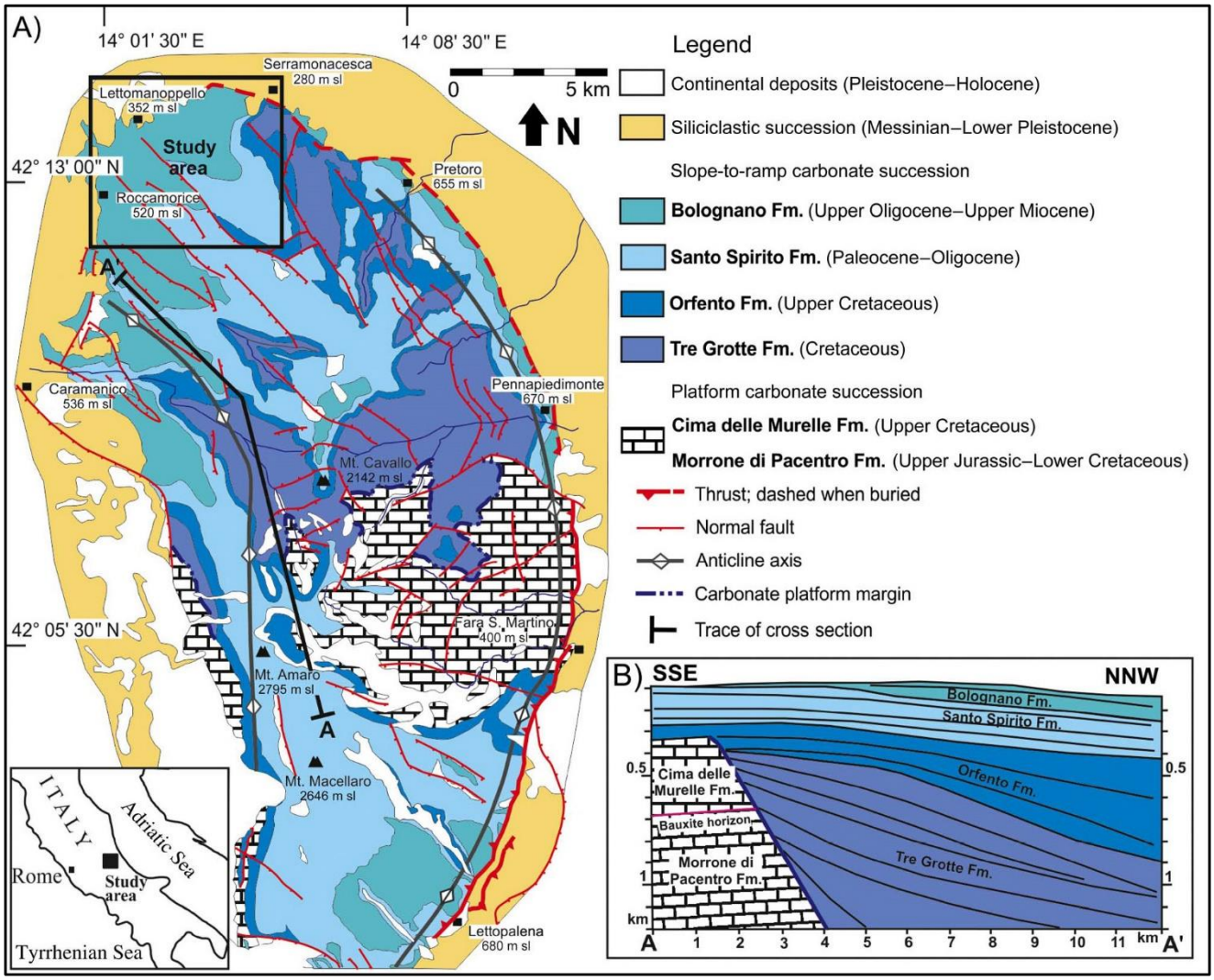

Fig. 1.1. Geological setting of the Majella Mountain. a) Schematic geological map (modified after Ghisetti and Vezzani, 1997). b) Stratigraphic scheme of the carbonate succession (modified after Vecsei, 1991).

The development of the Majella thrust-related anticline occurred during the Middle-to-Late Pliocene (Ghisetti and Vezzani, 2002; Scisciani et al., 2002). The internal deformation of this box-shaped fold, characterized by a steeply dipping to overturned eastern limb, mainly consists of high-angle normal, strike-slip and oblique-slip normal faults, small folds and different sets of opening-mode fractures, pressure solution seams and deformation bands (e.g., Marchegiani et al., 2006; Tondi et al., 2006; Antonellini et al., 2008; Agosta et al., 2009, 2010; Aydin et al., 2010; Rustichelli et al., 2012, 2016).

In the western part, the Majella anticline backlimb is crosscut by a major normal fault, named Caramanico fault, dipping 70°-80° westwards with up to 4200 meters of normal throw. Displacement along this fault has juxtaposed the Majella Mountain carbonates of the footwall, with Lower Pliocene marine siliciclastic deposits and Quaternary continental clastic deposits accumulated in the Caramanico basin (Ghisetti & Vezzani, 2002).

Both in the northern and in the southern parts of the structure a main NW-SE set of normal faults with a minor left-lateral component of movement is present. Faults have a vertical displacement on the order of tens of meters and cut across the carbonates of the Bolognano Formation within the study area. On the eastern limb of the structure, especially in its central part, a roughly E-W trending set of strike-slip faults and a N-S trending set of normal faults set were described (Tondi. et al., 2006; Antonellini et al., 2008).

1.2.1. The study area

The Roman Valley Quarry is located on the northern slopes of the Majella Mountain near the village of Lettomanoppello (Italy). This site has been known since Ancient Roman times for the extraction of bitumen, and was actively mined till the 1960s. This quarry facilitates the study of a well-exposed analogue of a fractured reservoir and allows gaining information about fracture and fault characteristics that influenced hydrocarbons migration (Agosta et al. 2009, Rustichelli et al., 2012, 2013).

In the northern part of the Majella Mountain, carbonates of the Oligocene-Miocene Bolognano Formation crop out at several documented locations (Crescenti et al., 1969; Vecsei & Sanders, 1999; Pomar et al., 2004; Brandano

et al., 2012, 2016a, b; Rustichelli et al., 2013). This formation consists of (i) relatively shallow-water skeletal rudstones, floatstones, grainstones, and packstones, which are made up of fragments of larger benthic foraminifera (LBF), bryozoans, red algae and lamellibranches, echinoid plates and spines, and (ii) deeper water marly wackestones and mudstones with planktonic foraminifera (Fig. 1.2).

Based on a variety of diagnostic characteristics, namely dominant biota in the skeletal grain assemblages and depositional architectures, Rustichelli et al. (2012, 2013) subdivided the Bolognano Fm. in five lithofacies (A, B, C, D, E). Each lithofacies is comprised of several facies with specific rock texture and dominant grain size. Within the study area only the lithofacies Au, B, C, E crop out (Fig. 2.2). The carbonate beds within the Roman Valley Quarry generally dip 10°–25° to NE.

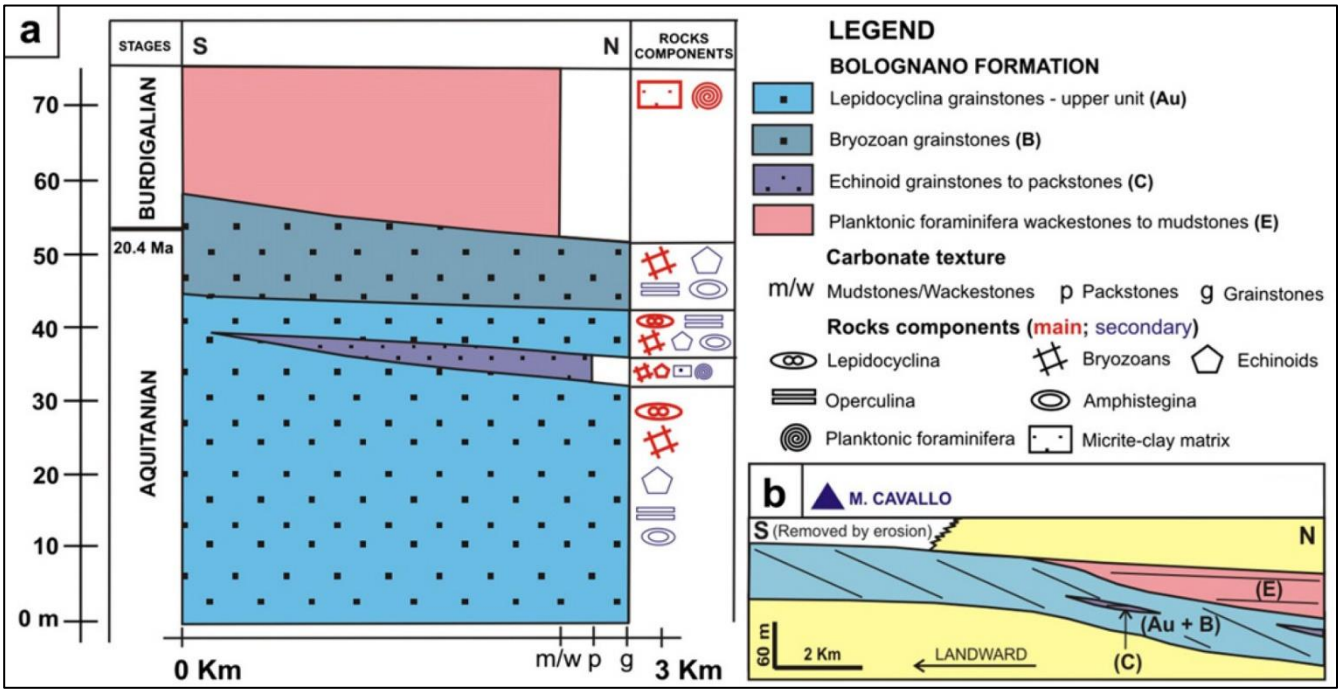

Fig. 1.2. a) Stratigraphic scheme of the lithofacies belonging to the Bolognano Formation (from Rustichelli et al., 2012). b) Schematic cross-section of the Majella Mountain platform margin showing the large-scale architecture of the lithofacies under study (modified after Mutti et al., 1997).

According to Rustichelli et al. (2013), the stratigraphic interval Au includes a 40-to 60-m thick alternation of two dominant facies: (1) medium- to coarse-grained bioclastic grainstones (Au1) and (2) medium-grained bioclastic grainstones (Au2). Lithofacies association B, bryozoan grainstones, consists of 10- to 15-m thick medium-grained grainstones, which mainly differs from facies association A in the type of biota (bryozoans vs. larger benthic foraminifera, especially Lepidocyclina) that dominate the skeletal grain assemblages. Lithofacies association C, echinoid grainstones to packstones, consists of 3- to 5-m thick alternations of two facies, both rich in echinoid plates and spines: (1) fine-grained bioclastic grainstones (C1) and (2) fine- to very fine-grained bioclastic packstones (C2). Argillaceous to marly beds, as much as 3-cm thick, are commonly intercalated with the two facies described above. Facies association E, planktonic foraminifera wackestones to mudstones, consists of a 60–65-m thick alternation of two facies: (1) marly wackestones (E1) and (2) marly mudstones (E2). Both facies have planktonic foraminifera as the predominant skeletal components of the rocks. Lithofacies associations A and B are both arranged in stacks ranging from decimeter to as much as 4-m thick packages of cross-beds bounded by subhorizontal large-scale truncation surfaces. However, lithofacies associations C and E are all arranged in planar beds, which are laterally extensive and onlap onto truncation surfaces present at the top of beds of lithofacies associations A and/or B. lithofacies associations A, C, and E are all composed of cyclic alternations of 10-cm to 2-m thick bed packages of different facies.

The exposed rocks are affected by background and fault-related fractures interpreted as mode I (joints), anti-mode I (pressure solution seams), sheared joints and sheared pressure solution seams (Agosta et al., 2009). According to these authors, background fractures are composed of one set of bed-parallel seams (PS1), two sets of cross-orthogonal bed-perpendicular seams (PS2a and PS2b, respectively), and one set of pressure solution seams oblique to bedding (PS3; Fig. 1.3a). The bed-parallel PS1 set is quite smooth (low roughness and low-amplitude peaks) and mainly localized at the contacts between adjacent beds, as well as within early-formed bed-parallel deformation bands. The two mutually orthogonal bed-perpendicular sets of PS crosscut each other, and often abut against PS1. Both PS2a and PS2b generally have a wavy profile and, in some cases, show evidence of shearing. PS2a strikes E–W to NW–SE and dips more than 70° either N or S; PS2b strikes about N–S and dips more than 75° either E or W. PS3 has a wavy irregular profile, contains mm-thick clay-rich residue material, and

abuts against PS1, PS2a and PS2b. Attitudes of PS3 are quite variable; most of them strike E–W and dip 45°–70° N. Individual PS3 localize at the contractional tips and/or irregularities of the sheared PS1 (Agosta et al. 2009).

In addition to the four sets described above, Agosta et al. (2009) identified three more fault-related structures. Two other sets of pressure solution seams (PS4, PS5) and a mode-one fracture set (JV) clustered along the slip surfaces. PS4 is oriented at a low angle to bedding, whereas PS5 is at a high-angle (Fig. 1.3b, c). Both structures abut against all those pertaining to the background deformation (PS1, PS2 and PS3 as well as the deformation bands). PS4 has a wavy profile and its fractures are up to several cm-long. These structures localize in the contractional quadrants of normally sheared PS2a and PS2b seams. PS5 has a wavy form and localizes in the contractional quadrants and/or irregularities of left-lateral sheared PS2a, as shown in some narrow pavements of the quarry (Agosta et al. 2009).

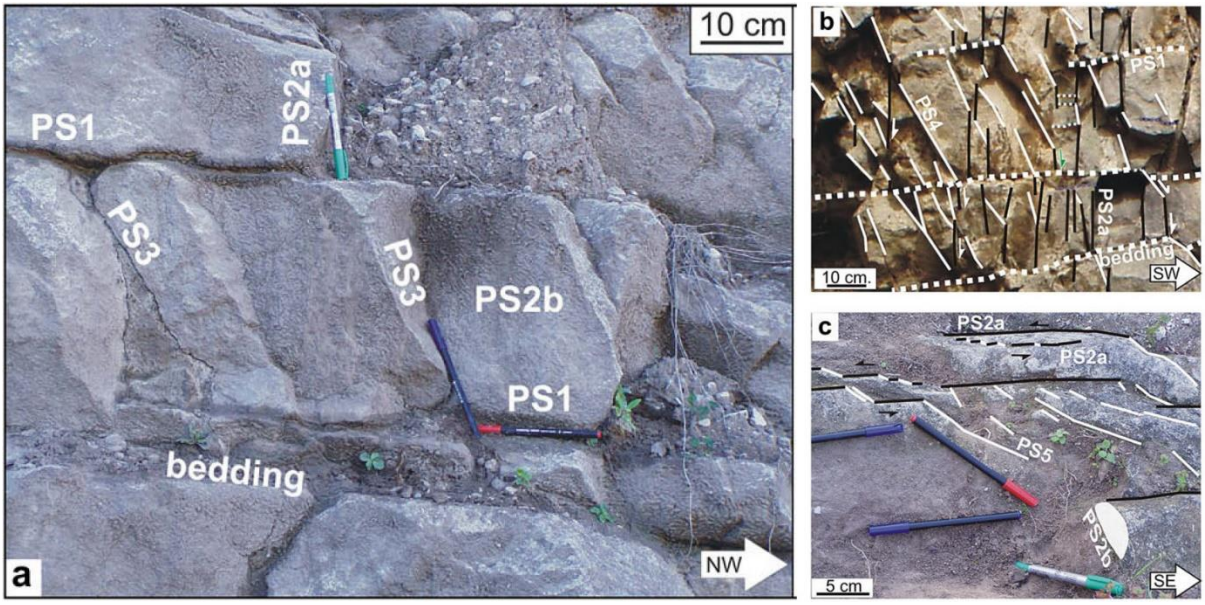

Fig. 1.3 a) Picture with background structures highlighted (PS1, PS2a, PS2b, PS3); b, c) Pictures of the fault related structures (PS4 and PS5) from Agosta et al. (2009).

Within the quarry, the Bolognano Fm. is crosscut by two NW-SE trending oblique-slip normal faults characterized by 10 m (NE Fault, Fig. 1.4) and 40 m (SW Fault, Fig. 1.5) of throw, and a minor left-lateral

component of slip. Due to having different amounts of slip, and dissimilar internal structure, the SW and NE fault are characterized by two different types of permeability structure. The SW Fault, oriented ≈N290° dipping about 75° N, has a seismically detectable throw and, according to Agosta et al. 2010, a conduit-barrier permeability structure (Caine et al., 1996). Conversely, the NE Fault, which has a sub-seismic throw, consists of a fractured zone where several smaller slip surfaces, oriented ≈N270° to ≈N315°, dipping 60° to 80° either to the north or to the south, interact forming many restraining and releasing jogs. The internal structure of the NE Fault is comprised of discontinuous pockets of fault breccia and intensely deformed carbonates surrounded by less-deformed carbonate rocks. According to Agosta et al. (2010) each fault plane forms a conduit for fault-parallel fluid flow; altogether, they form a distributed conduit permeability structure (Caine et al., 1996). Many small faults are present within the SW and NE fault damage zones, which either are confined to individual carbonate beds or crosscut several beds (Agosta et al., 2010).

The bitumen distribution suggests the main hydrocarbon flow occurred through the fault damage zones (Agosta et al., 2009, 2010). The depth of the source of hydrocarbons present in the Roman Valley Quarry is unknown. However, it is clear that the fluids were able to move upward within the fractured rock volumes preferentially within the extensional fault jogs, and then infiltrate laterally into the porous carbonate rocks hosting the faults (Agosta et al., 2010). Field data clearly indicate that the lithofacies B is the most pervaded by bitumen within the matrix followed by the lithofacies Au, conversely the lithofacies C and E do not present oil shows. Agosta et al. (2010) suggested that most of the hydrocarbon migration took place at the Middle-Upper Pleistocene age, when the faults were already exhumed near the surface, because of the presence of bitumen impregnated slope deposits of that age.

Fig. 1.4. Cross-sectional view of the NE Fault zone, showing the nearby bitumen-invaded fracture corridor on the footwall and the highly fractured bitumen-invaded damage zone of the hangingwall.

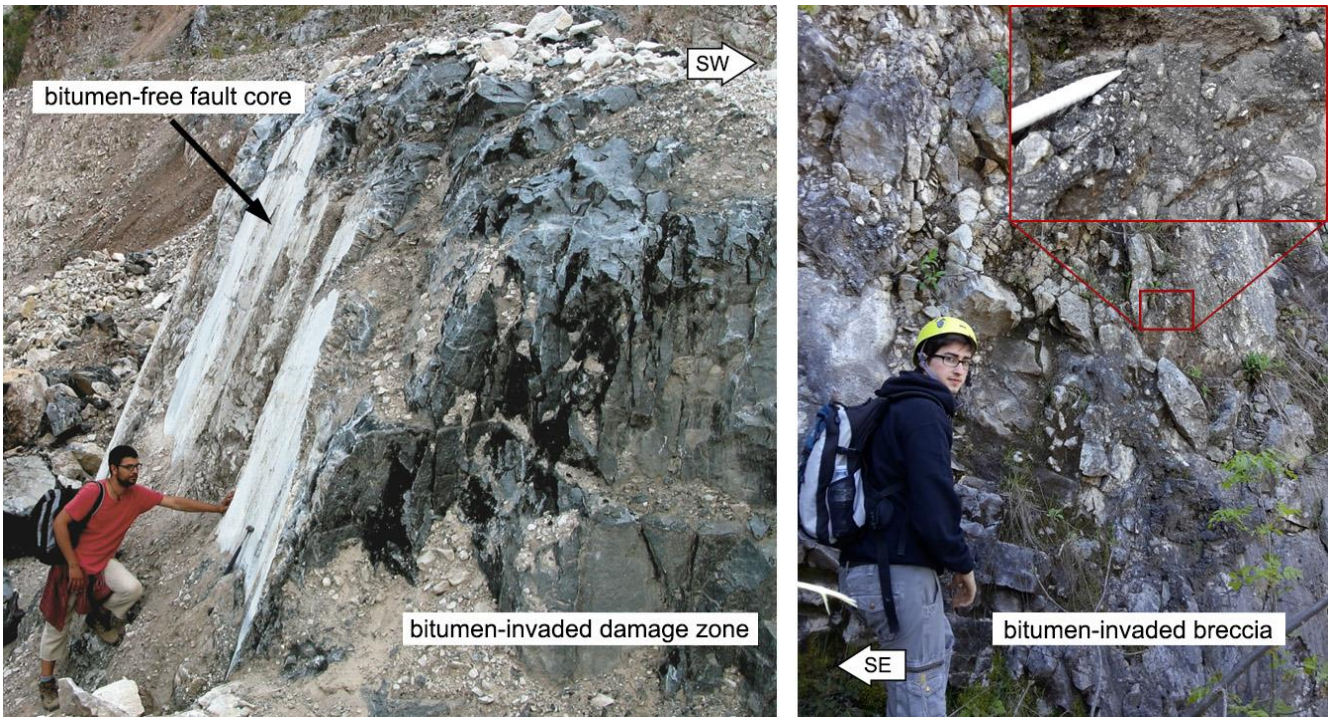

Fig. 1.5. Left: view of the SW fault core, in which the bitumen-free main slip surfaces are bounded, on the footwall side, by bitumen-rich fractured and fragmented carbonates of the fault damage zone (Agosta et al., 2010). Right: Highly fractured SW Fault zone with the bitumen invaded fault breccia.

1.3. Methodology

This work is subdivided in three tasks: i) data acquisition, experiments, ii) model building (DFN, static modelling, dual-porosity/permeability), iii) fluid flow simulations.

In the model construction phase, the reservoir properties (porosity ϕ, permeability k) of matrix and fractures were derived from laboratory and field-based discrete fracture networks models (DFNs), respectively. In the third phase, the dual-porosity/permeability model was used for simulating the fluid flow in two different scenarios of influx at the outcrop scale (400 x 300 x 250 m).

1.3.1. Fracture data acquisition and processing

Fracture data were acquired by means of 26 scanlines (Fig. 1.6), among which 15 were previously reported by Agosta et *al.* (2010). The following fracture parameters were documented: distance from the origin, height, aperture, orientation (dip azimuth and dip angle), abutting relationship, infilling material, the mechanical aperture (E), and the joint roughness coefficient (JRC). The mechanical aperture was measured with a caliper with an accuracy of 0.02 mm (Panza et *al.*, 2015, 2016; Zambrano et *al.* 2016). The JRC was measured by using the Barton comb on fracture surfaces (Olsson & Barton, 2001), within different lithofacies.

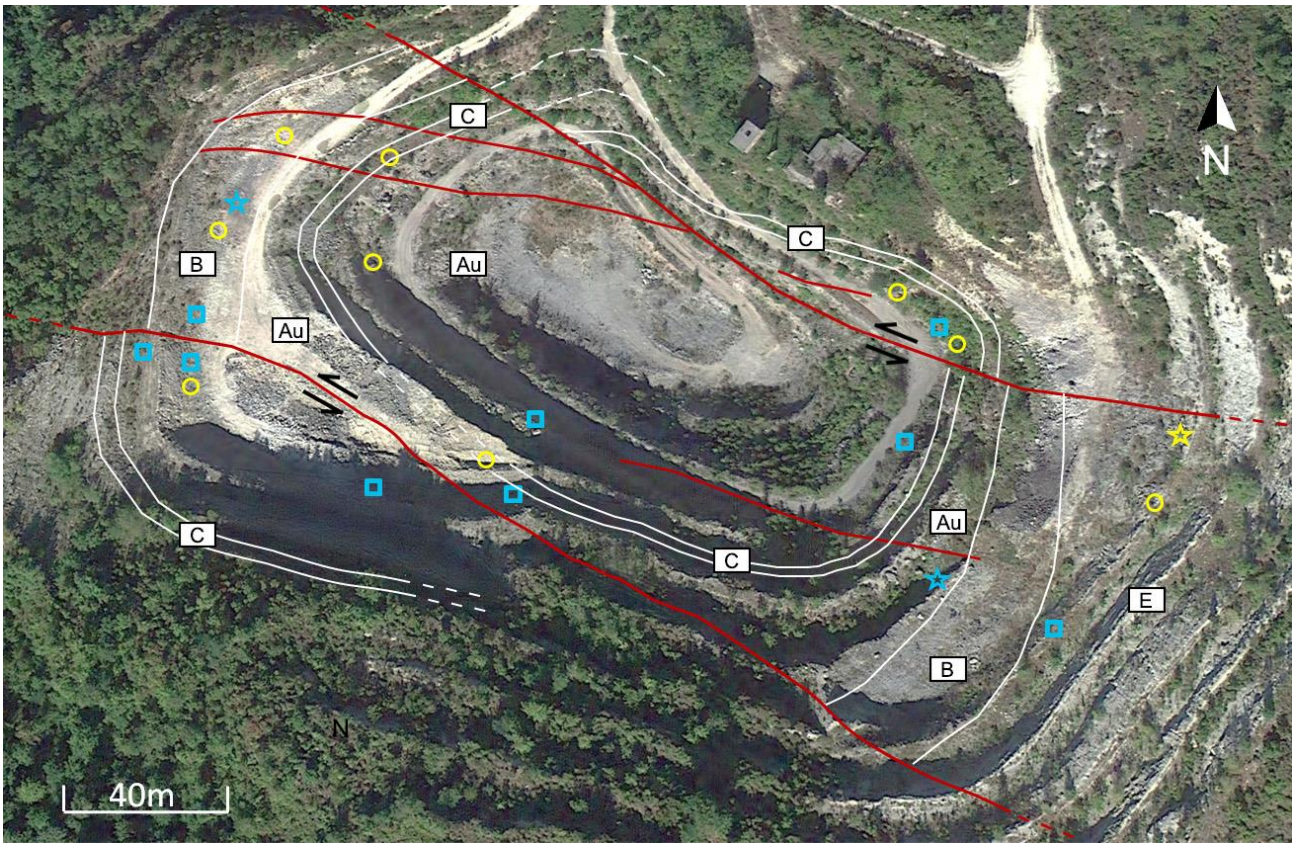

Fig. 1.6. Structural map of the Roman Valley Quarry and measurement locations. Notes: red lines= faults, white lines= lithofacies boundaries. Rectangles with letter indicate the lithofacies label. The box and circle symbols (□, ○) indicate measurement stations of single scanline, the star indicates a station of multiple scanlines. Data from Agosta et al. 2010 (blue); new data from this work (yellow).

The acquired dataset was processed to obtain the stochastic parameters needed to build the DFN models. The fractures were grouped in sets as defined by Agosta et al. (2009) based on orientation and abutting relationships. The variability of the orientation within the cluster is given by the Fisher K value (Fisher, 1953). The hydraulic aperture (e), necessary for calculating the fracture permeability (Snow, 1965), was derived from the mechanical aperture (E) and the JRC parameter based on the following equation (Barton, 1985):

(1) $$e = \frac{E^2}{JRC^{2.5}}$$

The hydraulic aperture was then corrected for a depth of 100 m, because at this depth the stress relaxation, which normally takes place at surface starts to be noticeably compensated. The correction was obtained by using the equation of aperture variation to depth proposed by Wei et al. (1995).

(2) $$\frac{e}{e_i} = 1 - \frac{Z}{A+BZ}$$

Where e_i is the initial hydraulic aperture at the ground surface, Z is the depth in meters and A (58) and B (1.02) are constants relative to the investigated initial hydraulic aperture.

The linear fracture intensity is given in terms of P10 (the number of fractures divided by the length of a scanline) and was obtained from scanline analysis performed on the walls of the quarry (Zambrano et al., 2016). To avoid sampling errors caused by preferential orientation, the Terzaghi (1965) correction was inserted into the equation for calculating the P10 as follows:

(3) $$P_{10} = \frac{N}{l * \cos \alpha}$$

Where N is the number of fractures measured on a scanline of length (l), and, α is the acute angle between the scanline and the mean orientation of a fracture set.

The height measurements obtained from the scanlines performed on the quarry walls were processed for determining the most appropriate power law cumulative distributions of height:

(4) $$CN(H) = A * H^{-c}$$

Where CN(H) is the cumulative number of fractures, c is the exponent of the cumulative distribution, and A is a constant. The cumulative distribution shows a straight line in a log-log plot of CN(H) versus H (Bonnet et al., 2001, and references therein).

The Aspect Ratio of the height (H) and the length (L) of the fracture (H/L) is often assumed to be a fixed value (e.g. 1:/2, 1/4) to simplify the model and because of limitations in measuring both dimensions of the same fracture. In the case of strata-bound fractures, the most sampled fractures in the quarry (*sensu* Agosta et al., 2010), previous authors fixed the H/L ratio to 1/4 (e.g. Panza et al. 2015, 2016). However, more accurate estimation of the aspect

ratio for strata-bound fractures (hosted in platform carbonates) has been performed by Zambrano et al., (2016) by DFN modelling using the length distribution and restricting the fracture height to bed thickness. These authors found that the aspect ratio (H/L) presents an asymmetric distribution varying between 1/1.8 to 1/4.2, with a mode near to 1/2 for fractures bounded by mechanical boundaries (strata, groups of strata). Considering these findings, a fixed aspect ratio of 1/2 is used in the constructed models for all the fractures, including the strata-bound structures.

1.3.2. DFN modelling

In order to model the contribution of fractures to the porosity and permeability of each lithofacies, several Discrete Fracture Network models were built using the 'Fracture Modelling' module of the software MOVE™ academic license provided by Midland Valley Exploration Ltd. to the University of Camerino. The models represented both background deformation (host rock fractures) and fault-related deformation (damage zones). The methodology, recently applied by other authors (Antonellini et al., 2014; Korneva et al., 2014; Panza et al., 2015, 2016; Zambrano et al. 2016), consists of defining five parameters for each fracture set: orientation (dip azimuth, angle of dip, and Fisher K value), length distribution, length/height ratio (single value), volumetric fracture intensity (P_{32}), and hydraulic aperture. The fracture modelling module of MOVE™ is designed for tight rocks (negligible matrix porosity) where porosity and permeability are provided only by the fractures. The software assigns zero values of porosity to those portions of the volume that are not crosscut by any fracture.

For both host rock and damage zone, DFN models were constructed for each lithofacies. The models are cubic in shape, measure 4 m per side, and consist of 64000 cells, each 10 x 10 x 10 cm in size. The host rock DFN models were populated only by background structures (PS2a, PS2b, PS3). The damage zone DFN models were populated with background fractures plus fault-related structures (PS2a, PS2b, PS3, PS4, JV), with exception of the PS5, as they are not common in fault zones (Panza et al., 2017). Furthermore, in this work, the bed-parallel

structures, PS1 and compaction bands (CB), are considered negligible for the fracture network modelling because of their limited length, ranging from 1 to 167 cm (Rustichelli et al., 2012).

The intensity (P_{32}) we assigned to each set of structures, in each lithofacies, was calculated using the workflow proposed by Golder Associates Ltd. (2009) and used by other authors (Antonellini et al. 2014; Korneva et al. 2014; Zambrano et al. 2016). The workflow recommends generating a scatter plot of input P_{32} versus P_{10} values calculated from the DFN modelling software, and fitting a linear intercept to this data to enable conversion of measured P_{10} values into P_{32}. To generate this scatter plot three preliminary (non-calibrated in terms of intensity) DFN models were built using three increasing values of P_{32}. The other parameters (i.e. orientation and height) of the modeled structures were kept equal in all the DFN models. Then several pseudo-wells (scanlines oriented perpendicular to the fracture plane) were "drilled" horizontally through each model to compute the intersections with different fracture sets. The number of intersections divided by the length of the wells gave a P_{10} value. A linear intercept of the data points was calculated to obtain a function in this form:

$$P_{32} = mP_{10} \quad (5)$$

Where m is the slope of the linear intercept. The P_{10} values obtained from field data and normalized for a bed thickness of 25 cm (representative average thickness of the 39 strata analyzed) were inserted into the equation to calculate a P_{32}. The arithmetic average of the calculated intensities was used to build the definitive DFN models (Fig. 1.12).

The fractures of each DFN model are first upscaled into the 10 x 10 x 10 cm cells, resulting in a fracture porosity value (ϕ), and a fracture permeability tensor (k_{ij}) for each cell. The fracture porosity, ϕ, is computed by dividing the total fracture volume contained in each cell, by the volume of the cell. The fracture permeability tensor, k_{ij}, is derived by using the method of Oda (1985), which is based on the geometrical properties of the fracture network, see Zambrano et al. (2016) for more details.

The effective geocellular fracture properties are then further upscaled using arithmetic upscaling in the directions perpendicular to the direction of interest (i, j or k), followed by harmonic averaging in the direction of interest. This results in a single porosity value and permeability tensor for each of the DFN models.

1.3.3. Porosity and permeability laboratory analysis

In order to obtain the porosity and permeability values of the host rock, laboratory measurements were carried out on unfractured rock samples collected from the different lithofacies (Tab. 1.2). The measurements were performed at "L'École et Observatoire des Sciences de la Terre (EOST), Strasburg (France)". Two cylindrical plugs (20-mm in diameter and 40-mm in length) were cored from each rock sample, one perpendicular and one parallel to bedding. Porosity was measured with two techniques: water saturation, and gas pycnometer (Accupyc 1330, see Baud et al., 2009 and Cilona et al., 2012 for more details). Permeability was measured using a gas permeameter using the transient (pulse-decay) method (Brace et al., 1968).

1.3.4. Static model construction

A dual-porosity/permeability model was built using the up-scaled reservoir properties (porosity and permeability) from the laboratory measurements and DFN models, representing the matrix and fracture systems respectively.

Using the software MOVE™, a Digital Elevation Model (DEM) and satellite imagery of the Roman Valley quarry were georeferenced (Fig. 1.7a). The DEM was produced using the software Agisoft PhotoScan®. Finally, the resultant surface is used to map the fault surfaces and the lithofacies boundaries (Fig. 1.7b). These surfaces have been imported into Petrel (licensed for academic use by Schlumberger®) to build the static model using "fault pillar gridding" (Fig. 1.7c). The lithofacies boundary surfaces were used to subdivide the grid into different zones representing the lithofacies within the Roman Valley Quarry (Fig. 1.7d).

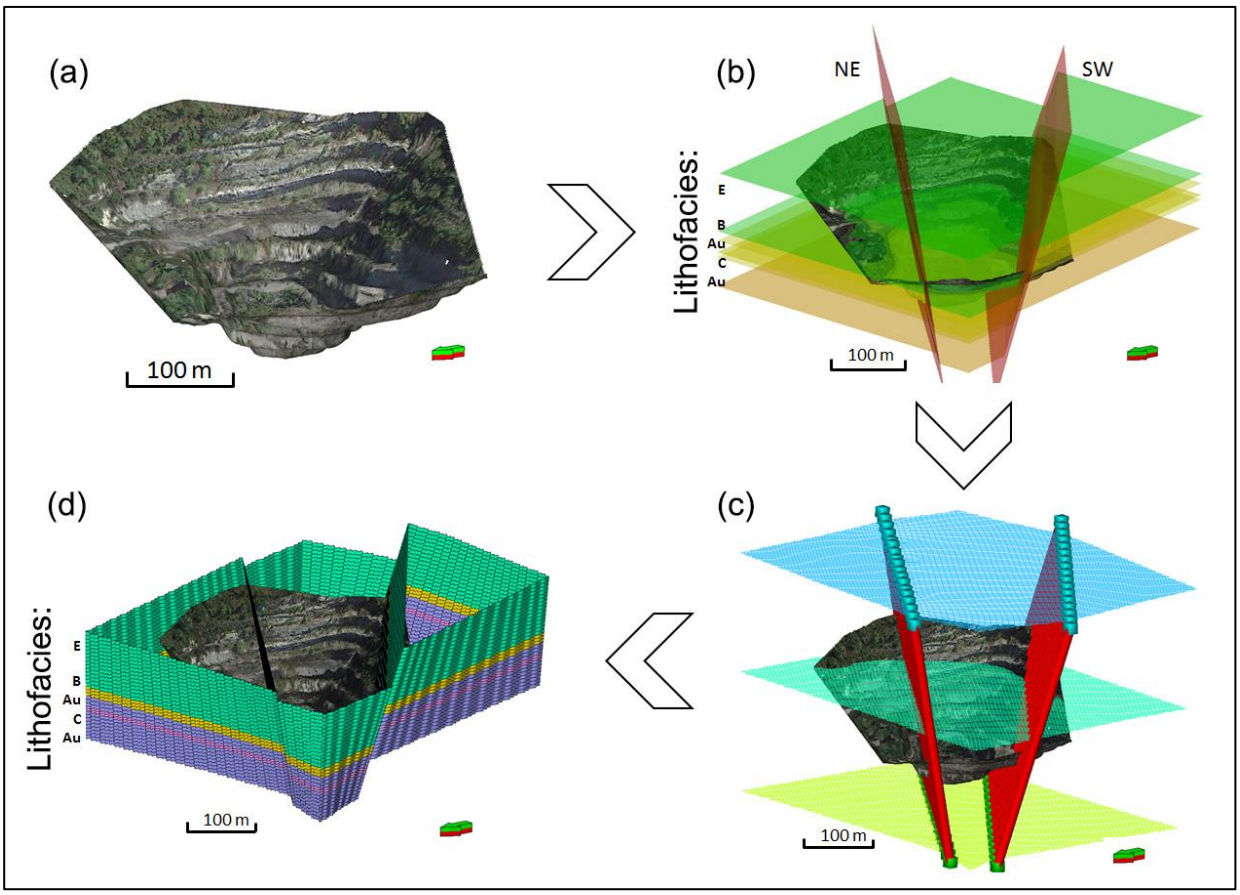

Fig. 1.7. a) Digital Elevation Model (DEM) of the Roman Valley quarry; b) the 3D map of the qurry and the lithofacies bounderies, the NE Fault surface (NE) and the SW Fault surface (SW). c) Pillar fault gridding skeleton; d) Edges of the static model where the lithofacies are displayed.

The obtained grid represents a geocellular volume 417x335 m-wide and 228 m-thick. This grid comprises of 482,856 cubic cells with a dimension of 4 m per side. Matrix porosity and a (isotropic) permeability, obtained from plug measurements (see Section 3.3), are assigned to each of the lithofacies. The fracture system has a porosity value and three distinct permeability values (k_{xx} k_{yy} k_{zz}) for each lithofacies, resulting from the upscaling of the corresponding DFN model. Furthermore, in the fracture system the damage zones belonging to the SW Fault and NE Fault have their own, distinct reservoir properties (Fig. 1.8c, d), also obtained from corresponding DFN models. As the size of the cells in this model, and the size of the DFN models are equal, there is no need for an additional up-scaling step.

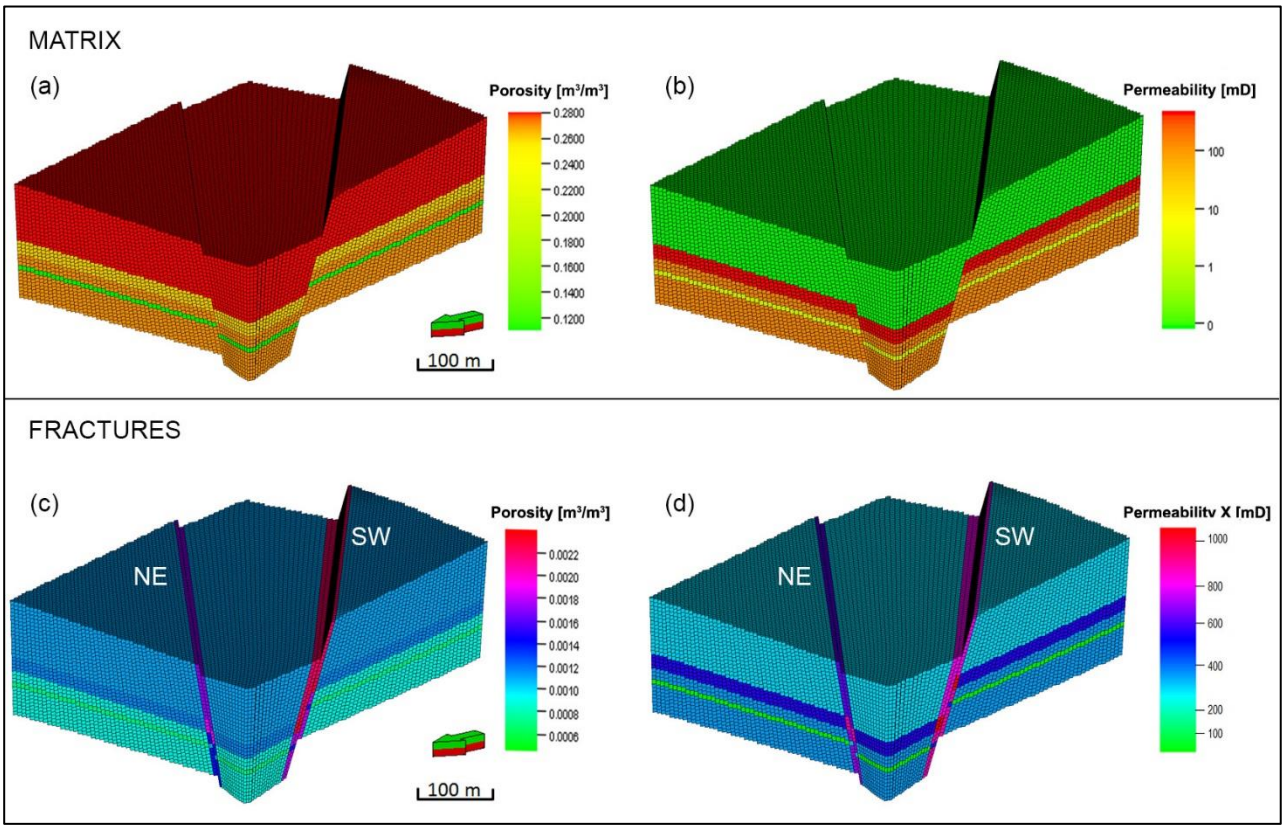

Fig. 1.8. Static models showing the matrix (a, b) and fracture (c, d) properties, with the porosity (a, c) and permeability (b, d) values for each lithofacies. The fracture system representation shows the porosiy and X-permeability values belonging to the NE Fault damage zones (NE) and SW Fault damage zones (SW).

1.3.5. Fluid flow simulations

Both matrix and fracture systems were imported into Dynamo (Shell proprietary software) for running dual-porosity/permeability flow simulations (DP/P). (Warren & Root, 1963; Gerke & Van Genuchten, 1993; Gong et al. 2008; Wei & Zhang, 2010).

DP/P simulations were developed for densely fractured reservoirs where the conductive fractures connect over distances larger than a typical grid cell size, and where they separate the matrix into individual matrix blocks that are smaller than the grid cell size. DP/P approximates the behavior of the matrix-fracture system by modelling the

fractures and the matrix as two separate media that act independently and which, at the scale of a grid cell, each have their own average saturation and pressure. To each grid cell two nodes are assigned: a matrix, and a fracture node, each with its own set of properties. Connections between nodes of neighboring grid cells allow for matrix-matrix and fracture-fracture flow (some DP/P simulators also use matrix-fracture connections between neighboring cells, to model e.g. re-imbibition, Por et al., 1989). To model the interaction between the fractures and the matrix blocks, a flow connection is created between the matrix and the fracture node. The transmissibility of this connection is dominated by the matrix permeability and is governed by a geometrical shape factor (Kazemi et al., 1976). The shape factor is purely geometric and is determined by the area of the fractures available to each matrix block, divided by the characteristic length of a matrix to fracture flow path inside a cell. The characteristic length depends on the orientation and density of the fractures and on the typical matrix-fracture flow direction, i.e., recovery mechanism.

In DP/P simulations all heterogeneities on a scale smaller than a single cell are lost, and so they work best for regular, uniform fracture sets. In this work, the main heterogeneity is found between stratigraphic layers, not inside a grid cell. The aim of this experiment is to evaluate how these heterogeneities, both stratigraphic and structural, affect the fluid flow, and to determine the volume of flow in the fractures compared to the flow in the matrix, in a scenario where hydrocarbons migrate through a water-filled reservoir. Only a single (water) phase was modelled, and the injected fluid was followed by assigning a tracer to the injectant. This shows the control of porosity and permeability in both fractures and matrix, of the different lithofacies on the fluid flow, but ignores two-phase effects such as capillary pressure and gravity between the water and the hydrocarbon phase. This simplification was made for two reasons: 1) the absence of two-phase rock property measurements and hydrocarbon characterization; and 2) we are mainly interested in the effect of permeability and porosity heterogeneity on the migration pathway. The simulation parameters are listed in Table 1.1. By ignoring the capillary pressure between the hydrocarbon injectant and the water present in the matrix, we model a matrix with zero capillary pressure and zero irreducible water saturation. Therefore, this simplification overestimates the amount of injectant that flows from the fractures to the matrix. Because of this, a relatively large geometrical shape factor has been used, which assumes matrix blocks of the size of the grid cell, i.e., in this case fractures spaced about 4 meters apart. Since we

are simulating migration of hydrocarbons through a reservoir, not filling a reservoir trap, we assume we can neglect buoyancy forces caused by density differences between the fluids.

Table 1.1. Fluid flow simulations parameters:

SF	**Rate**	**TS**	**MPV**	**FPV**
0.125 m^{-2}	0.05 PV/year (12.7 FPV/year)	1day	$3.8e^6$ m^3	$1.5e^4$ m^3

Notes: SF= Shape Factor; Rate=injection rate; TS= Time Step; MPV= Matrix Pore Volume; FPV= Fracture Pore Volume.

In this work, we show the results obtained from two simulations. The first experiment, simulating a horizontal influx of the tracer into the grid from the SW corner to the NE one, comprises of the following setting (Fig. 1.9a): i) the wells, producer and injector were located in the SW and NE corners, respectively; ii) the sealing fault segments (cataclasite) have an assigned permeability multiplier equal to 0, whereas the conductive fault segments (breccia) have an assigned permeability multiplier equal to 1; iii) the extent of injector well covers the entire height of the grid from top to bottom.

The second experiment differs from the previous one because the location of the injector well is moved to the bottom of the SW Fault in order to investigate if the fluid flow behavior is consistent with field-derived conclusions presented by Agosta et al. (2010). The authors advocated that in the Roman Valley quarry, hydrocarbons migrated upward from an undefined depth within the fractured rock volumes of the extensional fault jog and then, laterally infiltrated the porous carbonate rocks flanking the faults.

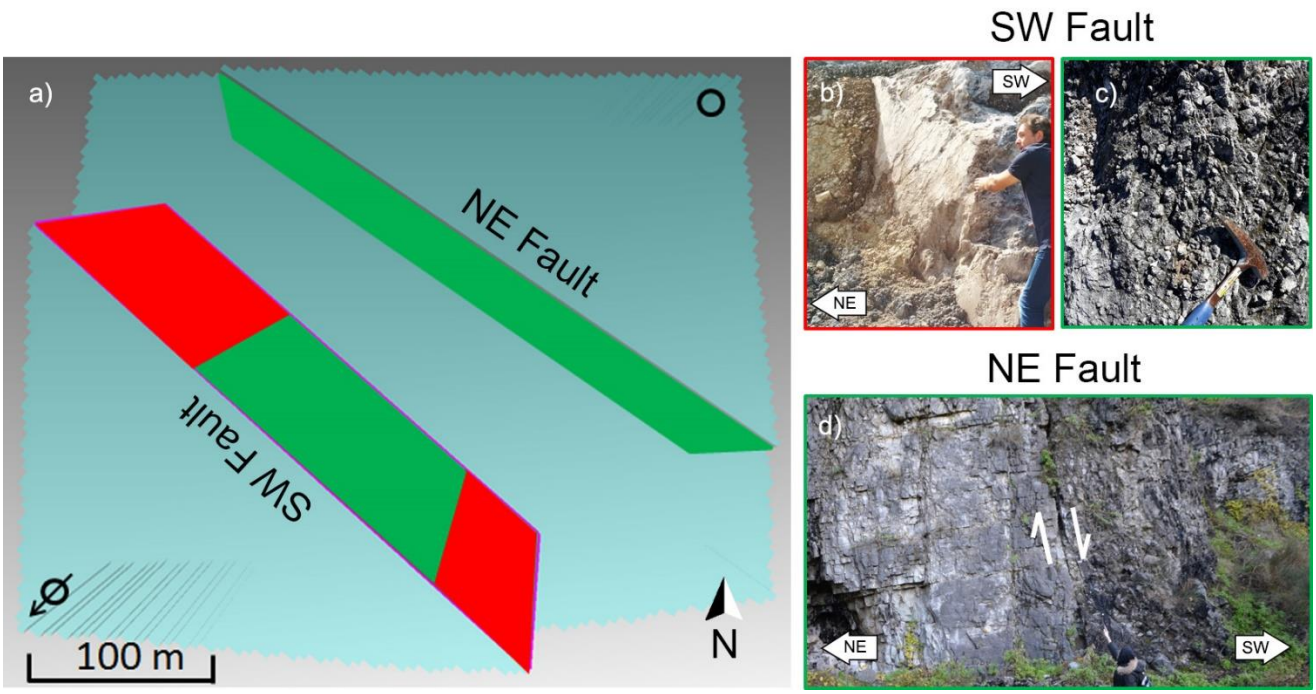

Fig. 1.9.: a) Grid viewed from above showing the base simulation settings: conductive fault segments (green) and the sealing fault segments (red). ⌀ well producer. ○ well injector; b) fault plane representing the "sealing segment" of the SW Fault; c) close-up of bitumen invaded fault breccia representing the "conductive segment" of the SW Fault; d) cross-sectional view of the NE Fault zone.

1.4. Results

1.4.1 Matrix porosity and permeability

The porosity and permeability measured in the selected samples are summed up in Table 1.2. Samples are denoted by the lithofacies abbreviation followed by the direction of the sample, where V is for vertical and H is for horizontal.

The measured porosity indicates that most of the lithofacies have a porosity in the range 26-29%, except for lithofacies C where porosity is about 12%. The lithofacies E showed the highest porosity (28.8%), followed by lithofacies Au (27.6%) and B (26.4%). The porosity results match with porosity measurements performed by Rustichelli et al. (2012, 2013). The grainstones, lithofacies Au and B, showed permeability values four orders of magnitude higher than the lithofacies with higher content of mud (lithofacies C and E). The permeability of lithofacies B and E are very isotropic (kV/ kH>0.8) in contrast to that of lithofacies C (kV/ kH<0.34).

Table 1.2. Porosity and permeability laboratory measurements on matrix samples.

Lithofacies-Orientation	$\Phi_{t\text{-}w}$ [%]	Φ_{pyc} [%]	k-gas [mD]
Au-V (grainstone)	28.4 (SD: 0.26)	27.6 (SD: 0.35)	86.13
Au-H (grainstone)	28.7 (SD: 0.32)	27.5 (SD: 0.90)	160.09
B-V (grainstone)	28.2 (SD: 1.01)	26.7 (SD: 0.38)	444.82
B-H (grainstone)	27.1 (SD: 1.20)	26.1 (SD: 0.50)	530.94
C-V (grain/packstone)	11.4 (SD: 2.29)	10.9 (SD: 0.82)	0.30 (SD: 0.49)
C-H (grain/packstone)	11.7 (SD: 2.23)	10.8 (SD: 0.44)	2.51 (SD: 3.96)
E-V (wack/mudstone)	28.5 (SD: 0.17)	28.6 (SD: 0.17)	0.085
E-H (wack/mudstone)	28.1 (SD: 0.43)	29.0 (SD: 0.43)	0.081

Notes: Results are represented by the arithmetic mean and the standard deviation (SD) if more than one sample were analyzed. $\Phi_{t\text{-}w}$ is the triple weight porosity considering a content of 100% of calcite, Φ_{pyc} is the porosity

obtained with the helium pycnometer and k-gas is the permeability measured by a gas permeameter. Samples were measured in two directions: vertical (V) and horizontal (H).

1.4.2. Fracture geometry and reservoir properties

The results of the analysis of the geometrical properties of the fractures, useful for building the DFN models, are summarized in Table 1.3. Obtained parameters are 1) orientation, 2) fracture intensity (P32), 3) height cumulative distribution parameters, and 4) hydraulic aperture (e).

Table 1.3. DFN model input data processed from quantitative fracture analysis.

Lithofacies /Location	Set	Orientation Dip/Dip_Azi	P_{32}	Height Distribution (min/max/c)	e
Au (SW Fault Damage Zone)	PS2a	82º/202º	8.46	0.12/ 0.52/ 2.3	47.5
	PS2b	86°/106°	6.32	0.12/ 0.50/ 1.2	50.4
	PS3	55°/016°	5.02	0.12/ 0.40/ 1.6	44.9
	PS4	64°/206°	2.08	0.10/ 0.30/ 1.6	38.6
	JV	87°/235°	3.12	0.08/ 0.26/ 1.1	78.7
B (SW Fault Damage Zone)	PS2a	82º/202º	11.84	0.18/ 0.46/ 2.2	52.9
	PS2b	86°/106°	5.44	0.14/ 0.40/ 1.7	50.4
	PS3	55°/016°	6.08	0.10/ 0.32/ 1.3	30.2
	PS4	64°/206°	3.59	0.10/ 0.30/ 1.1	55.5
	JV	87°/235°	7.02	0.16/ 0.34/ 2.1	69.5
C (Host Rock)	PS2a	82º/202º	6.94	0.14/ 0.48/ 0.6	50.4

	PS2b	86°/106°	5.72	0.12/ 0.48/ 0.5	28.3
	PS3	55°/016°	4.04	0.18/ 0.40/ 0.5	36.4
E (Host Rock)	PS2a	82º/202º	9.94	0.10/ 0.60/ 0.7	52.3
	PS2b	86°/106°	7.03	0.12/ 0.56/ 0.5	34.8
	PS3	55°/016°	6.97	0.16/ 0.36/ 0.6	28.2

Notes: Quantitative parameter: P_{32}= fracture intensity [m^2/m^3]; the cumulative distribution of the height [m] is represented by a negative exponential distribution with exponent c, limited by a minimum and a maximum value; e= hydraulic aperture [µm].

The Joint Roughness Coefficient (JRC), used to calculate the hydraulic aperture (e) has the following arithmetic mean: lithofacies Au (9.8; st. dev. 1.08); lithofacies B (10.35; st. dev. 1.64); lithofacies C (7.7; st. dev. 1.43); lithofacies E (7.1: st. dev. 1.5).

As shown in Tab. 1.3 for each lithofacies, PS2a has the highest value of volumetric fracture intensity (P32). In the field, it was not possible to collect data on the fracture intensity in the damage zone of the SW Fault within the lithofacies C and E. Due to the absence of these data in these two lithofacies, the damage zone fracture intensity was assigned by using a similar ratio (P32 host rock / P32 damage zones) of the other lithofacies (i.e., Au, B).

The fracture height distribution of each set can be fitted reasonably well by a power law function (correlation coefficient, R2 >0.85, Fig. 1.10). Deviations from the power law observed at small scale (H < 0.04 m) and large scale (H > 0.35 m) are interpreted as truncation and censoring effects, respectively. The truncation refers to underestimating the small fractures and the censoring to the incomplete observation of long fractures (Bonnet et al., 2001).

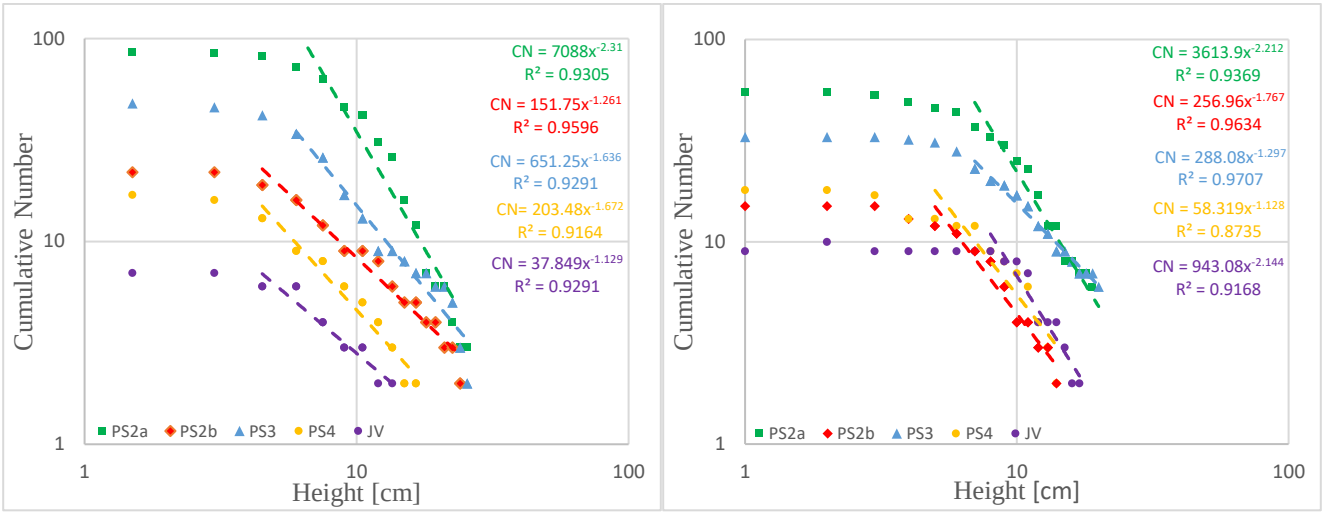

Fig. 1.10. Log-log graphs of the cumulative frequency distribution of fracture heights of lithofacies Au (a) and lithofacies B (b). The different colors indicate individual fracture sets. The height distribution is described by power laws with different exponents (c).

The hydraulic aperture (e) corrected to a depth of 100 m goes from a minimum of 28 µm to about 80 µm (Tab. 1.3). The PS3 structures have the thinnest aperture, whereas the JV are the more open structures (Fig. 1.11).

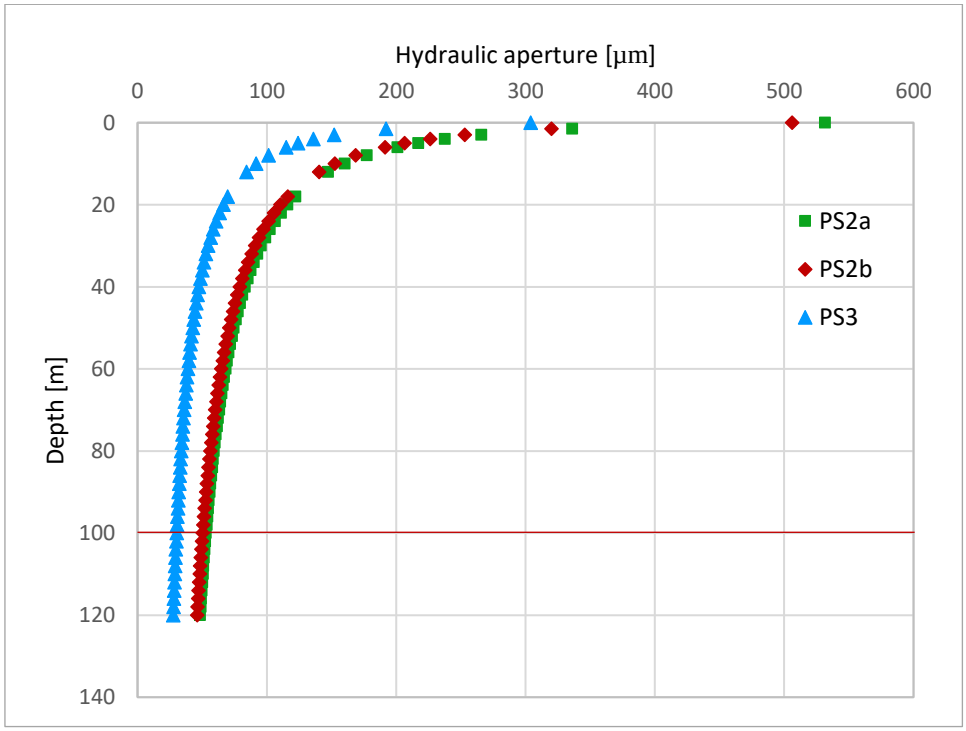

Fig. 1.11. Graph of the hydraulic aperture corrected to various depths.

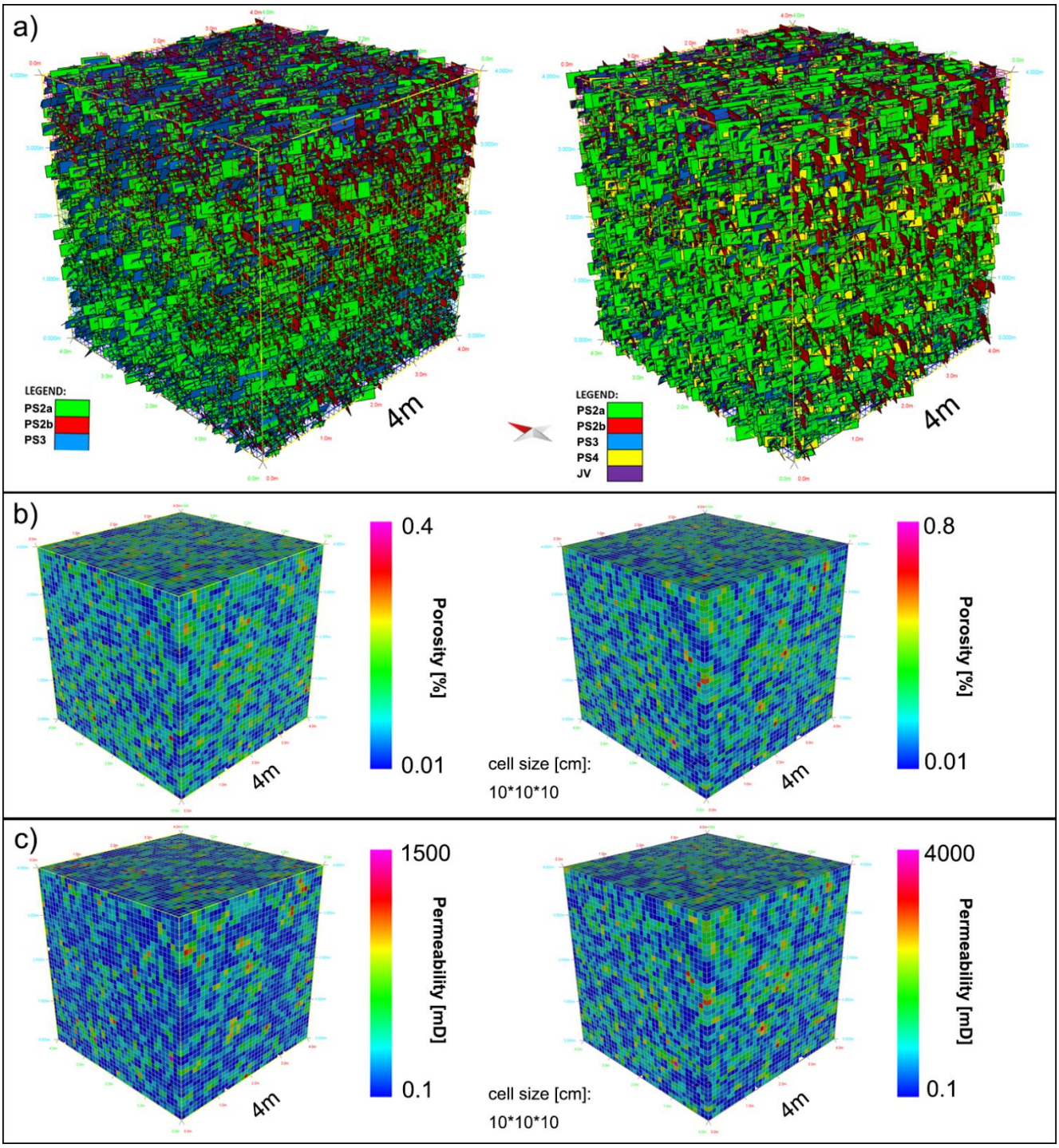

Fig. 1.12. A) Discrete Fracture Network model representing the host rock (left) and SW Fault damage zone (right) of the lithofacies Au. B) Upscaled porosity results. C) Upscaled permeability results K_{xx}.

The effective fracture permeability varies from 40 mD (host rock lithofacies C) to about 1000 mD (SW Fault DZ, lithofacies Au and B). The permeability tensor (kij) is given in terms of the different components (kxx, kyy, kzz, kxy kxz, kxy). The 'xx' direction corresponds to the East direction, 'yy' to the North direction, and 'zz' is to the vertical one. The greatest component of the fracture permeability tensor is the vertical one, kzz. The eastward component of permeability, kxx, is about a 0.8 times kzz, while the northward one, kyy, is about 0.4 times kzz. The permeability anisotropy is higher for the fault damage zone in comparison to the surrounding host rock, whereas the porosity is very low in both cases (<1%).

Table 1.4. Upscaled fracture porosity and permeability

	FACIES Au			**FACIES B**			**FACIES C**			**FACIES E**		
	HR	SWF	NEF	HR	SWF	NEF	HR	SWF	NEF	HR	SWF	NEF
Φ_f [%]	0.09	0.18	0.14	0.12	0.23	0.19	0.07	0.14	0.11	0.11	0.22	0.17
k_{xx} [mD]	225	652	447	344	985	683	105	304	208	197	570	391
k_{yy} [mD]	97	312	177	138	345	252	40	128	73	84	270	153
k_{zz} [mD]	257	813	526	410	1133	839	120	380	245	238	753	487

Notes: HR=Host Rock; SWF= SW Fault Damage Zone; NEF= Fault Damage Zone; Φ_f= Fracture porosity [%]; k_{xx}= average permeability along the horizontal axis (X); k_{yy}=average permeability along the horizontal axis (Y); k_{zz}= average permeability along the vertical axis (Z).

1.4.3. Fluid Flow Simulations

The dual-porosity/permeability numerical experiments are aimed at evaluating how the heterogeneities, both stratigraphic and structural, affect the fluid flow. The dual hydraulic behavior of the SW Fault, so how the fluid behaves encountering the conductive fault segment and the impermeable ones was of specific interest during this phase. Figures 1.13 and 1.14 show two different frames: one for matrix (host rock) and one for fractures, both represent the same simulation.

The first experiment, simulating a horizontal influx of the tracer into the grid from the SW corner to the NE one gives the following changes through time as shown in Figure 1.13:

(A) After three days: the injected tracer has moved into the fractures but has almost not moved into the matrix.

(B) After one week: the matrix of the lithofacies Au and B (higher ϕ and k) starts to be invaded by the injected tracer. Now the tracer through the fractures within the lithofacies Au and B flows clearly faster than in the lithofacies C and E.

(C) After three weeks: the tracer flows within matrix of the lithofacies Au and B and resulting in a decreased flux of the tracer within fractures in those lithofacies, (Fig. 1.13C).

(D) After six weeks: the tracer does not flow yet into the matrix of lithofacies C and E. Conversely, within the fractures the tracer crosses the SW Fault through the conductive fault segment and reaches the NE Fault, while it has surrounded the SW Fault sealing segments where the fault core is made up of cataclasite.

(E) After nine weeks: the tracer has not yet flowed into the matrix of the lithofacies C and E, where the permeability is lower than 1 mD. Through the fractures, the tracer reaches the producer and the NE Fault seems not to affect the flow both horizontally and vertically due to the little vertical displacement (8m) showing an intraformational lithofacies juxtaposition.

The second experiment shows similar results of the first one, in terms of fluid flow variations due to lithological heterogeneity. However, unlike the previous experiment, the injector well is located at the bottom of the SW Fault in order to simulate the influx of a tracer from an underlying source through a fault, and upward leaking toward the west (Fig. 1.14).

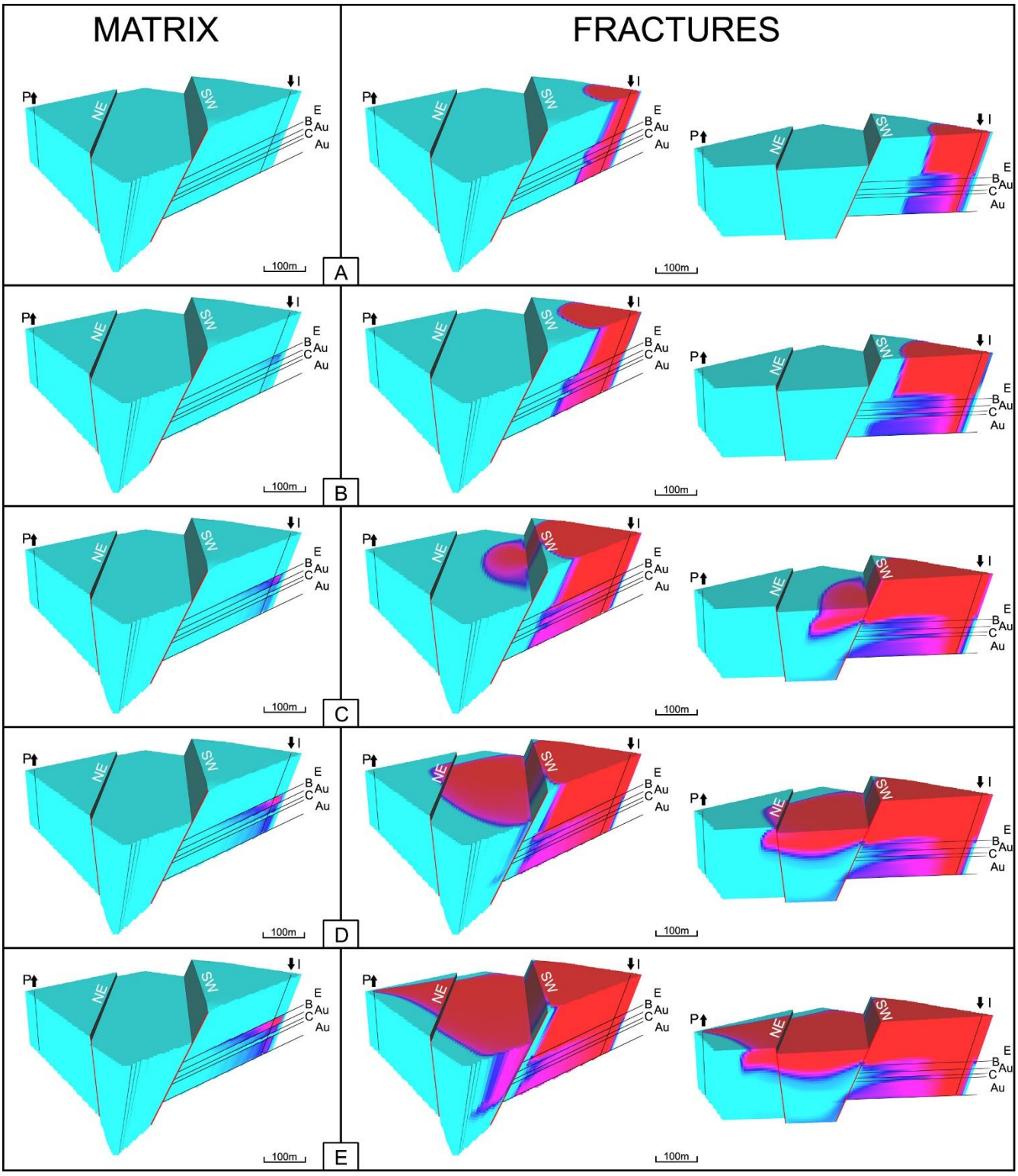

Fig. 1.13. Tracer concentration in matrix (left) and fractures (right). The rightmost images show the cross-section of the model. The color indicates the "tracer concentration": light blue = 0%, red = 100%. I = well injector; P= well producer. Time step simulation: A) 3 Days; B) 1 Week; C) 3 Weeks; D) 6 Weeks; E) 9 Weeks.

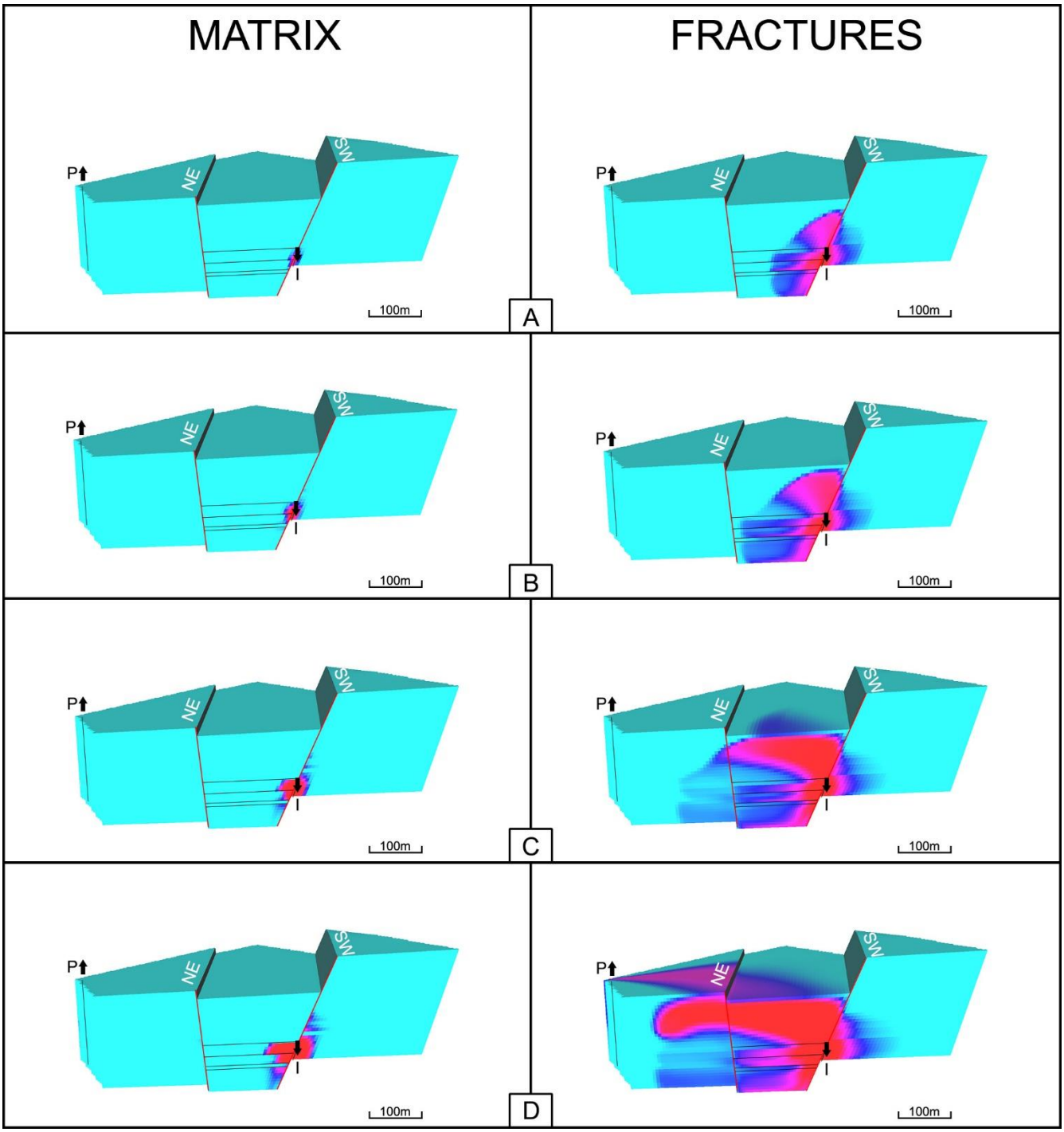

Fig. 1.14. Tracer concentration in matrix (left) and fractures (right). The color indicates the "tracer concentration": light blue = 0%, red = 100%. I = well injector; P= well producer. Time step simulation: A) 3 Days; B) 1 Week; C) 3 Weeks; D) 6 Weeks.

1.5. Discussion

In this section, the results of the stochastic models (DFN) and the fluid flow simulations are discussed and compared to the bitumen distribution observed in the field, where the hydrocarbon is mostly located along the main faults and from there to the adjacent host rock.

The DFN model results showed that high fracture density and connectivity seems to control the fluid flow along the fault damage zones. The components of the fracture permeability tensor subparallel to the faults (K_{xx} and K_{zz}) are about three times higher than the orthogonal one (K_{yy}). These results confirm the field-based interpretation of Agosta et al. (2010), who pointed out that the fluid flow is mainly localized along the tar-rich fractures with larger apertures that are located sub-parallel to the faults.

Other authors worked in the same study area, employing stochastic models (DFN), investigating permeability behavior of fault zones (Panza et al. 2018; Romano et al. 2017). Also, Panza et al. 2018 followed nomenclature and structure classification proposed by Agosta et al. 2009. These authors built several DFN models, using the MOVE™ software, employing different scales of geocellular volumes in which the background deformation (PS2a, PS2b, PS3), and fault related structures (PS4, PS5) along with incipient faults and medium faults were modelled to determine the relative porosity and permeability of fracture network. In terms of fracture porosity, the results obtained by Panza et al. 2018 and Romano et al 2017 are comparable with the results showed in this work, where the fracture porosity component is lower than 1%. For this reason, consistently with Panza et al. 2018, we can say that the matrix porosity, which in all the studied lithofacies ranges between ≈11 and 29%, plays the main role in fluid storage. Matrix porosity and permeability measured from plugs can contribute explaining why the hydrocarbon distribution changes in the different lithofacies. Indeed, the lithofacies Au and B, with high porosity ($\phi \approx 28\%$) and highest permeability (k from 86 to 530mD) are largely impregnated by bitumen into the primary porosity, whereas the lithofacies C and E appear not be invaded by bitumen within the matrix. The explanation for the absence of bitumen within the lithofacies E is given by the pore types. Indeed, in lithofacies E, Rustichelli et al. (2013) documented almost exclusively pores with diameter <20 μm (24-31%) and <1% of macropores (Rustichelli et al., 2013). The pore size is consistent with the very low permeability value ($k \approx 0.08$mD), measured

on the plug, and it would likely have a high capillary entry pressure and larger surface area in contact with the fluid (Zambrano et al., 2018). Whereas in lithofacies C, Rustichelli et al. (2013) documented layers with low amount of intergranular macroporosity (6%) and this could be likely be linked to the poor capacity of this lithofacies of storing bitumen in the matrix pore network.

The DFN model-derived the permeability values presented in this study (Fig. 1.12) are up-to-three orders of magnitude lower than the values obtained by Panza et al. (2018) and Romano et al. (2017) for models employing fault related structures (PS4, PS5) along with medium faults, and six orders of magnitude higher respect to the model of Panza et al. (2018) including only background deformation (PS2a, PS2b, PS3). This divergence could be explained by the different methods used to build DFN models. In particular, we believe that the workflows used to calculate the hydraulic aperture values had a strong impact on the permeability results. Indeed, the large discrepancy among the DFN model results could have been caused by two main differences in modelling workflow: i) in our study, fracture intensity was derived from scanlines and we used the workflow presented by Antonellini et al. (2014) to calculate the P_{32}, whereas Panza et al. (2018) calculated N, an alternative fracture intensity parameter, which indicates the number of fractures along the three axes directions, by using the fracture saturation ratio (S/T), defined as the ratio between the mean fracture spacing, S, and the bed thickness, T. This workflow tends to result into lower fracture intensity; ii) We measured the average JRC value of fractures in the field using the Barton's comb whereas Panza et al. (2018) assigned the maximum JRC value to pressure solutions and the minimum JRC value to joints and faults. These modelling choices lead to a significant variation of hydraulic aperture. Furthermore, we have also applied a depth correction to the hydraulic apertures, which resulted into an additional reduction of this parameter.

The upscaled porosity and permeability of the fractures, obtained from DFN models in the different lithologies, have been assigned to the grid used for the dual-porosity/permeability monophasic simulations. The results of the fluid flow simulations are analyzed only qualitatively since we are interested only in obtaining a general understanding of the flow distribution in the study area.

During the investigated timeframe, the injected fluid infiltrates the matrix only within the lithofacies Au and B, whereas it is not able to flow into the lithofacies C and E. These results are consistent with field observation, where the lithofacies Au and B show abundant bitumen impregnation into the primary porosity, whereas lithofacies C and E show negligible impregnation.

Field observations indicate that only the fractures within the most permeable rocks (lithofacies Au, B) are filled with bitumen (Agosta et al., 2010). Inversely, the fractures hosted in the tight lithofacies (i.e., C, E) have little or unclear traces of bitumen. Nevertheless, simulations indicated that fractures seem to enable a faster transport through the lithofacies E with respect to more permeable lithofacies B and Au. These results are consistent with the fact that, in a fractured porous medium, fluids flow faster in the fractures with respect to the matrix, and then migrate from fractures to matrix (Douglas and Arbogast, 1990). In other words, the flow is faster in fractures associated with lithofacies E because it is not able to migrate to the surrounding host rock. In contrast, because a greater volume of tracer is able to flow into the matrix component of the lithofacies Au and B less tracer volume is available for flowing into the fractures. This, in turn, results in a shortening of the fluid front with respect to the lithofacies E despite higher permeability. Simulations at higher geometrical shape factors, i.e. larger communication between fractures and the matrix, show a similar trend, but with increasing flow into the highly permeable matrix layers, and associated decrease of flow in the fractures in those layers.

The first numerical experiment (Fig. 1.13) assesses the influence of the SW Fault zone on the fluid flow in a scenario where fluid migrates orthogonally with respect to the fault. The fluid flow across the faults is strongly impacted by the fault rock type and its continuity. Fault cores composed of low porosity and low permeability cataclasite inhibit the flow across the fault (Billi et al. 2003; Micarelli et al. 2006), consistently with field observations where adjacent bitumen-invaded and free-tar rock volumes are isolated. However, fault segments dominated by fault breccia permit fluid flow across the fault (Billi et al. 2003; Korneva et al. 2014; Laurita et al. 2016). The simulations show that the fluid that crosses the conductive fault segment immediately surrounds the sealing fault segments. This suggests that even if the dominant fluid direction of migration direction (from SW to NE) coincides with the K_{yy} permeability component (sub-orthogonal to the faults), because K_{xx} permeability component (sub-parallel to the fault strike) is about three times higher than K_{yy}, then fluids spread along the fault

strike instead of directly crossing the fault (Caine & Forster, 1999; Jourde et al., 2002). This simulation highlights the importance of accounting for fault-induced permeability anisotropy while producing hydrocarbons from a reservoir. Along-strike variation and continuity of the type of fault rocks may result in large permeability anisotropy and have strong impact on the fluid pathways and volume of fluids stored (Flodin et al., 2001; Jourde et al., 2002; Faulkner et al., 2010).

The results of the second numerical experiment show that the tracer within fractures flows faster in the upward direction along the SW Fault damage zones with respect to the host rock. In fact, 100% tracer concentration (red color) along the damage zones reaches the surface (top boundary of the model) before being distributed in the horizontal direction (Fig 1.14B). This fluid flow behavior is consistent with field-derived conclusions presented by Agosta et al. (2010). The hydrocarbons migrated upward within the fractured rock volumes of the fault zones and then, laterally infiltrated the porous carbonate rocks flanking the faults.

1.6. Conclusions

This work focused on investigating the impact of structural and lithological heterogeneities on fluid flow within a porous carbonate reservoir by using monophasic fluid flow simulations through a dual-porosity/permeability model.

The porosity and permeability of four distinct lithofacies (Au, B, C and E) from the Bolognano Formation (Oligocene-Miocene ramp grainstones to mudstones) have been measured. Dual-porosity/permeability flow simulations were run in a layer-cake model, of the size of the Roman Valley Quarry subdivided in four lithofacies. In addition, two main fault zones (SW Fault and NE Fault) were discretely modelled to test the heterogeneity contribution of both damage zones (derived from DFN models) and fault cores (conductive in the fault breccia and sealing in the cataclasite).

The experiments give the following conclusions:

- Permeability, distribution and type of fault cores have a strong impact on the fluid migration across the fault zones.
- Fracture distribution within the fault damage zones and the derived-permeability anisotropy may influence the fluid migration even when the injector-producer wells are aligned perpendicular to the fault.
- The anisotropy derived by the interplay of fractures and fault core may affect the reservoir migration during production.

In this modelling exercise fractures have the main control on fluid migration. However, in the case of high matrix permeability, a large volume of tracer goes through the matrix component resulting in a decreased speed of the fluid front moving in the fractures. The fluid intrusion into the matrix reflects the field observations, where the bitumen shows are only in the most permeable lithofacies (Au, B) whereas the lithofacies C and E do not contain bitumen.

Finally, this work pointed out the need of combining very detailed field data analysis with conventional reservoir characterization to capture the effect of sub-seismic lithological and structural heterogeneities on flow and storage of fluids.

Acknowledgements

This research was supported by the FAR Project 2014 “Characterization and modelling of natural reservoirs of geofluids in fractured carbonate rocks”, funded by the University of Camerino, P.I. Prof. Tondi and the Reservoir Characterization Project (www.rechproject.com). T.V. carried out part of this work while being hosted by the Carbonate Research Team, Shell Global Solutions International B.V., his stay was sponsored by the Grant for “MsC graduates for further study or training outside Italy” from the University of Camerino. We would like to acknowledge the use of Dynamo (Shell proprietary software) and express our gratitude to Shell Italia for encouraging and supporting this integrated effort. We are grateful to Alan Pitts for revising the grammar and the orthography of this paper and to two anonymous reviewers whose comments improved the quality of the manuscript.

References

Agosta, F. & Kirschner, D.L. 2003. Fluid conduits in carbonate-hosted seismogenic normal faults of Central Italy. Journal of Geophysical Research 108, B4, 2221.

Agosta, F., Aydin, A., 2006. Architecture and deformation mechanism of a basinbounding normal fault in Mesozoic platform carbonates, central Italy. J. Struct. Geol. 28, 1445e1467.

Agosta, F., Alessandroni, M., Antonellini, M., Tondi, E., Giorgioni, M., 2010. From fractures to flow: a field-based quantitative analysis of an outcropping carbonate reservoir. Tectonophysics 490, 197e213.

Agosta, F., Alessandroni, M., Tondi, E., Aydin, A., 2009. Oblique-slip normal faulting along the northern edge of the Majella anticline: inferences on hydrocarbon migration and accumulation. Journal of Structural Geology 31, 674-690.

Al-Hinai, S., Q. J. Fisher, B. Al-Busafi, P. Guise, C. A. Grattoni, (2008). Laboratory measurements of the relative permeability of cataclastic fault rocks: An important consideration for production simulation modelling. Marine and Petroleum Geology, vol. 25, Issue 6, 473-485. Doi: 10.1016/j.marpetgeo.2007.07.005.

Antonellini M., Tondi E., Agosta F., Aydin A., Cello G. 2008. Failure modes in deep-water carbonates and their impact for fault development: Majella Mountain, Central Apennines, Italy., Marine and Petroleum Geology, 25, 1074–1096.

Antonellini M., Cilona A., Tondi E., Zambrano M. & Agosta F. (2014). Fluid-flow numerical experiments of faulted porous carbonates, Northwest Sicily (Italy). Marine and Petroleum Geology, 55, 186-201.

Aydin, A. 2000. Fractures, faults, and hydrocarbon entrapment, migration and flow. Marine and Petroleum Geology, 17, 797-814.

Aydin, A., Antonellini, M., Tondi, E., Agosta, F., 2010. Deformation along the leading edge of the Majella thrust sheet in central Italy. J. Struct. Geol. 32, 1291e1304. http://dx.doi.org/10.1016/j.jsg.2008.10.005.

Baud, P., Vinciguerra, S., David, C., Cavallo, A., Walker, E., Reuschle, T., 2009. Compaction and failure in high porosity carbonates: mechanical data and microstructural observations. Pure Appl. Geophys. 166, 869e898. http://dx.doi.org/10.1007/s00024-009-0493-2.

Bense, V.F., Gleeson, T., Loveless, S.E., Bour, O., Scibek, J., (2013). Fault zone hydrogeology. Earth Sci. Rev. 127, 171-192. Doi: 10.1016/j.earscirev.2013.09.008

Billi, A. 2005. Grain size distribution and thickness of breccia and gouge zones from thin (<1m) strike-slip fault cores in limestones. Journal of Structural Geology, 27, 1823-1837.

Billi, A., Salvini, F. & Storti, F. 2003. The damage zone-fault core transition in carbonate rocks: implications for fault growth, structure and permeability. Journal of Structural Geology, 25, 1779–1794.

Bonnet E., Bour O., Odling N., Davy P., Main I., Cowie P., Berkowitz B. (2001). Scaling of fracture systems in geological media. Reviews of Geophysics, 39 (3), 347-383.

Brace W.F. & Orange A.S., (1968). Further Studies of the Effects of Pressure on Electrical Resistivity of Rocks. Journal of Geophysical Research, vol. 73, n. 16, 5407-5420.

Brandano M., Cornacchia I., Raffi I, Tomassetti L. (2016a). The Oligocene-Miocene stratigraphic evolution of the Majella carbonate platform (Central Apennines, Italy). Sedimentary Geology, 333, 1-14.

Brandano M., Tomassetti L., Sardella R. and Tinelli C. (2016b). Progressive deterioration of trophic conditions in a carbonate ramp environment:the Lithothamnion Limestone, Majella Mountain (Tortonian–early Messinian, central Apennines, Italy). Palaios, DOI: 10.2110/palo.2015.022.

Brandano, M., L. Lipparini, V. Campagnoni, and L. Tomassetti, 2012. Downslope-migrating large dunes in the Chattian carbonate ramp of the Majella Mountains (Central Apennines, Italy): Sedimentary Geology, v. 255–256, p. 29–41, doi:10.1016/j.sedgeo.2012.02.002.

Caine, J.S., and Forster, C.B., 1999. Fault zone architecture and fluid flow: Insights from field data and numerical modeling, in Haneberg, W.C., et al., eds., Faults and subsurface fluid flow in the shallow crust: American Geophysical Union Geophysical Monograph 113, p. 101–127.

Caine, J.S., Evans, J.P. & Forster, C.B. (1996). Fault zone architecture and permeability structure. Geology, 24, 1025-1028.

Cello, G., Tondi, E., Micarelli, L. Invernizzi, C. 2001. Fault zone fabrics and geofluid properties as indicators of rock deformation modes. Journal of Geodynamics, 32, 543–565.

Cilona, A., Baud, P., Tondi, E., Agosta, F., Vinciguerra, S., Rustichelli, A., Spiers, C.J., 2012. Deformation bands in porous carbonate grainstones: field and laboratory observations. J. Struct. Geol. 45, 137e157. http://dx.doi.org/10.1016/j.jsg.2012.04.012.

Crescenti, U., A. Crostella, G. Donzelli, and G. Raffi, 1969. Stratigrafia della serie calcarea dal Lias al Miocene nella regione Marchigiano-Abruzzese: Memorie della Società Geologica Italiana 8, p. 343–420.

Dean R.H. & Lo L.L. 1988. Simulations of Naturally Fractured Reservoirs. SPE Reservoir Engineering, May 1988, pp. 638-648.

Douglas, J., Jr., & Arbogast, T., 1990. Dual-porosity models for flow in naturally fractured reservoirs, in: J.H. Cushman (Ed.), Dynamics of Fluids in Hierarchical Porous Media, Academic Press, London, pp. 177–221.

Faulkner, D.R., Jackson, C.A.L., Lunn, R.J., Schlische, R.W., Shipton, Z.K., Wibberley, C.A.J., Withjack, M.O., (2010). A review of recent developments concerning the structure, mechanics and fluid flow properties of fault zones. J. Struct. Geol. 32, 1557e1575.

Ferrill D. A., Winterle J., Wittmeyer G., Sims D., Colton S. & Armstrong A. (1999). Stressed rock strains groundwater at Yucca Mountain, Nevada. GSA Today, 9, 1-8.

Fisher, Q. & Jolley, S. (2007). Treatment of faults in production simulation models. Geological Society, London, Special Publications. 292. 219-233. Doi: 10.1144/SP292.13.

Flodin E.A., Aydin A., Durlofsky L.J. & Yeten B. (2001). Representation of fault zone permeability in reservoir flow models. SPE Annual Technical Conference and Exhibition, 30 September- 3 October, New Orleans, Louisiana.

Forster C.B. & Evans J.P. (1991). Hydrogeology of thrust faults and crystalline thrust sheets: results of combines field and modelling studies. Geophys. Res. Let., 18, 979-982.

Fossen, A., (2016). Structural Geology. Cambridge University Press, The Edinburgh Building, Cambridge CB2 8RU, UK, p. 524.

Fisher R. (1953). Dispersion on a sphere. Proc. R. Soc. Lond. A217 (1130), 295-305.

Garland, J., Neilson, J.E., Laubach, S.E., Whidden, K.J., 2012. Advances in carbonate exploration and reservoir analysis, in: Garland, J., Neilson, J.E., Laubach, S.E., Whidden, K.J. (Eds.), Advances in Carbonate Exploration and Reservoir Analysis. Geological Society of London, Special Publication 370, 1-15.

Gerke, H.H., & Van Genuchten, M.T. 1993. A Dual-Porosity Model for Simulating the Preferential Movement of Water and Solutes in Structured Porous Media. Water Resources Research, vol. 29, n. 2, pp. 305-31

Ghisetti, F. & Vezzani, L. 1998. Geometrie deformative ed evoluzione cinematica dell'Appennino centrale. Studi Geologici Camerti, XIV, 127-154.

Ghisetti, F. & Vezzani, L. 2002. Normal faulting, extension and uplift in the outer thrust belt of the central Apennines (Italy): role of the Caramanico fault. Basin Research, 14, 225-236.

Giorgioni, M., Iannace, A, D'Amore, M., Dati, F., Galluccio, L., Guerriero, V., Mazzoli, S., Parente, M., Strauss, C., Vitale, S., 2016. Impact of early dolomitization on multi-scale petrophysical hetero-geneities and fracture

intensity of low-porosity platform carbonates (Albian-Cenomanian, southern Apennines, Italy). Marine and Petroleum Geology, 73, 462-478.

Golder Associates Ltd. (2009) - Derivation of Basic Fracture Properties. Golder Associates Ltd., Portland, USA.

Gong B., Karimi-Fard M., Durlofsky L.J. 2008 Upscaling discrete fracture characterizations to dual-porosity, dual-permeability models for efficient simulation of flow with strong gravitational effects. March 2008 SPE Journal, pp. 58-67.

Graham, B., Antonellini, M., Aydin, A., 2003. Formation and growth of normal faults in carbonates within a compressive environment. Geology 31, 11e14.

Graham-Wall, B., Girgacea, R., Mesonjesi, A., Aydin, A., 2006. Evolution of fluid pathways through fracture controlled faults in carbonates of the Albanides fold-thrust belt. AAPG Bulletin 90, 1227-1249.

Hsieh C.M., Murley P. C., O'brien R. R. (1981) A field-funneling effect on the collection of alpha-particle-generated carriers in silicon devices. IEEE Electron Device Letters, vol. edl-2, no. 4, pp. 103-105.

Jourde H., Flodin E.A., Aydin A., Durlofsky L.J., Wen X.H. (2002). Computing permeability of fault zones in eolian sandstone from outcrop measurements. AAPG Bulletin, 86 (7) (2002), pp. 1187-1200.

Kazemi, H., Merrill, L. S., Porterfield, K. L., & Zeman, P. R. (1976). Numerical Simulation of Water-Oil Flow in Naturally Fractured Reservoirs. Society of Petroleum Engineers. SPE 5719-PA. 317-326.

Korneva I., Tondi E., Agosta F., Rustichelli A., Spina V., Bitonte R. & Di Cuia R. (2014a). Structural properties of fractured and faulted Cretaceous platform carbonates, Murge Plateau (Southern Italy). Marine and Petroleum Geology, 57, 312-326.

Marchegiani L., Van Dijk J. P., Gillespie P. A., Tondi E. & Cello G. 2006. Scaling properties of the dimensional and spatial characteristics of fault and fracture systems in the Majella Mountain, central Italy. In: Cello G. & Malamud B. (Eds) Fractal Analysis for Natural Hazards. Geological Society of London, Special Publications, 261, 113–131.

Matthai S., Aydin A., Pollard D., Roberts S. (1998). Numerical simulation of deviations from radial drawdown in a faulted sandstone reservoir with joints and zones of deformation bands. In: Jones G., Fisher Q. & Knipe R., Faulting, Fault Sealing and Fluid Flow in Hydrocarbon Reservoirs. Geological Society of London, Special Publication, 147, 157-191.

Micarelli, L., A. Benedicto, C. Invernizzi, B. Saint-Bezar, J.L. Michelot, P. Vergely, (2005). Influence of P/T conditions on the style of normal fault initiation and growth in limestones from the SE-Basin, France. Journal of Structural Geology, vol. 27, issue 9, 1577-1598. Doi: 10.1016/j.jsg.2005.05.004.

Micarelli, L., A. Benedicto, C.A.J. Wibberley (2006a). Structural evolution and permeability of normal fault zones in highly porous carbonate rocks. Journal of Structural Geology, vol. 28, issue 7, 1214-1227. Doi: 10.1016/j.jsg.2006.03.036.

Micarelli L., I. Moretti, M. Jaubert, H. Moulouel (2006b). Fracture analysis in the south-western Corinth rift (Greece) and implications on fault hydraulic behavior. Tectonophysics, vol. 426, issues 1-2, 31-59. Doi: 10.1016/j.tecto.2006.02.022.

Nieto J.E. & Jensen J. (2012). Analysis of fault 481 permeability using mapping and flow modelling, Hickory Sandstone Aquifer, Central Texas. Natural Resources Research, 21 (3).

Oda M. (1985). Permeability tensor for discontinuous rock masses. Geotechnique, 35 (4), 483-495.

Olsson R. & Barton N. (2001). An improved model for hydromechanical coupling during shearing of rock joints. Int J Rock Mech Min Sci, 38 (3), pp. 317-329.

Panza E., F. Agosta, M. Zambrano, E. Tondi, G. Prosser, M. Giorgioni, J.M. Janiseck (2015). Structural architecture and Discrete Fracture Network modelling of layered fractured carbonates (Altamura Fm., Italy) Ital. J. Geosci., 134 (3), pp. 409.

Panza E., F. Agosta, A. Rustichelli, M. Zambrano, E. Tondi, G. Prosser, M. Giorgioni, J.M. Janiseck (2016). Fracture stratigraphy and fluid flow properties of shallow-water, tight carbonates: the case study of the Murge Plateau (southern Italy) Mar. Petrol. Geol., 73, pp. 350-370.

Panza, E., Sessa, E., Agosta, F., Giorgioni, M., (2018). Discrete Fracture Network modelling of a hydrocarbon-bearing, oblique-slip fault zone: Inferences on fault-controlled fluid storage and migration properties of carbonate fault damage zones, Marine and Petroleum Geology, doi: 10.1016/j.marpetgeo.2017.09.009.

Pomar, L., Brandano, M., & Westphal, H. 2004. Environmental factors influencing skeletal grain sediment associations: a critical review of Miocene examples from the western Mediterranean. Sedimentology, 51, 627-651.

Por, G.J., P. Boerrigter, J.G. Maas, A. de Vries. (1989). A Fractured Reservoir Simulator Capable of Modeling Block-Block Interaction, Society of Petroleum Engineers SPE-19807-MS, 373-380.

Rawling G.C, Goodwin, L.B. & Wilson, J.L. 2001. Internal architecture, permeability structure, and hydrologic significance of contrasting fault-zone types. Geology, 29, 43–46.

Rustichelli, A., Agosta, F., Tondi, E., Spina, V., 2013a. Spacing and distribution of bed-perpendicular joints throughout layered, shallow-marine carbonates (Granada Basin, southern Spain). Tectonophysics 582, 188-204.

Romano, V., Hyman, J.D.H., Karra, S., Valocchi, A. J., Battaglia, M., Bigi, S., (2017) Numerical modeling of fluid flow in a fault zone: a case of study from Majella Mountain (Italy), Energy Procedia, 125, 556-560.

Rustichelli, A., Di Celma, C., Tondi, E. & Bianucci, G. 2016. Deformation within the Pisco Basin sedimentary record (southern Peru): Stratabound orthogonal vein sets and their impact on fault development. Journal of South American Earth Sciences, 65, 79–100.

Rustichelli, A., Tondi, E., Agosta, F., Cilona, A., Giorgioni, M., 2012. Development and distribution of bed-parallel compaction bands and pressure solution seams in the Bolognano Formation carbonates (Majella Mountain, Italy). J. Struct. Geol. 37, 181e199. http://dx.doi.org/10.1016/j.jsg.2012.01.007.

Rustichelli, A., Tondi, E., Agosta, F., Di Celma, C., Giorgioni, M., 2013a. Sedimentologic and diagenetic controls on pore-network characteristics of Oligocenee-Miocene ramp carbonates (Majella Mountain, central Italy). Am. Assoc. Petrol. Geol. Bull. 97, 487e524.

Rustichelli, A., Torrieri, S., Tondi, E., Laurita, S., Strauss, C., Agosta, F., Balsamo, F., 2016. Fracture characteristics in cretaceous platform and overlaying ramp carbonates: an outcrop study from Maiella mountain (central Italy). Mar. Petroleum Geol. 76, 68e87.

Scisciani, V., Tavarnelli, E., & Calamita, F. 2002. The interaction of extensional and contractional deformation in the outer zones of the Central Apennines, Italy. Journal of Structural Geology, 24, 1647-1658

Solano, N., Zambrano, L., Aguilera, R., 2011. Cumulative-gas-production distribution on the Ni-kanassin Formation, Alberta and British Columbia, Canada. SPE Reservoir Evaluation and Engineering 14, 357-376.

Terzaghi R. (1965). Sources of Error in Joint Surveys. Geotechnique 15, 287-304.

Tondi E., Antonellini M., Aydin A., Marchegiani L. & Cello G. 2006. Interaction between deformation bands and pressure solution seams in fault development in carbonate grainstones of Majella Mountain, Italy. Journal of Structural Geology, 28, 376-391.

Tondi, E. 2007. Nucleation, development and petrophysical properties of faults in carbonate grainstones: Evidence from the San Vito Lo Capo peninsula (Sicily, Italy). Journal of Structural Geology, 29, 614–628.

Tondi, E., Rustichelli, A., Cilona, Balsamo, F., Storti, F., Napoli, G., Napoli, G., Renda, P., Giorgioni, M., 2016. Hydraulic properties of fault zones in porous carbonates, examples from central and southern Italy. Italian J. Geosci. 135, 68e79. http://dx.doi.org/10.3301/IJG.2015.08 f.1.

Trimmer D.A., (1981). Design criteria for laboratory measurements of low permeability rocks. Geophys Res Lett, vol. 8, n. 9, Sept 1981, pp.973-975.

Vecsei A. & Sanders G.K.D. 1999. Facies analysis and sequence stratigraphy of a Miocene warm-temperate carbonate ramp, Montagna della Maiella, Italy. Sedimentary Geology, 123, 103-127.

Vecsei, A. 1991. Aggradation un Progradation eines karbonatplatform-Randes: Kreide bis Mittleres Tertiär der Montagna della Maiella, Abruzzen. Mitteilungen aus dem Geologischen Institut der Eidgenössischen Technischen Hochschule und der Universitat Zürich. Neue Folge, 294, pp. 169

Warren, J.E. and P.J., Root (1963). The behavior of naturally fractured reservoirs. Sot. Pet. Eng. J. 3(3): 245-255.

Wei Z., Egger P. Descoeudres F. (1995). Permeability predictions for jointed rock mass. Int. J. Rock Mech. Min. Sci. & Geomech. Abstr., 32 (3), 251-261.

Wei Z. & Zhang D. (2010). Coupled fluid-flow and geomechanics for triple-porosity/dual-permeability modeling of coalbed methane recovery. Int. J. Rock Mech. Min. Sci. & Geomech, vol. 47, pp. 1242-1253.

Zambrano M., Tondi E., Korneva I., Panza E., Agosta F., Janiseck J.M., Giorgioni M. (2016). Fracture properties analysis and discrete fracture network modelling of faulted tight limestones, Murge Plateau, Italy. Ital. J. Geosci., Vol. 135, No. 1, pp. 55-67. DOI: 10.3301/IJG.2014.42.

Zambrano, M., Tondi, E., Mancini, L., Arzilli, F., Lanzafame, G., Materazzi, M., & Torrieri, S., (2017). 3D Pore-network quantitative analysis in deformed carbonate grainstones. Marine and Petroleum Geology, 82, 251-264.

Zambrano, M., Tondi, E., Mancini, L., Lanzafame, G., Trias, F. X., Arzilli, F., Materazzi, M., Torrieri, S. (2018). Fluid flow simulation and permeability computation in deformed porous carbonate grainstones. Advances in Water Resources, 115. https://doi.org/10.1016/j.advwatres.2018.02.016

Zhang, X., and D.J. Sanderson (1997). Numerical modelling of the effects of fault slip on fluid flow around extensional faults, J. Struct. Geol., 18, 109-119.

CHAPTER

2

ANALYSIS OF FRACTURE ROUGHNESS CONTROL ON PERMEABILITY USING SFM AND FLUID FLOW SIMULATIONS: IMPLICATIONS FOR CARBONATE RESERVOIR CHARACTERIZATION

The present chapter has been published in Geofluids, Volume 2019, Article ID 4132386.

2. ANALYSIS OF FRACTURE ROUGHNESS CONTROL ON PERMEABILITY USING SFM AND FLUID FLOW SIMULATIONS: IMPLICATIONS FOR CARBONATE RESERVOIR CHARACTERIZATION

Miller Zambrano [1*], Alan Pitts [1], Ali Salama [1], Tiziano Volatili [1], Maurizio Giorgioni [2], Emanuele Tondi [1]

1. School of Science and Technology - Geology Division, University of Camerino, Italy.
2. Shell Italia Exploration and Production, Italy.

Abstract

Fluid flow through a single fracture is traditionally described by the cubic law, which is derived from the Navier-Stokes equation for the flow of an incompressible fluid between two smooth-parallel plates. Thus, the permeability of a single fracture depends only on the so-called hydraulic aperture which differs from the mechanical aperture (separation between the two fracture wall surfaces). This difference is mainly related to the roughness of the fracture walls, which has been evaluated in previous works by including a friction factor in the permeability equation or directly deriving the hydraulic aperture. However, these methodologies may lack adequate precision to provide valid results. This work presents a complete protocol for fracture surface mapping, roughness evaluation, fracture modeling, fluid flow simulation, and permeability estimation of individual fracture (open or sheared joint/pressure solution seam). The methodology includes laboratory-based high-resolution Structure from Motion (SfM) photogrammetry of fracture surfaces, Power Spectral Density (PSD) surface evaluation, synthetic fracture modeling, and fluid flow simulation using the Lattice-Boltzmann method. This work evaluates the respective controls on permeability exerted by the fracture displacement (perpendicular and parallel to the fracture walls), surface roughness, and surface pair mismatch. The results may contribute to defining a more accurate equation of hydraulic aperture and permeability of single fractures, which represents a pillar for the modeling and upscaling of the hydraulic properties of a geofluid reservoir.

Keywords: *Joints, Pressure solution seems, Fracture permeability, Hydraulic aperture*

2.1. Introduction

Fractures exert an important contribution on determining the migration and storage for geofluids, such as groundwater, and hydrocarbons. Thus, the analysis and modeling of fractures are imperative for characterizing reservoirs and simulating their behavior during the production stage. Fluid flow through fractures is traditionally described by the cubic law, derived from the Navier-Stokes equation for the flow of an incompressible fluid between two smooth-parallel plates (Snow, 1965). Thus, the permeability (intrinsic permeability) of a single fracture may be represented by the equation:

$$k = \frac{e^2}{12} \quad , \qquad \text{(eq. 1)}$$

Where, e corresponds to the hydraulic aperture. Since fractures are normally rough, the hydraulic aperture differs from the mechanical aperture (separation between the two fracture wall surfaces). The hydraulic aperture is in fact an equivalent value which can be derived from field analysis like tracer tests and hydraulic tests (Tsang, 1992), and laboratory fluid flow experiments (*e.g.*, Witherspoon et al., 1980).

Several authors have studied the effect of roughness of the walls on fracture permeability working with various materials, such as glass (Lomize, 1951), rocks (Louis, 1969) and concrete (de Quadros, 1982). These authors included a correction term, a so-called friction factor (f), on the permeability of rough fractures:

$$k = \frac{e^2}{12f} \quad , \qquad \text{(eq. 2)}$$

where the friction factor is defined by the common base equation:

$$f = \left[1 + c_1 \left(\frac{r_a}{2e}\right)^{c_2}\right] \qquad \text{(eq. 3)}$$

where, r_a is the difference between the highest peak and the lowest valley of the physical roughness, and both terms c_1 and c_2 are constants with slightly different values depending on the author. Thus, the friction factor depends only on the relative hydraulic roughness ($\frac{r_a}{2e}$) ignoring the frequency (or wavelength) of the asperities.

Another widely used methodology derives the hydraulic aperture from the mechanical aperture, E, and the joint roughness coefficient (JRC) as proposed Barton *et al.* (1985):

$$e = \frac{E^2}{JRC^{2.5}} \quad , \qquad \text{(eq. 4)}$$

where, the JRC is derived by comparing the fracture profile obtained with the Barton Comb with the standards tables provided by Barton & Choubey (1977). This methodology is perhaps the simplest and cheapest way to obtain fracture surface roughness values and has been widely used in outcrops studies (Zambrano et al., 2016; Panza et al., 2016; Panza et al., 2018; Volatili et al., 2019). The disadvantages of this method are related to the moderate resolution (about 1 mm) and the inaccuracy of the equation (4) at relatively wide apertures (with respect to the JRC value). For instance, considering a fracture with 100 μm mechanical aperture and a JRC equal to 2, the equation (4) gives a hydraulic aperture equal to 1767 μm.

Considering the previous arguments, the main objective of this work is to find empirical equations that describe the effect of fracture roughness on permeability at different apertures. In order to reach this goal, some problems which should be overcome are: i) to develop a protocol for mapping the fracture surface, ii) to evaluate the fracture roughness as a function of the wavelength of the asperities, iii) to validate the relationships using a significant number of samples, roughness values and aperture scenarios.

Various approaches have been reported in the literature for mapping the surface of fractures and faults in the field or laboratory involving the use of Lidar (Candela et al., 2009, 2012), laboratory profilometers (Renard et al., 2006, 2012, 2013), and SfM photogrammetry (*e.g.* Corradetti et al., 2017). Corradetti *et al.* 2017 applied SfM photogrammetry for mapping fracture surfaces obtaining 3D reconstructions with point-cloud densities of equal quality to Lidar-derived data. Among these methods, SfM photogrammetry shows great promise as it is inexpensive (photo-camera and processing software) and extremely flexible regarding the scales and conditions (applicable in the field and laboratory). For example, SfM photogrammetry has been successfully used as an analytical tool to gather geologic data from outcrop studies (Bemis et al., 2014; McCaffrey et al., 2005; Pitts et al.,

2017; Nesbit et al., 2018), as well as at smaller scales on fault surfaces (Corradetti et al., 2017) and fossilized human footprints (Zimmer et al., 2018).

Evaluation of fracture roughness is achieved by implementing the Power Spectral Density (PSD), which provides a more objective description based on the frequency distribution of the asperities in the Fourier domain. This approach has been successfully applied by previous authors for describing the roughness of fractures (*e.g.* Oglive et al., 2006) and fault surfaces (Candela et al., 2009, 2012; Renard et al., 2013; Corradetti et al., 2017). To increase the statistical significance of the results, approximately 2000 fractures were modeled using the software SYNFRAC (Ogilive et al., 2003, 2006; Isakov et al., 2001) creating computer generated synthetic fractures, using input parameters of the fractal dimension, fracture roughness (an output of the PSD analysis of real fractures), and the standard deviation of the asperities height.

A key benefit of incorporating computer-generated synthetic fractures is the capability to work with a large amount of fracture data to perform direct fluid flow simulations, such as: i) the finite difference method (*e.g.* Blunt et al., 2013), ii) the finite element method (*e.g.* Cardenas, 2008, 2009), iii) the finite volume method (*e.g.* Bijeljic et al., 2013), and the lattice-Boltzmann method (*e.g.* Sukop et al., 2008). The lattice-Boltzmann method (LBM) describes the flow of a large number of particles interacting with a medium and among themselves following the Navier-Stokes equation at the macroscopic scale (*e.g.* Ladd, 1944). The LBM has been implemented to compute permeability using 3D images of rocks and soft sediments obtained by micro-CT imaging techniques (Degruyter et al., 2010; Khan et al., 2012; Andrä et al., 2013; Shah et al., 2015; Zambrano et al., 2018) and from reconstructed models (Jin et al., 2004; Keehm et al., 2004; Wu et al., 2006) generating results consistent with laboratory measurements (Keehm et al., 2003, 2004). The simplest LBM is based on the Bhatnagar-Gross-Krook (BGK) collision operator, which consists of a single relaxation time approximation (Bhatnagar et al., 1954). Despite its widespread use, the BGK-LBM brings some issues, for example, the computed permeability values may be viscosity-dependent (Narvaez et al., 2010). An alternative approach involves the use of multiple relaxation times (MRT) methods, which solve the drawbacks of the BGK method and are characterized by more stability (d'Humières, 1992; d'Humières et al., 2002; Pan et al., 2006).

In this study, the permeability values of single isolated fractures (synthetic and natural) were calculated via LBM, using the PALABOS open source library (Latt, 2009). The method and the code have been previously implemented by Zambrano *et al*. (2018) for quantifying the permeability in deformed porous carbonates using X-Ray microtomography synchrotron-based images (Zambrano et al., 2017). Following these authors, rather than the BGK method (*e.g.* Degruyter *et al.*, 2010), the MRT approach has been adopted in the present study to assure that permeability values are viscosity-independent.

The selected study area, the Roman Valley Quarry (Fig. 2.1a), is an inactive quarry located at the northern termination of the Majella Mountain (Abruzzo region, Italy). The Majella Mountain is the orogenic expression of a thrust-related anticline, with internal deformation characterized by high-angle normal, strike-slip and oblique-slip normal faults, small folds, multiple sets of opening-mode fractures, pressure solution seams, and deformation bands (Cello et al., 1997; Ghisetti & Vezzani, 2002; Scisciani et al., 2002; Marchegiani et al., 2006;Tondi et al., 2006; Antonellini et al., 2008; Alessandroni, 2008; Agosta et al., 2009; Agosta et al., 2010; Aydin et al., 2010; Rustichelli et al., 2012, 2013, 2016).

The Roman Valley quarry has been heavily studied by previous authors focusing on the structural, sedimentological and diagenetic properties (Agosta et al., 2009, Rustichelli et al., 2013), fracture modeling (Panza et al., 2018; Volatili et al., 2019), and the fluid flow behavior of the fractured carbonates at the macroscale (Volatili et al., 2019). Here, the bitumen distribution suggests the main hydrocarbon flow occurred through the damage zones of the principle NW-SE oriented oblique slip faults (Agosta et al., 2009, 2010; Fig. 3.1b). The distribution of major lithofacies at the Roman Valley Quarry are another element influencing the presence of bitumen which has been previously described by Rustichelli *et al*. (Rustichelli et al., 2012, 2013; see table 2.1). Concerning the fractures, the most pervasive ones are represented by both pressure solution seams (often sheared with sliding/tearing mode displacement) and joints (opening mode fractures).

Considering the significance of these fractures, this work focused on investigating both cases of open mode and sheared fractures with a small sliding/tearing mode displacement, in the order of mm, in order to assume a

negligible wall wearing. For this last case, the mismatch between opposite walls was also computed due to its importance as a mechanism for maintaining fracture openings even at reservoirs depths.

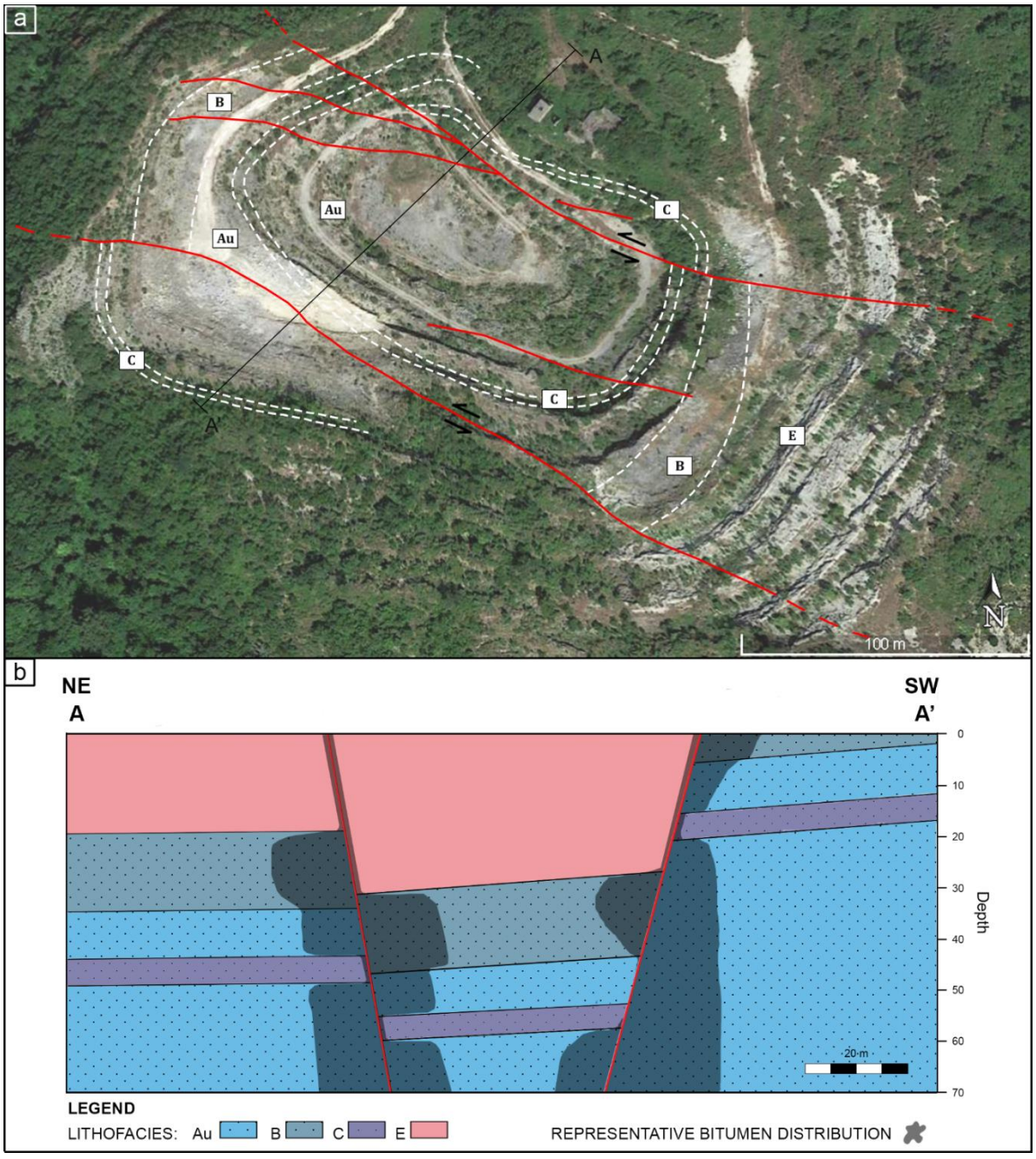

Figure 2.1. a) Structural map of the Roman Valley Quarry (modified after Volatili et al., 2019). Notes: red lines= faults, white dashed lines= lithofacies boundaries (see Table 2.1 for details), b) Stratigraphic and structural scheme of the study area, oil distribution is arbitrarily representative considering field observations (see Volatili et al., 2019 for more details).

2.2. Methodology

In this work, we present a multi-phase integrated methodology for characterizing fracture surfaces and their effect on permeability. This approach combines fracture surface scanning using Structure from Motion photogrammetry, a statistical and spectral description of individual natural fracture surfaces, modeling of synthetic fractures, and computational calculation of permeability by fluid flow simulation.

2.2.1. Sample Collection

During the summer of 2018, a suite of oriented hand samples was collected from the study site comprising 3 (i.e. Au, B, C) of the 4 major lithofacies of the Bolognano Formation present in the quarry (Fig. 2.2, Table 2.1). The field sampling procedure involved manually removing blocks containing fracture surfaces that showed minimal signs of physical and chemical weathering. Sampling targeted these specific lithofacies based on accessibility, quality of well-developed fracture surfaces, and the fact that they have been well documented in previous studies focused on fracture distribution and mechanical properties (Agosta et al., 2009, 2010; Panza et al., 2018; Volatili et al., 2019). After removal from the outcrop but prior to analysis, the rock samples were cleaned using a soft-bristled brush to remove debris and other obstructions but without abrading the surface.

Table 2.1. Characteristics of lithofacies exposed in the Roman Valley Quarry

Lithofacies		**Thickness**	**Φ_m [%]**	**k_m [mD]**	**Bitumen distribution**
Au:	Alternation of medium- to coarse-grained bioclastic grainstones (Au1) and medium-grained bioclastic grainstones (Au2).	40-to 60-m	~ 27.5	83.13 (V) 160.09 (H)	Abundant in both matrix and fractures near to faults
B:	Medium-grained grainstones.	10-to 15-m	~ 26.4	444.82(V) 530.94 (H)	Abundant in both matrix and fractures near to faults
C:	Alternations of two echinoid plates and spines rich facies: fine-grained bioclastic grainstones (C1) and fine- to very fine-grained bioclastic packstones (C2). Argillaceous to marly beds (<3 cm thick) are common.	10-to 15-m	~ 10.9	~ 0.30 (V) ~ 2.51 (H)	Absent in matrix and oil stain in fractures.
E:	Alternation of two planktonic foraminifera facies: marly wackestones (E1) and marly mudstones (E2).	60–65-m	~ 28.8	~ 0.085 (V) ~ 0.081 (H)	Absent in both matrix and fractures.

Notes: Lithofacies description from Rustichelli et al. (2013), matrix porosity (Φ_m) obtained with helium pycnometer and gas permeability (k_m) measurements (performed in both horizontal, H, and vertical, V, direction) were reported by Volatili et al. (2019), bitumen distribution from field observations (Agosta et al., 2010; Rustichelli et al., 2012, 2013).

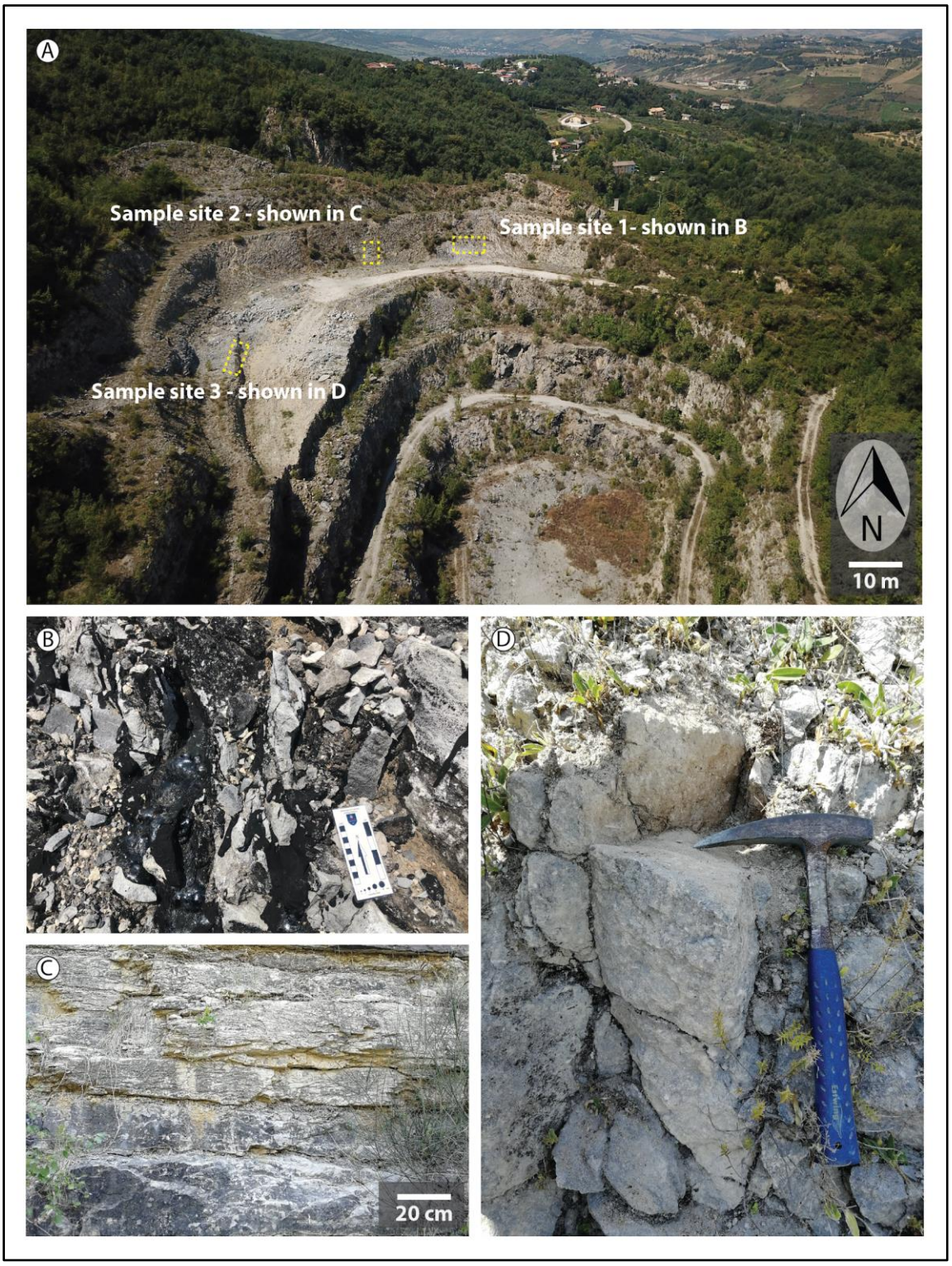

Figure 2.2. Sample location sites. A) Sampling locations inside the Roman Valley Quarry, B) Sample site 1 from lithofacies B with scale card showing centimeter increments. C) Sample site 2 from lithofacies Au, D) Sample site 3 from lithofacies C. Rock hammer for scale, 22 cm in length.

2.2.2. Mapping surface topography

The workflow for mapping surface topography involves the following key stages: (1) Fracture surface image set acquisition, (2) image alignment and three-dimensional digital rock model creation using SfM.

2.2.2.1. Image Set Acquisition

SfM photo scanning was performed at the University of Camerino photogrammetry laboratory (Fig. 2.3a). We used a tripod-mounted Canon EOS 100D with the standard kit lens fixed at 55mm. Images of samples were recorded inside a photo-lightbox to maintain full control of camera positions, ambient lighting and to reduce shadows and glare ensuring high image quality. To achieve >70% inter-photo overlap, fracture samples were placed on a 360-degree rotating stage and manually rotated at 10-degree angular increments between photos. After completing a full orbit of the object, the camera was reset at a new vertical position and the next orbit was conducted adhering to the same 10-degree increments however offset one position from the initial starting point. This procedure was repeated along three horizontal rotations from different vertical positions followed by 2-3 photos directly above the object oriented normal to the fracture surface.

2.2.2.2. Image alignment and three-dimensional model creation

Fracture surface models were aligned and processed using Agisoft PhotoScan Pro (www.agisoft.com). For each fracture surface, approximately 63 photos were used as input images to create the digital point cloud model. We follow the procedure described by Carrivick *et al*. 2016 and Zimmer *et al*. (2018) for camera settings and photo procedure, and Pitts *et al*. (2017) for image alignment and point cloud generation.

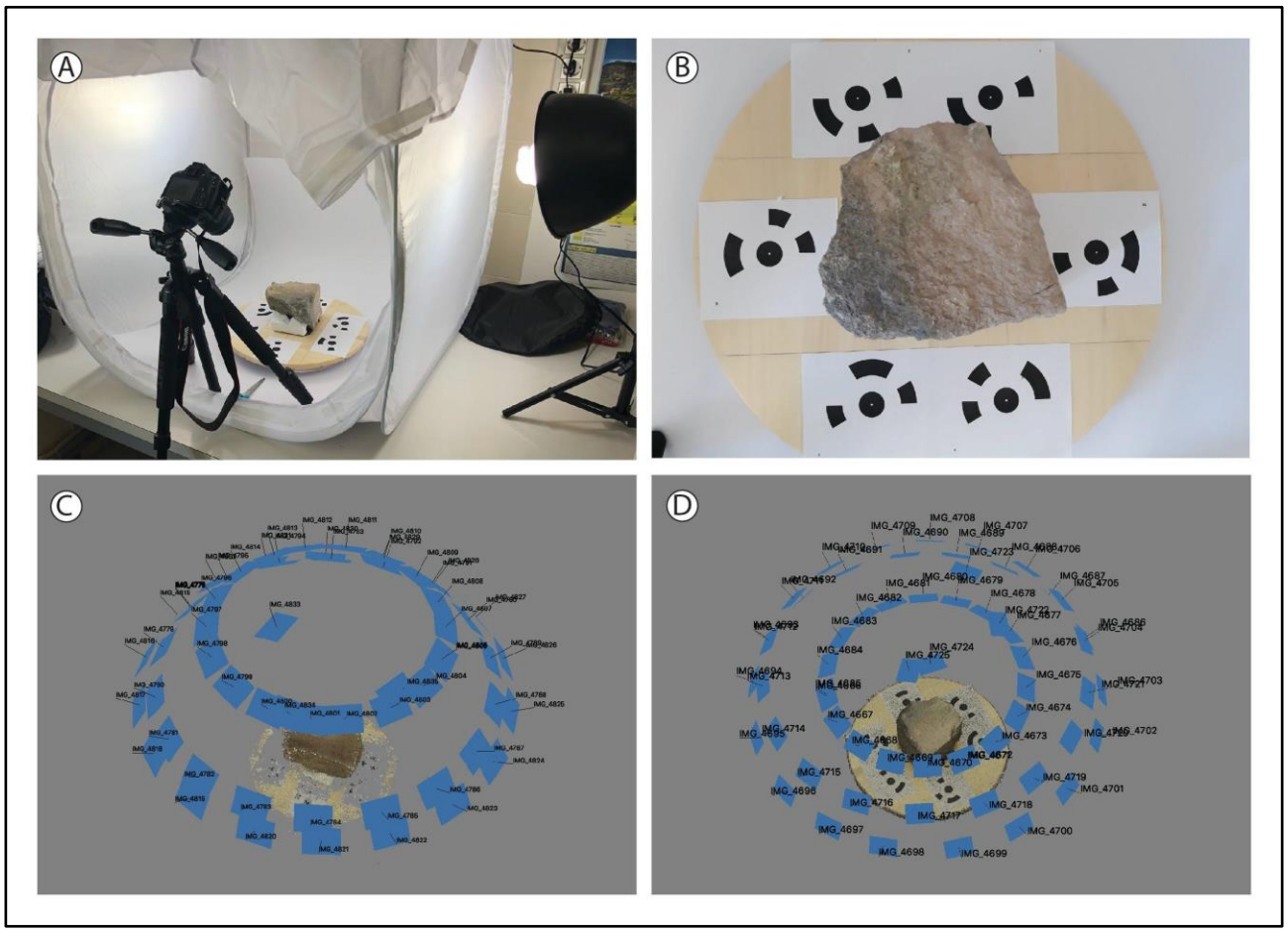

Figure 2.3. Photogrammetry setup and three-dimensional SfM procedure. A) Photo light box used in the photogrammetry lab. B) Collected sample placed on the rotating stage with unique photo-targets generated by Agisoft Photoscan. C) Sparse point cloud generated during the photo alignment phase of the SfM procedure. D) Fully rendered photo-realistic 3D model showing camera positions.

Agisoft-generated coded targets were placed inside the scene to aid in the imagery processing, these coded targets are automatically recognized by the software and help build connection points between the image sets (Fig. 2.3 b). Additionally, a 5-centimeter scale was placed on the sample surface to calibrate the spatial reference.

As a measure to define the error of the model, we follow the methodology established by Corradetti *et al.* (2017). This calls for modeling a piece of graph paper under the same condition as fracture imaging (same light, relative distance, number of photos). Under the assumption the graph paper is perfectly planar, the standard

deviation of the height of the scanned asperities is considered as the error of the model (Corradetti et al., 2017). In our case, this value is approximately 20 µm, whereas the point density (points/area) is 34 points / mm.

2.2.3. Fracture Surface Processing and Analysis

2.2.3.1. Extraction and processing of 3D fracture surface model.

Trimmed 3D Point clouds were exported from Agisoft as .XYZ text files. Then, a rectangular subregion of each fracture surface of interest was extracted from the point cloud and processed to remove undesirable trend and eventual noise (Fig. 2.4). This technique, previously documented by Corradetti *et al.* (2017), consists of: i) removing the artificial trend of the surface, ii) surface interpolation, and ii) sampling in a regular grid.

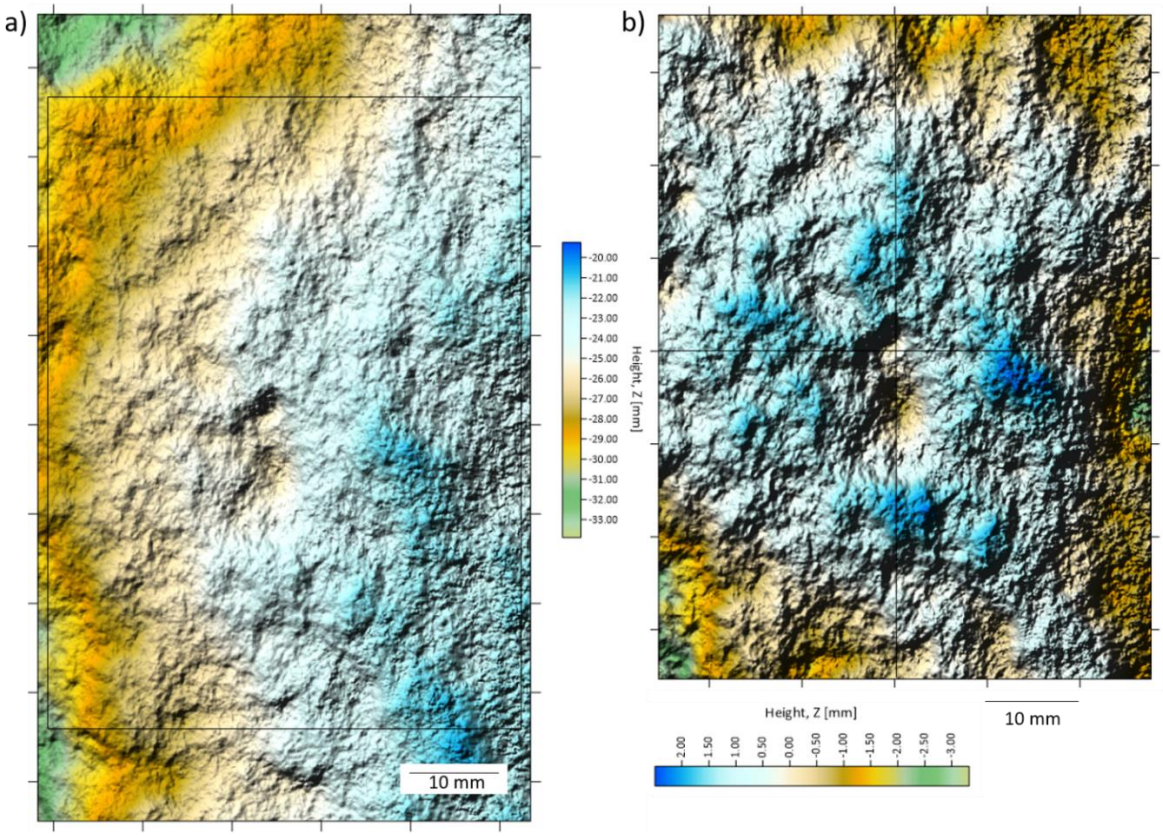

Figure 2.4. Fracture surface processing. a) Original exported fracture surface containing an artificial trend, b) resulting image after removing the artificial trend and assigning a new reference grid according to a millimeter scale.

2.2.3.2. Fracture roughness assessment

A complete description of the fracture roughness is given by the specification of two functions: the probability density function (depending on the media and standard deviation) for heights, and the PSD (Carrivick et al., 2016) (Fig. 2.5).

The Fourier power spectrum, P(k), is defined as the square of the modulus of the Fourier transform (Schuster, 1898). Considering a cross-section of the rock as a profile, this profile can be represented as a summation of sinusoidal components, each with its own amplitude, wavelength and phase. The squared amplitude of each sinusoid component is referred to as its "power" (Fig. 2.5b). The power spectrum regulated in an appropriate manner is referred to as the PSD, G (k), and it provides a valuable definition of surface roughness. The PSD as a function of k in a bi-logarithmic scale graph of a self-affine function exhibits an apparent linear slope, which is defined from the following power-law equation:

$$G(k) \propto k^{-\alpha} \quad , \qquad \text{(eq. 6)}$$

where the exponent of the power law α is related with the fractal dimension, D, (Brown, 1995), as follow:

$$D = ((7 - \alpha)) \; / \; 2 \qquad \text{(eq. 7)}$$

From a physical aspect, the fractal dimension shows the proportion of high-frequency to low frequency sinusoid components (roughness). High D values are related to a greater surface roughness. By stacking and normalizing the power spectra, it is possible to reduce the noise associated with a single profile and create a single spectrum which represents the entire rough surface in a given direction (*e.g.* Candela et al., 2012; Corradetti et al., 2017). The MATLAB script used to perform the procedures described above is partially modified from Corradetti *et al.* (2017).

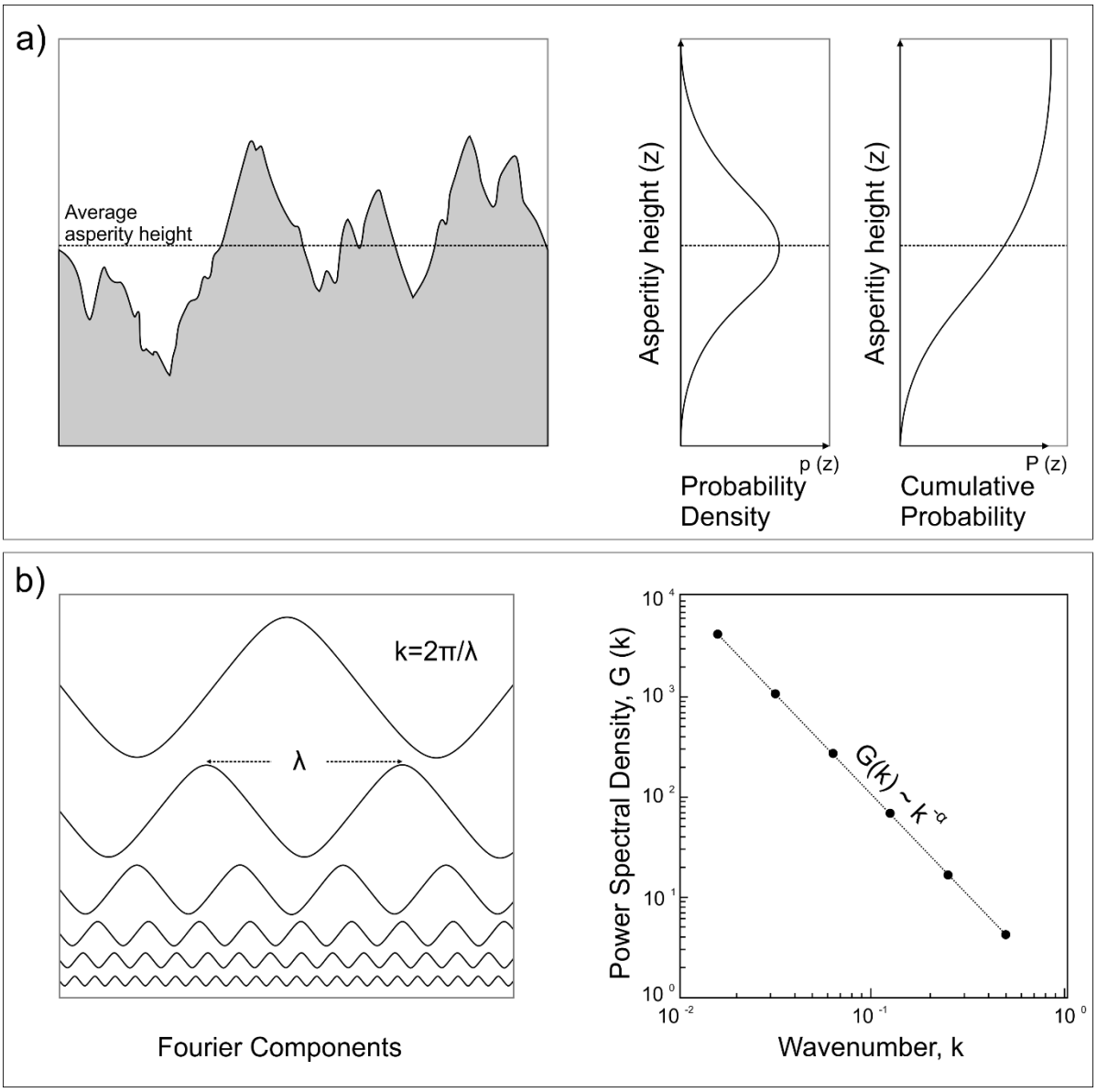

Figure 2.5. Illustration of a complete description of a surface roughness: a) in terms of height statistical distribution, probability density, b) in terms of frequencies distribution, Fourier power spectrum (modified from Brown, 1995).

2.2.4. Single Fracture Modeling

Since a limited number of natural fracture surfaces were available, additional synthetic fracture surfaces were used to strengthen the statistical significance of the results. Following the procedure described by Ogilvie et al., (2006), more than 2000 computer-generated synthetic fractures were created using the software SYNFRAC (Ogilive et al., 2003, 2006; Isakov et al., 2001). SYNFRAC is based on a mathematical model of a rough surface

reported by Brown (1995). The software can model open fractures by introducing mismatch values with the spatial and spectral roughness parameters. For the scope of the present study, the mismatch values were not considered for the surface modeling, however, were measured after the fracture modeling (see section 2.5.1).

The individual fracture surfaces (natural and synthetic) were used to model dilation associated with (Fig. 2.6): i) opening mode displacement (joint and/or opened pressure solution seam), various ranges of aperture, and ii) sliding/tearing mode displacement (sheared joint and/or sheared pressure solution seam). In both cases it is assumed that both walls are identical. In the second case, because the shear process is minimum, and the displacement in the order of mm, it is assumed that not physical wearing of the fracture surfaces has occurred. To illustrate different scenarios, a wide range of displacements (opening and sliding/tearing mode) were considered (The PYTHON code for fracture modeling is available at https://github.com/superrostom/synthetic-fracture).

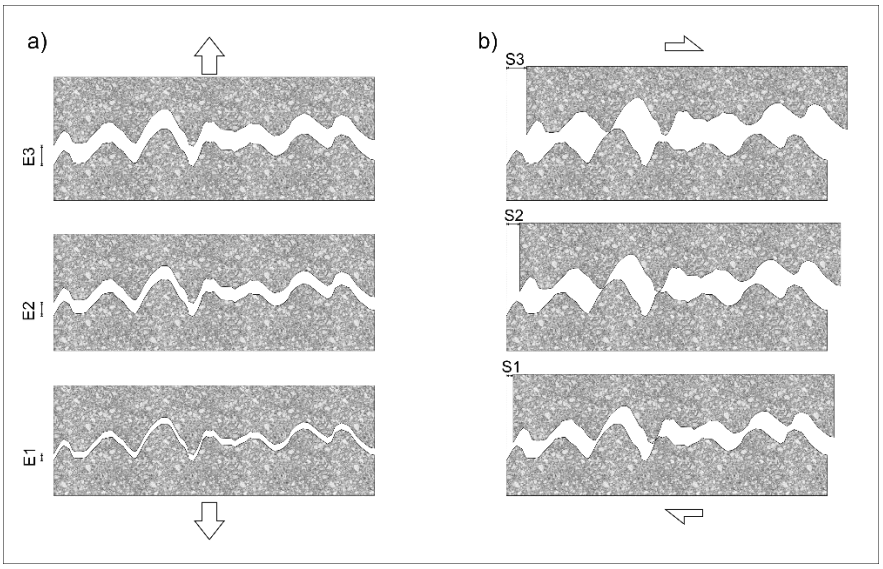

Figure 2.6. Mechanisms considered for possible fracture aperture generation in the study area: a) Opening mode displacement (joint and/or opened pressure solution seam), and b) sliding/tearing mode displacement (sheared joint and/or sheared pressure solution seam).

2.2.5. Lattice-Boltzmann method and permeability computation

Lattice-Boltzmann simulations were performed using the open-source computational fluid dynamics software PALABOS [48] following the methodology described by Zambrano *et al.* (2018).

This procedure consists of imposing a single-phase fluid flow through a 3D porous media maintaining a fixed pressure gradient between the inlet and outlet opposing faces of the model, the rest of the faces were padded. A bounce-back boundary condition was assigned to the fracture surfaces. An MRT collisional operator (d'Humières, 1992; d'Humières et al., 2002), with a D3Q19 lattice, is used instead of the popular BGK (Bhatnagar et al., 1954) as in Degruyter *et al.* (2010). Moreover, the geometry of the media is obtained by the SfM photogrammetry outputs and modeling differently than Degruyter *et al*. (2010) and Zambrano *et al.* (2018) who used X-ray micro CT images.

The simulation ended once the imposed steady state condition was reached (standard deviation of the average energy<10^{-4} after 1000 steps). Then, the permeability component parallel to the imposed flow was calculated applying Darcy's law,

$$\frac{\delta P}{\delta x} = \frac{\mu}{k} U \quad , \qquad \text{(eq. 9)}$$

where, $\delta P/\delta x$ is the pressure gradient, μ the fluid kinematic viscosity, and U the average fluid velocity (Fig. 2.7) per unit of area. The permeability was calculated, using the same procedure, in two orthogonal directions: along strike and along dip (k_x and k_y, respectively). In the case of sliding/tearing mode displacement, the x-direction corresponds to the slip direction. All the variables are handled in lattice units prior to permeability calculation. For convenience, permeability values were converted to millidarcy which is the most commonly used permeability unit in the oil industry. All the provided values of permeability correspond to a volume of 1.25 x 10^{-4} m^3 (50 x 50 x 50 mm^3).

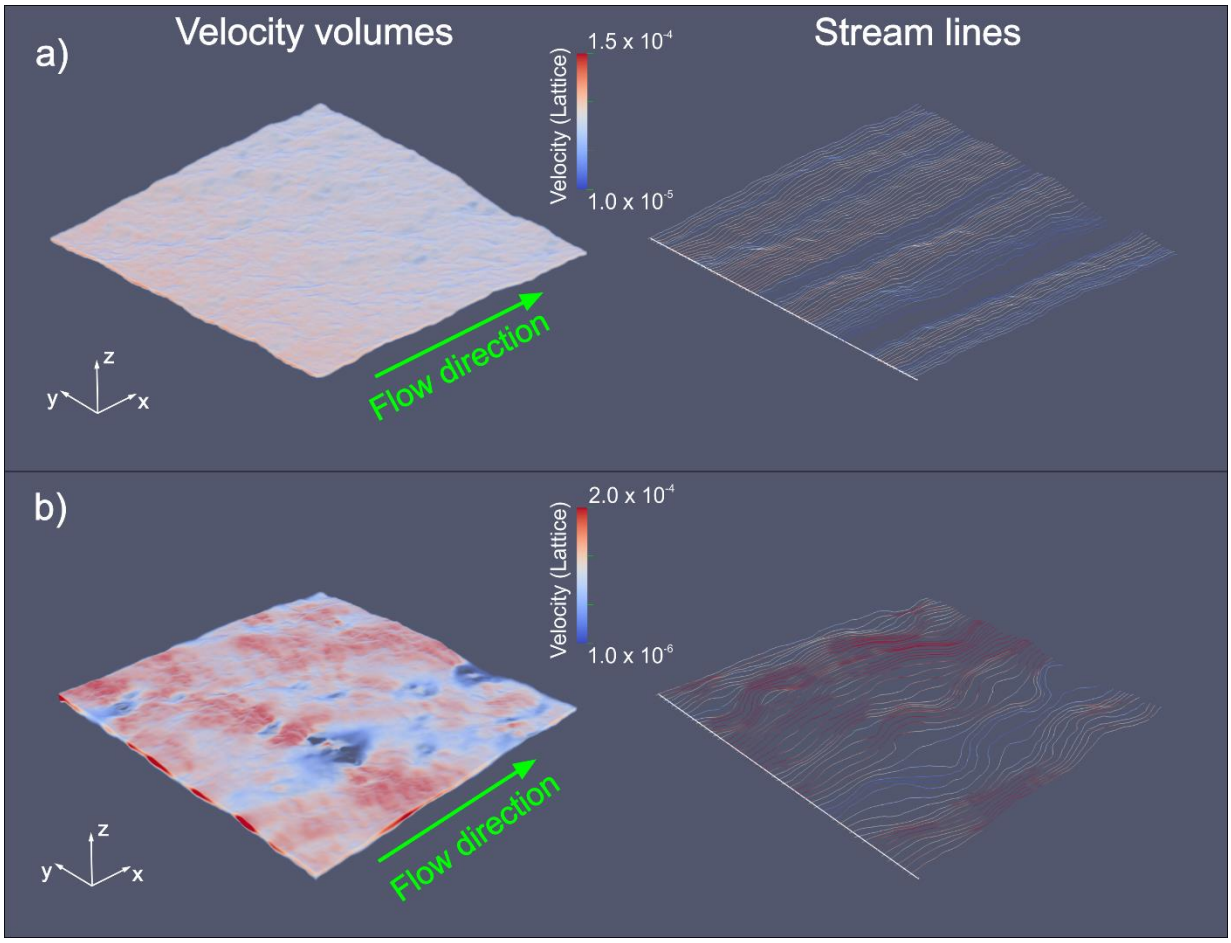

Figure 2.7. Examples of lattice velocity fields volumes with the corresponding streamlines: a) Fracture with opening mode displacement equals to 1 mm, and b) Fracture with sliding/tearing mode displacement equals to 50 mm. Both fractures have a considerable roughness (D = 2.5; Std. Dev. = 4 mm). The size of the samples is about 50 x 50 mm. Images are rendered using PARAVIEW software (Ahrens et al., 2005).

3.2.5.1. Mismatch evaluation

The mismatch between the opposite fracture walls is of extreme importance since this factor may keep fractures open even at reservoir depths. Since the mismatch was not imposed during the fracture modeling, it was measured after the generation of the synthetic fractures. The mismatch was evaluated only for the sliding/tearing mode fractures, whereas it was unnecessary in the case of opening mode fractures since the aperture is constant. For the evaluation of the mismatch value, the methodology of the Power Spectral Density ratio (PSDr), introduced by

Ogilvie *et al*. (2006) was followed. The methodology consists of obtaining a relationship between the PSD of the aperture and both surfaces of the fracture, as follows:

$$PSDr = \frac{PSD_{aperture}}{(PSD_{upper\_wall} + PSD_{lower\_wall})} \quad \text{(eq. 8)}$$

The results of this calculation can be represented in a graph where the parameters associated with the mismatch and the degree of mismatch between the surfaces at different wavelengths can be obtained (Fig. 2.8).

Following the definition of Ogilvie et al. (2006), these parameters are the following:

- Minimum Mismatch Length (ML_min): Wavelength at which the fractures start to match, indicated by the wavelength where the PSD ratio values falls below its maximum value (PSDr_max).
- Maximum Mismatch Length (ML_max): Wavelength at which the fracture opposing surfaces reach the maximum matching, thus the minimum value of PSD ratio (PSDr_min).

The calculation of these parameters was made using a MATLAB code. In this case, the (ML_min) is considered as the only reliable indicator of the mismatch due to the fact that the (ML_max) often falls outside the scale of the study (Fig. 2.8).

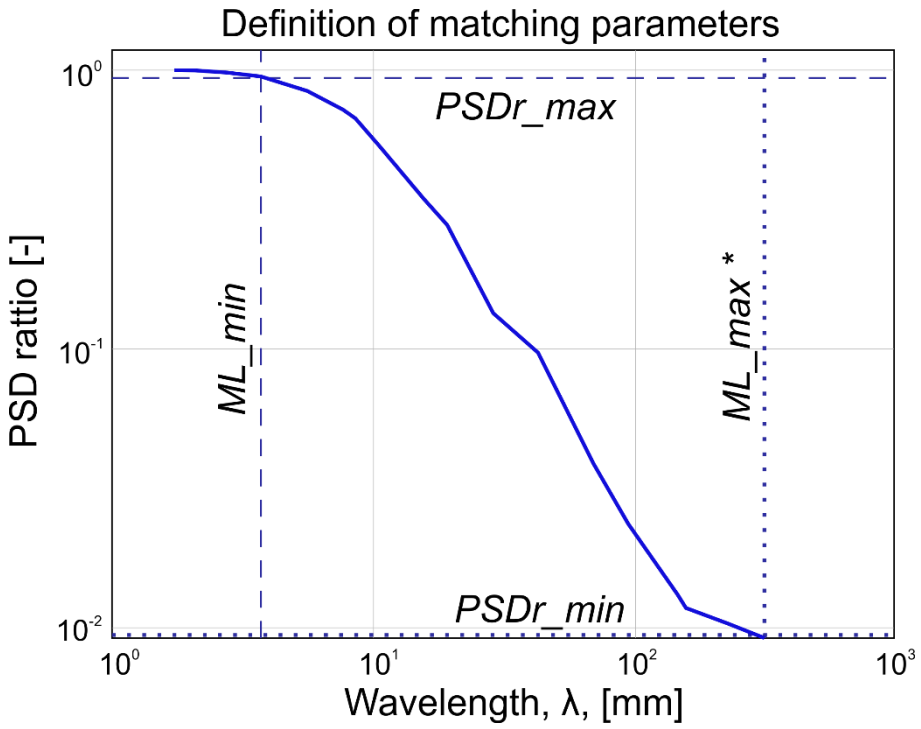

*Figure 2.8. A typical PSD ratio graph use for defining the mismatching parameters. *The Maximum Mismatch Length (ML_max) often falls at the limit or outside the studied wavelength range.*

2.3. Results

The results of this work consist of an analysis of surface topography performed on fracture samples from three lithofacies (Au, B, C), and the computed permeability in function of the fracture properties, including fractal dimension, opening and sliding/tearing displacement, and minimum mismatch length.

2.3.1. Fracture surface properties

In the table 2.2, the values correspond to the fractal dimension (D), the average height of asperities and their standard deviation. The traditional roughness measurement, JRC, was added to compare both techniques and the results with previous works in the same outcrop. For the fracture description, we followed Alessandroni (2008) and Agosta *et al.* (2009). The set PS2a corresponds to pressure solution seams (generated during background deformation) often sheared, with normal or left lateral kinematics, often impregnated by tar. The set PS2b corresponds to pressure solution seams (generated during background deformation) generally not sheared.

Table 2.2. Results of the surface analysis

	Field description			Surface Analysis			
ID	**Orientation**	**Set**	**Lithofacies**	**JRC**	**SD**	**Dx**	**Dy**
F-1	200/72	PS2a	Au	10	1.22	1.89	1.91
F-2	285/85	PS2b	Au	12	2.85	1.85	1.93
F-3	195/80	PS2a	B	9	1.49	1.90	1.78
F-4	210/V	PS2a	C-2	8	1.97	1.90	1.67
F-5	200/80	PS2a	C-1	10	1.66	1.85	1.96
F-6	120/85	PS2b	C-1	11	0.82	1.96	1.95

Notes: Orientation noted as dip direction/dip angle; SD stands for standard deviation of asperities height, Dx and Dy are the fractals dimensions in the strike and dip directions, respectively.

2.3.2. Permeability results

The results of the work are presented in Figures 2.9-14. In each graph, the different surface roughness values (expressed in fractal dimension) are illustrated. When pertinent, error bars are added to show the variability of the results. In the case of opening mode displacement, the results indicate the permeability increased proportional to the mechanical aperture following a positive power-law relationship (Fig. 2.9a). Similarly, the hydraulic aperture (derived from equation 1) is related with the mechanical aperture by means of a positive power law with exponents varying from 1.6 to 1.8 for fractal dimension (D) values between 1.6 to 2.5, respectively (Fig. 2.9b).

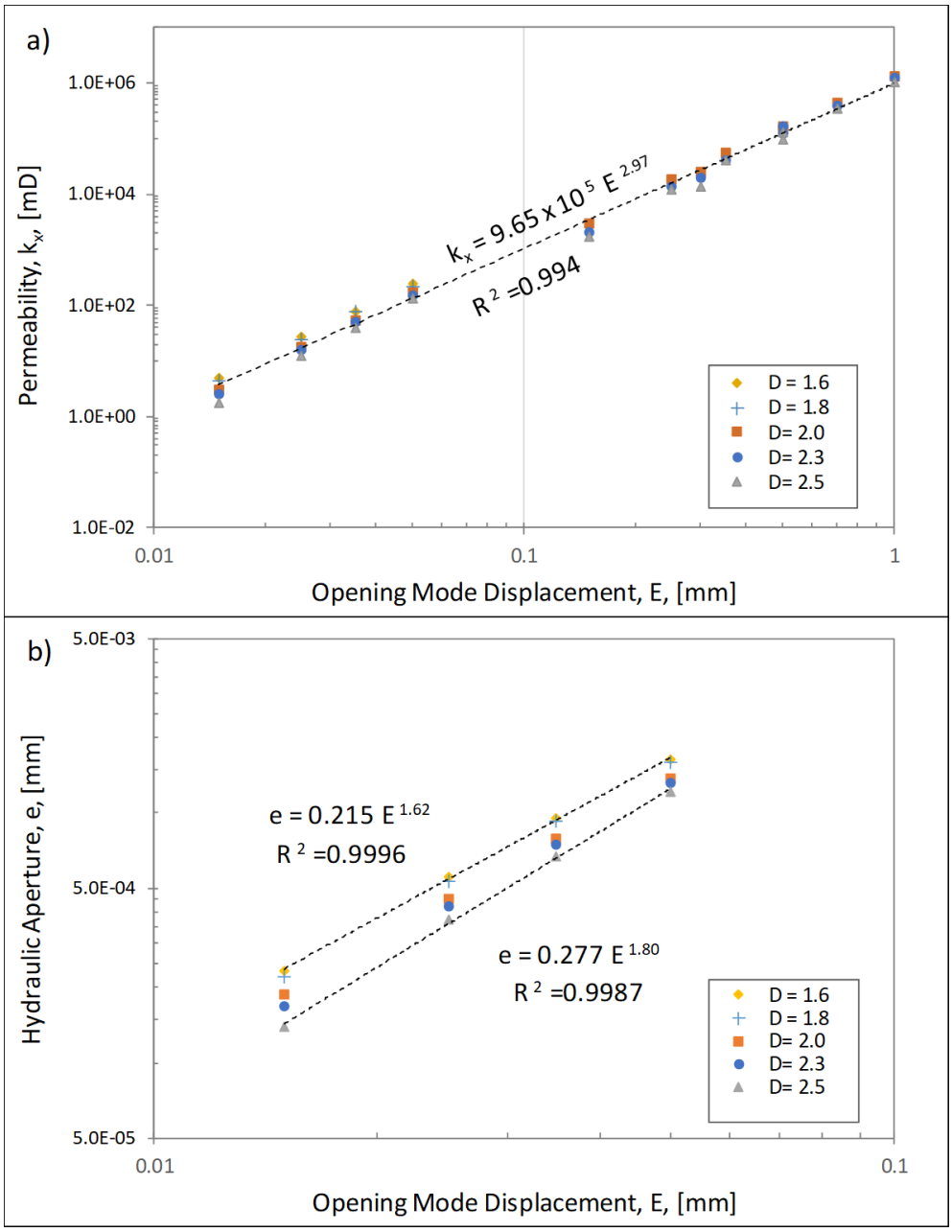

Figure 2.9. a) Single-fracture permeability versus opening mode displacement; results indicate a positive power-law relationship (nearly cubic), b) Hydraulic Aperture (computed with the equation 1) versus the opening mode displacement (mechanical aperture); the relationship follows a positive power law with exponent between 1.6 and 1.8. Axes are in logarithmic scale, and the dashed lines corresponds to the best-fitting power laws.

With respect to the case of sliding/tearing displacement, the results indicate that the permeability component parallel to the displacement (k_x) increases proportionally to the sliding/tearing displacement (S_x) following a

positive power-law relationship (Fig. 2.10a). The permeability component perpendicular to the displacement (k_y) is also related by a power-law with the sliding/tearing displacement (S_x). The anisotropy ratio, k_y / k_x, is generally higher for low values of fractal dimension (Fig. 2.10b). The anisotropy ratio value tends to decrease as a function of the sliding/tearing displacement (S_x) following a negative power-law relationship. The highest value of anisotropy was near 2.6 for fractal dimension (D) equal to 2.0 and sliding/tearing displacement (S_x) equal to 0.5 mm.

The fracture roughness, expressed in terms of fractal dimension (D), showed a different influence in the permeability on single fractures depending of their kinematic: opening or sliding/tearing mode. For the opening mode displacement case, the permeability is inversely proportional to the fractal dimension (Fig. 2.11a). This relationship follows a negative power-law with slope depending on the opening mode displacement values. A higher roughness (fractal dimension) implies a decrease in permeability. For the simulated scenarios, rough fractures (D = 2.5) showed permeability values between 45% to 65% lower than smooth fractures (D = 1.6). For fractures with the sliding/tearing displacement, the permeability is proportional to the fractal dimension following a positive power-law (Fig. 2.11b). In this case, an increment of the fractal dimension (roughness) from 2.0 to 2.5 represents an enhancement of the permeability in approximately one order of magnitude.

It is expected that this positive relationship between displacement-permeability should stabilize at a certain point, as the permeability and porosity cannot increase indefinitely. This behavior is observed when the porosity is evaluated at higher displacement values (Fig. 2.11). In this case, thanks to the simplified calculation of porosity in comparison with permeability, a large volume of data was considered (more than 2000 fractures). The porosity is proportional to the sliding/tearing displacement following a non-linear relationship with variable slope. The most important change of slope occurs near 10 mm and after approximately 30mm of sliding/tearing displacement where the porosity seems to stabilize is values between 3% and 4%. The fractures with higher fractal dimension (roughness) tends to have higher porosity, which agrees with the permeability results. As previously mentioned, these results do not take into account the possible physical wearing of the surfaces due to shearing particularly at high sliding/tearing displacement.

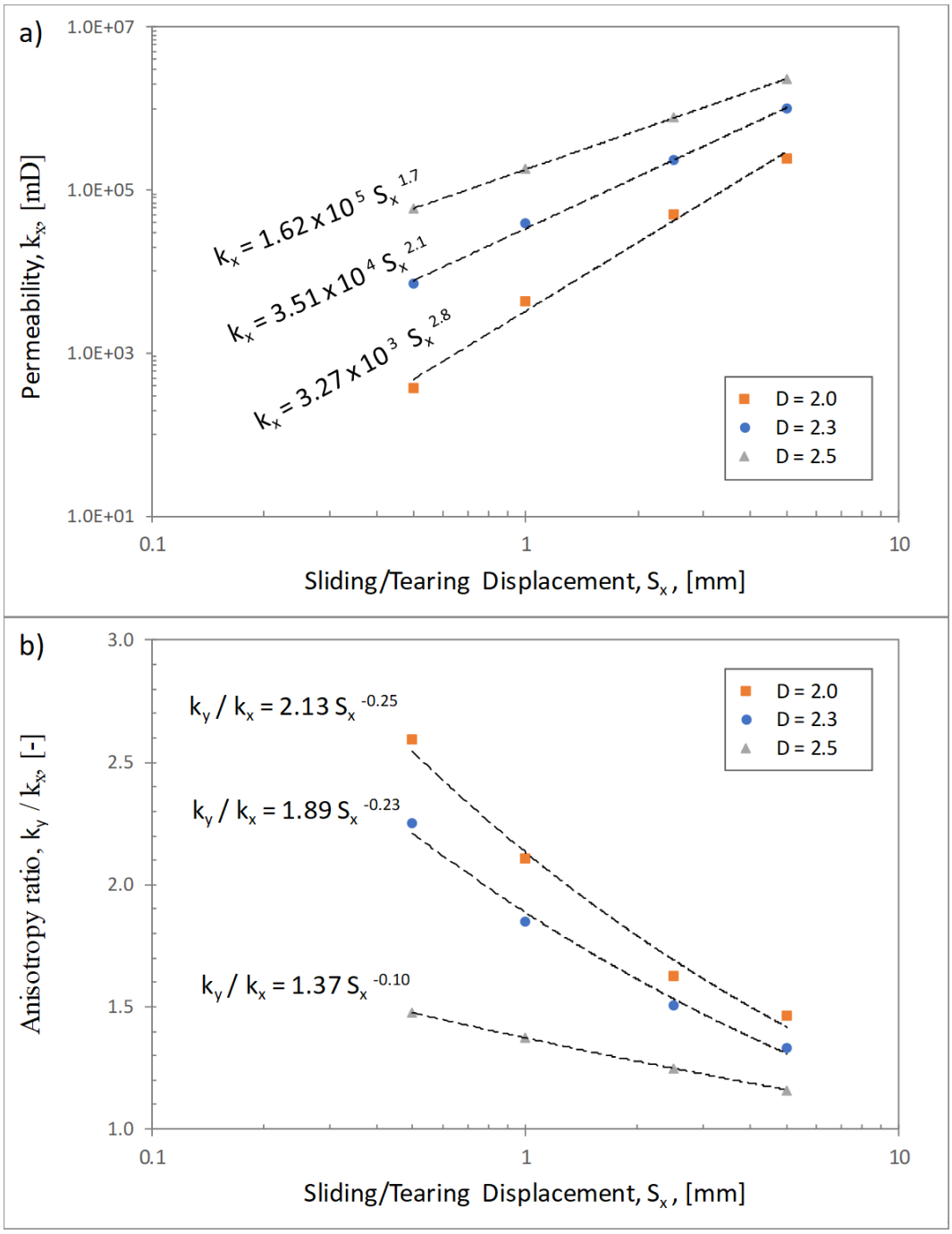

Figure 2.10. Single fracture permeability versus sliding/tearing displacement: a) permeability along the shear direction, b) Anisotropy permeability ratio, k_y / k_x, as function of sliding/tearing displacement. Axes are in logarithmic scale, and the dashed lines corresponds to the best-fitting power laws.

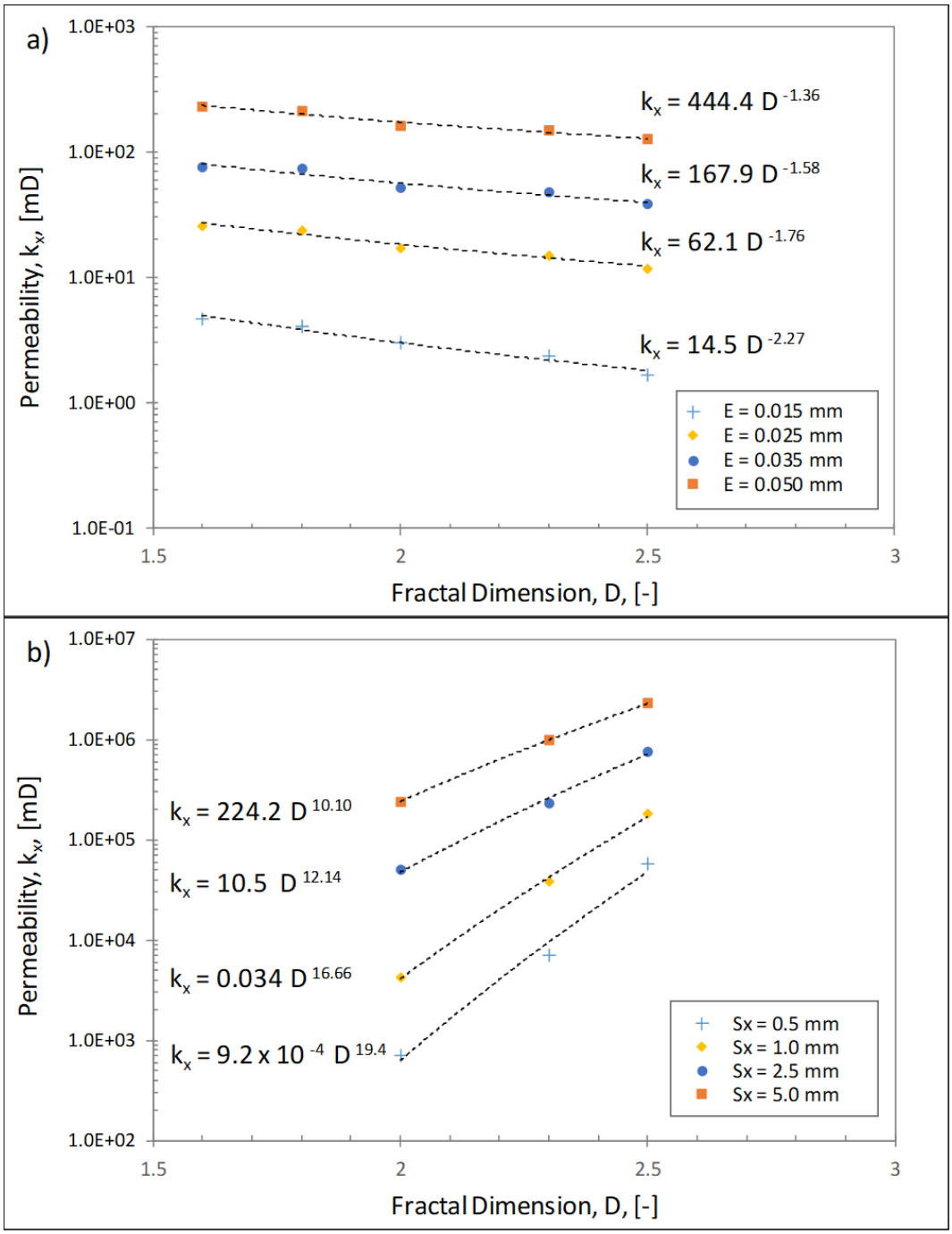

Figure 2.11. Permeability as a function of fractal dimension. a) Permeability versus open mode displacement. Note the inversely proportional control of the fractal dimension on permeability. b) permeability versus sliding/tearing displacement. Note the proportional control of the fractal dimension on permeability. Axes are in logarithmic scale, and the dashed lines corresponds to the best-fitting power laws.

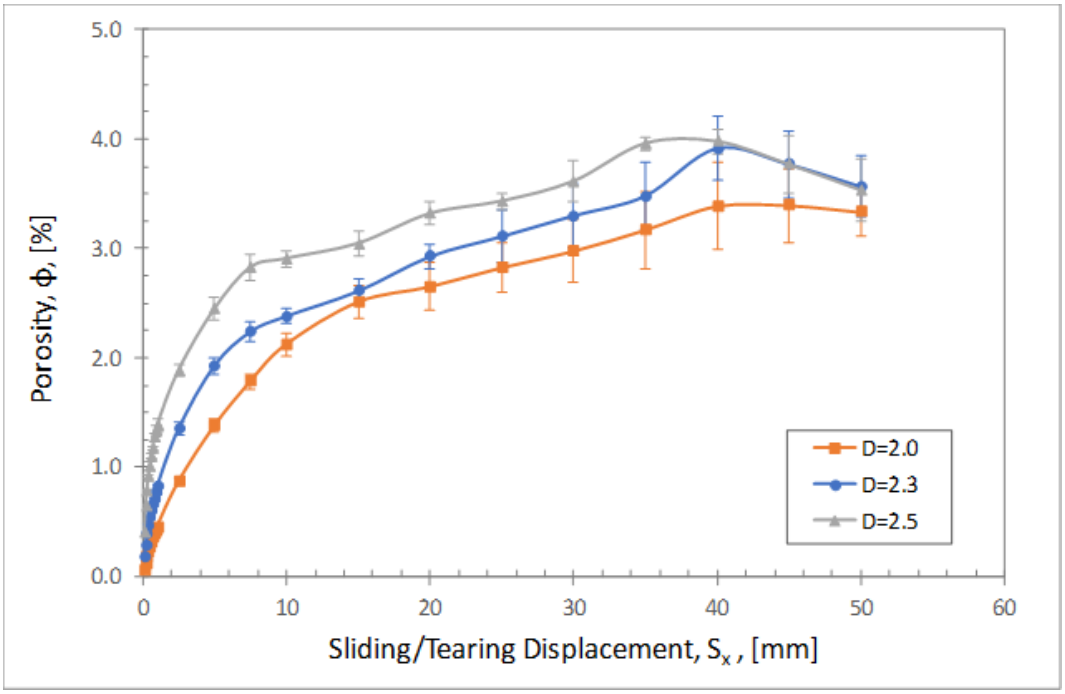

Figure 2.12. Porosity versus sliding/tearing displacement. Error bars indicate the standard error.

The fracture permeability is related to the porosity following a power law (Fig. 2.13), which differs from the theoretical relationship based on the smooth parallel-plates equation here we assumed also smooth parallel plates for the porosity). The power-law relationship seems to be unaffected by the roughness (fractal dimension). Similar behaviors were obtained for both permeability components k_x, and k_y.

The minimum mismatch length, ML_min, was evaluated as a function of the displacement (Fig. 2.14a). Results indicate that within the evaluated range (a maximum displacement of 5 mm) the minimum mismatch is linearly proportional to the displacement. The permeability is proportional to the minimum mismatch length following a power-law relationship (depending on the fractal dimension). In other words, higher values of fractal dimension imply a higher permeability for similar mismatch values.

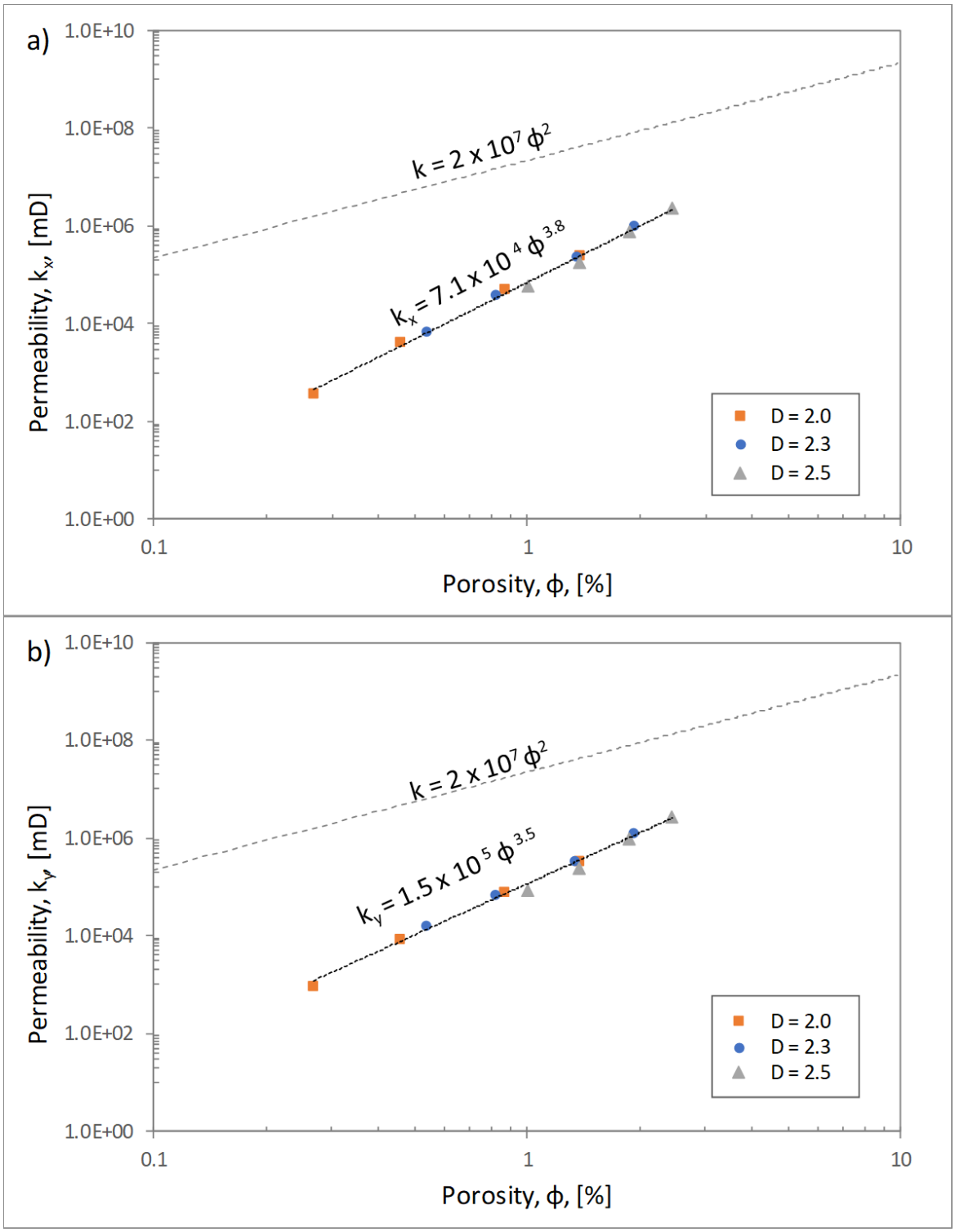

Figure 2.13. Permeability components - a) parallel to shear, k_x, and b) perpendicular to shear, k_y - versus porosity of a single fracture after sliding/tearing displacement. Dashed line represents the relationship permeability-porosity for ideal smooth fractures, whereas the dotted line (best-fitting power law) indicates the same relationship when roughness is included.

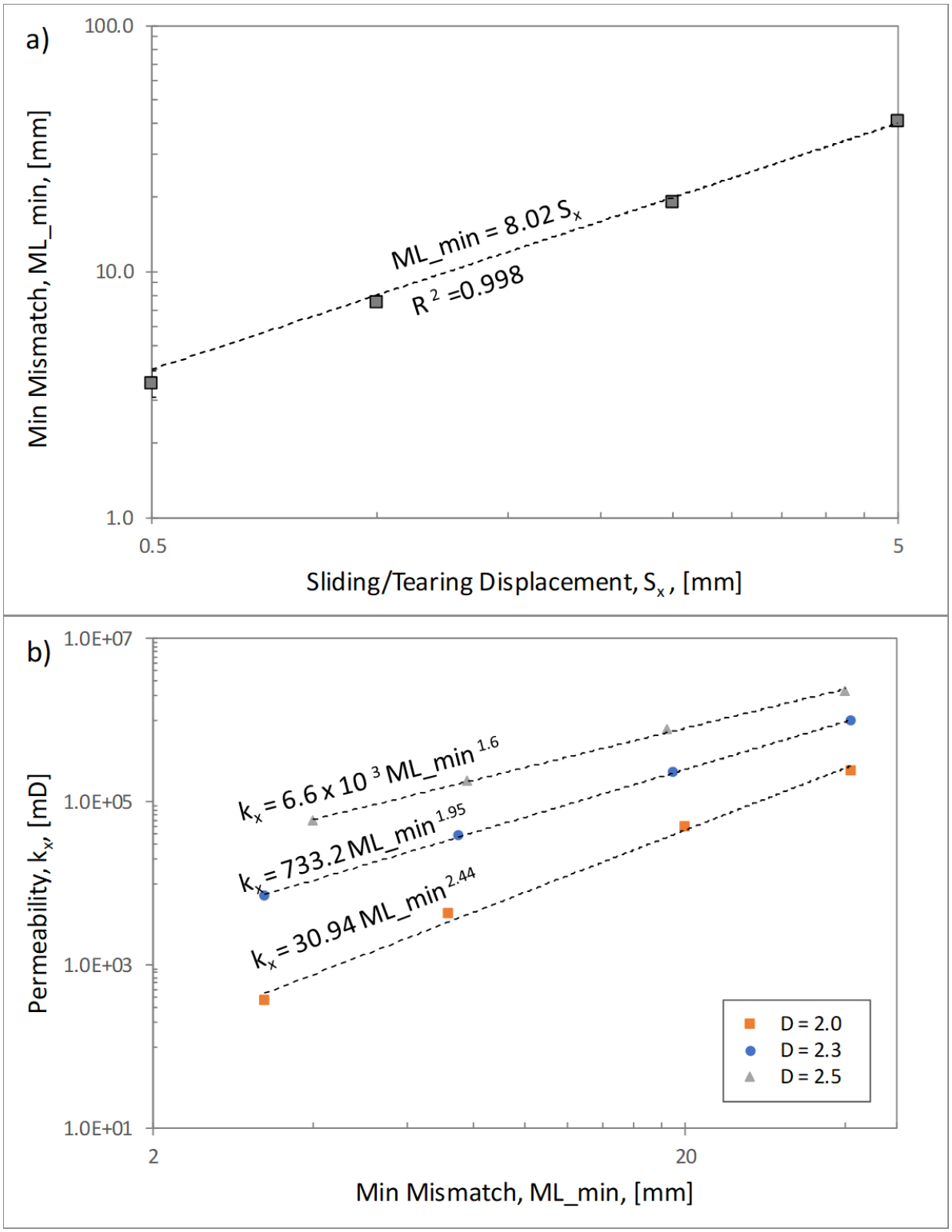

Figure 2.14. a) Minimum mismatch length versus sliding/tearing displacement, b) Permeability versus minimum mismatch length.

2.4. Discussion

The present work evaluates the effect of fracture surface features such as roughness, aperture, and mismatch on permeability using fracture surface scanning by SfM photogrammetry, numerical modeling, and lattice-Boltzmann fluid flow simulation.

2.4.1. SfM photogrammetry surface scanning

The results of this study demonstrate the versatility of the SfM procedure as an analytical tool which can be applied at a wide range of scales including millimeter-scale features such as fracture surfaces. The controlled conditions in the photogrammetry laboratory allowed a highly detailed scan and extraction of the micro surface topography of samples sized 30 x 30 x 30 cm producing a resolution of 0.25 mm and an estimated error of 0.09 mm. This method produces more realistic and applicable results than the traditional Barton Comb, with results comparable to those reported by Candela *et al*. (2009), Renard *et al*. (2013), and Corradetti *et al*. (2017) using both Lidar or laser profilometers. However, the SfM methodology is several orders of magnitude more cost-effective and is readily accessible. A future implementation of this study could include developing a workflow suitable for in situ field studies, however, more variables need to be controlled and results yielding lower accuracy are expected.

2.4.2. Fracture Roughness Characterization

This methodology proved to be highly efficient in expressing the fracture roughness allowing a more accurate and representative measure with respect to the relative hydraulic roughness (Lomize, 1951; Louis, 1969; de Quadros, 1982) or the JRC (Barton et al., 1985; Barton & Choubey, 1977). Another important aspect of these results is the reproducibility of synthetic fractures with similar characteristics. This step was important to increase the data volumes leading to greater statistical significance of the results and validity of the inferred relationships. The lattice-Boltzmann procedure also played a key role in this study as it allows the estimation of permeability values for controlled scenarios with different imposed properties (i.e. roughness, opening mode, and sliding/tearing displacement). This permits evaluation of the relationship between permeability, porosity, mismatch, and other

imposed properties. The computed permeability may present some impressions in low resolution models as previously reported by Zambrano *et al*. (2018). Therefore, permeability results may be considered not as the real values but only as approximations.

2.4.3. Permeability in function of fracture properties

Two situations were considered to explain the presence of open fractures, i) dilation due to opening mode displacement (joint or opened pressure solution seam) and ii) dilation due to mismatch caused by shearing and sliding/tearing displacement.

In the first case, the results followed the expectation and confirmed previous interpretations: i) permeability tends to increase with opening following a non-linear relationship, ii) a higher fractal dimension (greater roughness) correlates to lower permeability, iii) the effect of roughness is less significant at greater opening values. It is expected that higher roughness (higher frequencies of asperities) may exposed a wider area in contact with the migrating fluid, diminishing its velocity due to friction. Evidently, at higher opening values this effect should be less evident because it is the specific area (area/volume) which has a control on the permeability, as has been previously reported by Zambrano *et al*. (2018) for porous media.

The second case (sliding/tearing displacement) creates an aperture due to mismatch between the opposite walls of the fracture. We found significant differences between these two cases concerning the effect of the roughness of the permeability. In fact, the effect of roughness on permeability is inverse. Given the same displacement, fractures with higher roughness values permit the creation of larger voids and therefore enhance the fluid flow. So, the effect of friction exerted by the roughness has a secondary role in the case of mismatch due to sliding/tearing displacement. The continuous dilatancy of the fracture due to sliding/tearing displacement should cease at a certain value depending on the asperity frequencies present in the fracture. Of course, it is difficult to verify this with the behavior of real fractures, where a 20 mm sliding/tearing displacement likely leads to fracture wall wearing and the generation of cataclastic material (Agosta et al., 2009), eventually reducing permeability. However, our model has greater applicability to small displacements where the damage of the fracture walls is negligible.

The mismatch itself has a positive control on the permeability. The importance of this result is that the mismatch could be also produced by diagenetic processes (*e.g.,* cementation, dissolution) and shearing. Zambrano *et al.* (2018) using X-ray microtomographic images in shear compaction bands hosted in porous carbonates, showed the existence of complex channelized porous networks along shear surface within these structures.

2.4.4. Consequences to reservoir modeling

The results agree with the macroscale observations of previous authors in the study area, where both opened/sheared pressure solution seams and fault-related joints present the greatest values of aperture and the most important bitumen impregnation (Agosta et al., 2009, 2010; Panza et al., 2018; Volatili et al., 2019).

The relationship between permeability and porosity for rough fractures clearly deviates from the ideal smooth parallel plate case (for the studied scenarios). Fracture permeability is lower for the same porosity range (< 0.2 %) in comparison to the theoretical values. Instead, the power-law slope is higher, indicating a more important control of porosity as it was expected. The equation itself may be useful to estimate the permeability of fractures if the fracture porosity is known.

The findings have a significant impact on fracture modeling (*e.g.* Discrete Fracture Network). After their formation, both closing and opening mode fractures are often subjected to a shear process, and even with a small imperceptible sliding/tearing displacement they cannot be modeled as simple opening mode fracture. At reservoir depth, preexisting fractures (joints and pressure solution seams) that are favorably oriented to be sheared (accordingly to the orientations of the stress field which affected the area) may be characterized by a mismatch between the fracture walls enhancing the fracture opening.

2.5. Conclusions

We presented a new multi-faceted approach to characterize surface fracture roughness by SfM photogrammetry, numerical modeling, and computational fluid dynamics simulation. This methodology provides a better quantification of surface parameters that are not possible to obtain using former surface roughness measurement and analysis tools.

In addition, this study illustrates the crucial relationships between permeability and other fracture properties, such as roughness, porosity, opening mode-sliding/tearing displacement, and mismatch. The obtained relationships pointed out the following statements:

- In joints (opening mode fractures) and/or opened pressure solution seams, the roughness tends to reduce the permeability. Thus, the permeability is inversely proportional to the fractal dimension.
- In sheared joints and/or pressure solution seams (assuming an insignificant surface wearing) the sliding/tearing mode displacement may cause mismatch and therefore enhance the porosity and permeability. The validity of this behavior may depend on the point that displacement starts to produce cataclastic material. Small displacements and mismatch may be extremely important to guarantee storage and migration of geofluid at depth thanks to asperities-supported aperture.
- Porosity exerts a more important control on permeability in rough fractures (higher power-law slope). The empiric relationship may result in greater utility for estimating the fracture permeability if the fracture porosity is known.

Acknowledgements

This research was supported by the FAR Project 2014 “Characterization and modeling of natural reservoirs of geofluids in fractured carbonate rocks”, funded by the University of Camerino, Principal investigator Emanuele Tondi and the Reservoir Characterization Project (www.rechproject.com). We also acknowledge and thank Amerigo Corradetti for generously sharing his code for Power Spectral (PSD) analysis of surfaces and thoughtful conversations that helped move this work forward. The authors also thank GeoMORE s.r.l. (www.geomore.it) for providing access to computational resources used for fluid flow simulations.

References

Agosta, F., Alessandroni, M., Antonellini, M., Tondi, E., Giorgioni, M., 2010. From fractures to flow: a field-based quantitative analysis of an outcropping carbonate reservoir. Tectonophysics 490, 197-213.

Agosta, F., Alessandroni, M., Tondi, E., Aydin, A., 2009. Oblique-slip normal faulting along the northern edge of the Majella anticline: inferences on hydrocarbon migration and accumulation. J. Struct. Geol. 31, 674–690.

Ahrens, J., Geveci, B., Law, C., 2005. ParaView: An End-User Tool for Large Data Visualization, Visualization Handbook, Elsevier, ISBN-13: 978-0123875822.

Alessandroni, M., 2008. Structural Control on the Flow and Accumulation of Hydrocarbons in Carbonate Grainstones: An Example from the Bolognano Fm. (Majella Mt. Italy). Ph.D. thesis, University of Camerino, 167 pp.

Andrä, H., Combaret, N., Dvorkin, J., Glatt, E., Han, J., Kabel, M., Keehm, Y., … Zhan, X., 2013. Digital rock physics benchmarks—part II: computing effective properties. Comput. Geosci. 50, 33–43. http://dx.doi.org/10.1016/j.cageo.2012.09.008.

Antonellini M., Tondi E., Agosta F., Aydin A., Cello G., 2008. Failure modes in deep-water carbonates and their impact for fault development: Majella Mountain, Central Apennines, Italy., Marine and Petroleum Geology, 25, 1074–1096.

Aydin, A., Antonellini, M., Tondi, E., Agosta, F., 2010. Deformation along the leading edge of the Majella thrust sheet in central Italy. J. Struct. Geol. 32, 1291e1304. http://dx.doi.org/10.1016/j.jsg.2008.10.005.

Barton, N. & Choubey, V., 1977. The shear strength of rock joints in theory and practice. Rock Mechanics, 10 (1/2), 1-54.

Barton, N., Bandis, S. & Bakhtar, K., 1985. Strength, deformation and conductivity coupling of rock fractures. Int. J. of Rock Mech. Min. Sic., 22, 121-140.

Bemis, S. P., Micklethwaite, S., Turner, D., James, M. R., Akciz, S., Thiele, S. T., & Bangash, H. A., 2014. Ground-based and UAV-Based photogrammetry: A multi-scale, high-resolution mapping tool for structural geology and paleoseismology. J. Struct. Geol. 69, 163–178.

Bhatnagar, P.L., Gross E.P., Krook M., 1954. A model for collision processes in gases. I: small amplitude processes in charged and neutral one-component system. Phys. Rev. 94, 511-525

Bijeljic, B., Raeini, A., Mostaghimi, P., Blunt, M.J., 2013. Predictions of non-Fickian solute transport in different classes of porous media using direct simulation on pore-scale images. Phys. Rev.E 87 (1), 013011. https://doi.org/10.1103/PhysRevE. 87.013011

Blunt, M. J., Bijeljic, B., Dong, H., Gharbi, O., Iglauer, S., Mostaghimi, P., Paluszny, A., and Pentland, C. H., 2013. Pore-scale imaging and modeling. Adv. Water Resour., 51, 197–216.

Brown, S. R., 1995. Simple mathematical model of a rough fracture. Journal of Geophysical Research: Solid Earth, 100(B4), 5941-5952.

Candela, T., Renard, F., Bouchon, M., Brouste, A., Marsan, D., Schmittbuhl, J., Voisin, C., 2009. Characterization of fault roughness at various scales: implications of three-dimensional high-resolution topography measurements. Pure Appl. Geophys. 166 (10–11), 1817–1851. http://dx.doi.org/10.1007/s00024-009-0521-2.

Candela, T., Renard, F., Klinger, Y., Mair, K., Schmittbuhl, J., Brodsky, E.E., 2012. Roughness of fault surfaces over nine decades of length scales. J. Geophys. Res. 117 (B8), B08409. http://dx.doi.org/10.1029/2011JB009041.

Cardenas, M.B., 2008. Three-dimensional vortices in single pores and their effects on transport. Geophys. Res. Lett. 35, L18402. https://doi.org/10.1029/ 2008GL035343.

Cardenas, M.B., 2009. Direct simulation of pore level Fickian dispersion scale for transport through dense cubic packed spheres with vortices. Geochem. Geophys. Geosyst. 10, Q12014. https://doi.org/10.1029/2009GC002593.

Carrivick, J. L., Smith, M. W., & Quincey, D. J., 2016. Structure from Motion in the Geosciences. John Wiley & Sons.

Cello, G., Mazzoli, S., Tondi, E., Turco, E., 1997. Active tectonics in the central Apennines and possible implications for seismic hazard analysis in peninsular Italy. Tectonophysics 272, 43-68.

Corradetti, A., McCaffrey, K., De Paola, N., & Tavani, S., 2017. Evaluating roughness scaling properties of natural active fault surfaces by means of multi-view photogrammetry. Tectonophysics, 717, 599-606.

d'Humières, D., 1992. Generalized Lattice-Boltzmann equations, in: Rarefied Gas Dynamics: Theory and Simulations, Prog. Astronaut. Aeronaut., vol. 159, edited by B. D. Shizgal and D. P. Weave, pp. 450-458, AIAA, Washington, D. C.

de Quadros E.F., 1982. Determinação das características do fluxo de água em fraturas de rochas. Dissert. de Mestrado, Dept. of Civil Eng., Polytech. School, University of São Paulo (1982).

Degruyter, W., Burgisser, A., Bachmann, O., Malaspinas, O., 2010. Synchrotron X-ray microtomography and lattice Boltzmann simulations of gas flow through volcanic pumices. Geosphere, v. 6, no. 5, p. 470-481, doi: 10.1130/GES00555.1.

d'Humières, D., Ginzburg, I., Krafczyk, M., Lallemand P., and Luo., L-S., 2002. Multiple-Relaxation-Time Lattice Boltzmann Models in Three Dimensions, Phil. Trans. R. Soc. A, 360, 437-451.

Ghisetti, F. & Vezzani, L., 2002. Normal faulting, extension and uplift in the outer thrust belt of the central Apennines (Italy): role of the Caramanico fault. Basin Research, 14, 225-236.

Isakov, E., Ogilvie, S. R., Taylor, C. W., & Glover, P. W., 2001. Fluid flow through rough fractures in rocks I: high resolution aperture determinations. Earth and Planetary Science Letters, 191(3-4), 267-282.

Jin, G., Patzek, T.W., Silin, D.B., 2004. Direct prediction of the absolute permeability of unconsolidated consolidated reservoir rock. In: Proceedings of the SPE annual technical conference exhibition, Houston, TX. (SPE 90084)

Keehm, Y., 2003. Computational rock physics: Transport properties in porous media and applications, Ph.D. Dissertation, 135 pp., Stanford Univ., Stanford, Calif.

Keehm, Y., Mukerji, T., Nur, A., 2004. Permeability prediction from thin sections: 3D reconstruction and Lattice-Boltzmann flow simulation. Geophys. Res. Lett., 31, L04606, doi:10.1029/2003GL018761.

Khan, F., Enzmann, F., Kersten, M., Wiegmann, A., Steiner, K., 2012. 3D simulation of the permeability tensor in a soil aggregate on basis of nanotomographic imaging and LBE solver. J. Soils Sediments 12, 86–96. http://dx.doi.org/10.1007/s11368-011-0435-3.

Ladd, A. J. C., 1994. Numerical simulations of particulate suspensions via a discretized Boltzmann equation: Part 2. Numerical results, J. Fluid Mech., 271, 311-339.

Latt, J., 2009, Palabos, Parallel Lattice Boltzmann Solver: http://www.lbmethod.org/palabos/

Lomize, G. M., 1951. Flow in Fractured Rocks (in Russian), 127 pp., Gosenergoizdat, Moscow, 1951.

Louis, C, 1969. A study of ground water flow in jointed rock and its influence on the stability of rock masses. Rock Mech. Res. Rep. 10,90 pp. Imp. Coll., London.

Marchegiani L., Van Dijk J. P., Gillespie P. A., Tondi E. & Cello G., 2006. Scaling properties of the dimensional and spatial characteristics of fault and fracture systems in the Majella Mountain, central Italy. In: Cello G. & Malamud B. (Eds) Fractal Analysis for Natural Hazards. Geological Society of London, Special Publications, 261, 113–131.

McCaffrey, K. J. W., Jones, R. R., Holdsworth, R. E., Wilson, R. W., Clegg, P., Imber, J., ... & Trinks, I., 2005. Unlocking the spatial dimension: digital technologies and the future of geoscience fieldwork. J. Geol. Soc. London. 162, 927–938.

Narvaez, A., Zauner, T., Raischel, F., Hilfer, R., and Harting, J., 2010. Quantitative analysis of numerical estimates for the permeability of porous media from lattice-Boltzmann simulations, J. Stat. Mech., 11, P11026.

Nesbit, P. R., Durkin, P. R., Hugenholtz, C. H., Hubbard, S. M., & Kucharczyk, M., 2018. 3-D stratigraphic mapping using a digital outcrop model derived from UAV images and structure-from-motion photogrammetry. Geosphere. 14(6). DOI: 10.1130/GES01688.1

Ogilvie, S. R., Isakov, E., & Glover, P. W., 2006. Fluid flow through rough fractures in rocks. II: A new matching model for rough rock fractures. Earth and Planetary Science Letters, 241(3-4), 454-465.

Ogilvie, S. R., Isakov, E., Taylor, C. W., & Glover, P. W. J., 2003. Characterization of rough-walled fractures in crystalline rocks. Geological Society, London, Special Publications, 214(1), 125-141.

Pan, C., Luo, L.S., & Miller, C.T., 2006. An evaluation of lattice Boltzmann schemes for porous medium flow simulation. Computers & fluids, 35(8), 898-909.

Panza, E., Agosta, F., Rustichelli, A., Zambrano, M., Tondi, E., Prosser, G., Giorgioni, M., Janiseck, J.M., 2016. Fracture stratigraphy and fluid flow properties of shallow water, tight carbonates: the case study of the Murge Plateau (southern Italy). Mar. Petrol. Geol. 73, 350–370.

Panza, E., Agosta, F., Zambrano, M., Tondi, E., Prosser, G., Giorgioni, M., Janiseck, J.M., 2015. Structural architecture and Discrete Fracture Network modeling of layered fractured carbonates (Altamura Fm., Italy). Ital. J. Geosci. 134 (3), 409.

Panza, E., Sessa, E., Agosta, F., & Giorgioni, M., 2018. Discrete Fracture Network modeling of a hydrocarbon-bearing, oblique-slip fault zone: Inferences on fault-controlled fluid storage and migration properties of carbonate fault damage zones. Marine and Petroleum Geology, 89, 263-279.

Pitts, A. D., Casciano, C. I., Patacci, M., Longhitano, S. G., Di Celma, C., & McCaffrey, W. D., 2017. Integrating traditional field methods with emerging digital techniques for enhanced outcrop analysis of deep-water channel-fill deposits. Marine and Petroleum Geology, 87, 2-13.

Renard, F., Candela, T., Bouchaud, E., 2013. Constant dimensionality of fault roughness from the scale of micro-fractures to the scale of continents. Geophys. Res. Lett. 40 (1), 83–87. http://dx.doi.org/10.1029/2012GL054143.

Renard, F., Mair, K., Gundersen, O., 2012. Surface roughness evolution on experimentally simulated faults. J. Struct. Geol. 45, 101–112. http://dx.doi.org/10.1016/j.jsg.2012. 03.009.

Renard, F., Voisin, C., Marsan, D., Schmittbuhl, J., 2006. High resolution 3D laser scanner measurements of a strike-slip fault quantify its morphological anisotropy at all scales. Geophys. Res. Lett. 33 (4), L04305. http://dx.doi.org/10.1029/2005GL025038.

Rustichelli, A., Tondi, E., Agosta, F., Cilona, A., Giorgioni, M., 2012. Development and distribution of bed-parallel compaction bands and pressure solution seams in the Bolognano Formation carbonates (Majella Mountain, Italy). J. Struct. Geol. 37, 181e199. https://doi.org/10.1016/j.jsg.2012.01.007.

Rustichelli, A., Tondi, E., Agosta, F., Di Celma, C., Giorgioni, M., 2013. Sedimentologic and diagenetic controls on pore-network characteristics of Oligocenee-Miocene ramp carbonates (Majella Mountain, central Italy). Am. Assoc. Petrol. Geol. Bull. 97, 487e524

Rustichelli, A., Torrieri, S., Tondi, E., Laurita, S., Strauss, C., Agosta, F., Balsamo, F., 2016. Fracture characteristics in cretaceous platform and overlaying ramp carbonates: an outcrop study from Maiella mountain (central Italy). Mar. Petroleum Geol. 76, 68-87.

Schuster, A., 1898. On the investigation of hidden periodicities with application to a supposed 26-day period of meteorological phenomena. J. Geophys. Res. 3 (1), 13. http://dx.doi.org/10.1029/TM003i001p00013.

Scisciani, V., Tavarnelli, E., & Calamita, F. 2002. The interaction of extensional and contractional deformation in the outer zones of the Central Apennines, Italy. Journal of Structural Geology, 24, 1647-1658.

Shah, S.M., Gray, F., Crawshaw, J.P., Boek, E.S., 2015. Micro-computed tomography pore scale study of flow in porous media: effect of voxel resolution. Adv. Water Resour. 000, 1–12. http://dx.doi.org/10.1016/j.advwatres.2015.07.012.

Snow D., 1965. A parallel Plate Model of Fractured Permeable Media (PhD thesis). Berkeley: University of California.

Sukop, M.C., Huang, H., Lin, C.L., Deo, M.D., Oh, K., & Miller, J.D., 2008. Distribution of multiphase fluids in porous media: Comparison between lattice Boltzmann modeling and micro-x-ray tomography. Physical Review E, 77(2), 026710.

Tondi, E., Antonellini, M., Aydin, A., Marchegiani, L., Cello, G., 2006. The role of deformation bands, stylolites and sheared stylolites in fault development in carbonate grainstones of Majella Mountain, Italy. J Struct Geol, 28: 376-391, doi:10.1016/j.jsg.2005.12.001.

Tsang, Y.W., 1992. Usage of "Equivalent Apertures " for Rock Fractures as Derived From Hydraulic and Tracer Tests . Water Resources Research , vol . 28, no . 5 : 1451-1455 .

Volatili, T., Zambrano, M., Cilona, A., Huisman, B. A. H., Rustichelli, A., Giorgioni, M., Vittori, S., & Tondi, E., 2019. From fracture analysis to flow simulations in fractured carbonates: The case study of the Roman Valley Quarry (Majella Mountain, Italy). Marine and Petroleum Geology. 100, 95-110. https://doi.org/10.1016/j.marpetgeo.2018.10.040.

Witherspoon P, A., J. S. Y. Wang, K. Iwai, and J. E. Gale, Validity of cubic law for fluid flow in a deformable rock fracture, Water Resour. Res., 16(6), 1016-1024, 1980.

Wu, K., Dijke, M.I.J., Couples, G.D., Jiang, Z., Ma, J., Sorbie, K.S., Crawford, J., Young, I., Zhang, X., 2006. 3D stochastic modeling of heterogeneous porous media - applications to reservoir rocks. Transp. Porous Media 65, 443–467. http://dx.doi.org/10.1007/ s11242-006-0006-z.

Zambrano, M., Tondi, E., Korneva, I., Panza, E., Agosta, F., Janiseck, J.M., Giorgioni, M., 2016. Fracture properties analysis and discrete fracture network modeling of faulted tight limestones, Murge Plateau, Italy. Ital. J. Geosci. 135 (1), 55–67. https://doi.org/ 10.3301/IJG.2014.42.

Zambrano, M., Tondi, E., Mancini, L., Arzilli, F., Lanzafame, G., Materazzi, M., & Torrieri, S., 2017. 3D Pore-network quantitative analysis in deformed carbonate grainstones. Marine and Petroleum Geology, 82, 251-264.

Zambrano, M., Tondi, E., Mancini, L., Lanzafame, G., Trias, F.X., Arzilli, F., Materazzi, M., Torrieri, S., 2018. Fluid flow simulation and permeability computation in deformed porous carbonate grainstones. Adv. Water Resour. 115. https://doi.org/10.1016/j. advwatres.2018.02.016.

Zimmer, B., Liutkus-Pierce, C., Marshall, S. T., Hatala, K. G., Metallo, A., & Rossi, V., 2018. Using differential structure-from-motion photogrammetry to quantify erosion at the Engare Sero footprint site, Tanzania. Quaternary Science Reviews, 198, 226-241.

CHAPTER

3

PORE-SCALE DUAL-POROSITY AND DUAL-PERMEABILITY MODELING IN AN EXPOSED MULTI-FACIES POROUS CARBONATE RESERVOIR

The present chapter has been published in Marine and Petroleum Geology 128 (2021) 105004

3. PORE-SCALE DUAL-POROSITY AND DUAL-PERMEABILITY MODELING IN AN EXPOSED MULTI-FACIES POROUS CARBONATE RESERVOIR

Miller Zambrano [1], Tiziano Volatili [1], Lucia Mancini [2, 3], Alan Pitts [1], Maurizio Giorgioni [4], Emanuele Tondi [1]

[1] School of Science and Technology - Geology Division, University of Camerino, Italy.
[2] Elettra-Sincrotrone Trieste S.C.p.A., 34149 Basovizza, Trieste, Italy.
[3] LINXS—Lund Institute of Advanced Neutron and X-ray Science, 223 70 Lund, Sweden.
[4] Shell Italia Exploration and Production, Rome, Italy.

Abstract

Fracture networks in porous carbonates can control, assist, or even contribute negatively to reservoir quality. In scenarios where fractures and matrix pore systems are of similar importance, a dual-porosity/permeability (DP/P) modeling approach is necessary or at least recommendable for the reservoir characterization. These workflows are well established at the reservoir scale, however at the microscale, the interaction between fractures and porous matrix needs to be further investigated.

The aim of this work is to assess the contribution of meter-scale fractures (macrofractures) to the porosity and permeability in a porous carbonate reservoir analogue at the microscale. To reach this objective, we created DP/P models at the microscale through the integration of two different methods of 3D imaging such as, high-resolution synchrotron X-ray microtomography (SR micro-CT) and Structure from Motion (SfM) photogrammetry. Quantitative analyses of pristine rock and DP/P models were performed to evaluate the contribution of macrofracture segments to the porosity and connectivity of the pore network. These results were integrated with single-phase flow simulations for calculating permeability values. Different scenarios were modelled in order to systematically evaluate the control exerted by fracture roughness parameters (i.e., asperity height distribution and fractal dimension) on porosity and permeability in various lithofacies.

The key analyzed samples come from the Roman Valley quarry located at the Majella Mountain (central Italy), which has been widely investigated due to the presence of consistent bitumen impregnations distributed in pervious medium-to-coarse grainstones and along two main fault zones. The results of this study demonstrate the utility of

obtaining DP/P microscale models as complementary approach to explain the hydrocarbon distribution in fractured multi-facies porous carbonates. We document the potential of macrofracture segments to provide neo-connected porosity by linking up adjacent isolated or partially isolated matrix pore networks in impervious carbonate rocks. In pervious carbonate lithofacies, fault-related macrofractures can enhance permeability and contribute to bitumen migration and distribution, whereas the increment of storage capacity is limited since these rocks are already fully connected. In the case of impervious carbonate lithofacies, results indicate that the actual contribution of neo-connected pores to fluid transport is limited, which agrees with outcrop observations.

Keywords: *pore-fracture dual media, porous grainstones, rough fractures, matrix porosity, fracture porosity, X-ray microtomography, synchrotron radiation, heavy oil*

3.1. Introduction

In fractured reservoirs, fluid storage and migration can be enhanced or impeded depending on the fracture network hydraulic behavior and their interaction with the matrix pore system, composed of interparticle and intraparticle voids. According to their hydromechanical performance, fractured reservoirs can be classified into four types (Nelson, 2001): type I) those where the storage capacity (i.e., porosity) and migration (i.e., permeability) depend entirely on the fracture system, type II) where fractures provide essential permeability, type III) where fractures provide permeability assistance, and type IV) where fractures behave as barriers and/or contribute negatively to fluid flow.

In type I reservoirs (e.g., tight carbonates), the permeability depends on two factors, the geometrical properties of the fracture network and the hydraulic aperture. The geometrical properties are defined as fracture length distribution, orientation, and intensity. These factors control the connectivity and determine whether fluids can pass through certain stratigraphic mechanical boundaries, such as single beds, bed packages, and bed package associations (Panza et al., 2016; Zambrano et al., 2016; Corradetti et al., 2018; Massaro et al., 2018). The hydraulic aperture is controlled by the pore space between the opposite walls of the fracture, the mismatch between both surfaces, displacement, and the fracture roughness (Lomize, 1951; Louis, 1969; Witherspoon et al., 1980; Barton et al., 1985; Tsang, 1992; Lee and Cho, 2002; Zambrano et al., 2019b). Contrary to the type I, in type IV reservoirs (e.g., deformed porous carbonates), structural features like deformation bands and/or fractures sealed by secondary mineralization may represent buffer zones which contribute to compartmentalization (Aydin, 2000; Tondi, 2007; Antonellini et al., 2014; Kaminskaite et al., 2019) and create significant anisotropy (Cilona et al., 2012; Tondi et al., 2012, 2016; Zambrano et al., 2018).

The most puzzling cases, in terms of quality assessment, are the reservoir types II and III. In these kinds of reservoirs, there is a hybrid hydraulic behavior where the storage is determined by the matrix porosity as well as fractures at the scale of particles (called microfractures in this paper), bed-scale fractures (called macrofractures in this paper) enhance the fluid migration. The interaction between the matrix porosity and macrofracture systems can be described by Dual-Porosity/Permeability (DP/P) models that consider the influence of both matrix and fracture pore space systems (Warren and Root, 1963; Gerke and van Genuchten, 1993; Gong et al., 2008; Wei and

Zhang, 2010; Volatili et al., 2019). These models require the definition of transmissibility parameters that govern the interaction between the two pore systems (Kazemi et al., 1976).

In reservoir characterization, the petrophysical model is based on structural, sedimentological, geophysical and geomechanical data (Masaferro et al., 2004; Hwang et al., 2018; Takougang et al., 2019; Bagni et al., 2020; Espejel et al., 2020; Mendez et al., 2020). The petrophysical properties of the matrix porosity systems can be assessed by means of laboratory analysis of cores and plug samples. The porosity and pore size distribution are commonly estimated using microscopy or indirect laboratory methods, such as helium pycnometer and mercury injection (Baud et al., 2009; Cilona et al., 2012; Trippetta et al., 2020). In addition, advanced three-dimensional (3D) imaging techniques like X-ray (Blunt et al., 2013; Wildenschild and Sheppard, 2013; Cilona et al., 2014; Ji et al., 2015; Arzilli et al., 2016; Baud et al., 2017; Zambrano et al., 2017; Riegel et al., 2019), or Neutron computed microtomography (de Beer and Middleton, 2006; Hall, 2013; Zambrano et al., 2019a) may provide accurate microscale information of the matrix porosity system. Further integration of quantitative image analysis and direct fluid simulations are usually performed to understand the control of pore properties on fluid flow (Degruyter et al., 2010; Blunt et al., 2013; Zambrano et al., 2018).

Although the use of DP/P models is a routine task in the hydrocarbon reservoir assessment workflow, the interaction of fractures and matrix porosity at the microscale remains poorly understood. Here we present a methodology that combines high-resolution synchrotron X-ray microtomography (SR micro-CT), SfM photogrammetry, fracture modeling, and fluid flow simulations with the objective of understanding between fractures and matrix pore space systems in an oil-bearing multi-facies carbonate reservoir.

3.2. Geological settings

This investigation is focused on several carbonate lithofacies from the Majella Mountain (central Italy), which is an east-verging thrust-related anticline formed during the middle-to-late Pliocene (Ghisetti and Vezzani, 2002; Scisciani et al., 2002) involving a 2 km-thick Jurassic to Miocene carbonate succession, vastly documented by Crescenti (1969), Mutti et al. (1996, 1997), Vecsei and Sanders (1999), and Brandano et al. (2012, 2016a). At Majella Mountain, the main large deformational features are high-angle normal, strike-slip and oblique-slip faults; whereas the predominant meso-scale correspond to multiple sets of opening-mode fractures, pressure solution seams, and deformation bands (Marchegiani et al., 2006; Tondi et al., 2006; Antonellini et al., 2008; Agosta et al., 2009, 2010; di Cuia et al., 2009; Aydin et al., 2010; Rustichelli et al., 2012, 2013, 2016; Scrocca et al., 2013).

The rock samples studied in this work come from a widely studied location known as the Roman Valley quarry (Fig. 3.1). In this quarry, the hydrocarbon (bitumen) distribution is controlled by the lithofacies, faults, and fracture networks (Agosta et al., 2010; Rustichelli et al., 2012, 2013; Panza et al., 2018; Volatili et al., 2019; Romano et al., 2020). The exposed rocks belong to the Bolognano formation (upper Oligocene – upper Miocene), which has been described by many studies in the last few decades (Mutti et al., 1997; Vecsei and Sanders, 1999; Pomar et al., 2004; Carnevale et al., 2011; Brandano et al., 2012, 2016a, 2016b; Rustichelli et al., 2012, 2013; Reuter et al., 2013; Scrocca et al., 2013). According to these authors, the Bolognano formation consists of shallow-water skeletal rudstones, floatstones, grainstones, and packstones, as well as deeper water marly wackestones and mudstones. Consistently, Scrocca et al. (2013) documented the presence of several bitumen seeps in the northern sector of the Majella Mountain, most of which occur within the Bolognano Formation. This rock formation is a productive reservoir in the Adriatic offshore area, such as the Ombrina Mare and Katia oil fields (Mattavelli and Novelli, 1988; Zappaterra, 1994; Katz et al., 2000; Cazzini et al., 2015).

Rustichelli et al. (2012, 2013) thoroughly described the sedimentological and diagenetic properties of this formation. The authors divided the Bolognano formation into five facies associations: A- *Lepidocyclina* grainstones (separated in two members, upper and bottom member Au and Ab respectively), B- Bryozoan grainstones, C-Echinoid grainstones to packstones, D- Echinoid and planktonic foraminifera packstones to wackestones, E- Planktonic foraminifera wackestones to mudstones. Similarly, Brandano et al. (2016) offered an

alternative classification dividing the Bolognano formation in five lithofacies associations: *Lepidocyclina* calcarenites, Cherty marly limestones, Bryozoan calcarenites, Hemipelagic marls/ marly limestones, and *Lithothamnion* limestones. For the purpose of this work, we follow the classification proposed by Rustichelli et al. (2012, 2013) due to a more detailed description and differentiation of the carbonate lithofacies exposed in the studied outcrop.

In the Roman Valley quarry, the lithofacies Au, B, C, and E crop out (Fig. 3.1, Table 3.1). Rustichelli et al. (2013) provided accurate 2D and 3D porosity analyses for these lithofacies, further investigated by additional laboratory measurements of porosity and permeability performed by Volatili et al. (2019). Based on the petrophysical properties and the hydrocarbon content (Table 3.1), the lithofacies can be divided in pervious (Au and B) and impervious (C and E). For the pervious lithofacies, previous authors (Rustichelli et al., 2012, 2013; Volatili et al., 2019) have determines values of porosity in the range of 24-32% and permeability values between 80-550 mD (Volatili et al., 2019). Moreover, porosity values three times lower have been reported in nearby areas for the same lithofacies (Trippetta and Geremia, 2019; Ruggieri and Trippetta, 2020; Trippetta et al., 2020). According to Trippetta and Geremia (2019), these rocks can reach up to 71% of oil saturation (Volume of oil/Volume of pores). In the case of impervious lithofacies, Rustichelli et al. (2013) and Volatili et al. (2019) reported porosity values of near 10 % and 28 % for lithofacies C and E, respectively. For both lithofacies, the permeability is lower than 2.5 mD providing poor condition to fluid migrations through the matrix pore space (Volatili et al., 2019).

In the studied outcrop, the exposed rocks dip 10°–25° to the NE and are crosscut by two NW-SE trending oblique-slip normal linking faults (Fig. 3.1a) with 10s of meters of throw and a left-lateral component of slip (Agosta et al., 2009; Giorgioni et al., 2011). The macrofracture systems characterizing this area have been described by previous authors (Tondi et al., 2006; Agosta et al., 2010; Rustichelli et al., 2012; Panza et al., 2018; Volatili et al., 2019; Romano et al., 2020) and consist of background and fault-related macrofractures.

The hydrocarbons in the area likely migrated during the late Messinian to late Pleistocene (Lavenu et al., 2014). However, the migration mechanism of the hydrocarbon is quite debated by two contrasting models. In the first

model, both matrix and fracture porosity play important roles in the bitumen distribution. The migration of bitumen is timed after the formation of oblique main NW-SE faults dated in the middle Pleistocene (Agosta et al., 2009, 2010). In this model, hydrocarbons migrated through fractured fault zones and then laterally through the surrounding porous carbonates. Agosta and coworkers documented the fault-related reservoir compartmentalization responsible of a heterogeneous distribution of bitumen in the adjacent pervious rocks.

The second model proposes that most of the faults in the area may not influence the hydrocarbon distribution since postdate the main oil migration (Lipparini et al., 2018). This statement is made on an accurate and highly detailed hydrocarbon distribution analysis (Lipparini et al., 2018) and the evidence of an earlier migration during the late Messinian (Iadanza et al., 2013). According to Lipparini et al. (2018), the closest well to the Roman Valley quarry exceptionally showed the presence of fractures interpreted as fault related due to the proximity to the fault linkage area described by Agosta et al. (2009, 2010). In addition, the bitumen content at the evaluated well reaches the outstanding values of near 17 % of the total rock volume in comparison to the rest of the area where it varies between 2 % and 12 % (Lipparini et al., 2018). Therefore, the second migration model explains the presence and anomalous distribution of oil in the Roman Valley quarry by the occurrence of a possible tertiary migration (Trippetta et al., 2020).

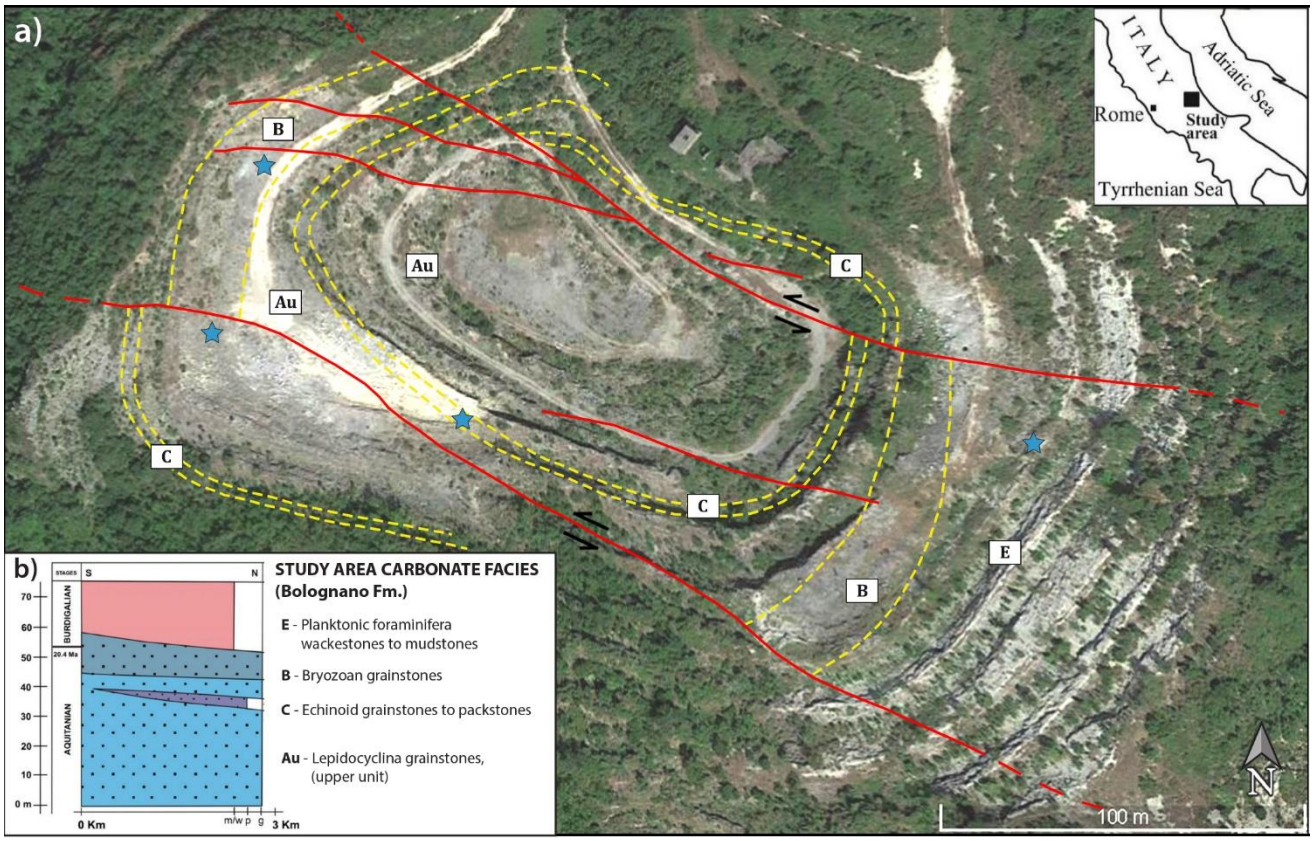

Fig. 3.1: a) Structural map of the Roman Valley quarry (modified after Volatili et al. 2019). Notes: red lines indicate faults; yellow dashed lines indicate lithofacies boundaries (see Table 3.1 for detail); blue stars indicate the sample locations. b) Stratigraphic scheme of the lithofacies (Bolognano Fm.) outcropping in the study area (from Rustichelli et al., 2012).

Table 3.1. Characteristics of lithofacies exposed in the Roman Valley quarry

Lithofacies	Φ_{2D_t} [%]	Φ_{2D_i} [%]	Φ_{3D_t} [%]	mΦ [%]	k_{gas} [mD]	Bitumen impregnation
Au: Medium-to-coarse-grained bioclastic grainstones.	15.69	10.46	23.9	7.3	83.13 (V) 160.09 (H)	Abundant in both matrix and macrofractures near to faults
B: Medium-grained grainstones.	24.6	19.4	32.1	7.5	444.82 (V) 530.94 (H)	Abundant in both matrix and macrofractures near to faults
C: Fine-grained bioclastic grainstones to packstones	10.8	6.5	10.2	3.7	~0.30 (V) ~2.51 (H)	Absent in matrix and oil stain in macrofractures.
E: Planktonic foraminifera marly wackestones to mudstones.	1.4	0.0	29.9	28.5	~0.085 (V) ~0.081 (H)	Absent in both matrix and macrofractures.

Notes: Lithofacies descriptions and average matrix porosity with different methods from Rustichelli et al. (2013); two-dimensional (2D) total Φ_{2D_t}, 2D interparticle porosity Φ_{2D_i}, total thre-dimensional porosity Φ_{3D_t}, and microporosity mΦ. Gas permeability k_{gas} performed in both horizontal (H) and vertical (V), directions from Volatili et al. (2019). Bitumen distribution is obtained from field observations (Agosta et al., 2010; Rustichelli et al., 2013).

3.3. Methods

3.3.1. Sample preparation

A sample from each lithofacies outcropping in the Roman Valley quarry was analyzed including the pervious lithofacies (Au, and B) and impervious lithofacies (C, and E). The pervious lithofacies are characterized by high porosity values between 20-35% and permeability in the hundreds of mD (Table 3.1). The impervious lithofacies (permeability < 3 mD) are characterized by a wider range of total porosity 10-30% (Table 3.1). For SR micro-CT experiments, the samples were cut into cylinders of nearly 3.0 mm in diameter to guarantee an optimal penetration of X-rays compatibly with the energy range available at the beamline.

3.3.2. Synchrotron radiation computed microtomography (SR micro-CT)

SR micro-CT data were acquired at the SYRMEP beamline of the Elettra synchrotron facility (Basovizza, Trieste, Italy). At the SYRMEP beamline, a bending magnet source located at about 24 m from the sample stage permits the delivery of a nearly parallel X-ray beam characterized by high spatial coherence (Tromba et al., 2010). These characteristics allow the exploitation of propagation-based phase-contrast effects enhancing the visibility of interfaces related to abrupt phase changes in the investigated samples (Cloetens et al., 1997). In comparison to absorption mode, phase images look sharper, and objects smaller than the pixel size of the detector or with similar linear attenuation coefficients could be detected and analyzed.

In this study, phase-contrast 3D imaging was used to characterize the matrix pore morphology with high accuracy and contrast to noise ratio through a quantitative analysis of morphological and petrophysical properties of the matrix pore space (Baker et al., 2012). Tomographic scans were acquired using a filtered white beam (filters: 1.5 mm Si + 1.0 mm Al) corresponding to a mean X-ray energy of ca. 27 keV. The detector consisted of a 16-bit, water-cooled, sCMOS macroscope camera (Hamamatsu C11440-22C) with a 2048 ×2048 pixels chip coupled, through a high numerical aperture optics, to a 17 μm -thick LSO: Tb scintillator screen.

For each sample, 1800 projections were acquired over a total scan angle of 180° with an exposure time per projection of 2.5 seconds. The sample-to-detector distance was set at 150 mm (for the lithofacies Au, C, and E)

and 200 mm (for the lithofacies B). The effective pixel size of the detector was set to 1.4 μm for the lithofacies Au, C, and E, whereas for the lithofacies B, it was set to 1.8 μm. The minor differences in the setup for the sample B were intended to cover a wider volume of the sample. 3D image processing and analysis were performed following the methodology described by Arzilli et al. (2016) and Zambrano et al. (2017). The SYRMEP set-up has previously been successfully used to obtain 3D images of carbonate and siliciclastic rocks allowing the extraction of valuable information about pore morphology, connectivity, and permeability at the pore scale (Blunt et al., 2013; Cilona et al., 2014; Arzilli et al., 2016; Riegel et al., 2019). The tomographic slice reconstruction was performed using the SYRMEP Tomo Project software developed at Elettra (Brun et al., 2015) and powered by the ASTRA toolbox (Palenstijn et al., 2011) and TomoPy (Gürsoy et al., 2014). Ring artifacts, circular noise typically appearing in tomographic images due to local failures of the detectors, were removed with the most appropriate algorithms (Rivers, 1998; Münch et al., 2009) available in the same software. Prior to tomographic reconstruction, a single-distance phase-retrieval algorithm (Paganin et al., 2002) was applied to the projection images to increase the reliability of quantitative morphological analysis reducing 'phase artifacts' and enhancing the contrast between pores and rock components (framework grains, cement, matrix). The γ parameter (ratio between the real and imaginary parts of the refractive index of the material) was optimized following the approach reported by Arzilli et al. (2015).

The post-processing procedure, including filtering and segmentation, and the quantitative analysis were performed using the *Pore3D* software library, custom-developed at Elettra (Brun et al., 2010). To smooth the reconstructed images while preserving the edges of the features of interest, a 3D bilateral filter (Tomasi and Manduchi, 1998; Voltolini et al., 2011) was applied to the reconstructed volume. For extracting the pores, the 3D images were segmented using the automatic multiphase k-means clustering algorithm (Hartigan, 1975; Hartigan and Wong, 1979), setting 3 to 4 classes of objects, depending on the sample microstructure, density, and mineral content. The extraction of the connected pore network was achieved using a self-developed script powered by the tool 'Find Connected Structures' of the Fiji software (Schindelin et al., 2012). For the analysis, cubic volumes of interests (VOIs) with a side of 1000 pixels were extracted from the central part of the samples to avoid the wedge effects. The criterium for this selection was based on a representative elementary volume analysis for the total

porosity, using as criteria of stabilizations of the property values (Fig. 3.2) when the coefficient of variation falls below a given threshold (Zhang et al., 2000; Zambrano et al., 2017). According to this approach the volumes can be considered representative of the sample microstructure after reaching 720-pixel size volume for the most heterogenous of the samples (lithofacies Au).

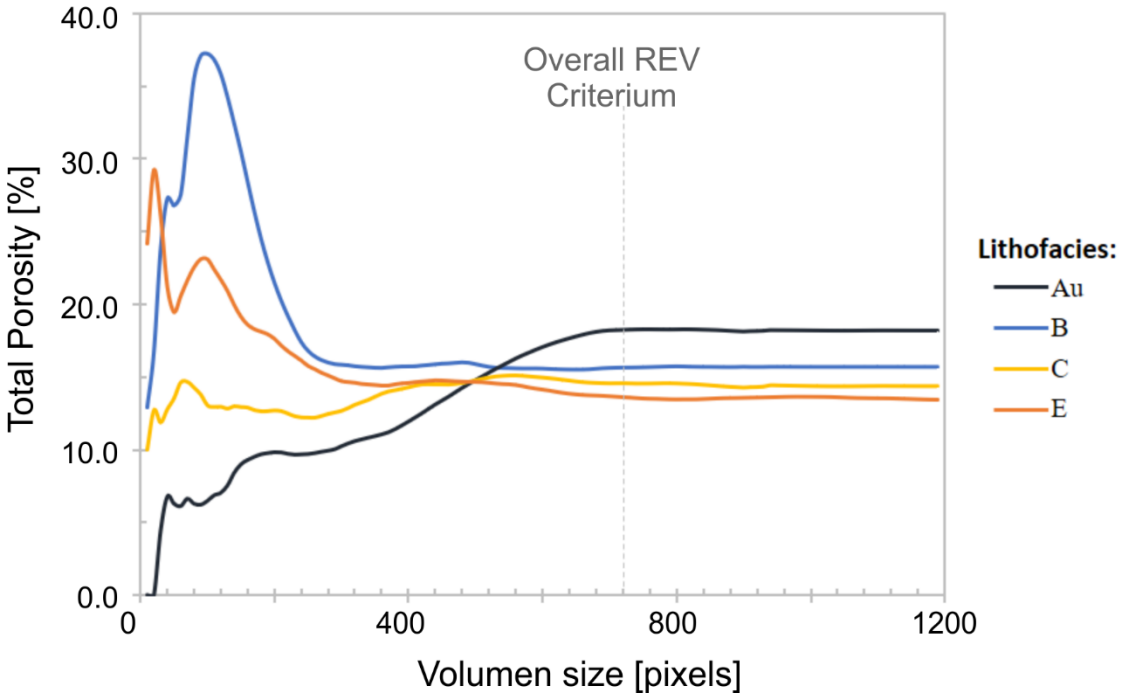

Fig. 3.2: Visual representation of the representative elementary volume (REV) determination using the total porosity calculation in volumes of interest (VOIs) with different dimensions.

3.3.3. Structure from Motion (SfM) imaging and dual-porosity modeling

Since macrofractures are more elusive to X-ray micro-CT (Ramandi et al., 2016), their modeling at the microscale represents an alternative approach (Zambrano et al., 2019b). Fracture surface topography can be accurately obtained by using either laser scanning or SfM photogrammetry (Candela et al., 2009, 2012; Renard et al., 2013; Corradetti et al., 2017, 2020). The analysis of the asperity height and wavelength distribution provide useful parameters that permit the realistic modeling of macrofracture surfaces (Brown, 1995; Isakov et al., 2001; Ogilvie et al., 2003, 2006; Zambrano et al., 2019b).

For the studied area, the workflow of fracture surface scanning and analysis has been documented by Zambrano et al. (2019b). In short, the methodology reported by these authors consists of five steps: 1) Collecting

macrofracture surface samples showing minimal signs of physical and chemical weathering; 2) Performing close-range SfM dense photo-scanning to completely envelope the sample; 3) Photo alignment and digital point cloud model construction using the Agisoft Metashape Pro (formerly Photoscan) software (www.agisoft.com); 4) Filtering, interpolating and regular-grid surface sampling; 5) Analysis of the asperity heights and wavelength distribution by means of statistical and Fourier analysis (Fig. 3.3a).

In this work, a series of pore-scale models were created including matrix porosity volumes (entirely based on SR micro-CT images) and DP/P volumes (matrix + macrofracture). To generate the DP/P models, the rough macrofractures segments were modeled using the software SYNFRAC (Isakov et al., 2001; Ogilvie et al., 2003, 2006; Zambrano et al., 2019b) following the procedure described by Ogilvie et al. (2006). In this software, open fractures can be modeled (Fig. 3.3b) by using different algorithms and parameters such as roughness controlled by both the fractal dimension (D) and asperity height (h) distribution (described by its standard deviation), and mismatch parameters (i.e., mismatch length, transition length, maximum/minimum matching fraction) defined by the power spectrum density ratio (Ogilvie et al., 2006). The power spectrum density ratio (PSDr) is derived from the relationship between the PSD of the aperture and both opposite fracture wall surfaces, as follow:

$$PSDr = \frac{PSD_{aperture}}{\left(PSD_{upper\_wall} + PSD_{lower\_wall}\right)}$$

The results of this calculation can be used to obtain the parameters associated with the mismatch between the surfaces at different wavelengths (Ogilvie et al., 2006). Ogilvie and coworkers defined these parameters as follows: 1) the *Minimum mismatch fraction* (minMF) determines the required correlation between the fracture surfaces at small scale. The value corresponds to the wavelength of the Fourier components below which the fractures start to match (*Minimum mismatch length*), thus the wavelength where the PSD ratio fall below its maximum value. 2) The *Maximum mismatch fraction* (maxMF) determines the required correlation between the fracture surfaces at large scale. It is defined as the wavelength of the Fourier components above which the opposite fracture surfaces reach the maximum matching (*Maximum mismatch length*), thus the minimum value of PSD ratio. 3) The *Mismatching length* (ML), defined as the wavelength value equidistant between the minimum and maximum

mismatch length. 4) *Transition length* (TL) is the difference in wavelength between the minimum and maximum mismatch length.

In this work, we have modeled macrofractures segments with mismatching fracture surfaces caused by submillimeter sliding/tearing displacement (Zambrano et al., 2019b). To model macrofractures with these characteristics both mismatch length and transition length were fixed to approximately 50 µm. In addition, the *maximum matching fraction* and the *minimum matching fraction* were set to the maximum (1) and minimum (0) correlations values, respectively, in order to simulate fracture surfaces that correlate at low and high wavelength domains. The main reason for fixing these parameters is to reduce the mismatch influence into the porosity and permeability. However, for complementary information the reader is directed to the sensitivity analysis provided in Appendix A and the previous investigation fully covering this issue performed by Zambrano et al. (2019b).

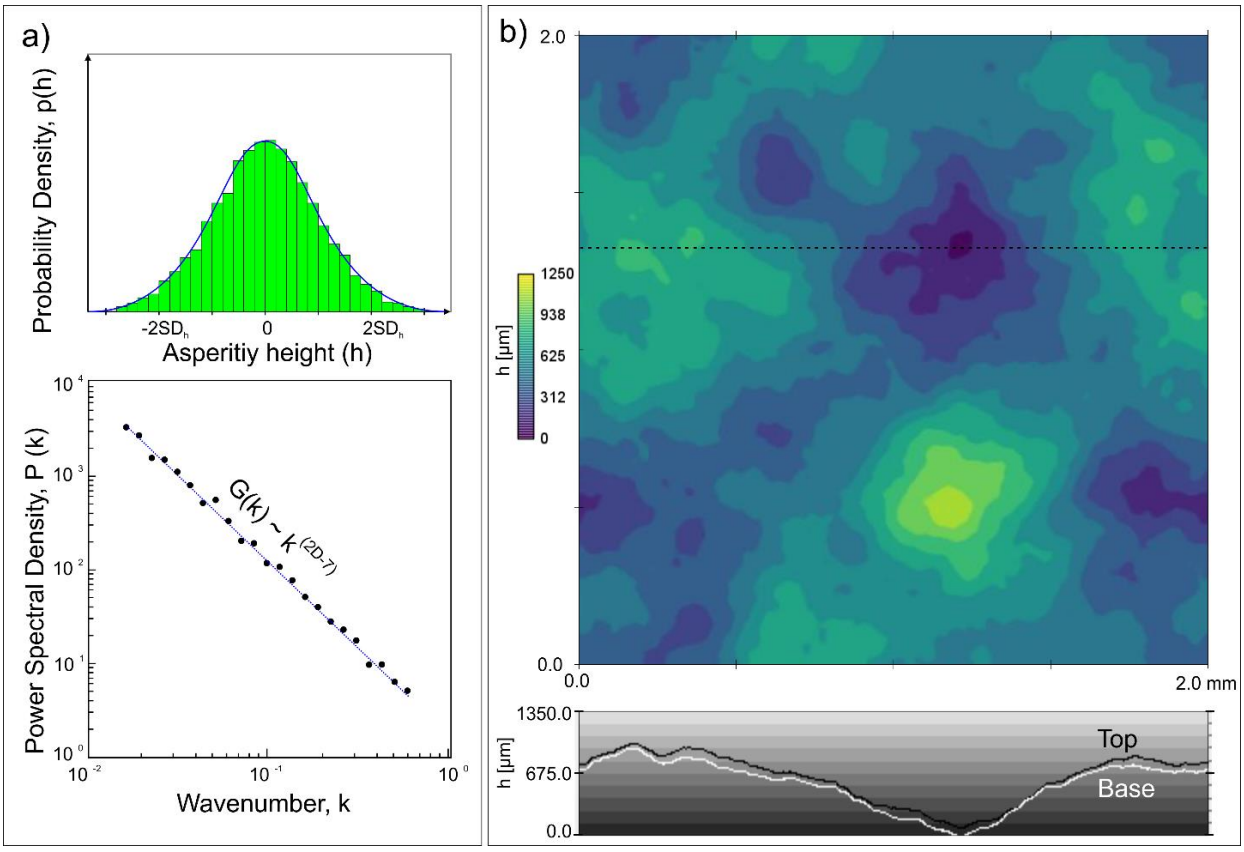

Fig. 3.3: Fracture analysis and synthetic fracture generation. a) Functions defining the fracture surface topography. Probability density of the fracture asperity height and the Fourier power spectrum modified after

(Brown, 1995). b) Fracture surface generated in SYNFRAC using the standard deviation of asperity height (SDh) and the fractal dimension (D).

After this setting, macrofractures segments were modeled by varying the fracture roughness parameters (Fig. 3.3): fractal dimension (D) and standard deviation of asperity height (SD_h). Zambrano et al. (2019b) reported values between 0.8 mm and 2.9 mm for the SD_h, and values of D between 1.6 and 2.0. In this work, we have recalculated the values of SD_h since the scale is different respect to Zambrano et al. (2019b). At the scale of pores, the SD_h varies between 50 μm and 240 μm. Conversely, the fractal dimension (not affected by the scale) remained constant. To increase the significance of our analysis, a sensitivity analysis was performed considering a reasonable data-based range of variability for both parameters (i.e., D, SD_h). After this, the modeled macrofractures segments were integrated to the pore-network extracted from the SR micro-CT images to create a dual porosity model at pore scale.

3.3.4. Quantitative image analysis

The analysis of the textural properties of the pore network was performed using a combination of tools available in the *Pore3D* software. The *Basic textural analysis* module (Zandomeneghi et al., 2010) was applied to extract three parameters: 1) Connected porosity [%]: the volume of connected pores divided by the total volume, 2) Isolated porosity [%]: the volume of isolated pores divided by the total volume (spurious isolated small pores likely associated to random noise with volume lower than 8 μm^3 were excluded), and 3) Specific surface area [mm^{-1}]: the surface area of pores divided by their total volume.

Then, connectivity indicators were derived from the skeletonized pore network of both pristine rock and DP/P models. The skeletonization is a thinning procedure where a 3D digital object is simplified to a 1D version (composed of branches and nodes) preserving its topology (Lindquist and Venkatarangan, 1999). The skeletonization of the connected pore network was performed by applying the Gradient Vector Flow (GVF) algorithm (Brun and Dreossi, 2010) within *Pore3D*. The extracted connectivity indicators were: 1) Connectivity Density [mm^3]: a scalar value derived from the skeleton of the connected pore network representing the number

of redundant connections normalized to the total rock volume. 2) Coordination number [unitless]: The average number of branches that spread out from each node.

3.3.5. Computational Fluid Dynamics (CFD) simulations

To estimate permeability from the matrix and dual-porosity system, we performed CFD experiments using the open-source software PALABOS (Latt et al., 2020) based on the lattice-Boltzmann method (LBM) following the methodology addressed by Zambrano et al. (2018). This methodology (Degruyter et al., 2010; Zambrano et al., 2018, 2019b) consists of imposing a single-phase fluid flow through the pore-network model by maintaining a fixed pressure gradient between the inlet and outlet faces of the volume while keeping the rest of the faces padded. The connected pore surface was converted to bounce-back boundary conditions. For the simulation, a Multiple Relaxation Times (MRT) approach was used (d'Humieres, 2002) with a D3Q19 lattice that generates viscosity-independent results of permeability. Once steady-state flow conditions were reached, the permeability of the volume was calculated using Darcy's law.

3.4. Results

3.4.1. Matrix pore-network petrophysical properties

The rock matrix petrophysical properties (fracture free pore network) were derived from SR micro-CT images. The raw results of the tomographic experiments consist of as-reconstructed gray-scale virtual sections of the studied samples (Fig. 3.4, 3.5). Different rock elements (grains made of calcite or siliceous minerals), and pores are observed and can be labelled by different gray levels. In the images, whitish areas correspond to calcite grains and/or cement, small bright white areas are rarely present in the images and may represent impurities (likely silica or oxides) in the carbonate rock. Areas with dark gray to black colors are associated to pore space, whereas intermediate gray is likely to be pores below the resolution of the images. Pore space can be filled with bitumen or gaseous phases (i.e., air, gas), however the differentiation is quite difficult due to the similar response to X-rays.

The microtomographic raw images show significant differences of textures between the pervious and the impervious lithofacies. The extraction of quantitative parameters from SR micro-CT images permits an objective evaluation of the matrix pore network (Table 3.2), including different properties (i.e., porosity, specific surface area, connectivity) which are useful to better understand the differences among the evaluated rocks.

In the cases of the recognized pervious lithofacies (i.e., Au and B) due to their high permeability (Table 3.1), interparticle pores are quite dominant (Fig. 3.4a, b). In lithofacies Au, the dominant diameter of these pores varies between 60 to 200 μm. In lithofacies B, the dominant pores size is in the range of 50 to 150 μm. The higher pore diameters of sample Au with respect to sample B is represented by lower values of the specific surface area for the sample Au respect to the B (Table 3.2). Intraparticle pores within bioclasts are less frequent, and often connected with the interparticle ones when bioclasts are broken. These pores can show different sizes depending on the bioclast architecture. In sample Au, few stylolites at the grain contact were detected. In lithofacies B, some bright areas probably associated with oxides or silica grains were recognized (Fig. 3.4b). Peculiarly, in the lithofacies B sample (Fig. 3.4b, see the inset), two fluid phases filling the pores are distinguished corresponding to bitumen and gas of unknown composition (possibly hydrocarbon volatiles). The bitumen is impregnating the

rock occupying almost the entire pore space, whereas the gas is distinguished by the form of bubbles trapped in the viscous bitumen.

For the lithofacies classified as impervious (i.e., C and E), the pore space is mostly represented by intraparticle pores within bioclasts (Fig. 3.4c, d). The low amount or absence of interparticle voids is likely related to pervasive fine-grained material occupying this space. The lithofacies C sample contains isolated pores with a dominant diameter of 25 μm and is characterized by the presence of pervasive stylolites which are partially open and connected with the intraparticle pores. In lithofacies E, the dominant isolated pore size is near 30 μm, however light gray areas indicate the presence of pores below the resolution of the X-ray images.

The connectivity differences among the studied lithofacies can be visually evaluated considering the 3D iso-surface renderings of segmented images showing the connected and isolated pores in green and red colors, respectively (Fig. 3.5). The segmented 3D X-ray images reveal that most of the pores in pervious lithofacies B and Au are connected (Fig. 3.5a, b). The quantitative analysis (Table 3.2) indicates that pervious rocks are characterized by high values of connected porosity between 12% and 19 %, and a minor quantity of isolated pores (<1.0%). In particular, the lithofacies Au is slightly more porous than the lithofacies B. The quantitative analysis also indicates high values of the connectivity density (Table 3.2), particularly higher for the lithofacies B with respect to Au. Impervious lithofacies C and E (Fig. 3.5 c and d, respectively) are mainly composed of isolated pores with a porosity up to 16 %. In the case of lithofacies C, the detected partially open stylolites can generate clusters of connected pores of near 2% (Fig. 3.5 c). These connected pore clusters have high values of connectivity density, and they are preferentially connected in direction of the stylolite.

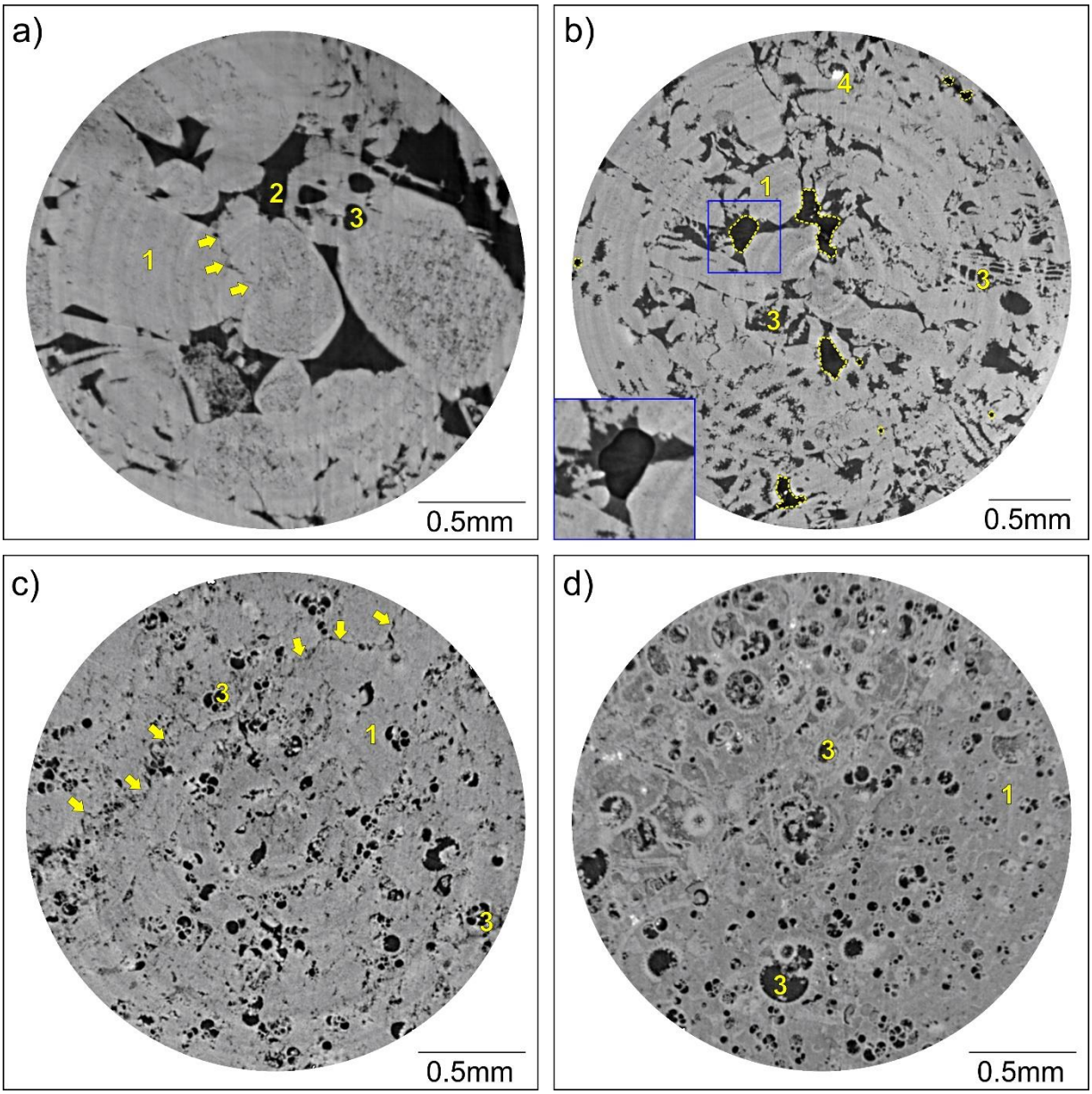

Fig. 3.4. SR micro-CT raw images (virtual sections of the studied rock samples from Roman Valley quarry): a) lithofacies Au (isotropic voxel size of 1.4 μm), b) lithofacies B (isotropic voxel size of 1.8 μm), c) lithofacies C (isotropic voxel size of 1.4 μm) and d) lithofacies E (isotropic voxel size of 1.4 μm). 1: Calcite grains/cement, 2: Interparticle pores, 3: Intraparticle pores, 4: Rare impurities likely silica or oxides. Stylolites are marked by yellow arrows. In sample of lithofacies B (b), unknown-gas bubbles trapped in the bitumen were detected (marked with yellow dotted lines and evidenced in the inset).

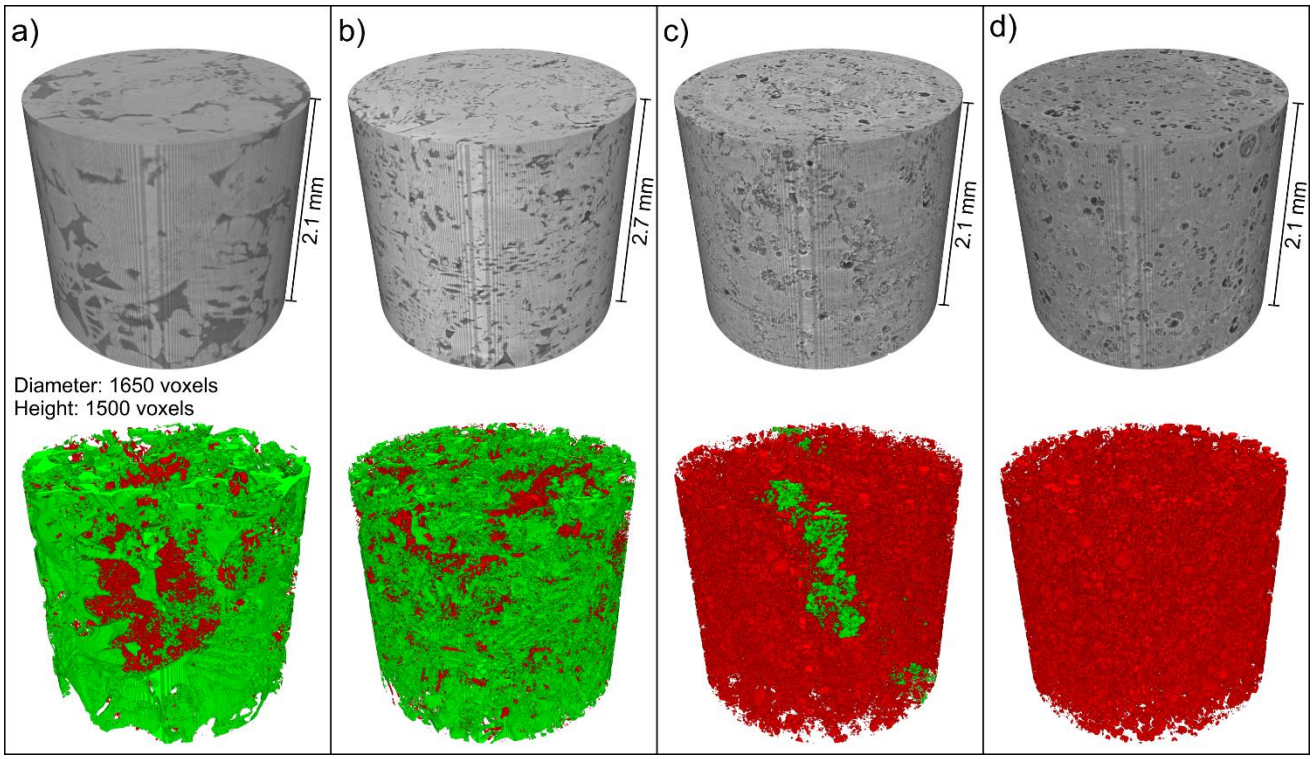

Fig. 3.5. 3D renderings obtained from SR micro-CT data for samples of Roman Valley quarry (Abruzzo, Italy) a) lithofacies Au (isotropic voxel size of 1.4 μm), b) lithofacies B (isotropic voxel size of 1.8 μm), c) lithofacies C (isotropic voxel size of 1.4 μm) and d) lithofacies E (isotropic voxel size of 1.4 μm). Cylinders have a diameter of 1650 voxels and a height of 1500 voxels. Raw data in grayscale, connected and isolated pores are evidenced in green and red, respectively.

3.4.2. Petrophysical properties of the DP/P models

In general, the hydraulic properties (porosity and permeability) of the studied rock samples are enhanced by the presence of macrofractures (Table 3.2), due to the addition of the fracture porosity. However, these elements have a dissimilar impact on the pervious (Au, B) with respect the impervious (C, E) lithofacies. To evaluate effects associated to the macrofractures on the different lithofacies, we have introduced the 'neo-connected porosity' (pores that were originally isolated and now connected by the intersecting fracture). In terms of the storage capacity, the effect of fractures in pervious lithofacies is quite negligible due to neo-connected porosity values lower than 0.032%. This limited influence of fractures in linking up nearby isolated pores is likely associated to the fact that the pore-network in these lithofacies is already well-connected (Fig. 3.6). The increments of neo-connected porosity by fractures are up to 1.7 % and 4.1 % for the lithofacies C and E, respectively. This significant increase of neo-connected porosity is due to the higher involvement of adjacent small cluster of pores (lithofacies C, Fig. 3.7a, b) or isolated pores (lithofacies E, Fig. 3.7c, d) to the main percolative pore space. The ability of fractures to increase the neo-connected porosity will varies on the physical and fractal dimension of the fractures, where fractures with higher amplitude or frequency of the asperities will involve more isolated pores. In the DP/P models, rough fractures (SD_h=250 μm, D=2.0) could collect 2-5 times more isolated pores than smooth fractures (SD_h=30 μm, D=1.6).

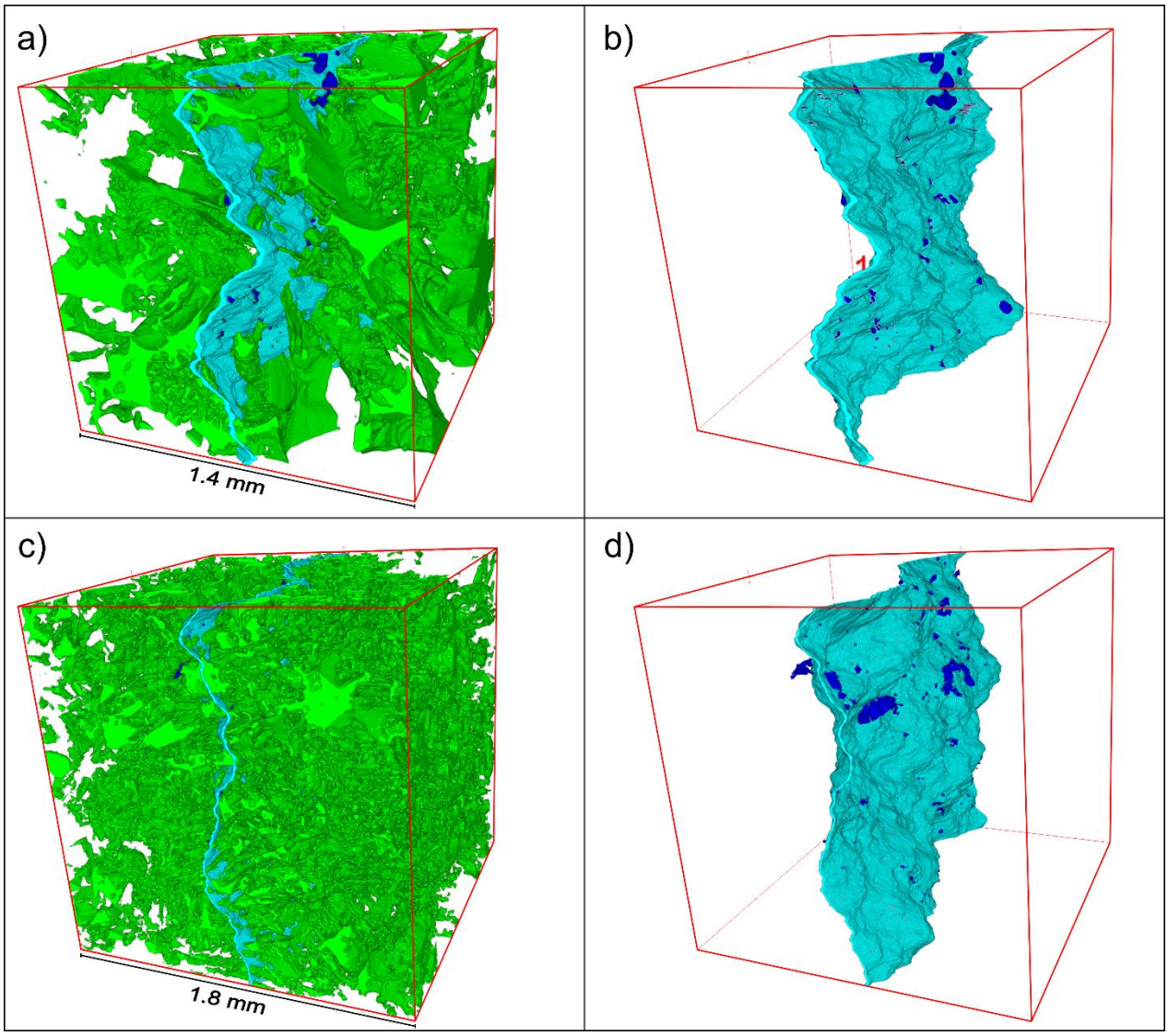

Fig. 3.6: 3D renderings of DP/P models at the microscale for the pervious lithofacies: a) DP/P for the lithofacies Au with a macrofracture segment and b) a detail of the 'neo-connected' porosity, c) DP/P for the lithofacies B with a macrofracture segment and d) a detail of the new connected porosity. The primary connected pore space is in green, fracture is in cyan and pores that were originally isolated and now connected ('neo-connected pores') by the intersecting fracture are in blue. Volumes corresponds to cubes of 1000 voxels per side. The voxel size for lithofacies Au and B is 1.4 µm and 1.8 µm, respectively.

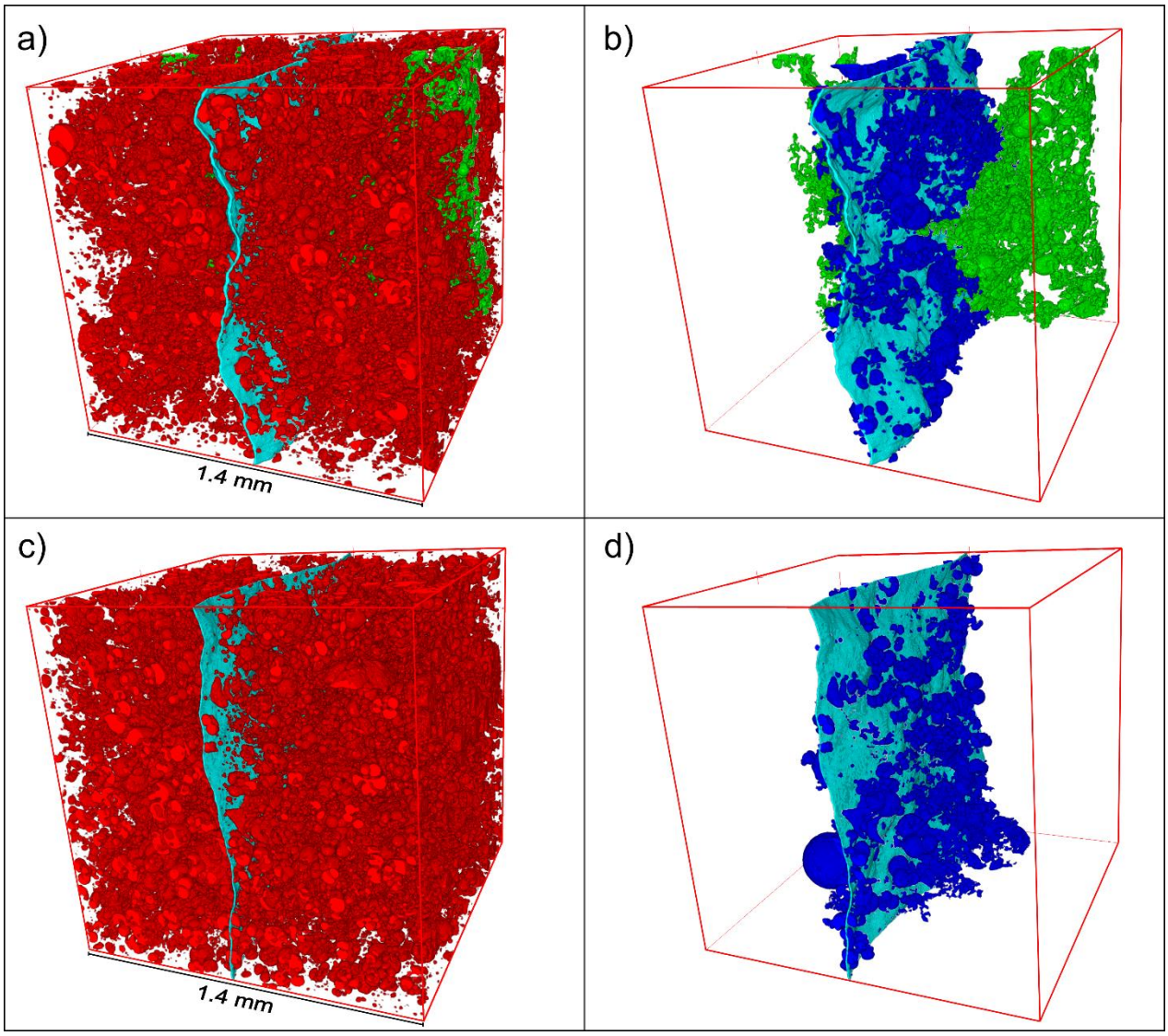

Fig. 3.7: 3D renderings of DP/P models at the microscale for the impervious lithofacies: a) DP/P for the lithofacies C with a macrofracture segment and b) a detail of the 'neo-connected' porosity, c) DP/P for the lithofacies E with a macrofracture segment and d) a detail of the 'neo-connected' porosity. The primary isolated pores are shown in red. The primary connected pore space is in green (likely partially open stylolites in lithofacies C), fracture is in cyan and pores that were originally isolated and now connected ('neo-connected pores') by the intersecting fracture are in blue. Volumes corresponds to cubes of 1000 voxels per side with voxel size of 1.4 µm.

In the DP/P models, the skeletonized pore networks (Fig. 3.8) and the lattice-Boltzmann velocity volumes (Fig. 3.9) indicate the presence of the fractures characterized by a dense subnetwork composed of narrow pores and pore throats. In the case of lithofacies Au, the difference of diameter between the primary pores and the fractures is significant (Fig. 3.8a, b). This is translated to a marginal contribution of the modelled macrofracture segment to the fluid transport (Fig. 3.9 b). For the lithofacies B, the pathways diameters and the velocity magnitude are similar (Fig. 3.8c, d, 3.9b). In fact, it is quite difficult to observe any difference in skeletonized volume. For the pervious lithofacies, the connectivity indicators (i.e., connectivity density and coordination number) tend to slightly decrease respect to the pristine rock. In the case of impervious lithofacies the macrofracture segment is the main connected pore space, therefore the skeletonized pore network (Fig. 3.8e, f) and the lattice Boltzmann velocity (Fig. 3.9e, f) basically mimic the shape of the modelled macrofracture. For the impervious lithofacies, the neo-connected pores, including locally connected pore clusters (partially open stylolites, Fig. 3.9f), provides a negligible contribution to fluid transport with lattice-Boltzmann velocity values two orders of magnitude lower than the ones related to the macrofractures.

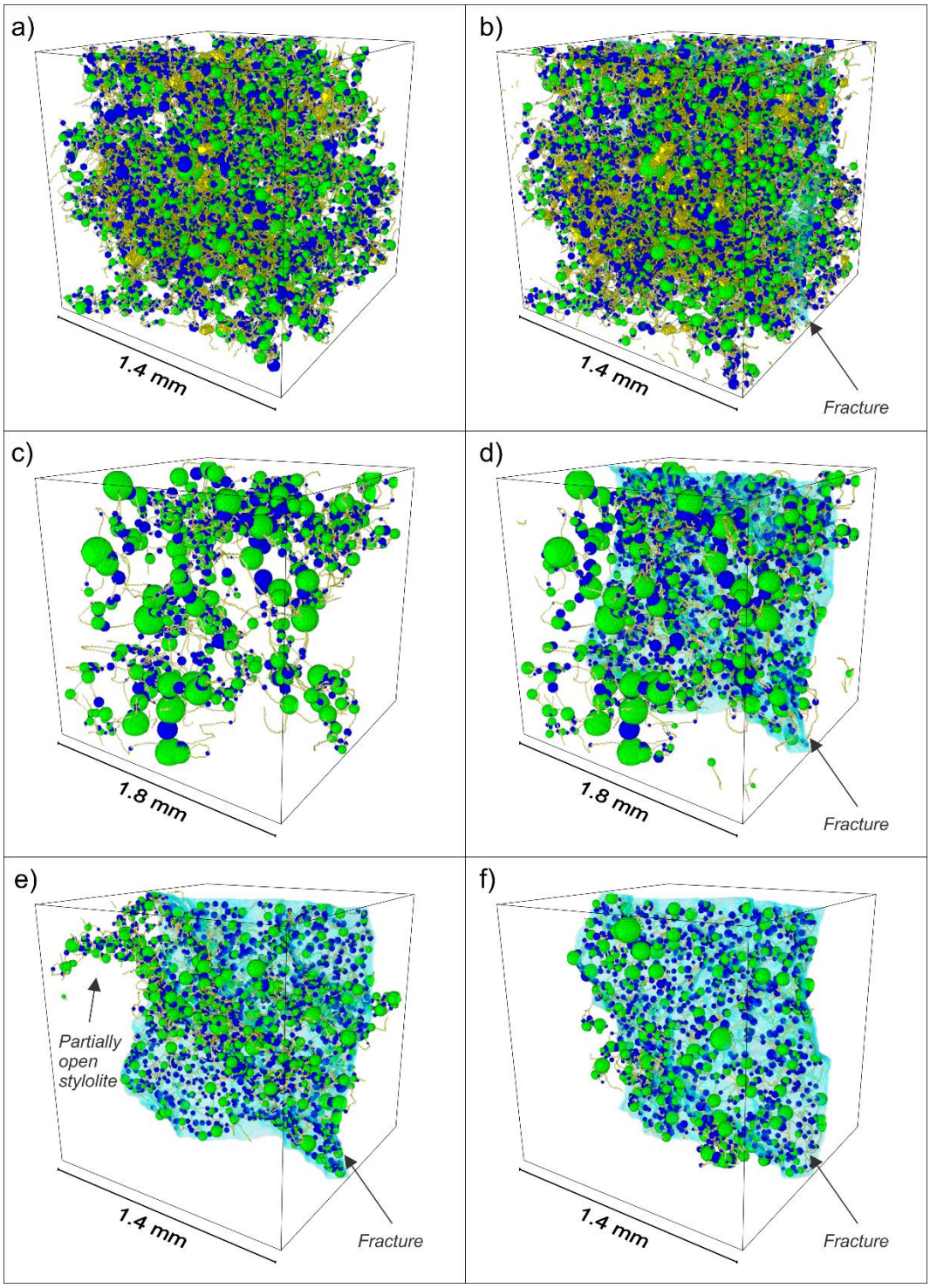

Fig. 3.8: 3D renderings of the skeletonized pore networks corresponding to a) pristine lithofacies Au, b) DP/P model of lithofacies Au, c) pristine lithofacies B, d) DP/P model of Lithofacies B, e) DP/P model of lithofacies C, f) DP/P model of lithofacies E. The volumes are cubes of 1000 voxels per side. Skeleton is composed of branches in yellow, pores in green and throats in blue. Modelled macrofracture segments are shown in transparency.

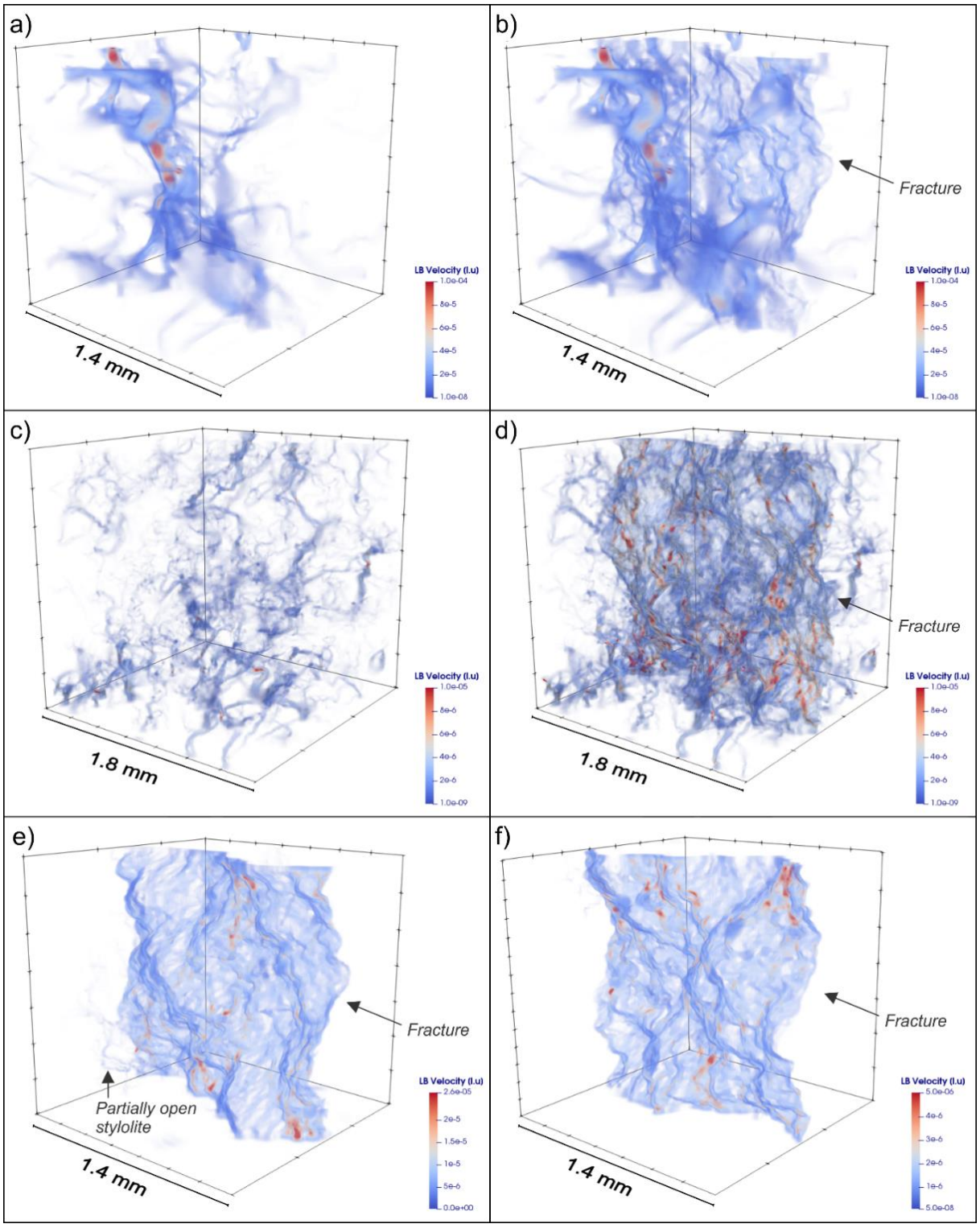

Fig. 3.9: 3D renderings of the lattice-Boltzmann (LB) velocity corresponding to a) pristine lithofacies Au, b) DP/P model of lithofacies Au, c) pristine lithofacies B, d) DP/P model of Lithofacies B, e) DP/P model of lithofacies C, f) DP/P model of lithofacies E. The volumes are cubes of 1000 voxels per side. Velocity magnitude is given in lattice units (l.u.), warmer colors.

The sensitivity analysis performed in this study is fully encompassed in the graphs shown in figure 3.10, where the relationship between porosity (i.e., connected, and neo-connected porosity) and permeability, represented in logarithmic scale, is referred to three main variables: i. lithofacies, ii. the standard deviation of asperity height (SD_h), and iii. the fractal dimension (D) of the modelled macrofracture segments. In general, the relationship between connected porosity and permeability (Fig. 3.10a) shows an increasing trend for all lithofacies according to the magnitude of roughness expressed by the fractal dimension and the lithofacies Au and B are more clustered at higher porosity and permeability. Whereas the relationship between the neo-connected porosity and permeability depicts different trends for pervious and impervious lithofacies, showing a steep increment of permeability for the lithofacies C and E accordingly to the increasing of the fractal dimension of the fracture segment. The increment of permeability in the DP/P models is in the order of a few hundred of millidarcies (Table 3.3). However, these values are limited to the modeled millimetric volumes, for any consideration at larger scale these values need to be upscaled.

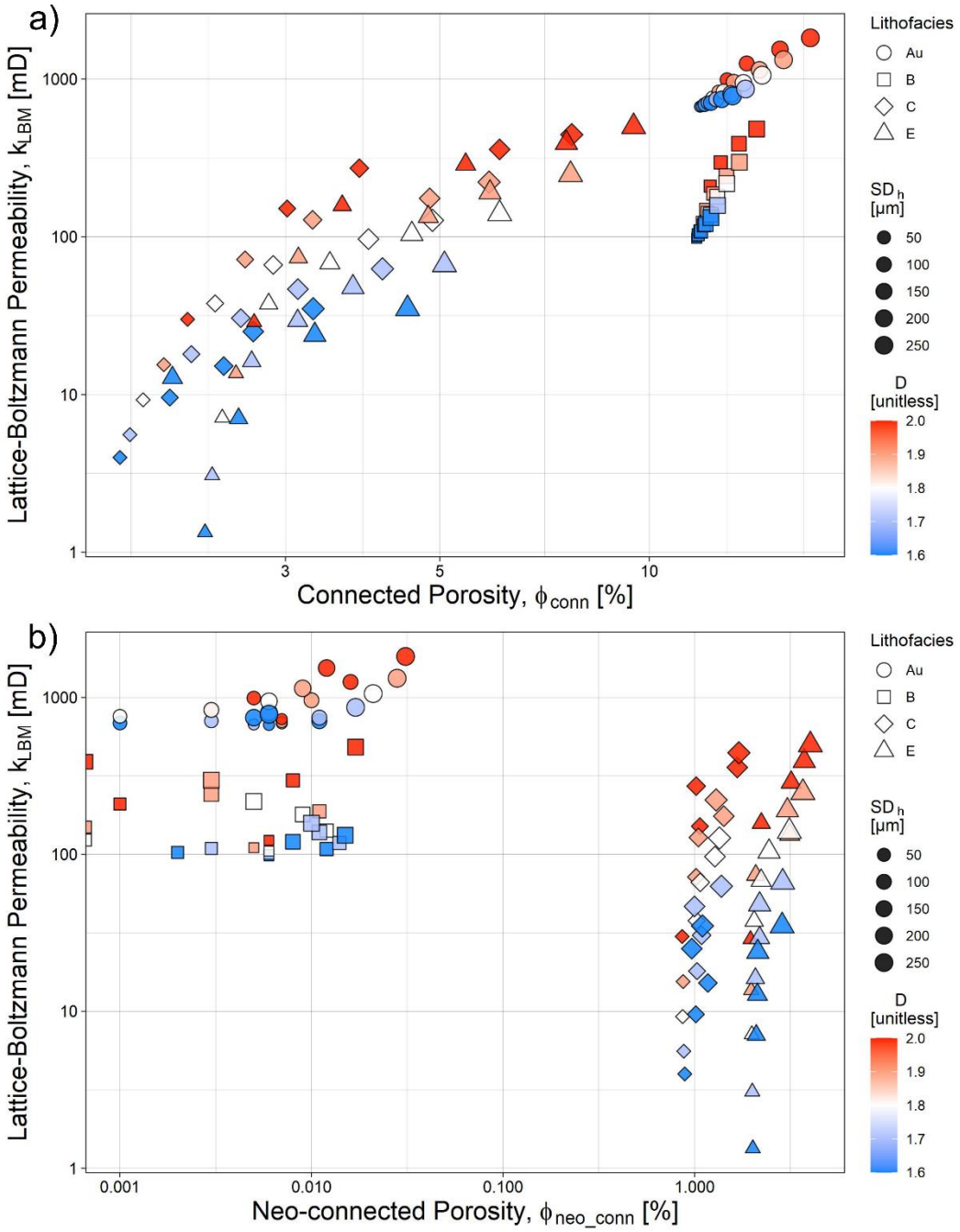

Fig. 3.10: Permeability vs porosity scatter plots of the DP/P models for the different studied lithofacies. a) Permeability vs connected porosity, b) Permeability vs neo-connected porosity. The size of the symbols is referred to the standard deviation of asperity height (SDh) in microns, whereas the color bar represents the fractal dimension (D)of the modelled macrofracture segment.

*Table 3.**2**. Summary of the quantitative analysis of the pore network.*

Lithofacies	Connected pore space		Isolated pore space				
	Φ_c	SSA_c	Φ_i	SSA_i	CD		k_{LBM}
	[%]	[mm^{-1}]:	[%]	[mm^{-1}]:	[mm^{-3}]:	CN	[mD]:
Au-Pristine rock	15.9 ± 2.8	10.3 ± 0.20	0.85 ± 0.1	2.92 ± 0.42	512.5 ± 48.9	4.0 ± 0.12	667.5 ± 48.9
Au-Fractured rock	17.6 ± 1.3	11.3 ± 0.02	-	-	497.4 ± 14.8	3.8 ± 0.01	918.8 ± 296.5
B-Pristine rock	13.3 ± 0.5	20.2 ± 0.50	0.92 ± 0.1	2.95 ± 0.19	1664.4± 69.4	4.1 ± 0.02	95.3 ± 10.2
B-Fractured rock	14.1 ± 0.7	11.0± 0.05	-	-	1618.5 ± 1.7	4.1 ± 0.01	177.6 ± 97.8
C-Pristine rock*	2.0 ± 1.2	4.4 ± 0.02	9.65 ± 0.1	23.4 ± 0.35	-	-	-
C-Fractured rock	4.7 ± 1.5	8.0 ± 0.02	-	-	765.6 ± 15.4	4.1 ± 0.02	98.3 ± 116.3
E-Pristine rock	-	-	15.7 ± 1.7	31.86 ± 2.87	-	-	-
E-Fractured rock	4.2 ± 1.9	3.8 ± 0.1	-	-	558.3± 34.4	4.2± 0.02	105.1 ± 129.8

*Notes: Connected porosity Φ_c, specific surface areas for connected pores SSA_c. Isolated Porosity Φ_i, specific surface areas for isolated pores SSA_i. Connectivity indicators: connectivity density CD and coordination number CN. Permeability obtained using the lattice-Boltzmann simulation k_{LBM}. *In the analyzed volume of the lithofacies C, a partially open stylolite is included, otherwise the connected porosity is negligible.*

3.5. Discussion

3.5.1. Hydrocarbon distribution according to pore-scale observations

The connected porosity and connectivity results are consistent with the high permeability values obtained with lattice-Boltzmann simulations, and the laboratory measurements by Volatili et al. (2019). In addition, the overall results agree with the field-based observations where the bitumen impregnation is only present in the most pervious lithofacies, Au and B, and along the fault zones the faulted areas characterized by an increment in fracture intensity (Agosta et al., 2009, 2010; Rustichelli et al., 2012, 2013; Panza et al., 2018; Volatili et al., 2019; Romano et al., 2020). Both pervious lithofacies present a high value of connected porosity, between 13% and 22%. These results agree with previous SR X-ray micro-CT (voxel size = 9.0 μm) analyses performed on similar samples, where porosity values vary in the range of 13% - 25 % (Cilona et al., 2014; Arzilli et al., 2016). In agreement with the observations of Arzilli et al. (2016), the pore space in lithofacies Au and B is highly connected (Fig. 3.5a, b) showing connectivity density values ranging from 500 mm^{-3} to 1700 mm^{-3}. The combination of high porosity and connectivity can explain the presence of bitumen up to 17% of the rock volume reported by Lipparini et al. (2020).

On the other hand, lithofacies C and E provide adverse storage and migration capabilities due to the isolated character of the dominant intraparticle pores (Fig. 3.5c, d). The relatively high porosity (>10%) consist of isolated small pores (high values of specific surface area) that limit the percolation of fluids. In agreement with our results, Rustichelli et al. (2013) documented that lithofacies E is characterized by mainly microporosity content (about 29%). Furthermore, lithofacies C is dissected by bed-parallel stylolites, as largely documented by previous authors (Rustichelli et al., 2013). The connected cluster of pores associated with partially open stylolites may explain the permeability anisotropy reported by Volatili et al. (2019) for this lithofacies (Table 3.1). According to these authors, in lithofacies C, the bed-parallel permeability component is about ten times higher than the vertical component. Since the matrix connected porosity is negligible, a reasonable explanation is that pore clusters associated with stylolites may contribute to this anisotropy. In low porosity carbonates, the increment of porosity associated with stylolites is a common finding (Rustichelli et al., 2015; Baud et al., 2016). Moreover, the possibility of positive contribution of stylolites to fluid migration have been demonstrated by previous studies (Heap et al.,

2014; Koehn et al., 2016; Bruna et al., 2019). In our case study, the actual contribution of these features to the hydrocarbon transport and storage are likely to be limited as was shown in the lattice-Boltzmann velocity volumes (Fig. 3.9e). These results agree with field observation where no heavy oil traces have been reported in these stylolites. However, further discussion about sealing integrity should consider other elements not discussed in this work like capillary entry pressure and interaction between the fluid phases (e.g., brines or gas) in the rock.

Porosity values of the pristine rock obtained from the SR micro-CT images (Table 3.2) are between 2-3 times lower than laboratory analysis reported by previous authors (Rustichelli et al., 2012, 2013; Trippetta and Geremia, 2019; Volatili et al., 2019; Ruggieri and Trippetta, 2020; Trippetta et al., 2020). This difference of porosity can be explained by heterogeneities of the evaluated rock formation, and more likely by the presence of undetected pores with size below the achievable spatial resolution in the analyzed volume. If we consider the minimum pore size included in the analysis (pore diameter near 4 μm), at least one third of the pores in the lithofacies B are undetected according to the available pore-throats diameter distribution obtained with mercury injection (Cilona et al., 2014). It is estimated that for lithofacies B, about 4% of the rock volume correspond to isolated pores within bioclast or microsparry cement (Rustichelli et al., 2013; Cilona et al., 2014; Arzilli et al., 2016). This led to the safe assumption that part of this sub-resolution and bitumen-free pore space can be connected as it has been documented by previous pycnometer measurements performed by Trippetta et al. (2020). The contribution of these sub-resolution micropores for bitumen storage is linked to a difficult recovery (Gao et al., 2019).

The estimated permeability during the simulations is similar to the values of matrix permeability reported by Volatili et al. (2019), however, differences between our results and previous laboratory measurements (Rustichelli et al., 2013; Trippetta and Geremia, 2019; Volatili et al., 2019; Trippetta et al., 2020) were noted. A possible explanation could be the limited contribution of undetected sub-resolution pores to fluid flow as proposed by Arzilli et al. (2016) for these rocks, that means, undetected pores do not affect the permeability in a relevant manner since the fluid transport is controlled by pores with diameter significatively larger. Similar findings were reported for porous grainstones of alike characteristics by Zambrano et al. (2018), where pores with a diameter less than 10 μm provide a negligible contribution to permeability. This behavior seems to be typical in carbonates with a pore-

space bimodal distribution, where the most connected and larger interparticle pore space dominates the rock bulk permeability (Zhu et al., 2010; Ji et al., 2015; Wang et al., 2020).

3.5.2. Effect of macrofractures in fluid storage and migrations

The presence of highly deformed rock volumes given by fault interaction in linkage areas like in Roman Valley quarry, clearly enhance the fluid migration capability (Agosta et al., 2009, 2010; Panza et al., 2018; Volatili et al., 2019; Romano et al., 2020) explaining the exceptional hydrocarbon saturation in this area reported by Lipparini et al. (2018).

In the pervious lithofacies (Au and B), the results indicated that macrofractures may provide a relatively minor increment of neo-connected porosity (Fig. 3.11a, b) with respect to the already high matrix porosity. This is also supported by a null or insignificant increment of the connectivity parameters. Nevertheless, the permeability can increase a few hundreds of mD in DP/P models. This increment of permeability should have a lower impact after upscaling. Such impact depends on the fracture intensity and connectivity.

In the impervious lithofacies (C and E), the increment of the neo-connected porosity and permeability given by macrofractures insertion is relatively more significant due to the negligible primary matrix connected porosity and permeability values. In the case of strongly isolated pore networks, like in lithofacies E, only a few pores are connected to the modeled macrofracture segments (Fig. 3.7c, d). In lithofacies C, both isolated pores and local pore-network clusters (associated with partially open stylolites) can be embedded into the main percolative pore space supported by the inserted macrofracture segment (Fig. 3.7a, b). Regardless of the presence of these pore clusters, bitumen is not invading the matrix pore space of lithofacies C, but it is limited to few unclear traces on exposed fracture surfaces (Volatili et al., 2019). This situation was also observed at the scale of the pores in the lattice-Boltzmann simulations, where the velocity is at least two order of magnitude lower in the pore clusters in comparison with the macrofractures (Fig. 3.9).

3.5.3. Effect of fracture roughness on porosity and permeability of the DP/P models

In this section, we discuss the uncertainties of the obtained DP/P models through the application of sensitivity analysis using parameters associated with the fracture roughness parameters (i.e., D, SD_h). The fracture related porosity consists of the fracture pore space itself, which is given by the mismatch between the opposite fracture surfaces, plus the isolated pores that have been connected due to the presence of the macrofracture segment (neo-connected porosity).

In DP/P models, both porosity and permeability are directly proportional to both fracture roughness parameters. The higher roughness permits a creation of more space between fractures for similar mismatch conditions. This result is comparable to increment of porosity and aperture at higher roughness (fractal dimension) in fractures with equals sliding/tearing displacement as documented by Zambrano et al (2019). However, rougher fractures are likely to slide or tear with greater difficulty (Barton et al., 1985). Another aspect that we considered in the sensitivity analysis is the ability of the fracture segment to link up isolated pores to the main percolative pore space as a function of the fracture roughness (Fig. 3.11). The results indicate that in general the neo-connected porosity increase proportionally to the fracture roughness parameters. This is likely related to the fact that fractures with a higher roughness are characterized by a greater surface per unit of volume. This control is more evident in impervious lithofacies than in pervious ones, likely controlled by the abundancy and distribution of isolated micropores that can be linked up by macrofractures segments.

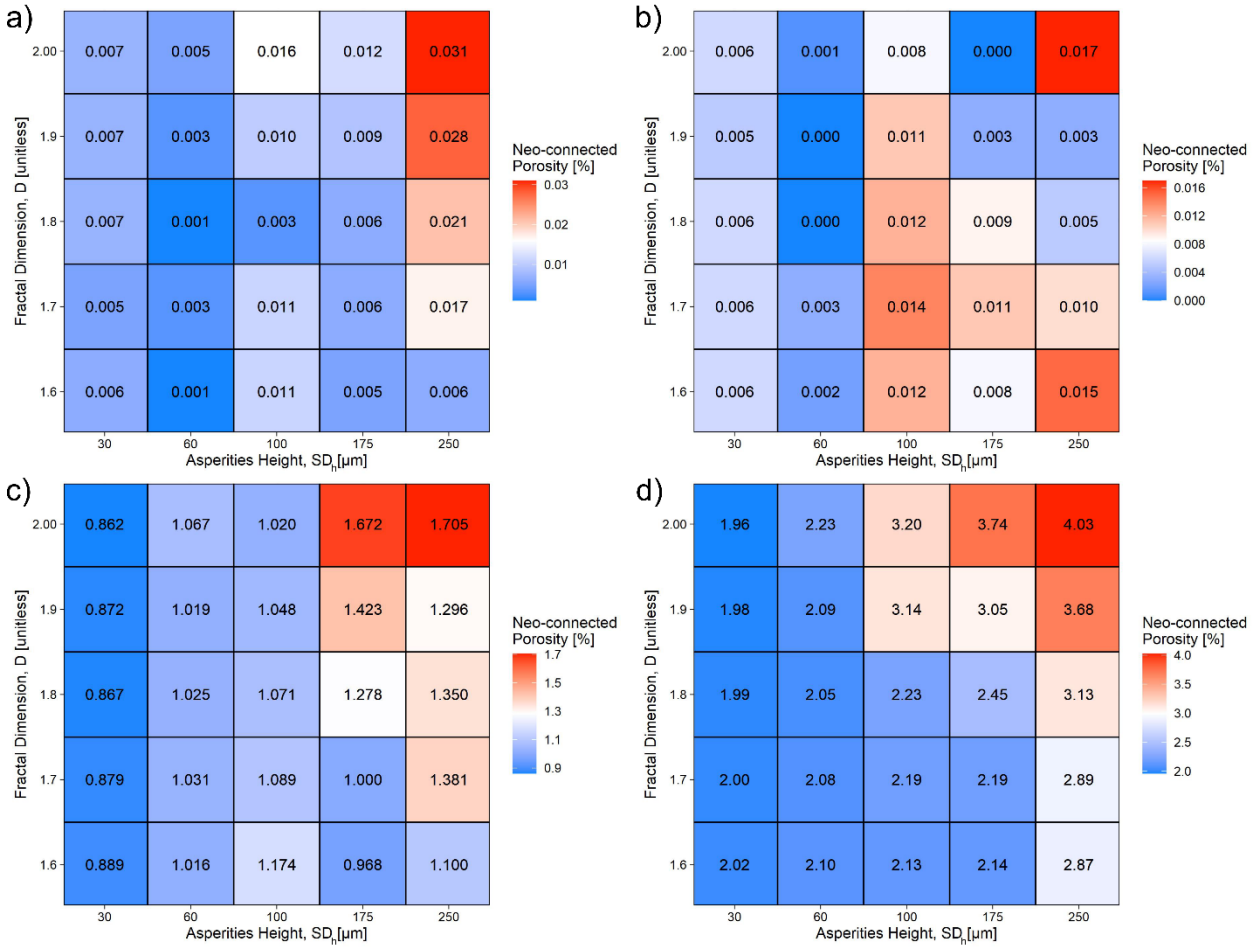

Fig. 3.11: Neo-connected porosity gained by the insertion of macrofracture segments as a function of fracture roughness parameters: fractal dimension (D) and standard deviation of asperity height (SDh) for the a) lithofacies Au, b) lithofacies B, c) lithofacies C, and d) lithofacies E.

3.5.4. Considerations for modeling and upscaling

In terms of porosity contribution of macrofractures, our results are in accordance with previous estimations (Agosta et al., 2010; Panza et al., 2018; Volatili et al., 2019; Romano et al., 2020), where the fracture porosity is lower than 1.1%. However, these studies present upscaled fracture permeability differing by several orders of magnitude given by the use of outcrop-based apertures. To avoid this issue, our methodology of simulating mismatching fractures can provide an alternative approach to the widespread use of aperture values measured at outcrop conditions that leads to overestimation of the fracture permeability.

A limitation of our modeling approach is the difficulty to access the mismatch parameters or the actual aperture at different depth conditions or stress field orientation. Therefore, our method should be integrated with geomechanics and petrophysical data in order to calibrate the results. The documented analysis and output results should be used as complementary method to other analyses and sources of data due to clear representativeness limitations. Under these considerations, the results presented here regarding the macrofracture-related increment of permeability and porosity may be used for a rapid estimation of the petrophysical properties of fractured porous rocks following similar upscaling procedures like the one proposed by (Antonellini et al., 2014), which integrate the hydraulic properties of narrow deformation features (millimetric deformation bands) with discrete fracture modeling that includes the missing variables in this work (i.e., dimensions, intensity, and orientation of macrofractures).

3.6. Conclusion

The presented workflow integrates a multifaceted approach involving high-resolution synchrotron X-ray microtomography, SfM photogrammetry, fracture modeling, and fluid flow simulation at the microscale. The results here demonstrate the utility for obtaining dual-porosity/permeability models at the pore scale, that may explain macroscopic phenomena of a reservoirs (e.g., heterogeneous hydrocarbon distribution). This microscale characterization integrates the contribution of matrix and macrofracture pore systems without the need of defining building models that depends on the definition of transmissibility parameters that govern the interaction between both systems. As an alternative to rely on fracture aperture values from outcrops, the implemented methodology also provides, through a sensitivity analysis, a range of porosity and permeability related to fracture roughness properties (i.e., the fractal dimension, D, and standard distribution of asperity height, SD_h).

Our results indicate that macrofractures have a more significant increment of neo-connected porosity in impervious lithofacies in comparison with pervious ones. This increment of the connected porosity in the DP/P models of the impervious lithofacies is related to the capability of macrofracture segments to link up adjacent isolated or partially isolated matrix pore space, whereas in the pervious lithofacies the pores are already well-connected. The permeability increment, in the order of a few hundreds of millidarcy in all the lithofacies, demonstrates a significant fracture control in the fluid transport. In the case of pervious carbonate rocks, fault-related macrofracture network can provide anisotropy, influencing bitumen distribution and migration. In the impervious lithofacies, despite the presence of connected pore clusters (i.e., lithofacies C), the bitumen is not able to invade matrix is evident from field observations.

While this study is focused on pore-scale fluid transport, this approach can be integrated with other sources of data for upscaling the hydraulic properties of dual-porosity/permeability reservoirs involving fault-related macrofracture networks and heterogeneous lithofacies.

Acknowledgments

This research was supported by the Reservoir Characterization Project (www.rechproject.com). We acknowledge Elettra Sincrotrone Trieste for providing access to its synchrotron radiation facilities and the use of the software *Pore3D*. We thank Gabriele Lanzafame (now at University of Catania, Italy), and Fabio Arzilli (now at Manchester University, UK) for assistance in using beamline SYRMEP. We acknowledge Danica Jablonska (University of Camerino) for kindly support to the final revision of the manuscript. Two anonymous reviewers and the editor Laura Tomassetti are acknowledged for useful comments that drastically improved the quality of the final manuscript.

Appendix A- Sensitivity analysis: roughness and mismatch vs fracture aperture

In this sensitivity analysis we have explored the variation of fracture aperture influenced by the parameters related to fracture roughness (standard deviation of asperity height, SD_h, and fractal dimension, D) and mismatch (transition length, mismatch length, maximum and minimum matching fraction). For the sensitivity analysis we used a simple one-factor-at-a-time approach, where one property was change keeping the rest constant. The results consist of a series of maps that permit understanding the impact of these variables on the aperture of a rough fracture.

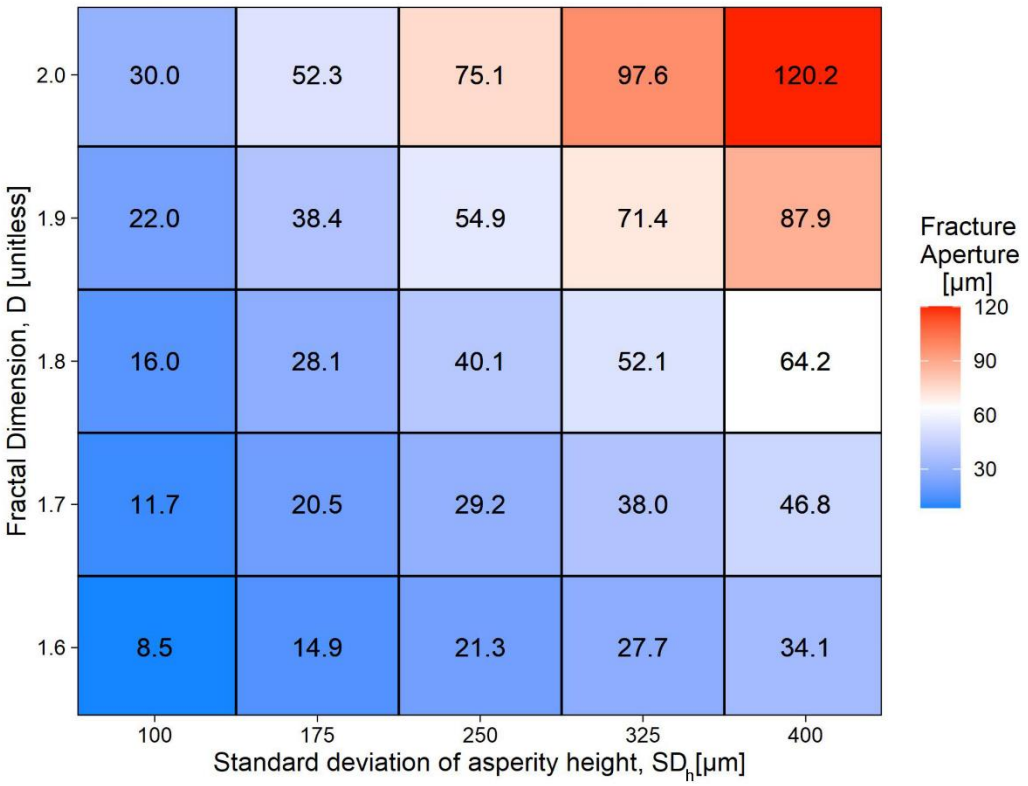

Fig. 3A-1: Sensitivity analysis of the fracture aperture due to roughness parameters: Fractal dimension (D), and standard deviation of asperity height (SDh).

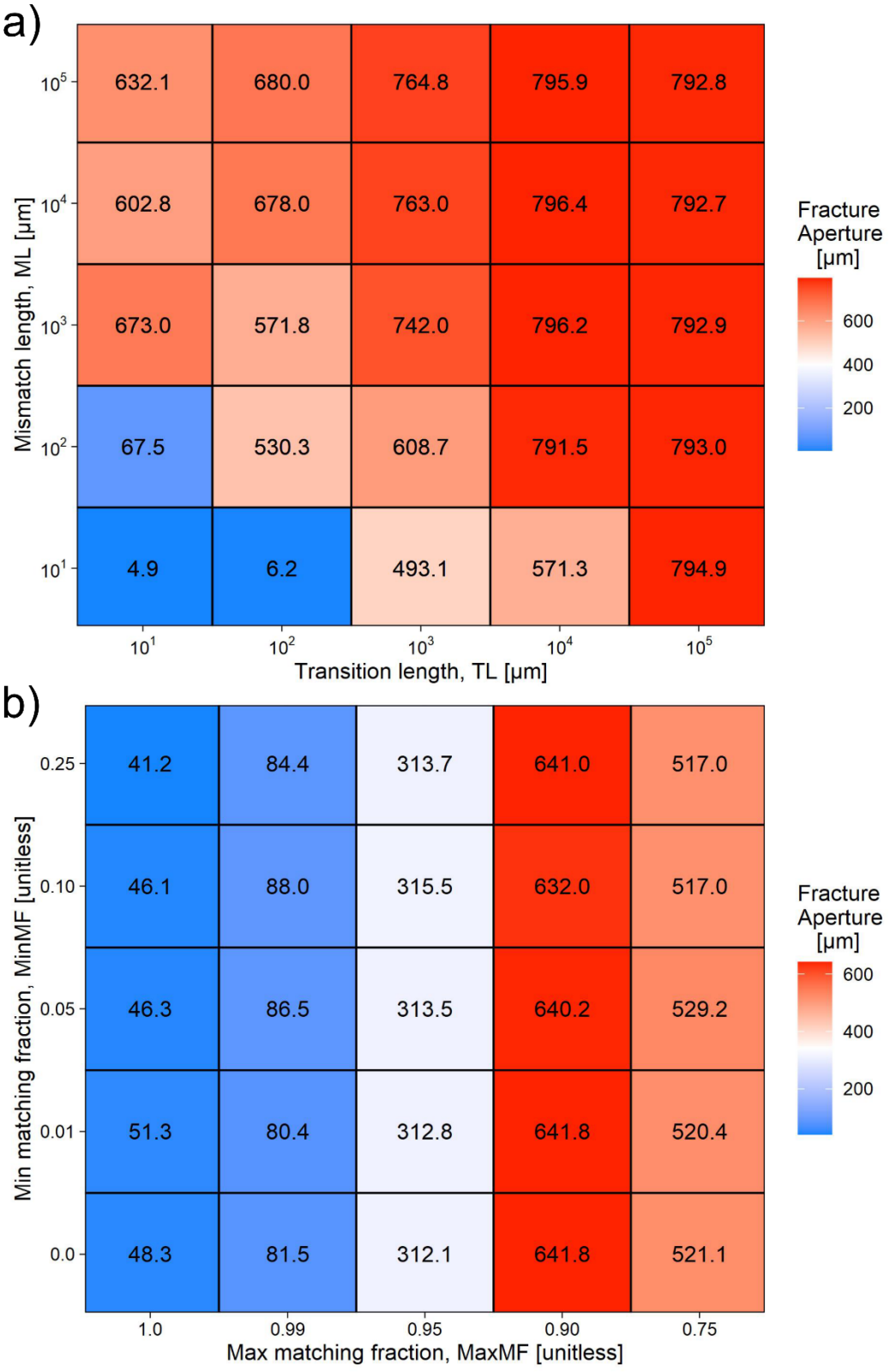

Fig. 3A-2: Sensitivity analysis of the fracture aperture due to mismatch parameters. a) transition length and mismatch length, b) maximum and minimum matching fraction.

The fracture aperture seems directly proportional to the roughness parameters (Fig. 3 A-1). Similar effect has been discussed by Zambrano et al. (2019b). These authors documented the positive impact of the fractal dimension on the porosity and the permeability in mismatching fractures.

In the case of mismatch length and transition length, the fracture aperture is directly proportional to both (Fig. 3.A-2a). In other words, higher the wavelength where mismatch occurs, larger the aperture. Also, larger the difference between the minimum and maximum mismatch length, greater the aperture. For the matching fractions, the trend is more complex (Fig. 3.A-2b). When the maximum matching fraction decrease from 1.0 to 0.9, there is an increment of the aperture. However, below this value the behavior is more erratic. This erratic behavior is more dramatic for the minimum matching fraction. In these regards, we state that this topic deserves a special attention in further investigations.

References

Agosta, F., Alessandroni, M., Antonellini, M., Tondi, E., Giorgioni, M., 2010. From fractures to flow: A field-based quantitative analysis of an outcropping carbonate reservoir. Tectonophysics 490, 197–213.

Agosta, F., Alessandroni, M., Tondi, E., Aydin, A., 2009. Oblique normal faulting along the northern edge of the Majella Anticline, central Italy: Inferences on hydrocarbon migration and accumulation. Journal of Structural Geology 31, 674–690.

Antonellini, M., Cilona, A., Tondi, E., Zambrano, M., Agosta, F., 2014. Fluid flow numerical experiments of faulted porous carbonates, Northwest Sicily (Italy). Marine and Petroleum Geology 55.

Antonellini, M., Tondi, E., Agosta, F., Aydin, A., Cello, G., 2008. Failure modes in deep-water carbonates and their impact for fault development: Majella Mountain, Central Apennines, Italy. Marine and Petroleum Geology 25, 1074–1096.

Arzilli, F., Cilona, A., Mancini, L., Tondi, E., 2016. Using synchrotron X-ray microtomography to characterize the pore network of reservoir rocks: A case study on carbonates. Advances in Water Resources 95, 254–263.

Arzilli, F., Mancini, L., Voltolini, M., Cicconi, M.R., Mohammadi, S., Giuli, G., Mainprice, D., Paris, E., Barou, F., Carroll, M.R., 2015. Near-liquidus growth of feldspar spherulites in trachytic melts: 3D morphologies and implications in crystallization mechanisms. Lithos 216, 93–105.

Aydin, A., 2000. Fractures, faults, and hydrocarbon entrapment, migration and flow. Marine and petroleum geology 17, 797–814.

Aydin, A., Antonellini, M., Tondi, E., Agosta, F., 2010. Deformation along the leading edge of the Maiella thrust sheet in central Italy. Journal of Structural Geology 32, 1291–1304.

Bagni, F.L., Bezerra, F.H., Balsamo, F., Maia, R.P., Dall'Aglio, M., 2020. Karst dissolution along fracture corridors in an anticline hinge, Jandaíra Formation, Brazil: Implications for reservoir quality. Marine and Petroleum Geology 115, 104249.

Baker, D.R., Mancini, L., Polacci, M., Higgins, M.D., Gualda, G.A.R., Hill, R.J., Rivers, M.L., 2012. An introduction to the application of X-ray microtomography to the three-dimensional study of igneous rocks. Lithos 148, 262–276.

Barton, N., Bandis, S., Bakhtar, K., 1985. Strength, deformation and conductivity coupling of rock joints. In: International Journal of Rock Mechanics and Mining Sciences & Geomechanics Abstracts. Elsevier, pp. 121–140.

Baud, P., Exner, U., Lommatzsch, M., Reuschlé, T., Wong, T., 2017. Mechanical behavior, failure mode, and transport properties in a porous carbonate. Journal of Geophysical Research: Solid Earth 122, 7363–7387.

Baud, P., Rolland, A., Heap, M., Xu, T., Nicolé, M., Ferrand, T., Reuschle, T., Toussaint, R., Conil, N., 2016. Impact of stylolites on the mechanical strength of limestone. Tectonophysics 690, 4–20.

Baud, P., Vinciguerra, S., David, C., Cavallo, A., Walker, E., Reuschlé, T., 2009. Compaction and failure in high porosity carbonates: Mechanical data and microstructural observations. Pure and Applied Geophysics 166, 869–898.

Blunt, M.J., Bijeljic, B., Dong, H., Gharbi, O., Iglauer, S., Mostaghimi, P., Paluszny, A., Pentland, C., 2013. Pore-scale imaging and modelling. Advances in Water resources 51, 197–216.

Brandano, M., Cornacchia, I., Raffi, I., Tomassetti, L., 2016a. The Oligocene–Miocene stratigraphic evolution of the Majella carbonate platform (Central Apennines, Italy). Sedimentary geology 333, 1–14.

Brandano, M., Lipparini, L., Campagnoni, V., Tomassetti, L., 2012. Downslope-migrating large dunes in the Chattian carbonate ramp of the Majella Mountains (Central Apennines, Italy). Sedimentary Geology 255, 29–41.

Brandano, M., Tomassetti, L., Sardella, R., Tinelli, C., 2016b. Progressive deterioration of trophic conditions in a carbonate ramp environment: the Lithothamnion Limestone, Majella Mountain (Tortonian–early Messinian, central Apennines, Italy). Palaios 31, 125–140.

Brown, S.R., 1995. Simple mathematical model of a rough fracture. Journal of Geophysical Research: Solid Earth 100, 5941–5952.

Brun, F., Dreossi, D., 2010. Efficient curve-skeleton computation for the analysis of biomedical 3d images-biomed 2010. Biomedical Sciences Instrumentation 46, 475–480.

Brun, F., Mancini, L., Kasae, P., Favretto, S., Dreossi, D., Tromba, G., 2010. Pore3D: A software library for quantitative analysis of porous media. Nuclear Instruments and Methods in Physics Research Section A: Accelerators, Spectrometers, Detectors and Associated Equipment 615, 326–332.

Brun, F., Pacilè, S., Accardo, A., Kourousias, G., Dreossi, D., Mancini, L., Tromba, G., Pugliese, R., 2015. Enhanced and flexible software tools for X-ray computed tomography at the Italian synchrotron radiation facility Elettra. Fundamenta Informaticae 141, 233–243.

Bruna, P.-O., Lavenu, A.P.C., Matonti, C., Bertotti, G., 2019. Are stylolites fluid-flow efficient features? Journal of Structural Geology 125, 270–277.

Candela, T., Renard, F., Bouchon, M., Brouste, A., Marsan, D., Schmittbuhl, J., Voisin, C., 2009. Characterization of fault roughness at various scales: Implications of three-dimensional high resolution topography measurements. In: Mechanics, Structure and Evolution of Fault Zones. Springer, pp. 1817–1851.

Candela, T., Renard, F., Klinger, Y., Mair, K., Schmittbuhl, J., Brodsky, E.E., 2012. Roughness of fault surfaces over nine decades of length scales. Journal of Geophysical Research: Solid Earth 117.

Carnevale, G., Patacca, E., Scandone, P., 2011. Field Guide of the Post-Conference Excursions (Scontrone, Palena and Montagna della Majella) 4-5 March 2011.

Cazzini, F., Zotto, O.D., Fantoni, R., Ghielmi, M., Ronchi, P., Scotti, P., 2015. Oil and gas in the Adriatic foreland, Italy. Journal of Petroleum Geology 38, 255–279.

Cilona, A., Baud, P., Tondi, E., Agosta, F., Vinciguerra, S., Rustichelli, A., Spiers, C.J., 2012. Deformation bands in porous carbonate grainstones: Field and laboratory observations. Journal of Structural Geology 45, 137–157.

Cilona, A., Faulkner, D.R., Tondi, E., Agosta, F., Mancini, L., Rustichelli, A., Baud, P., Vinciguerra, S., 2014. The effects of rock heterogeneity on compaction localization in porous carbonates. Journal of Structural Geology 67, 75–93.

Cloetens, P., Pateyron-Salomé, M., Buffiere, J.Y., Peix, G., Baruchel, J., Peyrin, F., Schlenker, M., 1997. Observation of microstructure and damage in materials by phase sensitive radiography and tomography. Journal of Applied Physics 81, 5878–5886.

Corradetti, A., McCaffrey, K., de Paola, N., Tavani, S., 2017. Evaluating roughness scaling properties of natural active fault surfaces by means of multi-view photogrammetry. Tectonophysics 717, 599–606.

Corradetti, A., Tavani, S., Parente, M., Iannace, A., Vinci, F., Pirmez, C., Torrieri, S., Giorgioni, M., Pignalosa, A., Mazzoli, S., 2018. Distribution and arrest of vertical through-going joints in a seismic-scale carbonate platform exposure (Sorrento peninsula, Italy): insights from integrating field survey and digital outcrop model. Journal of Structural Geology 108, 121–136.

Corradetti, A., Zambrano, M., Tavani, S., Tondi, E., Seers, T.D., 2020. The impact of weathering upon the roughness characteristics of a splay of the active fault system responsible for the massive 2016 seismic sequence of the Central Apennines, Italy. GSA Bulletin.

Crescenti, U., 1969. Stratigrafia della serie calcarea dal Lias al Miocene nella regione marchigiano-abruzzese (parte I, Descrizione delle serie stratigrafiche). Mem. Soc. Geol. It 8, 155–204.

de Beer, F.C., Middleton, M.F., 2006. Neutron radiography imaging, porosity and permeability in porous rocks. South African Journal of Geology 109, 541–550.

Degruyter, W., Burgisser, A., Bachmann, O., Malaspinas, O., 2010. Synchrotron X-ray microtomography and lattice Boltzmann simulations of gas flow through volcanic pumices. Geosphere 6, 470–481.

d'Humieres, D., 2002. Multiple–relaxation–time lattice Boltzmann models in three dimensions. Philosophical Transactions of the Royal Society of London. Series A: Mathematical, Physical and Engineering Sciences 360, 437–451.

di Cuia, R., Shakerley, A., Masini, M., Casabianca, D., 2009. Integrating outcrop data at different scales to describe fractured carbonate reservoirs: example of the Maiella carbonates, Italy. First break 27.

Espejel, R.L., Alves, T.M., Blenkinsop, T.G., 2020. Multi-scale fracture network characterisation on carbonate platforms. Journal of Structural Geology 140, 104160.

Gao, Y., Raeini, A.Q., Blunt, M.J., Bijeljic, B., 2019. Pore occupancy, relative permeability and flow intermittency measurements using X-ray micro-tomography in a complex carbonate. Advances in Water Resources 129, 56–69.

Gerke, H.H., van Genuchten, M.T., 1993. A dual-porosity model for simulating the preferential movement of water and solutes in structured porous media. Water resources research 29, 305–319.

Ghisetti, F., Vezzani, L., 2002. Normal faulting, extension and uplift in the outer thrust belt of the central Apennines (Italy): role of the Caramanico fault. Basin Research 14, 225–236.

Giorgioni, M., Cilona, A., Tondi, E., Agosta, F., 2011. Fault Zone Properties In The Roman Valley Quarry Reservoir Analogue: Insight For Well Logs, Core And Field Data. In: Offshore Mediterranean Conference and Exhibition. Offshore Mediterranean Conference.

Gong, B., Karimi-Fard, M., Durlofsky, L.J., 2008. Upscaling discrete fracture characterizations to dual-porosity, dual-permeability models for efficient simulation of flow with strong gravitational effects. Spe Journal 13, 58–67.

Gürsoy, D., de Carlo, F., Xiao, X., Jacobsen, C., 2014. TomoPy: a framework for the analysis of synchrotron tomographic data. Journal of synchrotron radiation 21, 1188–1193.

Hall, S.A., 2013. Characterization of fluid flow in a shear band in porous rock using neutron radiography. Geophysical Research Letters 40, 2613–2618.

Hartigan, J.A., 1975. Clustering Algorithms John Wiley & Sons. Inc., New York, NY.

Hartigan, J.A., Wong, M.A., 1979. Algorithm AS 136: A k-means clustering algorithm. Journal of the royal statistical society. series c (applied statistics) 28, 100–108.

Heap, M.J., Baud, P., Reuschlé, T., Meredith, P.G., 2014. Stylolites in limestones: Barriers to fluid flow? Geology 42, 51–54.

Hwang, S., Jang, S., Hoang, N.D., Pham, H.G., 2018. Well path design by integrating the analysis of wireline logs and the interpretation of seismic data for a fractured basement reservoir in Cuu Long Basin, Viet Nam. Marine and Petroleum Geology 93, 315–330.

Iadanza, A., Sampalmieri, G., Cipollari, P., Mola, M., Cosentino, D., 2013. The "Brecciated Limestones" of Maiella, Italy: Rheological implications of hydrocarbon-charged fluid migration in the Messinian Mediterranean Basin. Palaeogeography, Palaeoclimatology, Palaeoecology 390, 130–147.

Isakov, E., Ogilvie, S.R., Taylor, C.W., Glover, P.W.J., 2001. Fluid flow through rough fractures in rocks I: high resolution aperture determinations. Earth and Planetary Science Letters 191, 267–282.

Ji, Y., Hall, S.A., Baud, P., Wong, T., 2015. Characterization of pore structure and strain localization in Majella limestone by X-ray computed tomography and digital image correlation. Geophysical Journal International 200, 701–719.

Kaminskaite, I., Fisher, Q.J., Michie, E.A.H., 2019. Microstructure and petrophysical properties of deformation bands in high porosity carbonates. Journal of Structural Geology 119, 61–80.

Katz, B.J., Dittmar, E.I., Ehret, G.E., 2000. A geochemical review of carbonate source rocks in Italy. Journal of Petroleum Geology 23, 399–424.

Kazemi, H., Merrill Jr, L.S., Porterfield, K.L., Zeman, P.R., 1976. Numerical simulation of water-oil flow in naturally fractured reservoirs. Society of Petroleum Engineers Journal 16, 317–326.

Koehn, D., Rood, M.P., Beaudoin, N., Chung, P., Bons, P.D., Gomez-Rivas, E., 2016. A new stylolite classification scheme to estimate compaction and local permeability variations. Sedimentary Geology 346, 60–71.

Latt, J., Malaspinas, O., Kontaxakis, D., Parmigiani, A., Lagrava, D., Brogi, F., Belgacem, M. ben, Thorimbert, Y., Leclaire, S., Li, S., Marson, F., Lemus, J., Kotsalos, C., Conradin, R., Coreixas, C., Petkantchin, R., Raynaud, F., Beny, J., Chopard, B., 2020. Palabos: Parallel Lattice Boltzmann Solver. Computers & Mathematics with Applications.

Lavenu, A.P.C., Lamarche, J., Salardon, R., Gallois, A., Marié, L., Gauthier, B.D.M., 2014. Relating background fractures to diagenesis and rock physical properties in a platform–slope transect. Example of the Maiella Mountain (central Italy). Marine and Petroleum Geology 51, 2–19.

Lee, H.S., Cho, T.F., 2002. Hydraulic characteristics of rough fractures in linear flow under normal and shear load. Rock Mechanics and Rock Engineering 35, 299–318.

Lindquist, W.B., Venkatarangan, A., 1999. Investigating 3D geometry of porous media from high resolution images. Physics and Chemistry of the Earth, Part A: Solid Earth and Geodesy 24, 593–599.

Lipparini, L., Trippetta, F., Ruggieri, R., Brandano, M., Romi, A., 2018. Oil distribution in outcropping carbonate-ramp reservoirs (Maiella Mountain, Central Italy): Three-dimensional models constrained by dense historical well data and laboratory measurements. AAPG Bulletin 102, 1273–1298.

Lomize, G.M., 1951. Flow in Fractured Rocks, 197. Gosenergoizdat, Moscow, Russia.

Louis, C., 1969. A study of groundwater flow in jointed rock and its influence on the stability of rock masses, Imperial College. Rock Mechanics Research Report 10, 1–90.

Marchegiani, L., van Dijk, J.P., Gillespie, P.A., Tondi, E., Cello, G., 2006. Scaling properties of the dimensional and spatial characteristics of fault and fracture systems in the Majella Mountain, central Italy. Geological Society, London, Special Publications 261, 113–131.

Masaferro, J.L., Bourne, R., Jauffred, J.C., 2004. Three-dimensional seismic volume visualization of carbonate reservoirs and structures.

Massaro, L., Corradetti, A., Vinci, F., Tavani, S., Iannace, A., Parente, M., Mazzoli, S., 2018. Multiscale fracture analysis in a reservoir-scale carbonate platform exposure (sorrento peninsula, Italy): implications for fluid flow. Geofluids 2018.

Mattavelli, L., Novelli, L., 1988. Geochemistry and habitat of natural gases in Italy. In: Organic Geochemistry In Petroleum Exploration. Elsevier, pp. 1–13.

Mendez, J.N., Jin, Q., González, M., Zhang, X., Lobo, C., Boateng, C.D., Zambrano, M., 2020. Fracture characterization and modeling of karsted carbonate reservoirs: A case study in Tahe oilfield, Tarim Basin (western China). Marine and Petroleum Geology 112, 104104.

Münch, B., Trtik, P., Marone, F., Stampanoni, M., 2009. Stripe and ring artifact removal with combined wavelet—Fourier filtering. Optics express 17, 8567–8591.

Mutti, M., Bernoulli, D., Eberli, G.P., Vecsei, A., 1996. Depositional geometries and facies associations in an Upper Cretaceous prograding carbonate platform margin (Orfento Supersequence, Maiella, Italy). Journal of Sedimentary Research 66, 749–765.

Mutti, M., Bernoulli, D., Stille, P., 1997. Temperate carbonate platform drowning linked to Miocene oceanographic events: Maiella platform margin, Italy. Terra Nova 9, 122–125.

Nelson, R., 2001. Geologic analysis of naturally fractured reservoirs. Elsevier.

Ogilvie, S.R., Isakov, E., Glover, P.W.J., 2006. Fluid flow through rough fractures in rocks. II: A new matching model for rough rock fractures. Earth and Planetary Science Letters 241, 454–465.

Ogilvie, S.R., Isakov, E., Taylor, C.W., Glover, P.W.J., 2003. Characterization of rough-walled fractures in crystalline rocks. Geological Society, London, Special Publications 214, 125–141.

Paganin, D., Mayo, S.C., Gureyev, T.E., Miller, P.R., Wilkins, S.W., 2002. Simultaneous phase and amplitude extraction from a single defocused image of a homogeneous object. Journal of microscopy 206, 33–40.

Palenstijn, W.J., Batenburg, K.J., Sijbers, J., 2011. Performance improvements for iterative electron tomography reconstruction using graphics processing units (GPUs). Journal of structural biology 176, 250–253.

Panza, E., Agosta, F., Rustichelli, A., Zambrano, M., Tondi, E., Prosser, G., Giorgioni, M., Janiseck, J.M., 2016. Fracture stratigraphy and fluid flow properties of shallow-water, tight carbonates: The case study of the Murge Plateau (southern Italy). Marine and Petroleum Geology 73.

Panza, E., Sessa, E., Agosta, F., Giorgioni, M., 2018. Discrete Fracture Network modelling of a hydrocarbon-bearing, oblique-slip fault zone: Inferences on fault-controlled fluid storage and migration properties of carbonate fault damage zones. Marine and Petroleum Geology 89, 263–279.

Pomar, L., Brandano, M., Westphal, H., 2004. Environmental factors influencing skeletal grain sediment associations: a critical review of Miocene examples from the western Mediterranean. Sedimentology 51, 627–651.

Ramandi, H.L., Armstrong, R.T., Mostaghimi, P., 2016. Micro-CT image calibration to improve fracture aperture measurement. Case Studies in Nondestructive Testing and Evaluation 6, 4–13.

Renard, F., Candela, T., Bouchaud, E., 2013. Constant dimensionality of fault roughness from the scale of micro-fractures to the scale of continents. Geophysical Research Letters 40, 83–87.

Reuter, M., Piller, W.E., Brandano, M., Harzhauser, M., 2013. Correlating Mediterranean shallow water deposits with global Oligocene–Miocene stratigraphy and oceanic events. Global and Planetary Change 111, 226–236.

Riegel, H., Zambrano, M., Balsamo, F., Mattioni, L., Tondi, E., 2019. Petrophysical properties and microstructural analysis of faulted heterolithic packages: A case study from Miocene turbidite successions, Italy. Geofluids 2019.

Rivers, M., 1998. Tutorial introduction to X-ray computed microtomography data processing. University of Chicago.

Romano, V., Bigi, S., Carnevale, F., Hyman, J.D., Karra, S., Valocchi, A.J., Tartarello, M.C., Battaglia, M., 2020. Hydraulic characterization of a fault zone from fracture distribution. Journal of Structural Geology 104036.

Ruggieri, R., Trippetta, F., 2020. Petrophysical properties variation of bitumen-bearing carbonates at increasing temperatures from laboratory to model. Geophysics 85, MR297–MR308.

Rustichelli, A., Tondi, E., Agosta, F., Cilona, A., Giorgioni, M., 2012. Development and distribution of bed-parallel compaction bands and pressure solution seams in carbonates (Bolognano Formation, Majella Mountain, Italy). Journal of Structural Geology 37, 181–199.

Rustichelli, A., Tondi, E., Agosta, F., di Celma, C., Giorgioni, M., 2013. Sedimentologic and diagenetic controls on pore-network characteristics of Oligocene–Miocene ramp carbonates (Majella Mountain, central Italy) Sedimentologic and Diagenetic Controls on Pore-Network Characteristics. AAPG bulletin 97, 487–524.

Rustichelli, A., Tondi, E., Korneva, I., Baud, P., Vinciguerra, S., Agosta, F., Reuschlé, T., Janiseck, J.-M., 2015. Bedding-parallel stylolites in shallow-water limestone successions of the Apulian Carbonate Platform (central-southern Italy). Italian Journal of Geosciences 134, 513–534.

Rustichelli, A., Torrieri, S., Tondi, E., Laurita, S., Strauss, C., Agosta, F., Balsamo, F., 2016. Fracture characteristics in Cretaceous platform and overlying ramp carbonates: An outcrop study from Maiella Mountain (central Italy). Marine and Petroleum Geology 76, 68–87.

Schindelin, J., Arganda-Carreras, I., Frise, E., Kaynig, V., Longair, M., Pietzsch, T., Preibisch, S., Rueden, C., Saalfeld, S., Schmid, B., 2012. Fiji: an open-source platform for biological-image analysis. Nature methods 9, 676–682.

Scisciani, V., Tavarnelli, E., Calamita, F., 2002. The interaction of extensional and contractional deformations in the outer zones of the Central Apennines, Italy. Journal of Structural Geology 24, 1647–1658.

Scrocca, D., Brandano, M., Petracchini, L., Lipparini, L., 2013. Analysis of an exhumed oil accumulation: the Oligo-Miocene carbonate ramp deposits of the Maiella Mountain (Central Italy). AAPG-ER Newsletter 8, 2–4.

Takougang, E.M.T., Bouzidi, Y., Ali, M.Y., 2019. Characterization of small faults and fractures in a carbonate reservoir using waveform inversion, reverse time migration, and seismic attributes. Journal of Applied Geophysics 161, 116–123.

Tomasi, C., Manduchi, R., 1998. Bilateral filtering for gray and color images. In: Sixth International Conference on Computer Vision (IEEE Cat. No. 98CH36271). IEEE, pp. 839–846.

Tondi, E., 2007. Nucleation, development and petrophysical properties of faults in carbonate grainstones: evidence from the San Vito Lo Capo peninsula (Sicily, Italy). Journal of Structural Geology 29, 614–628.

Tondi, E., Antonellini, M., Aydin, A., Marchegiani, L., Cello, G., 2006. The role of deformation bands, stylolites and sheared stylolites in fault development in carbonate grainstones of Majella Mountain, Italy. Journal of structural geology 28, 376–391.

Tondi, E., Cilona, A., Agosta, F., Aydin, A., Rustichelli, A., Renda, P., Giunta, G., 2012. Growth processes, dimensional parameters and scaling relationships of two conjugate sets of compactive shear bands in porous carbonate grainstones, Favignana Island, Italy. Journal of Structural Geology 37, 53–64.

Tondi, E., Rustichelli, A., Cilona, A., Balsamo, F., Storti, F., Napoli, G., Agosta, F., Renda, P., Giorgioni, M., 2016. Hydraulic properties of fault zones in porous carbonates, examples from central and southern Italy. Italian Journal of Geosciences 135, 68–79.

Trippetta, F., Geremia, D., 2019. The seismic signature of heavy oil on carbonate reservoir through laboratory experiments and AVA modelling. Journal of Petroleum Science and Engineering 177, 849–860.

Trippetta, F., Ruggieri, R., Brandano, M., Giorgetti, C., 2020. Petrophysical properties of heavy oil-bearing carbonate rocks and their implications on petroleum system evolution: Insights from the Majella Massif. Marine and Petroleum Geology 111, 350–362.

Tromba, G., Longo, R., Abrami, A., Arfelli, F., Astolfo, A., Bregant, P., Brun, F., Casarin, K., Chenda, V., Dreossi, D., 2010. The SYRMEP Beamline of Elettra: Clinical Mammography and Bio-medical Applications. In: AIP Conference Proceedings. American Institute of Physics, pp. 18–23.

Tsang, Y.W., 1992. Usage of "equivalent apertures" for rock fractures as derived from hydraulic and tracer tests. Water Resources Research 28, 1451–1455.

Vecsei, A., Sanders, D.G.K., 1999. Facies analysis and sequence stratigraphy of a Miocene warm-temperate carbonate ramp, Montagna della Maiella, Italy. Sedimentary Geology 123, 103–127.

Volatili, T., Zambrano, M., Cilona, A., Huisman, B.A.H., Rustichelli, A., Giorgioni, M., Vittori, S., Tondi, E., 2019. From fracture analysis to flow simulations in fractured carbonates: The case study of the Roman Valley Quarry (Majella Mountain, Italy). Marine and Petroleum Geology 100.

Voltolini, M., Zandomeneghi, D., Mancini, L., Polacci, M., 2011. Texture analysis of volcanic rock samples: quantitative study of crystals and vesicles shape preferred orientation from X-ray microtomography data. Journal of Volcanology and Geothermal Research 202, 83–95.

Wang, L., Zhang, Y., Zhang, N., Zhao, C., Wu, W., 2020. Pore structure characterization and permeability estimation with a modified multimodal Thomeer pore size distribution function for carbonate reservoirs. Journal of Petroleum Science and Engineering 107426.

Warren, J.E., Root, P.J., 1963. The behavior of naturally fractured reservoirs. Society of Petroleum Engineers Journal 3, 245–255.

Wei, Z., Zhang, D., 2010. Coupled fluid-flow and geomechanics for triple-porosity/dual-permeability modeling of coalbed methane recovery. International Journal of Rock Mechanics and Mining Sciences 47, 1242–1253.

Wildenschild, D., Sheppard, A.P., 2013. X-ray imaging and analysis techniques for quantifying pore-scale structure and processes in subsurface porous medium systems. Advances in Water Resources 51, 217–246.

Witherspoon, P.A., Wang, J.S.Y., Iwai, K., Gale, J.E., 1980. Validity of cubic law for fluid flow in a deformable rock fracture. Water resources research 16, 1016–1024.

Zambrano, M., Hameed, F., Anders, K., Mancini, L., Tondi, E., 2019a. Implementation of Dynamic Neutron Radiography and Integrated X-Ray and Neutron Tomography in Porous Carbonate Reservoir Rocks. Frontiers in Earth Science 7.

Zambrano, M., Pitts, A.D., Salama, A., Volatili, T., Giorgioni, M., Tondi, E., 2019b. Analysis of fracture roughness control on permeability using SFM and fluid flow simulations: Implications for carbonate reservoir characterization. Geofluids 2019.

Zambrano, M., Tondi, E., Korneva, I., Panza, E., Agosta, F., Janiseck, J.M., Giorgioni, M., 2016. Fracture properties analysis and discrete fracture network modelling of faulted tight limestones, Murge Plateau, Italy. Italian Journal of Geosciences 135, 55–67.

Zambrano, M., Tondi, E., Mancini, L., Arzilli, F., Lanzafame, G., Materazzi, M., Torrieri, S., 2017. 3D Pore-network quantitative analysis in deformed carbonate grainstones. Marine and Petroleum Geology 82.

Zambrano, M., Tondi, E., Mancini, L., Lanzafame, G., Trias, F.X., Arzilli, F., Materazzi, M., Torrieri, S., 2018. Fluid flow simulation and permeability computation in deformed porous carbonate grainstones. Advances in Water Resources 115.

Zandomeneghi, D., Voltolini, M., Mancini, L., Brun, F., Dreossi, D., Polacci, M., 2010. Quantitative analysis of X-ray microtomography images of geomaterials: Application to volcanic rocks. Geosphere 6, 793–804.

Zappaterra, E., 1994. Source-rock distribution model of the Periadriatic region. AAPG bulletin 78, 333–354.

Zhang, D., Zhang, R., Chen, S., Soll, W.E., 2000. Pore scale study of flow in porous media: Scale dependency, REV, and statistical REV. Geophysical research letters 27, 1195–1198.

Zhu, W., Baud, P., Wong, T., 2010. Micromechanics of cataclastic pore collapse in limestone. Journal of Geophysical Research: Solid Earth 115.

CHAPTER

4

OUTCROP-SCALE FRACTURE ANALYSIS AND SEISMIC MODELLING OF A BASIN-BOUNDING NORMAL FAULT IN PLATFORM CARBONATES, CENTRAL ITALY

The present chapter has been submitted in Journal of Structural Geology.

4. OUTCROP-SCALE FRACTURE ANALYSIS AND SEISMIC MODELLING OF A BASIN-BOUNDING NORMAL FAULT IN PLATFORM CARBONATES, CENTRAL ITALY

[1]Volatili T., [2]Agosta F., [3]Cardozo N., [1]Zambrano M., [4]Lecomte I, [1]Tondi E.

[1] School of Science and Technology - Geology Division, University of Camerino, Italy.
[2] Department of Science, University of Basilicata, Italy
[3] Department of Petroleum Engineering, University of Stavanger, Norway
[4] Department of Earth Science, University of Bergen, Norway

Abstract

Faults are characterized by a complex internal architecture. In platform carbonates, the geometry, attitude, and distribution of fault-related fractures and subsidiary faults can largely affect the petrophysical properties and hydraulic behavior of the fault zone. This work investigates the footwall damage zone of a seismic scale normal fault (throw ~ 300 m) from a structural, petrophysical and seismic point of view. The studied Venere Fault (VF) bounds the intra-mountain Fucino Basin (central Italy) and crosscut Lower Cretaceous platform carbonates. The footwall damage zone of the Venere Fault (VF-DZ) is well exposed in the 400 x 200 m Santilli Quarry. There, we assess the amounts of outcrop-scale fracture porosity and permeability by performing in-situ permeability measurements and fracture analyses. The results show a power-law decay of fracture intensity away from the fault core, which is strongly influenced by subsidiary faults. An outcrop-based, digital 2D model of the VF-DZ is constructed and populated with acoustic properties (Vp, Vs and density) derived from both the matrix and fracture porosities. This base model is enlarged five times and used for seismic modelling to investigate the seismic signature of the VF-DZ under different but realistic geological and geophysical parameters. Seismic modelling suggests that within the modelled damage zone and for wave frequencies of 20-40 Hz, seismic impedance contrasts associated to subsidiary faults may be imaged, depending on the degree of fracture porosity, fracture aperture, and the illumination angle (a measure of the maximum dip that can be imaged), the last two parameters being controlled by overburden depth. These results have implications for the seismic interpretation and characterization of fault zones in carbonates, and hence for the evaluation of fluid migration paths through these structures.

Keywords: *Tight Carbonates, Fracture Porosity, Fracture Permeability, PSDM, Seismic Modelling*

4.1. Introduction

The geometrical and structural properties of brittle faults are very difficult to recognize in the subsurface. Although seismic reflection data are successfully used for fault network interpretation, a few studies document the architecture and seismic attributes of single faults (i.e., Cohen et al., 2006; Dutzer et al., 2010; Liao et al., 2019). Both seismic modelling and attribute-based interpretation have been employed to characterize the geometry of single fault zones, and assess their surrounding deformation (Botter et al., 2016; Cunningham et al., 2019) according to their seismic disturbance zone (Iacopini et al., 2016). In fact, although fractures are below seismic resolution, their cumulative effect could be detected as a distortion of the seismic signal (Chopra and Marfurt, 2009; Li et al., 2015), and their main orientation estimated by structural seismic attributes (Michelena et al., 2013; Mendez et al., 2020). Synthetic fault models and their associated seismic response show the potential for characterizing damage zones using seismic attributes (Botter et al., 2017). However, since the interpretation in subsurface of sub-seismic structures across fault zones (i.e., subsidiary faults, fracture networks) are often affected by either a limited spatial distribution of 1D well data or an under-size resolution of these structures in seismic data, it is not clear how the seismic anomalies from these areas correlate with actual fracture distribution and petrophysical properties.

Focusing on fault damage zones, which commonly surround the fault cores and include thick volumes of fractured and faulted host rocks still preserving some of their original features (Caine et al., 1996; Aydin, 2000; Gudmundsson et al., 2001; Sagy et al., 2001; Rotevatn et al., 2007), many studies document common trends of both fracture density and intensity (Wilson et al., 2003; Faulkner et al., 2006, Mitchell and Faulkner, 2009; Savage and Brodsky, 2011; Johri et al., 2014). Although these trends have been verified in many outcrops, fracture parameters do not always scale proportionally with fault displacement (Anders and Wiltschko, 1994; Shipton and Cowie, 2003; Myers and Aydin, 2004; Mayolle et al., 2019; Mercuri et al., 2020). In this regard, several authors consider the role played by stress distribution along the evolving main slip surfaces on the localization of fault-related fracture clusters, assuming cohesive end zone models, different scales of mechanical unit thickness, and failure modes (Cowie and Scholz, 1992; Davatzes and Aydin, 2003; De Joussineau et al., 2007a, b; Mayolle et al., 2021).

This work focuses on an integrated outcrop-based characterization and seismic modelling of a 100's m-thick footwall damage zone in low-porosity carbonates. The study fault, known as the Venere Fault (VF, Fig. 4.1), bounds eastward the intramontane Fucino Basin (Central Italy), and juxtaposes Lower Cretaceous platform carbonates on the footwall against Plio-Quaternary fluvio-lacustrine sediments on the hanging wall (Cavinato et al., 2002). By studying in detail, the fractured and faulted carbonates exposed along the eastern and western walls of the active Santilli Quarry (Fig. 4.2), which are oriented approximately orthogonal to the main slip surface (MSS), we document the inner structure of the Venere fault damage zone (VF-DZ).

We investigate the complexity of the internal architecture of the VF-DZ from the structural, petrophysical, and seismic points of view. To evaluate the uncertainties in the seismic characterization and fluid-flow modelling of large faults in low-porosity carbonates, we integrate outcrop-based geological and petrophysical models of the VF-DZ with seismic modelling to generate seismic images of the fault zone. Specifically, we use a pre-stack depth migration (PSDM) algorithm (Lecomte, 2008), a seismic modelling approach that has been successfully applied to fault zones (Lecomte et al., 2016). The described workflow leads to the investigation of the distribution of petrophysical properties (porosity, permeability) across the VF-DZ. First, quantitative fracture analysis and in-situ permeability measurements across the VF-DZ are performed. Then, the outcrop-scale 2D petrophysical model is further constrained by merging it with a digital outcrop model (DOM) of the fault zone, constructed using photogrammetry techniques. This base model has property zones (including acoustic properties) that obey the geometrical and spatial relationships observed in the outcrop. Finally, an enlarged version of the base model is used for seismic modelling and sensitivity analyses of the impact of both geological and geophysical parameters on the seismic signature of the VF-DZ.

4.2. Structural setting of the Fucino Basin

The Fucino Basin lies in the Peri-Adriatic outer portion of the central Apennines fold-and-thrust belt, Italy (Vezzani and Ghisetti, 1998; Vezzani et al., 2010). The central Apennines are characterized by primarily east-verging regional-scale thrusts, which formed during Late Miocene–Pliocene compressional tectonics (Bigi et al., 1992; Ghisetti and Vezzani, 1999). Since Late Pliocene–Early Pleistocene, the imbricated fold-and-thrust belt has been crosscut and dissected by NW-SE striking normal faults, which mainly dip SW, and to a less degree by E-W striking normal faults. The central Apennines were uplifted and exhumed from shallow crustal depths during Plio-Quaternary times (Ghisetti and Vezzani 1999, 2002). As testified by the 1915 Avezzano earthquake (Ms = 7.0), tectonic extension is still ongoing, with major seismic normal faults bounding the eastern side of the Fucino Basin (Boschi et al., 1997; Lanari et al., 2021 and references therein). Regarding the Avezzano earthquake, paleoseismological investigations document pure dip-slip extension (Michetti et al., 1996; Galadini and Galli, 1999), although minor right-lateral slip was determined in the Fucino Basin area by means of detailed fault scarps analysis (Piccardi et al., 1999). Overall, a ca. 300 m throw, and an average slip rate of 0.4 to 1.0 mm/year were estimated for the Venere fault and the study area of the Fucino Basin (Cavinato et al., 2002; Roberts and Michetti, 2004; Faure Walker et al., 2010).

In this work, we focus on key outcrops located within the active Santilli Quarry. There, the whole footwall damage zone of the Venere Fault (VF-DZ) is nicely exposed allowing a full 3D characterization (Fig. 4.2). The platform carbonates consist of Lower Cretaceous limestones (Vezzani and Ghisetti, 1998), which mainly include carbonate boundstones with very low values of porosity and permeability (Agosta et al. 2007). After detailed analysis of their attitude, nature, distribution, abutting and crosscutting relations, Agosta and Aydin (2006) identified the fundamental fracture modes and main structural elements related to the processes of VF-DZ nucleation and growth. These authors documented three different orders of subsidiary faults according to their dimension and throw. The 1st order fault includes the main slip surface (MSS) and a cataclastic fault core, up to 1 m-thick, made up of grain- and matrix-supported cataclasites (Agosta and Aydin, 2006; Ferraro et al., 2018; Merico et al., 2020). These fault rocks were partially cemented by meteoric-derived fluids, which mainly infiltrated along the MSS (Ghisetti et al., 2001; Agosta and Kirschner, 2003; Agosta et al., 2008). The 2nd order faults include cm-

thick fault cores made up and grain-supported cataclasites. The 3rd order faults show throws up to a few meters and include fragmented carbonate rocks and less fault breccia. Previous works along the VF-DZ also analyzed the mineralogical, petrographic, textural, petrophysical, and ultrasonic properties of the fault rock assemblage (Agosta et al., 2007; Ferraro et al., 2019, 2020). Focusing on the results of petrophysical analysis, these authors documented a closely linear porosity-permeability relationship in the uncemented fault rocks. On the contrary, the cemented cataclasites that localize along the MSS show constant low values of permeability, like the host rock permeability, and varying values of porosity. Ferraro et al. (2020) interpreted this behavior as due to the presence of moldic porosity associated to the selective dissolution of survivor grains within the cemented cataclasites.

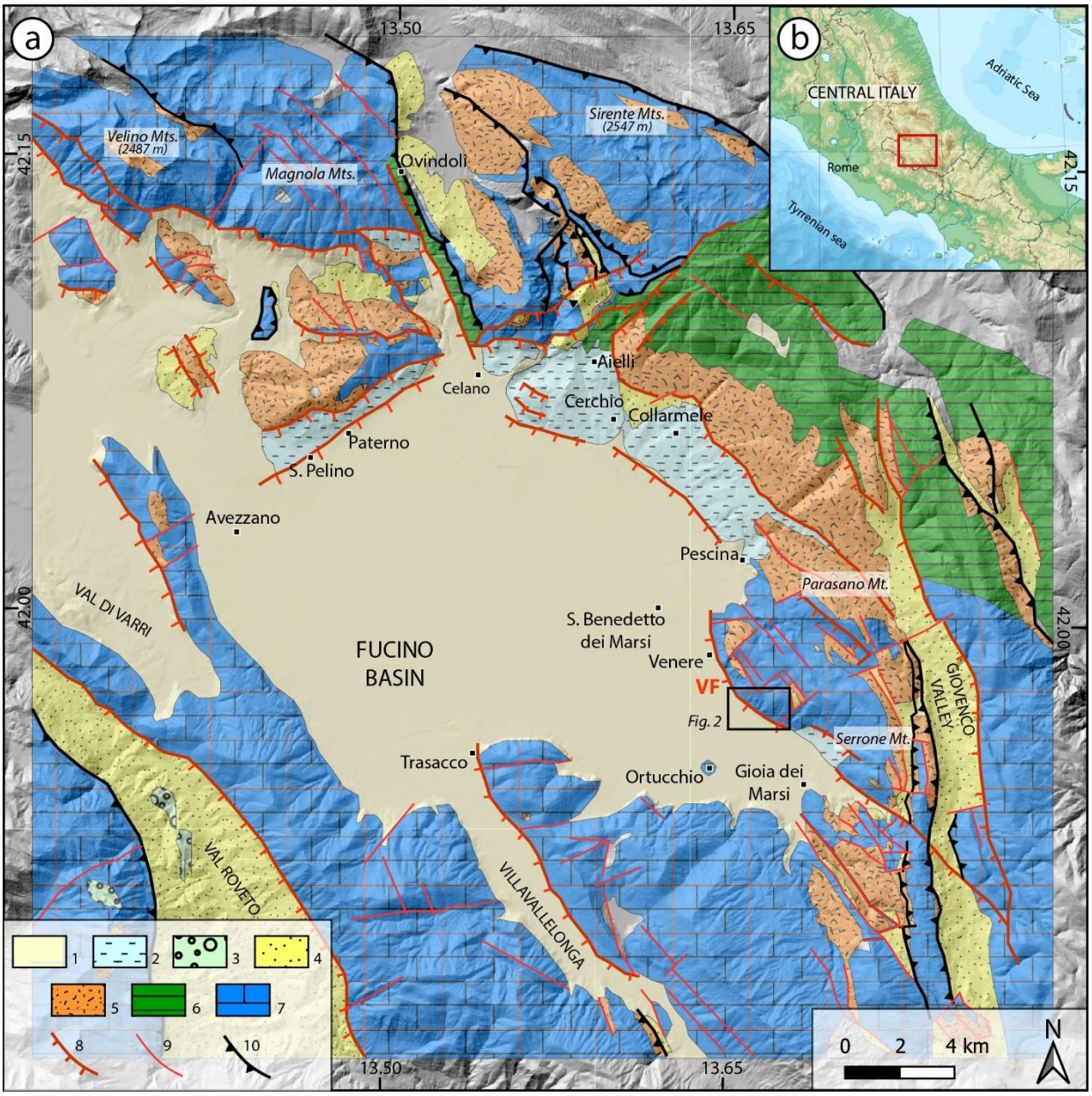

Fig. 4.1. Geological map of the Fucino Basin and surrounding areas (modified after Cavinato et al., 2002). 1) Alluvial deposits (Upper Pleistocene– Holocene); 2) Lacustrine deposits (Upper Pleistocene–Holocene); 3) Lacustrine–lagoonal deposits (Upper Messinian); 4) Lazio–Abruzzi flysch deposits (Lower Messinian); 5) Marine carbonate ramp (Lower Miocene); 6) Slope and marginal Latium–Abruzzi carbonate platform (Eocene–Lower Cretaceous); 7) inner carbonate platform (Upper Cretaceous-Middle Jurassic); 8) Normal fault; 9) Indistinct high-angle fault; 10) Thrust fault.

4.3. Methods

We use a workflow designed to investigate the VF zone through an integrated multidisciplinary approach. The inner structure of the VF-DZ is analyzed by coupling the structural data acquired in the field and digital-based measurements on a virtual model of the outcrop. The petrophysical properties of the fault-related fracture network (fracture porosity and fracture permeability) are obtained by integrating the in-situ permeability measurements with the results of quantitative fracture analysis. The resulting VF-DZ model includes the variations of the estimated values of fracture porosity and acoustic properties (P-wave velocity, S-wave velocity, and bulk density). Finally, an enlarged version of this model is employed as input data to perform seismic modeling simulating different geological and geophysical scenarios, which provide useful information on the imaging of the fault zone.

4.3.1. Structural analysis

The field structural analysis is conducted along two exposed walls, respectively labelled as eastern and western, cropping out in the Santilli Quarry (Fig. 4.2). Both eastern and western walls are ca. orthogonal to the MSS, and respectively expose the footwall damage zone located at the south-eastern tip and along the central portion of the VF. As mentioned before, on each study wall, we integrate the field-based fracture analysis with its virtual modelling.

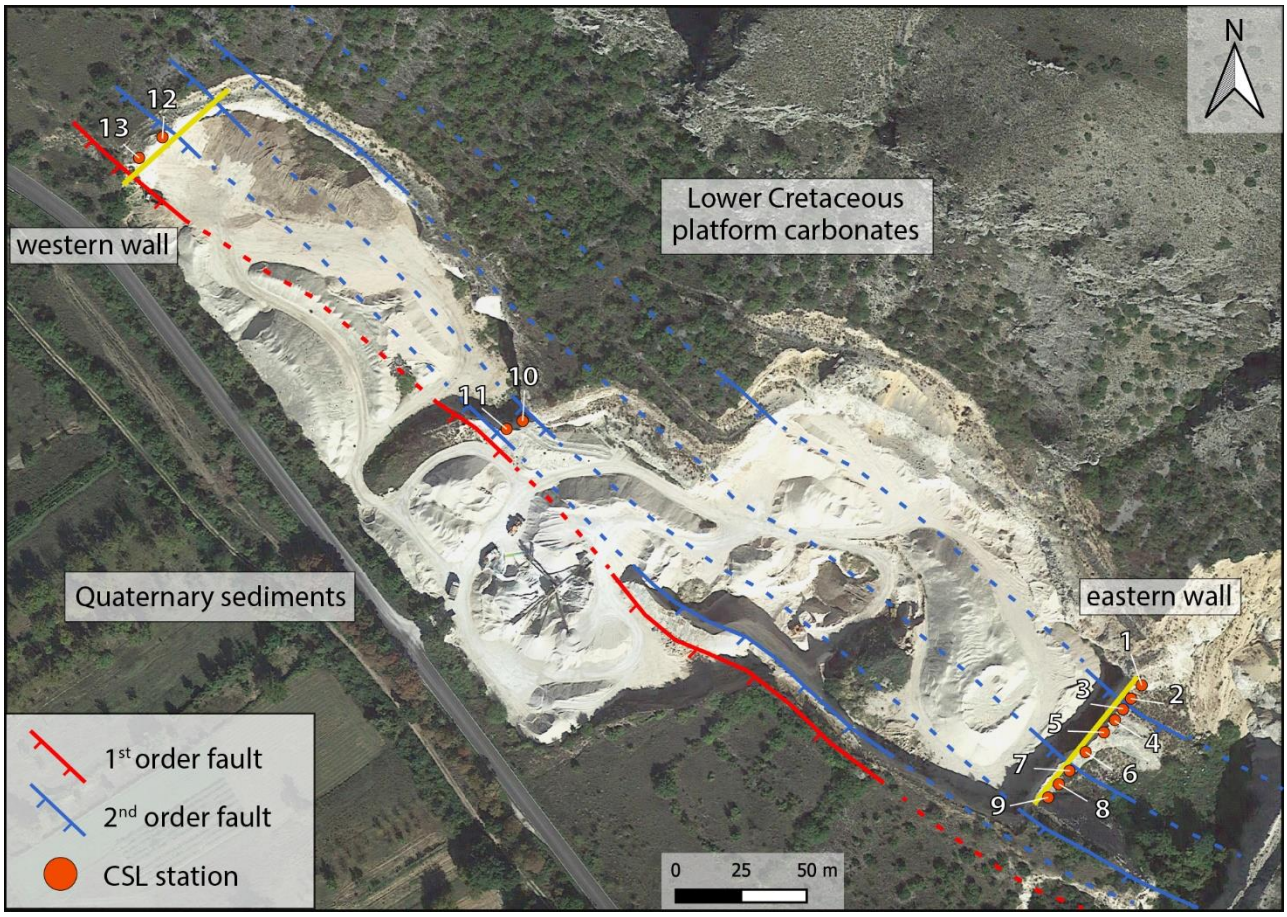

Fig. 4.2. Google Earth image (lat-long: 41.971°, 13.661°) of the study area with the main structural elements and studied sections. The 1st order fault is the main slip surface of the Venere Fault, and the study focuses on the northern footwall block, which consists of tight Lower Cretaceous platform carbonates. CSL stands for circular scanline.

4.3.1.1. Circular scan line analysis

A total of 13 circular scan line measurements (CSL) are performed at specific sites (orange circles in Fig. 4.2) to assess the amount of fracture properties across the VF-DZ. At each site, we calculate the values of fracture density (P_{20}), which is the number of fractures per area [m^{-2}], fracture intensity (P_{21}), which is the sum of fracture heights per area [m^{-1}], and mean fracture length (l), which is expressed in [m]. These parameters are estimated using the following equations (Mauldon et al., 2001):

$$P_{20} = \frac{m}{2\pi \times r^2} \quad (1)$$

$$P_{21} = \frac{n}{4r} \quad (2)$$

$$l = \frac{n}{m}\left(\frac{\pi r}{2}\right) \quad (3)$$

where *n* is the number of fracture intersections within a circular scan line, and *m* is the number of fracture terminations within the circular scan line. An optimal circle radius *r* of 0.1 m is chosen in order to avoid biases related to undersampling of fractures (Rohrbaugh et al., 2002), and multiple heterogeneity domains in a single survey. The required minimum number of 30 fracture terminations is always respected. Thus, the CSL size and the derived fracture properties (porosity and permeability) are assumed to be representative of single sampling stations.

The CSL analyses document the variation of both fracture density and intensity as function of the distance to both the main fault and the subsidiary faults, which respectively correspond to the 1st and 2nd order faults of Agosta and Aydin (2006). The presence of subsidiary faults tends to generate localized deformation, changing the apparent decay of the fracture parameters away from the MSS, due to the superposition of multiple secondary fault damage zones. Savage and Brodsky (2011) proposed how to model the composite curve of fracture intensity across a fault zone characterized by subsidiary faults by using a superposition of power-law functions. Following the same approach, we decompose the estimated fracture intensity distribution into two main power-law functions, which correspond to the main and subsidiary faults, respectively. To obtain the coefficients of both power-law equations, an optimization approach is adopted by using a generalized reduced gradient nonlinear algorithm (Lasdon et al., 1974). This procedure consists of iteratively varying the constants of the power-law equations until the lowest sum of squared errors between the best-fit model and the original data is obtained. Since the 3rd order faults are characterized by poorly developed, vertically discontinuous damage zones (Agosta and Aydin, 2006), their contribution is not incorporated in the fracture intensity decay model.

4.3.1.2. Photogrammetry analysis

Photogrammetric surveys are performed along both eastern and western walls by means of an Unmanned Aerial Vehicle (UAV). Then, by using the Structure from Motion (SfM) photogrammetry, we construct a Digital Outcrop Model (DOM) (James and Robson, 2012). The aerial photographs are taken using the DJI Phantom 4 Pro UAV, which is equipped with a 12Mp onboard camera, and 0.5 inches image sensor. In the field, the UAV flew at distances between ~ 2 and 5 m from the study walls. Each digital model is then built using ~200 overlapping photos. The general SfM processing procedure follows the methods described by Pitts et al. (2017) using the Agisoft Metashape software (Fig. 4.3a). The output DOMs consist of high-resolution surface meshes containing more than 30 million faces, and associated point clouds (up to 250 million points).

The main advantage of using DOMs is the ability to obtain additional information regarding the geometry of subsidiary structural elements in the footwall VF-DZ (Fig. 4.3b-e). The DOM point clouds are imported into the CloudCompare software for further interpretation, and the measure of length, throw, dip direction and dip of subsidiary 2nd order faults (Fig. 4.3e). These data are obtained by using the semi-automatic fracture tracing method (Thiele et al., 2017). In addition, the high resolution orthomosaics (near 1.5 mm/pix) from the DOM are used for the construction of the VF-DZ base model. The eastern and western walls orthomosaics are merged into a single 2D section representing the footwall DZ. In this model, the 2nd order faults, and the largest 3rd order faults cover a more representative area. Subsequently, the entire 2D geological model is populated with petrophysical and acoustic properties, as described in the following section.

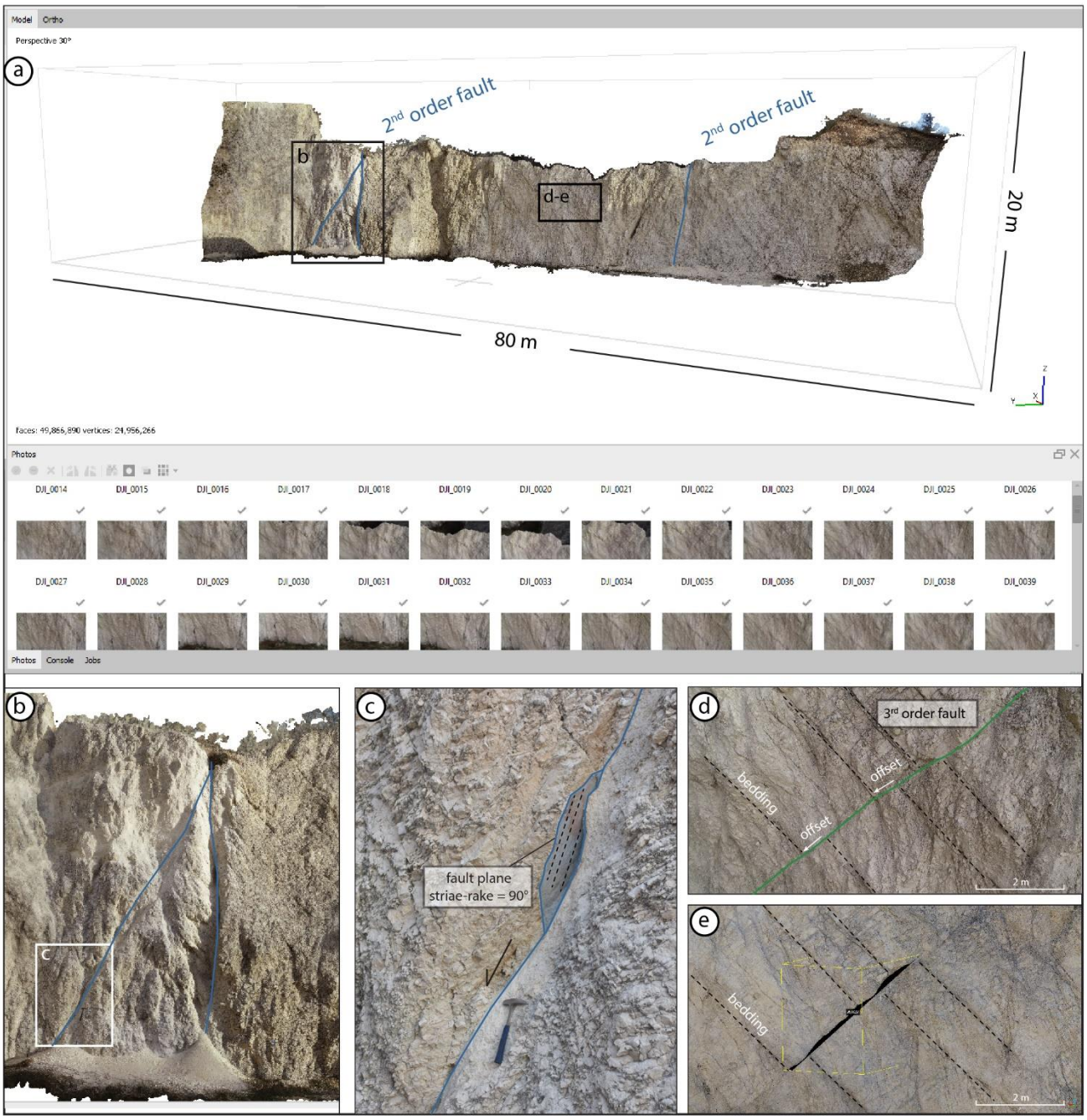

Fig. 4.3. (a) Digital outcrop model (DOM) of the eastern wall with interpreted 2nd order faults. (b) DOM close-up of a 2nd order fault and (c) field photo showing in detail the fault plane. (d) Field photo showing a 3rd order fault and (e) DOM dense point cloud of same area for measurements.

4.3.2. Petrophysical and acoustic properties

4.3.2.1. Fracture porosity

The amount of fracture porosity was calculated from the fracture density (P_{20}) across the damage zone, using the following equation:

$$\phi_{CSL} = P_{20} \times l \times E \quad (7)$$

where l is the mean fracture length calculated from the CSL analysis, and E is the mechanical fracture aperture estimated from a linear relationship with the fracture length, which is supported in the literature (e.g., Klimczak et al., 2010; Ghanbarian et al., 2018). We evaluate three scenarios of fracture porosity by varying the ratio E/l:

- Φ_{CSL1}, which assumes E/l = 0.01 and returns an average fracture aperture close to the one observed in the field (≈ 2x10^{-4} m);
- Φ_{CSL2}, which assumes E/l = 0.005 and provides intermediate fracture aperture values;
- Φ_{CSL3}, which assumes E/l = 0.001 and results in very small average fracture aperture of just few microns, likely resembling the fracture aperture at greater kilometer depths.

4.3.2.2. Fracture permeability

In situ permeability measurements are carried out using a portable air permeameter, TinyPerm (Balsamo et al., 2010; Filomena et al., 2014; Tondi et al., 2016). To avoid biases due to surface irregularities and weathering, in the field the sampling sites are cleaned and cleared out of detritus (Antonellini et al., 2014; Riegel et al., 2019). A maximum of 9 measurements are taken in each CSL station.

To obtain a reliable permeability value at each CSL station, the hydraulic aperture, e, is first calculated using the equation for smooth parallel plates (Snow, 1969):

$$e = \sqrt{k_i \times 12} \quad (4)$$

where k_i [m^2] is the average permeability for each CSL station, derived from the permeability measurements. Then, the fracture permeability k_f is calculated as follow:

$$k_f = \frac{n}{L}\left(\frac{e^3}{12}\right) \quad (5)$$

where n / L is the linear fracture intensity [m^{-1}], the number of fractures (n) per unit of length (L). To take advantage of our areal fracture survey approach, eq. 5 is modified to obtain the equivalent fracture permeability k_e as follows:

$$k_e = P_{21}\left(\frac{e^3}{12}\right) \quad (6)$$

The impact of fractures orientation is not considered for the estimation of the equivalent fracture permeability. However, k_e is assumed to resemble the along-fault permeability component since the in-situ permeability measurements are taken in single fractures oriented sub-parallel to the MSS. According to the CSL analyses, the fractures are highly connected and therefore we assume that the fracture network is above the percolation threshold.

4.3.2.3. Seismic velocities and density

To perform the seismic modelling of the VF-DZ, the base model is populated with the P wave velocity Vp, S wave velocity Vs, and density, estimated from the field measurements. The Vp is derived from the porosity by discriminating the effect of fracture and matrix porosity according to Kumar and Han (2005). These authors use a differential effective medium (DEM), which defines the contribution of interparticle pores (matrix) and crack-shaped pores (fractures) on P wave velocity. To automate the selection of Vp values, we use a Matlab function powered by the curve fitting toolbox, which includes both matrix and fracture porosity components and delivers a Vp value in agreement to Kumar and Han (2005). For the sake of simplification of the implemented Vp-porosity

relationship, the effect of fracture and matrix pore networks anisotropy is not considered. For matrix porosity, we consider values near 0.8% as reported by Agosta et al. (2007). For the fracture porosity, we use the values estimated in section 3.2.1. The Vs values are obtained using a Vp/Vs ratio of 1.9, which is a typical value for carbonates (Miller, 1992). The seismic velocities and density of the fault core are assigned using data from Agosta et al. (2007). Finally, the bulk density, ρ, is calculated assuming a water saturated porous medium, using the following equation:

$$\rho = \rho_m(1 - \Phi) + \rho_f\Phi \quad (9)$$

where ρ_m is the matrix density, which is equivalent to the density of calcite (2.71 g/cm^3), ρ_f is the density of the fluid (water, 1.0 g/cm^3) and Φ is the total porosity, including both fracture and matrix porosity.

4.3.3. Seismic modelling

Seismic imaging simulations are used to evaluate the seismic expression of the VF-DZ and the inner structures considering different geological and geophysical scenarios. A based grid with 1x1 m^2 cells is built-up by combining the information from the DOMs and the petrophysical and acoustic properties. The eastern and western grids are merged into a single 2D section representing the footwall VF-DZ. Then, the fracture domains (FDs) are extrapolated to a larger scale to include the surrounding geology of both the footwall and the hanging wall. This results in a more complete fault zone model, which is less biased by low contrasts of seismic impedance.

The synthetic seismic data are generated using the pre-stack depth migration (PSDM) simulator implemented in the SeisRoX^{TM} software. This simulator reproduces the effects of seismic imaging in the PSDM domain by acting as an image-processing method distorting an input reflectivity grid (Lecomte, 2008; Lecomte et al., 2015; Lecomte & Kaschwich, 2018). PSDM images can thus be rapidly simulated by spatial convolution with detailed 3D reflectivity models. This methodology was previously successfully employed to reproduce synthetic seismic images of faults and folds (Botter et al., 2014, 2016; Anell et al., 2016; Lecomte et al., 2016; Grippa et al., 2019; Wood et al., 2015; Wrona et al., 2020).

The method considers a spatial convolution operator called the Point-Spread Function (PSF), which ideally depends on the acquisition geometry, velocity model, and input wavelet, involving 3D angle-dependent illumination and resolution effects (Lecomte, 2008; Lecomte et al., 2015, 2016). The workflow and basic elements included in the 2(3)D PSF-based convolution approach are shown in Figure 4.4, whereas an extended description of this technique is given in Lecomte (2008). The main input to the PSDM simulator is an incident-angle dependent reflectivity model (Fig. 4.4a), which is derived from the acoustic properties of the model, i.e., density, Vp and Vs. The PSF is ideally calculated by ray-based modelling in a background velocity model for a given acquisition geometry (seismic survey), first generating so-called illumination vectors, then using the latter and a wavelet to form a PSDM filter in the wavenumber domain (Fig. 4.4b). In the absence of a given survey and background velocity model, as is the case for the present work, an angle of maximum illumination and a selected incident angle suffice to form a generic PSDM filter, which can be combined with a wavelet to add the frequency dependency. The angle of maximum illumination means that geological dips steeper than that angle will not be imaged, even if corresponding to detectable contrasts in the acoustic impedance. In the spatial domain (Fig. 4.4c), the PSF is the Fourier-equivalent of the PSDM filter in the wavenumber domain obtained by applying an inverse Fast Fourier transform (FFT^{-1}) to the PSDM filter. The modelling can thus also be seen as a convolution in the spatial domain between the input reflectivity and the PSF. In the wavenumber domain, the PSDM filters are multiplied with the reflectivity grid after first converting the latter by Fast Fourier transform (FFT), and an inverse FFT (FFT^{-1}) of the product yields the final simulated PSDM image (Fig. 4.4d).

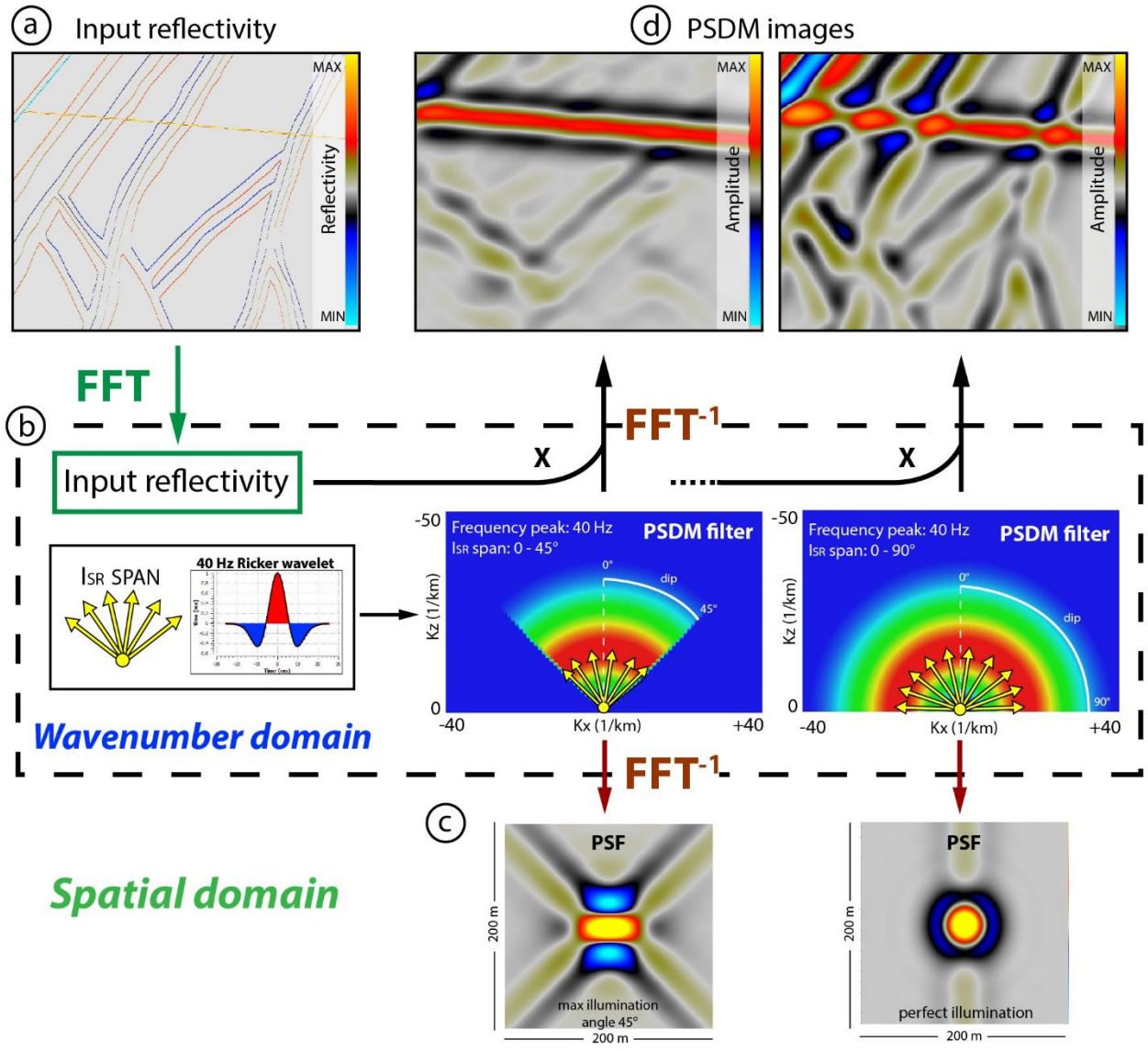

Fig. 4.4. Workflow and Basic elements for generating PSDM seismic images. (a) 2D Input Reflectivity model, which is converted to the wavenumber domain through a Fast Fourier Transform (FFT). (b) The PSDM filters are generated in the wavenumber domain by combining a selected dominant frequency Ricker wavelet with an assigned maximum illumination angle (ISR span; Lecomte et al., 2008), here varying from 45° to 90° (perfect illumination). (c) The PSFs are obtained in the spatial domain by inverse Fast Fourier Transform (FFT^{-1}) of PSDM filters. (d) Finally, the PSDM images are generated by the product of the input reflectivity grid with the PSDM filters in the wavenumber domain, converted to the spatial domain by applying an inverse Fast Fourier Transform (FFT^{-1}).

4.3.3.1. Geological and geophysical parameters

For the simulations, we focus on understanding the seismic expression of the fault damage zone under different geological and geophysical parameters as summarized in Figure 4.5. Most of the VF-DZ structures are at sub-seismic scales, and would not be detected in industry seismic (~20-40 Hz frequencies) at km depths. To test the impact of a structure like the VF-DZ at such depths and with standard seismic frequencies, we enlarge five times the geological model. This procedure is reasonable since fault zones mostly have a fractal nature, which means that their dimension scales with fault displacement (Fossen & Gabrielsen, 1996; Faulkner et al., 2011; Torabi et al., 2020), whereas their fracture abundance variation is insensible to fault size (Scholz, 2019, and references therein). Scibek (2020) also highlights the occurrence of similar petrophysical properties in fault damage zones regardless of their dimension.

Since the field data are limited to the footwall of the VF-DZ, we build three different geological models (GMs), which differ in terms of surrounding lithology above (footwall) and adjacent (hanging wall) to the outcrop model as follows:

i. GM1 carbonates with 10% matrix porosity.

ii. GM2 carbonates with 5% matrix porosity.

iii. GM3 saturated shales with constant acoustic properties: Vp = 2.5 km/s, Vs = 0.8 km/s, and density = 2.4 g/cm^3 (data from Bourbie et al., 1992).

These three models test the effect of different surrounding impedance contrasts on the seismic signature of the VF-DZ. In the GM1 and GM2 models, the VF-DZ is surrounded by the lithology observed in the footwall. Differently, in the GM3 model the fault zone is surrounded by shales of the Fucino Basin. For the three models, the petrophysical and acoustic properties of the carbonates are varied by considering three fracture aperture scenarios corresponding to 0.01, 0.005, and 0.001 times the mean fracture length of the fault zone (Fig. 4.5). To test the effect of these different geological parameters, the geophysical parameters are fixed, and they include a Ricker wavelet of 30 Hz dominant frequency, and a 60° illumination angle. To complete the sensitivity analysis,

geophysical parameters controlling the PSF are varied for the model GM2. Specifically, we test the effect of different illumination angles (45, 60 and 90°), and wavelet frequencies (20, 30 and 40Hz).

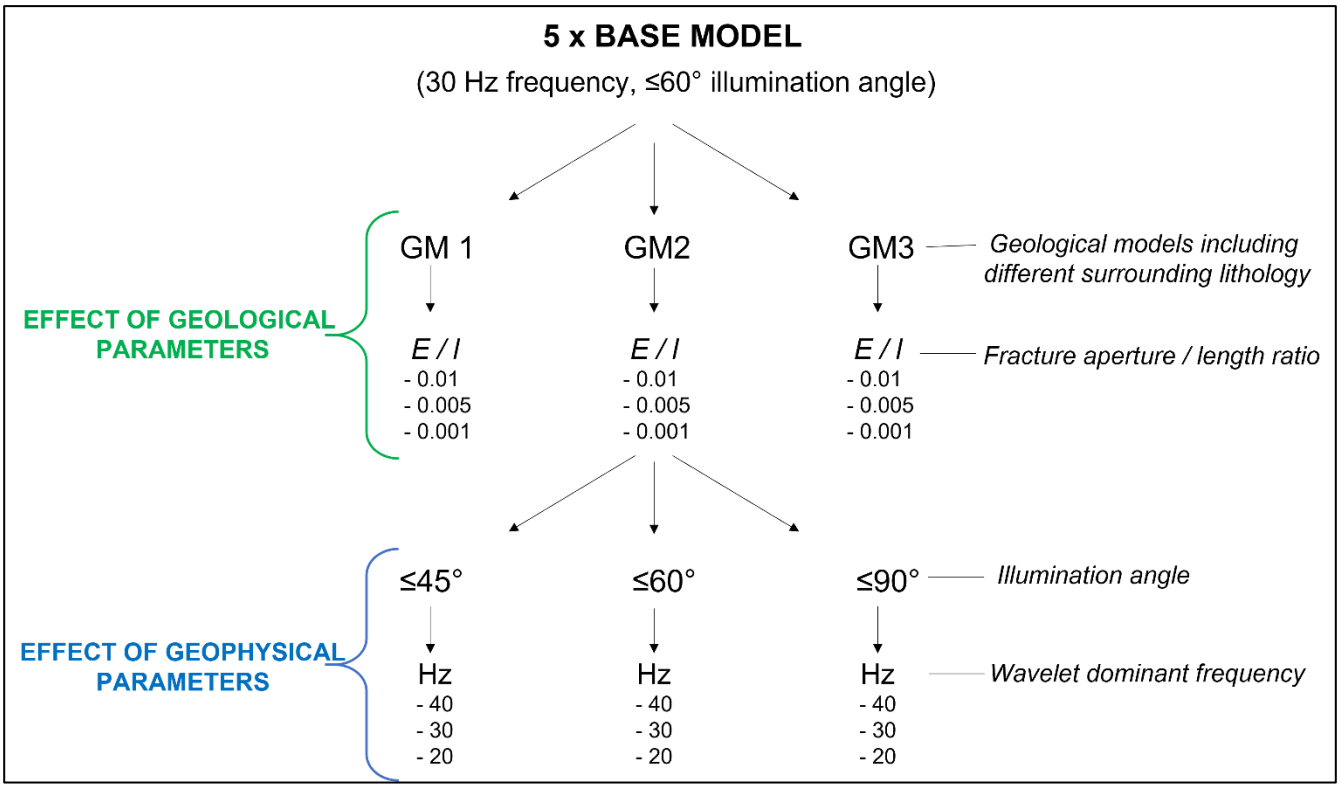

Fig. 4.5. Chart flow of the seismic models indicating both the geological and geophysical conditions that were tested.

4.4. Results

4.4.1. Fracture properties

The VF-MSS (1st order fault) is laterally continuous throughout the study area (Fig. 4.2). The strike direction of this fault varies from N138E (southern edge of the Santilli Quarry) to N116E (northern edge), whereas its dip angle is ≈ 50° SW. The well-developed slickenlines present on the fault planes show pitch angles forming clusters at ca. 90° and ca. 105° along the southern and northern edges of the quarry, respectively. The 100 m-thick footwall VF-DZ includes four 2nd order faults, which roughly strike NW-SE, and form high-angle synthetic structural elements with respect to the MSS (Figs. 4.2, 4.3). The spacing in between adjacent 2nd order faults increases away from the MSS. Hereafter, we document the detailed architecture of two walls orthogonal to the MSS labelled as eastern and western walls, respectively.

The eastern wall is crosscut by two 2nd order faults (Figs. 4.2, 4.6a). The 2nd order fault closer to the MSS strikes N125E, and dip 65° SW, whereas the other one strikes N134E, and dip 85° SW. The latter fault is associated to a conjugate splay oriented N126E/64° NE. The amount of displacement solved by these faults cannot be established. Both 2nd order faults include a few m-thick fault damage zone encompassing uncemented (poorly cemented in places) fault cores made up of 5 to 20 cm-thick cataclasites (Fig. 4.7a, b). We document a total of 47 3rd order faults. Overall, they strike N100E to N150E, dip 50 to 80° NE (Fig. 4.6c), and are hence antithetic with respect to the MSS. Based upon displacement of the carbonate beds, the 3rd order faults are characterized by throw values ranging from 5 to 60 cm. These faults are made up of discontinuous pods of brecciated carbonates that localize along the slip surfaces (Fig. 4.7c). We note that the bedding attitude along the whole eastern wall varies from ca. N120E/45° SW, away from the MSS, to ca. N120E/60° SW close to it.

The western wall exposes the MSS, and it is crosscut by two 2nd order faults striking ≈ N130E, and dipping 60° to 70°SW (Fig. 4.6b). These 2nd order faults are therefore conjugate structural elements with respect to the MSS. The amount of displacement solved by these faults cannot be established. Their inner structure is made up of 5 to 10 cm-thick cataclasites. The western wall is also crosscut by 39 3rd order faults, most of which are synthetic to the MSS fault. Altogether, these subsidiary faults show a wider range of attitudes with respect to those crosscutting

the eastern wall. They strike N40E to N160E, and dip 40 to 80° (Fig 4.6c). Regarding the amount of displacement, it is not possible to establish it due to the lack of evident stratigraphic markers. The inner structure of these faults includes 2 to 5 cm-thick uncemented fault core, mainly characterized by fragmented and comminuted carbonates. We note that the density of the 3rd order faults is not homogeneous within the western wall, showing an increment by a factor of ca. 2 approaching the MSS (from about 20 m-distance). The bedding attitude measured along the western wall is somehow constant at values of ca. N150E/15° NE.

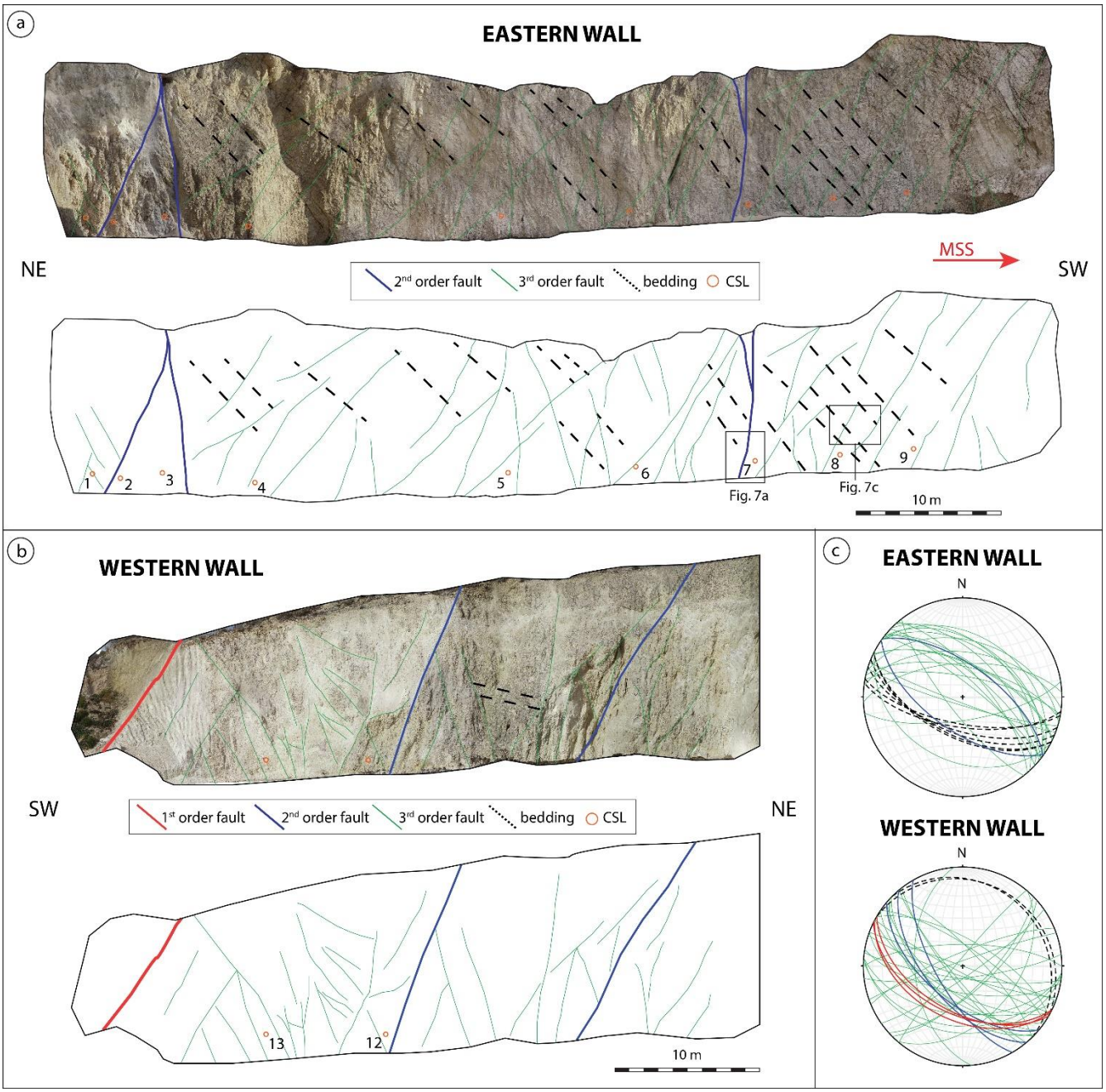

Fig 4.6. Orthomosaics and line drawings of the structures documented along the a) eastern wall and b) western wall. c) Faults and bedding planes in lower hemisphere, equal area stereonets. Lines' legend is similar to (a) and (b). CSL# show the location of the circular scan lines.

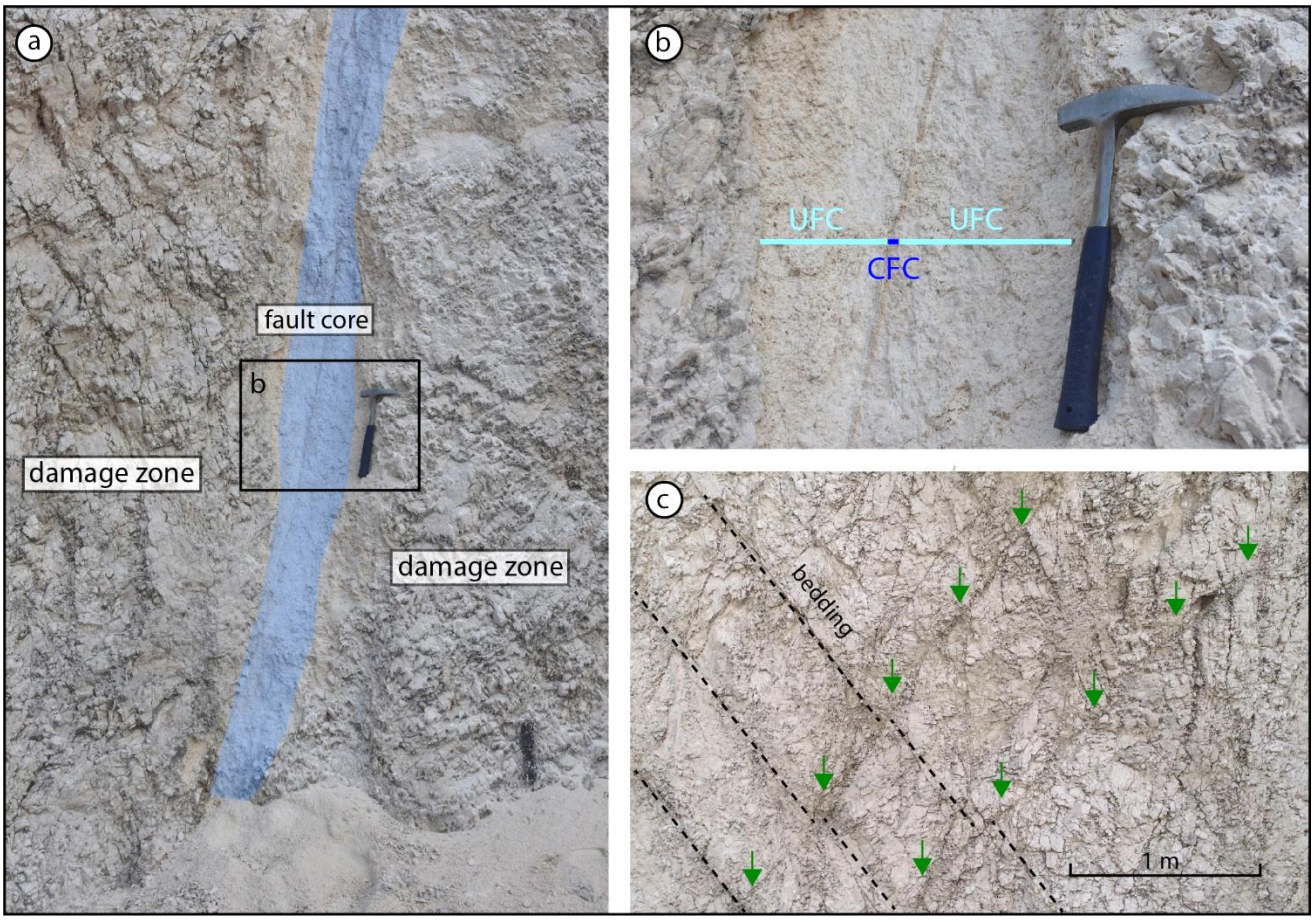

Fig 4.7. Detail of the inner architecture of subsidiary faults on the eastern wall. a) 2nd order fault zone and associated close-up in (b), b) uncemented (UFC) and cemented (CFC) fault rocks, c) two 3rd order faults highlighted by green arrows, including pods of fault breccia and clearly offsetting bedding.

The results of the CSL analyses are summarized in Table 4.1, and reported in Figures 4.8a, and 4.8b. The computed values of fracture density (P_{20}), fracture intensity (P_{21}), and mean fracture length (l) are also shown as normalized values with respect to the largest ones (Fig. 4.8c). In the latter figure, data are progressively ordered by considering the distance of single CSLs from the MSS for a quick graphical comparison (red line for MSS, blue lines for 2nd order faults).

Although it is difficult to distinguish in the field the extent of 2nd order fault damage zones from surrounding deformation, a further analysis of the fracture intensity (P_{21}) shows that its decay as function of distance (D) from the MSS can be decomposed into two main trends, which are respectively related to the 1st and 2nd order faults (Fig. 4.9). The optimal solution obtained by applying the minimum squares technique generates a modelled decay with a mean absolute error (MAE) of 0.07 (dashed black line in Fig. 4.9). The modelled decay of fracture intensity is represented by power-law functions ($P_{21} = c \times d^{-n}$), as reported in literature (Savage & Brodsky; 2011). It consists of a main, broader decay with an exponent n = 0.5, a scaling factor c = 700, and a distance D (dashed red line in Fig. 4.9), representative of the 1st order fault; and smaller, more localized decays with n = 0.52, c = 56, and distance to the subsidiary structure d_i, representative of the 2nd order faults.

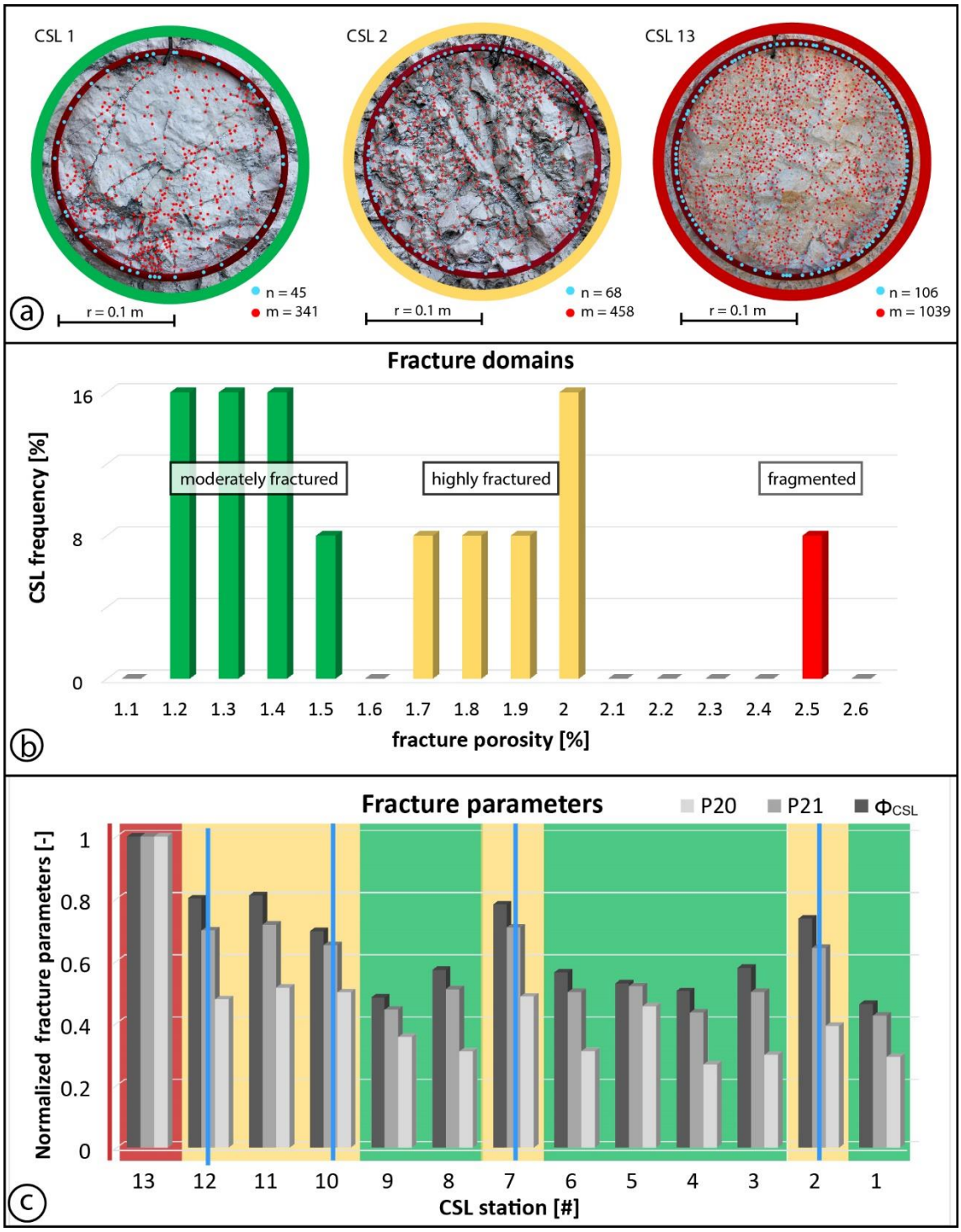

Fig 4.8. (a) Examples of circular scan lines CSL (circle radius = 0.1 m) from the eastern wall (1 and 2), and western wall (13). Blue dots (n) are fracture intersections, and red dots (m) are fracture terminations. (b) fracture domains related to Φ_{CSL} classes. The fracture porosity was estimated using a E/l aspect ratio of 0.005 for reference. (c) Normalized P20, P21, and Φ_{CSL} histograms. Red line is the location of the MSS, and blue lines are the locations of the 2nd order faults. Colors in the background refer to the fracture domains in (b).

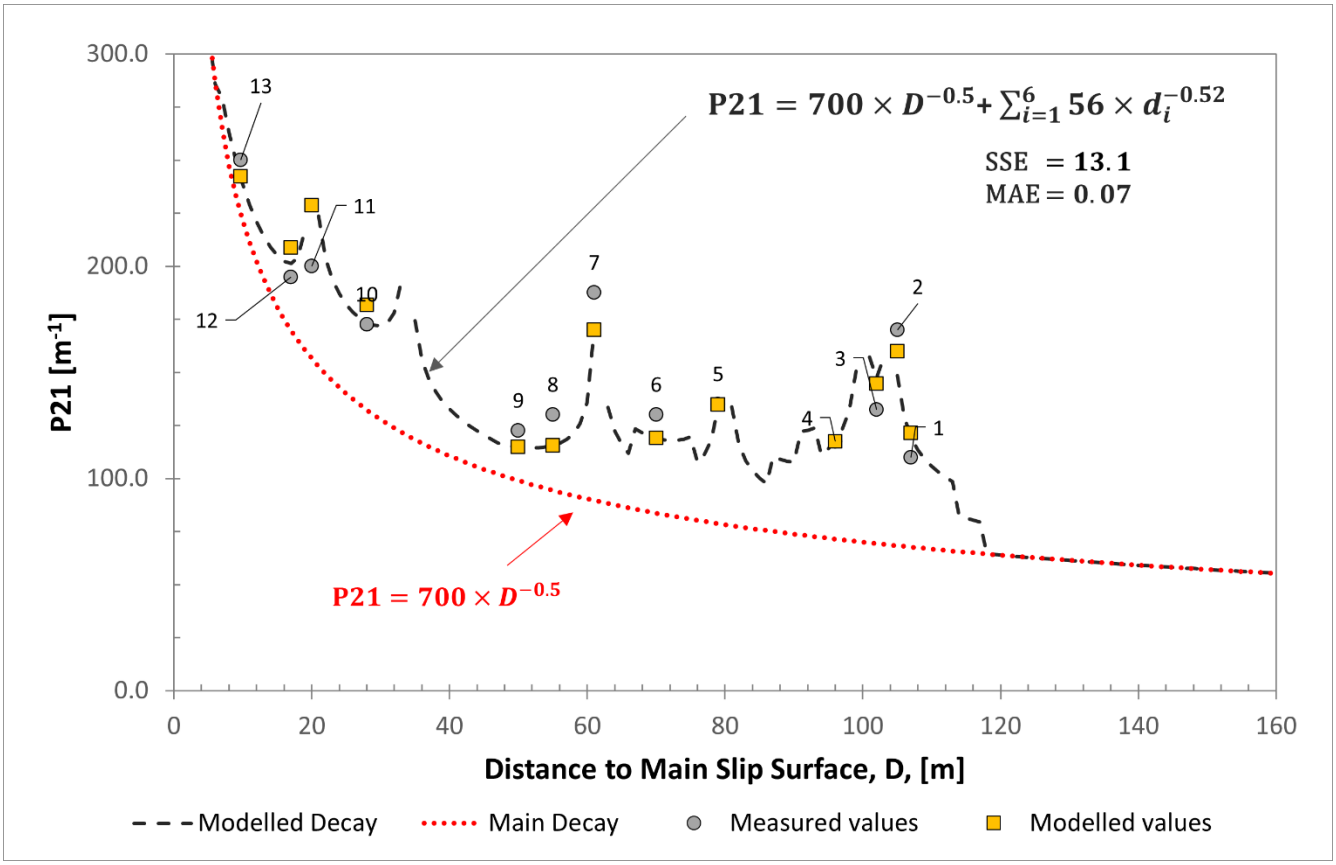

Fig 4.9. Decay of the fracture density P_{21} with respect to the distance to the MSS (D) and the distance to subsidiary n structures (d_i) modelled as a superposition of power law functions corresponding to 1st and 2nd order faults. Labels correspond to CSL number. SSE: Standard square error, MAE: Mean Absolute Error.

4.4.2. Petrophysical properties

The calculated fracture porosity (Φ_{CSL}) and the equivalent fracture permeability (k_e) are summarized in Table 4.1 and Figure 4.10. In general, across the VF-DZ both fracture porosity and permeability values show a decreasing trend away from the MSS, which is consistent with the reported fracture intensity decay. The fracture permeability derived from field CSL measurements shows median values ranging from $1.1E^{-12}$ to $5.8E^{-15}$ m^2. The range of variability at each CSL station is comprised between 1 and 2 orders of magnitude, considering the first and third quartile values of the permeability distribution, respectively (Fig. 4.10). Generally, the calculated values of permeability are in agreement with the values of fracture porosity documented for the fracture domains. However, in proximity of the 2nd order faults (CSL #2, #7, #12), the calculated values of fracture permeability are up to 3

orders of magnitude lower than the surrounding rock, regardless of the estimated high fracture porosity values (Fig. 4.10).

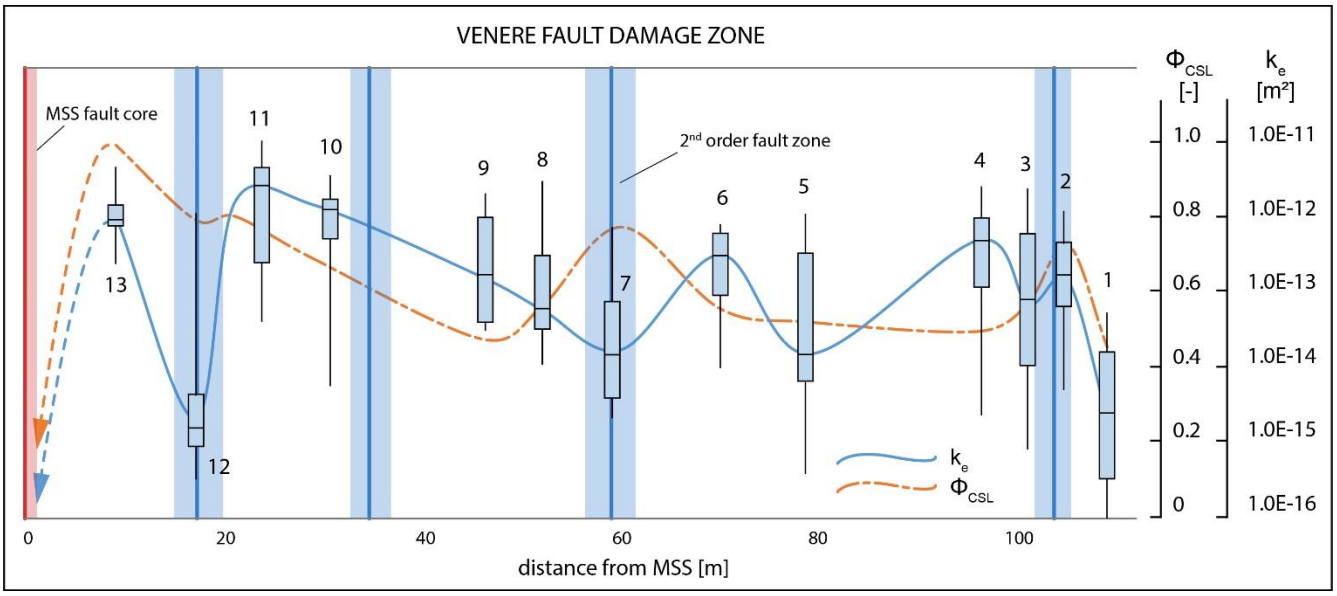

Fig 4.10. Petrophysical properties measured on the CSL stations across the VF-DZ (Labels correspond to CSL number). ΦCSL is fracture porosity normalized with respect to the maximum value. Thus, the ΦCSL trend is independent of the applied aspect E/l ratio. ke is shown by a box (limited by the 1st and 3rd quartile) and whisker plot in logarithmic scale, to illustrate the high variability of fracture permeability across the damage zone. Red line is the location of the MSS, and blue lines are the locations of the 2nd order faults.

The Φ_{CSL} values [%] are strongly dependent on the assumed fracture aspect ratio (*E/l*). The high-end member ($\Phi_{CSL}1$), *E/l* = 0.01, gives as a result an average mechanical aperture, *E*, of 0.2 mm with Φ_{CSL} values ranging from 2.2 to 4.9 %. On the other hand, the low-end member ($\Phi_{CSL}3$), *E/l* = 0.001, gives as a result an average mechanical aperture, *E*, of 0.02 mm with Φ_{CSL} values not exceeding 1%. The combined analysis of fracture density/intensity and fracture porosity is therefore key to assess the three main fracture domains (FD, Fig. 4.8b). We also compare the values obtained for these domains with those after the most conservative case, *E/l* = 0.005, which are hence used as a reference. The first fracture domain (Φ_f > 2.1%) corresponds to the fragmented carbonates, which are

present close to the MSS (< 20 m from the MSS, western wall of the quarry). The second domain is highly fractured (Φ_f = 1.6-2.20 %), and corresponds to rock volumes located 20 to 40 m away from the MSS. The third domain is moderately fractured (Φ_f = 1.1-1.6 %) and is present > 40 m away from the MSS and 5-to-20 m away from the 2nd order faults. This domain includes all meso-scale fault-related fractures and those associated to the 3rd order faults (Fig. 4.8c).

Table 4.1. Detailed data derived at the CSL stations.

CSL ID	P_{20} [m^{-2}]	P_{21} [m^{-1}]	l [cm]	$\Phi_{CSL}1$ [%]	$\Phi_{CSL}2$ [%]	$\Phi_{CSL}3$ [%]	k_e [m^2]
1	5.4E+03	112.5	2.0	2.24	1.12	0.22	5.83E-15
2	7.3E+03	170	2.3	3.57	1.78	0.36	3.18E-13
3	5.6E+03	132.5	2.4	2.80	1.40	0.28	7.71E-14
4	5.0E+03	115	2.4	2.44	1.22	0.24	5.41E-13
5	8.5E+03	137.5	1.6	2.56	1.28	0.26	1.65E-14
6	5.8E+03	132.5	2.3	2.73	1.37	0.27	9.17E-13
7	9.0E+03	187.5	2.1	3.79	1.90	0.38	1.89E-14
8	5.8E+03	135	2.3	2.77	1.38	0.28	7.53E-14
9	6.6E+03	117.5	1.8	2.34	1.17	0.23	2.85E-13
10	9.3E+03	172.5	1.9	3.38	1.69	0.34	1.59E-12
11	9.6E+03	190	2.0	3.93	1.97	0.39	1.75E-12
12	8.9E+03	185	2.1	3.89	1.94	0.39	2.3E-15
13	1.9E+04	265	1.6	4.85	2.43	0.49	1.11E-12

Notes: P_{20} = fracture density; P_{21}= fracture intensity; l = mean fracture length; $\Phi_{CSL}1$, $\Phi_{CSL}2$ and $\Phi_{CSL}3$ = fracture porosities from CSL analysis with E/l = 0.01, 0.005 and 0.001, respectively; k_e = median value of fracture permeability (Eq. 6).

4.4.3. Petrophysical and seismic velocity model

Since the amount of fracture porosity is modelled as function of distance from 1st and 2nd order faults (Fig. 4.11), we include the three FDs (respectively fragmented, highly fractured, and moderately fractured carbonates) in the 2D base model. In addition, far (≈ 130 m) from the MSS, the modelled fracture intensity and porosity are lower than the values reported from the CSL analyses within the VF-DZ (Figs. 4.8 and 4.9). Therefore, we added

a new fracture domain called weakly fractured carbonates, which is associated to the host rock of the VF zone. In this domain, the values of fracture intensity are almost stable (coefficient of variation < 0.5%) and the fracture porosity (for *E/l* = 0.005) is ~ 0.7%.

Both the calculated density and seismic velocity should mimic the values of fracture porosity because they are derived from this parameter. However, as explained in section 3.2.3, the seismic velocities have a more complex relationship with the fracture porosity (Kumar and Han, 2005). The calculated porosity, density, P-wave velocity, and the resultant reflectivity model of the GM2 fault zone model is shown in Figure 4.11, and in tabulated format in Table 4.2.

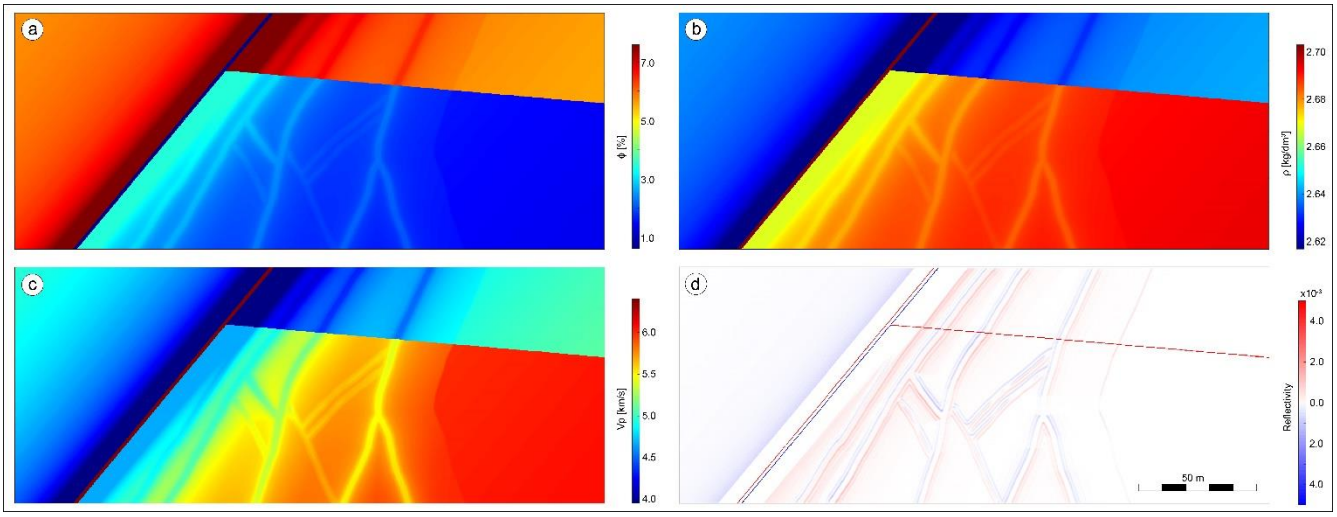

Fig 4.11. a) Porosity (φ), b) Bulk density (ρ), and c) P-wave velocity (Vp) of the GM2 base model, assuming an E/l ratio = 0.005.

Table 4.2 Summary of the modelled petrophysical and seismic velocity properties of the main fracture domains within the Venere fault zone.

Fracture Domain		φ [%]			Vp [km/s]			Vs [km/s]			ρ [g/cc]		
	E/l	0.010	**0.005**	0.001	0.010	**0.005**	0.001	0.010	**0.005**	0.001	0.010	**0.005**	0.001
φ_m = 0.8 %													
Fragmented		6.20	**3.50**	1.34	3.45	**4.67**	6.07	1.81	**2.46**	3.20	2.63	**2.67**	2.69
Highly Fracture		5.20	**3.00**	1.24	3.87	**4.92**	6.12	2.04	**2.59**	3.22	2.65	**2.67**	2.69
Moderately Fractured		4.00	**2.40**	1.12	4.43	**5.32**	6.19	2.33	**2.80**	3.26	2.66	**2.68**	2.70
Weakly Fractured		3.00	**1.90**	1.02	4.92	**5.69**	6.29	2.59	**3.00**	3.31	2.67	**2.69**	2.70
		1.90	**1.35**	0.91	5.69	**6.07**	6.27	3.00	**3.19**	3.30	2.69	**2.69**	2.70
φ_m = 5.0 %													
Fragmented		10.40	**7.70**	5.54	3.02	**3.96**	5.15	1.59	**2.08**	2.71	2.58	**2.62**	2.64
Highly Fracture		9.40	**7.20**	5.44	3.29	**4.19**	5.23	1.73	**2.21**	2.75	2.60	**2.62**	2.64
Moderately Fractured		8.20	**6.60**	5.32	3.74	**4.47**	5.32	1.97	**2.36**	2.80	2.61	**2.63**	2.65
Weakly Fractured		7.20	**6.10**	5.22	4.19	**4.74**	5.40	2.21	**2.50**	2.84	2.62	**2.64**	2.65
		6.10	**5.55**	5.11	4.74	**5.14**	5.49	2.50	**2.71**	2.89	2.64	**2.64**	2.65
Fault core			**0.60**			**6.43**			**3.22**			**2.64**	

Note: Matrix porosity= 0.8% and fault core porosity = 0.6% according to Agosta et al. (2007). A second case considers a matrix porosity =5.0%.

4.4.4. Seismic models

The geological and geophysical parameters adopted for the seismic modelling of the VF zone are summarized in section 3.3.1 (Fig. 4.5). The base model including the FDs distribution, fracture porosity and acoustic properties (Fig. 4.11a-c) was tested, and a sensitivity analysis was applied to evaluate the (PSDM) seismic signature of the VF-DZ.

4.4.4.1. Impact of geological parameters

To perform a sensitivity analysis based on different geological parameters, we use the 3 different geological models (GM1-3), which differ from each other in terms of surrounding lithologies (cf. Section 3.3.1, and fig. 4.5). In general, we observe that only the FDs characterized by a higher fracture porosity variation (fragmented carbonates, and highly fractured carbonates) are visible in the seismic image due to their higher impedance contrasts (Figs. 4.11 and 4.12). It is also clear that the area corresponding to the 2nd order fault farther from the MSS is not very visible. The internal architecture of the VF-DZ is imaged in more detail in model GM2 (Fig. 4.12b). Differently, in model GM1 the higher matrix porosity of the surrounding rocks provides a stronger reflector. Its seismic response masks the weaker reflection related to the reflector near the MSS, which corresponds to the interface between the fragmented and highly fractured carbonates in the vicinity of the 2nd order fault closest to the MSS (Fig. 4.12a). This effect is more pronounced in model GM3 (Fig. 4.12c) due to an even higher impedance contrast as result of the overlying shales.

The fracture mechanical aperture, which is controlled by the fracture aspect ratio E/l, significantly affects the imaging of the FDs within the VF-DZ. In the first scenario (high values of fracture aperture, E/l = 0.01), the details of the internal architecture of the damage zone are highlighted by relatively high amplitude reflectors that are stronger in the GM2 model, and weaker in the GM1 and GM3 models (Figs. 4.12a, b, and c). In the second scenario (intermediate values of fracture aperture, E/l = 0.005), the FDs' location and geometry are still recognizable from lower amplitude reflectors in all three GM models, although some details are lost (Figs. 4.12d, e, and f). Finally, in the third scenario (lowest fracture aperture, E/l = 0.001), the FDs are not observable in any of the GM models (Figs. 4.12g, h, and i).

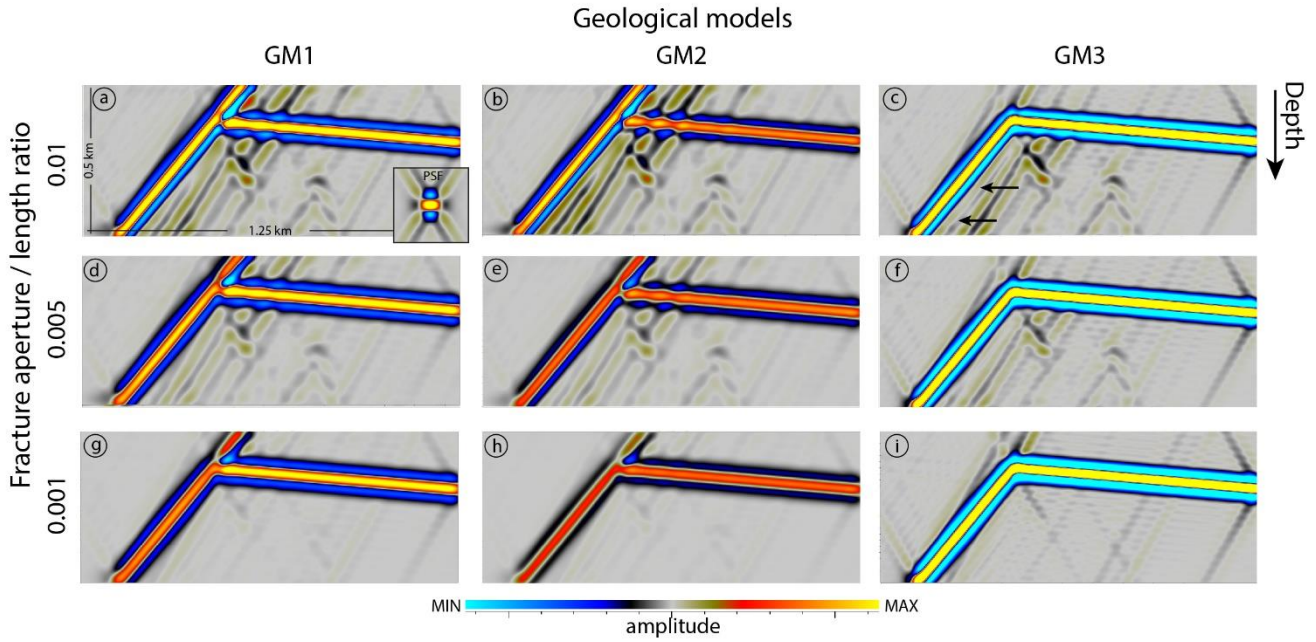

Fig 4.12. Seismic signature of the VF-DZ for three different geological models (GM1 to GM3) and fracture aspect ratios (E/l = 0.01, 0.005 and 0.001). (a, d, g) GM1 model, hanging wall and footwall overlying carbonates with 10% matrix porosity, (b, e, h) GM2 model, hanging wall and footwall overlying carbonates with 5% matrix porosity, (c, f, i) GM3 model, hanging wall and footwall overlying shales. In all simulations, we use a 30 Hz dominant frequency and 60° illumination angle. The inset in (a) shows the PSF. The black arrows on c indicate the area with missing reflectors, masked by the seismic response of a stronger reflector related to the surrounding lithology.

4.4.4.2. Effect of geophysical conditions

The aim of this section is to investigate the seismic signature of the VF-DZ by varying the maximum angle of illumination for dominant wavelet frequencies of 20, 30 and 40 Hz. We include only the results for the GM2 model and E/l = 0.005. The maximum illumination angles applied in this study are 45°, 60°, and 90°, which are respectively considered as intermediate (corresponding to a standard seismic illumination), high, and perfect illuminations with the latter being in practice not attainable. The VF-DZ shows a great variation in seismic signature as the maximum illumination angle varies (Fig. 4.13). As expected, at perfect illumination (90°) the seismic signature of the VF-DZ shows illumination of the FDs related to the 2nd order faults (Figs. 4.13c, f, and

i). At high illumination angle (60°), some details of the VF-DZ inner architecture re lost due to the lack of illumination of reflecting structures steeper than 60°. However, the FDs are still detectable on the seismic image, and can be partially interpreted (Figs. 4.13b, e, and h). On the contrary, the seismic sections modeled with a 45° maximum illumination angle do not show the MSS, and the FDs are only present as discontinuous/vanishing reflectors, resulting in seismic disturbance zones inherited by segments of antithetic structures with lower dip angle (Figs. 4.13a, d, and g). The decreasing dominant wavelet frequency clearly impacts the seismic image. This is particularly evident in the lowest frequency case (20 Hz, Figs. 4.13g, h, and i), where most details are lost resulting in a blurred seismic image of the VF-DZ.

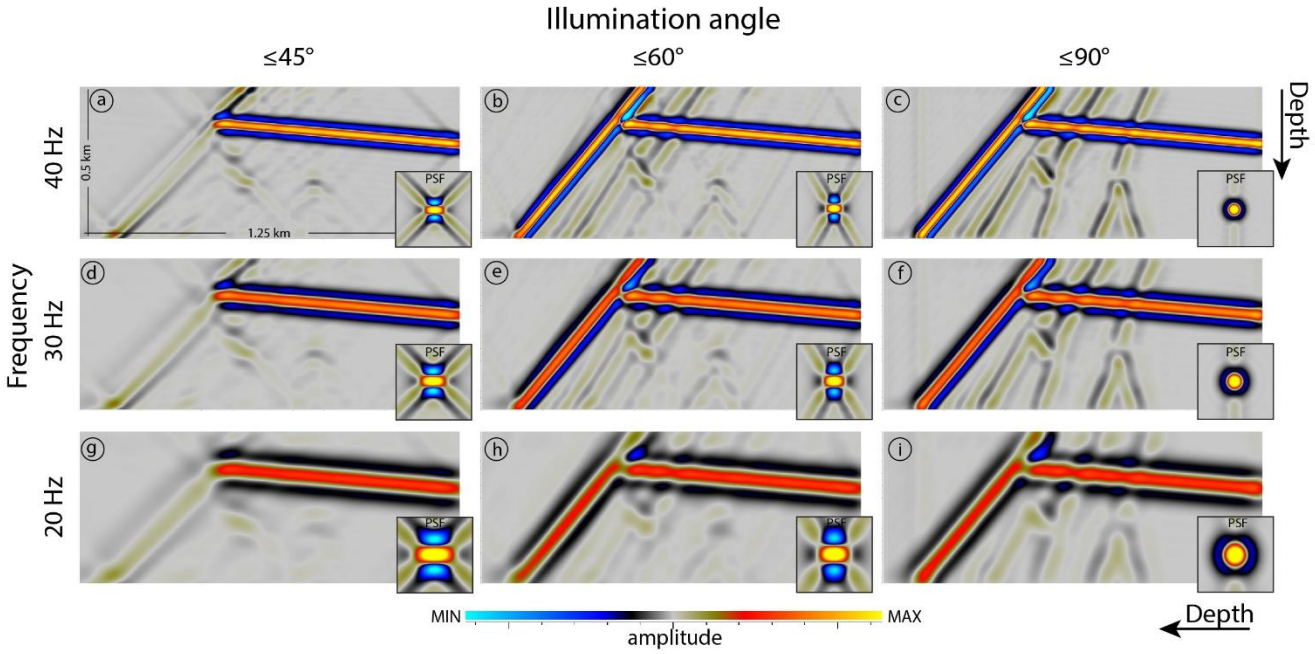

Fig 4.13. Seismic signature of the VF-DZ for different illumination angles (45, 60 and 90°, left to right) and dominant wavelet frequencies (40, 30 and 20 Hz, top to bottom). The PSFs (insets) indicate the vertical and horizontal resolution of the seismic image. For this set of simulations, we used the middle-member case GM2 and E/l = 0.005.

4.5. Discussion

4.5.1. Fault damage zone architecture

The integration of observations and measurements on the outcrop and the DOMs allow us to obtain an accurate representation of the main structural complexity of the VF-DZ, specifically of both attitude and distribution of subsidiary faults. In agreement with Agosta & Aydin (2006), the MSS shows almost pure dip-slip kinematics, and minor right-lateral slip. The 2nd order faults are subparallel, and mainly synthetic to the MSS. Differently, the 3rd order faults show greater attitude variation, and cluster along the eastern wall close to the southern tip of the VF. Such a clustering is interpreted as due to along-strike kinematics variations associated to the processes of fault lateral growth by segment linkage, as similarly documented for carbonate fault damage zones exposed at the northern edge of the Fucino Basin (Mercuri et al., 2020, and references therein).

The results of CSL analyses are employed to calculate the main fracture parameters such fracture density, P20, and intensity, P21. Such a procedure is relatively quicker than traditional linear scanlines performed in carbonate fault damage zones (Panza et al., 2016; Zambrano et al., 2016; Giuffrida et al., 2019, 2020; Volatili et al., 2019), and permits to assess the possible effects of fault growth by segment linkage (Cowie and Shipton, 1998; Soliva and Benedicto, 2004) on fracture abundance across the fault damage zone. We computed a power law decay of fracture intensity from the MSS (cf. Fig. 4.9) within the VF-DZ, which is consistent with the nucleation regime proposed by Cowie et al. (1993) based on 2D fracture density values. Such a decay is quite similar to the logarithmic decay of fracture frequency documented for carbonate damage zones by Mayolle et al. (2019). In fact, the latter authors not only found a very similar multiscale fracture-distance relation, but also documented the presence of additional smaller secondary peaks of fracture frequency due to the effects of secondary faults on fracture distribution.

4.5.2. Petrophysical properties

Previous studies on permeability distribution in carbonate fault damage zones based on different methods such as discrete fracture network modelling (Panza et al., 2018; Volatili et al. 2019, Romano et al 2020, Smeraglia et

al., 2021), in-situ measurements (Antonellini et al., 2014, Tondi et at., 2016; Riegel et al., 2019), laboratory tests of plugs derived from hand specimens (Bauer et al., 2016; Trippetta et al., 2017), and drill core samples and slug/injection tests (Westphal et al., 2004; Gabay et al., 2014) described a permeability range comprised between 10^{-16} and 10^{-11} m^2. We show that the median values calculated in this work for fracture permeability vary from 10^{-15} to 10^{-12} m^2 across the VF-DZ (Fig.4.10). These values lie within the range above, and also highlight that the decreasing trend of the petrophysical properties moving away from the MSS present some divergencies near the 2nd order faults. This divergence is also shown in the fracture porosity-permeability cross plot (Fig. 4.14). There, we document a power-law, poro-perm best-fit line of data gathered from CSL stations distant from the 2nd order faults (blue dots in Fig. 4.14), but not for the CSL stations near the 2nd order faults (orange squares in Fig. 4.14). This behavior is possibly linked to a variable fracture aspect ratio (*E/l*), and/or to greater carbonate dissolution and subsequent precipitation (healing), along the 2nd order faults (cf. Agosta & Aydin, 2006). We note that Riegel et al (2019) also proposed that interconnected fracture networks may facilitate the cementation process in fault damage zones. We note that an unevenly distribution of fault healing due to the coexistence of healed and opened fractures is predicted for active fault zones (Mizoguchi & Ueta, 2013).

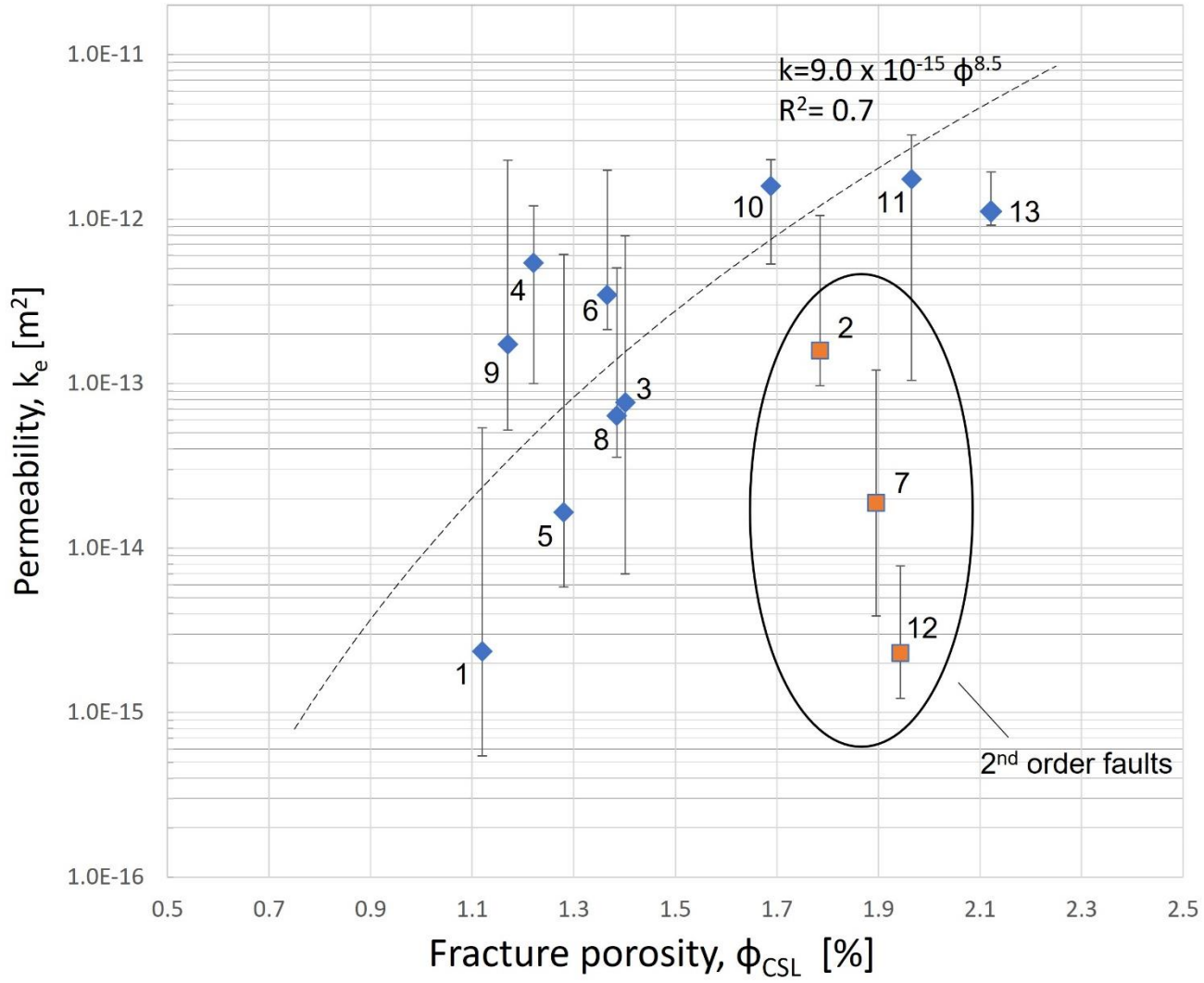

Fig. 4.14. Fracture porosity-permeability relationship. Labels correspond to CSL number. The dashed line corresponds to the power-law best-fit line of the CSL stations not affected by 2nd order faults (blue dots). The orange squares are stations on the 2nd order faults. The error bars stand for the first and third quartile of the equivalent permeability (ke). ΦCSL here referred to 0.005 E/l aspect ratio for reference.

4.5.3. Seismic modelling

Several studies documented the benefit of using field-based geological models as input data for seismic modeling (i.e., Rabbel et al., 2018; Grippa et al., 2019; Wrona et al., 2020). This procedure was proposed to unravel the seismic response of complex stratigraphy and structural heterogeneities. Some works used digital outcrop models for seismic modelling (Anell et al., 2016; Lubrano-Lavadera et al., 2018). In this contribution, we

document that the use of an integrated field- and digital-based model of the VF-DZ allows the investigation of the seismic signature of a complex fault architecture by considering various geological and geophysical parameters. In fact, despite the lack of model constraints such as well data, survey geometry, and background velocity model, the versatility offered by the PSF-based convolution modelling technique allows us to perform a sensitivity analysis of the (PSDM) seismic signature of the VF zone.

According to the results, the first set of simulations (cf. Fig. 4.12) shows a slight obliteration of the internal architecture of the VF-DZ by the masking effect of the strong and regular reflectors in the GM1 to GM3. This means that the surrounding lithology does not significantly affect the seismic VF-DZ imaging. Conversely, the fracture mechanical aperture seems to be a crucial parameter. In fact, the sensitivity analysis based on the fracture aspect ratio (E/l) demonstrates that the fault architecture is not imaged in the low-end case (E/l = 0.001), thus suggesting that if fracture porosity is below 1%, due to very small average fracture aperture (few microns), their FDs would not give high enough impedance contrasts to be imaged on seismic.

The second set of simulations investigating the effect of geophysical parameters (cf. Fig. 4.13), identify the 30 Hz dominant frequency as the lowest frequency required to image the internal architecture of the VF-DZ, without losing details depicting the FDs. However, since the model of the fault zone was enlarged five times to simulate reasonable dominant frequencies commonly observed in conventional seismic at km depth (i.e., 20, 30, and 40 Hz), this means that a much higher frequency (100-160 Hz) is required to image the fault zone in its actual size, and shallower depth. Similarly, the illumination angle, which in an actual seismic survey is determined by the background velocity model and a given survey geometry, shows how the steepest features (i.e., MSS and 2nd order faults) are barely imaged by angles below 45° (Fig. 4.13a, d, g). Therefore, at standard or low illumination angles (and larger depths), the fault would be only detected by the vertical offset of gently dipping reflectors.

4.5. Conclusions

We presented a multidisciplinary integrated characterization of a seismic scale (throw ≈ 300 m) normal fault zone, the Venere Fault (VF), which cuts across Upper Jurassic-Lower Cretaceous platform carbonates and bounds

the eastern side of the Fucino Basin (central Italy). The VF damage zone (VF-DZ) architecture was investigated in terms of fracture density/intensity distribution, and porosity/permeability. By combining field structural analysis with digital image analysis, in accordance with previous studies, the results highlight the profound control exerted by subsidiary faults on both fracture abundance and petrophysical properties. The field- and digital-based 2D model of the VF-DZ was then populated with elastic properties (i.e., Vp, Vs and density values) derived from the porosity of both the matrix and fracture components. The resultant model depicts subsidiary structures that impart heterogeneity to the fault zone. This model was the input to seismic modelling that allowed us to perform a sensitivity analysis according to various geological (surrounding lithology and fracture aperture) and geophysical parameters (wave frequency and illumination angle). To test the impact of a structure like the VF-DZ at km-depths and with standard seismic frequencies (~20-40 Hz) the model was enlarged 5 times. The main outcomes of this work are the following:

- Fracture abundance distribution does not decrease smoothly away from the main slip surface (MSS). We documented a power-law decay of 2D fracture intensity away from the MSS, consistent with a nucleation regime of the carbonate fault damage zone. Such a decay is profoundly affected by the occurrence of subsidiary faults.

- Both fracture porosity and permeability show a decreasing trend away from the MSS. However, they are also profoundly affected by subsidiary faults. In fact, the computed amounts of fracture porosity increase by a factor of 2-3, whereas permeability decreases down to 3 orders of magnitude.

- The most relevant geological parameter affecting the seismic signature of the VF-DZ is the fracture aperture, which decreases with overburden depth. When this parameter yields fracture porosity values below 1%, the internal architecture of the damage zone is not imaged on seismic. Higher impedance contrasts by different surrounding lithologies slightly conceal the reflectors close to the MSS, without drastically compromising the VF-DZ signal.

- High (100-160 Hz) frequencies are required to image the VF-DZ in its actual size. The same fault model enlarged five times, requires a minimum frequency of 30 Hz to be properly imaged. The

illumination angle strongly influences the seismic image. A realistic illumination angle of 45° still images the subsidiary structures within the VF-DZ but some details are lost.

The applied methodology is greatly adaptable to different geologic settings. Coupling petrophysical outcrop-based models with seismic modelling can therefore improve the seismic interpretation and characterization of fault zones. In particular, the variations of fracture abundance along subsidiary structures can be imaged on seismic data by using appropriate damage zone sizes, and both geological and geophysical parameters. This is of particular interest for reservoir characterization in carbonates, where the heterogeneity of fracture density/intensity given by subsidiary faults or fracture corridors play a crucial role on the fluid storage and migration properties of large-scale fault zones.

Acknowledgements

Data reported in this manuscript are part of the first author's PhD Thesis Dissertation. The core of the manuscript was written during an Erasmus visit of the first author to the University of Stavanger. Mr. Santilli is warmly thanked for letting us free access to the study quarry. Fabrizio Balsamo (University of Parma) is acknowledged for the portable air permeameter employed during outcrop analysis. Francesco Ferraro is also acknowledged for the help provided in the field during the first circular scanline measurements. Furthermore, we thank NORSAR Innovation for providing academic license of SeisRoX Pro 2019. This research was funded by the Reservoir Characterization Project (www.rechproject.com) and the FAR Unicam project "Novel Approach for Seismic Hazard Analysis—NoHard''.

References

Agosta, F., & Kirschner, D. L. (2003). Fluid conduits in carbonate-hosted seismogenic normal faults of central Italy. Journal of Geophysical Research: Solid Earth, 108(B4).

Agosta, Fabrizio, & Aydin, A. (2006). Architecture and deformation mechanism of a basin-bounding normal fault in Mesozoic platform carbonates, central Italy. *Journal of Structural Geology*, *28*(8), 1445–1467.

Agosta, F., Prasad, M., & Aydin, A. (2007). Physical properties of carbonate fault rocks, fucino basin (Central Italy): implications for fault seal in platform carbonates. Geofluids, 7(1), 19-32.

Agosta, F. (2008). Fluid flow properties of basin-bounding normal faults in platform carbonates, Fucino Basin, central Italy. Geological Society, London, Special Publications, 299(1), 277-291.

Anders, M. H., & Wiltschko, D. V. (1994). Microfracturing, paleostress and the growth of faults. *Journal of Structural Geology*. https://doi.org/10.1016/0191-8141(94)90146-5

Anell, I., Lecomte, I., Braathen, A., & Buckley, S. J. (2016). Synthetic seismic illumination of small-scale growth faults, paralic deposits and low-angle clinoforms: A case study of the Triassic successions on Edgeøya, NW Barents Shelf. *Marine and Petroleum Geology*. https://doi.org/10.1016/j.marpetgeo.2016.07.005

Antonellini, M., Cilona, A., Tondi, E., Zambrano, M., & Agosta, F. (2014). Fluid flow numerical experiments of faulted porous carbonates, Northwest Sicily (Italy). *Marine and Petroleum Geology*. https://doi.org/10.1016/j.marpetgeo.2013.12.003

Aydin, A. (2000). Fractures, faults, and hydrocarbon entrapment, migration and flow. *Marine and Petroleum Geology*. https://doi.org/10.1016/S0264-8172(00)00020-9

Balsamo, F., Storti, F., Salvini, F., Silva, A. T., & Lima, C. C. (2010). Structural and petrophysical evolution of extensional fault zones in low-porosity, poorly lithified sandstones of the Barreiras Formation, NE Brazil. Journal of Structural Geology. https://doi.org/10.1016/j.jsg.2009.10.010

Bauer, H., Schröckenfuchs, T. C., & Decker, K. (2016). Hydrogeological properties of fault zones in a karstified carbonate aquifer (Northern Calcareous Alps, Austria). Hydrogeology Journal, 24(5), 1147-1170.

Bigi, G., Cosentino, D., Parotto, M., Sartori, R., Scandone, P., 1992. Structural Model of Italy, scale 1:500, 000, 6 sheets. CNR, Quaderni di Ricerca Scientifica 114.

Boschi, E., Guidoboni, E., Ferrari, G., Valensise, G., 1997. Catalogo dei forti terremoti in Italia dal 461 A.C. al 1990. ING-SGA (Ed.), pp. 644.

Botter, C., Cardozo, N., Hardy, S., Lecomte, I., & Escalona, A. (2014). From mechanical modeling to seismic imaging of faults: A synthetic workflow to study the impact of faults on seismic. Marine and Petroleum Geology. https://doi.org/10.1016/j.marpetgeo.2014.05.013

Botter, C., Cardozo, N., Hardy, S., Lecomte, I., Paton, G., & Escalona, A. (2016). Seismic characterisation of fault damage in 3D using mechanical and seismic modelling. *Marine and Petroleum Geology*. https://doi.org/10.1016/j.marpetgeo.2016.08.002

Botter, C., Cardozo, N., Qu, D., Tveranger, J., & Kolyukhin, D. (2017). Seismic characterization of fault facies models. *Interpretation*. https://doi.org/10.1190/int-2016-0226.1

Bourbie, T., O. Coussy, B. Zinszner, and Miguel C. Junger (1992) Acoustics of Porous Media, The Journal of the Acoustical Society of America 91 , 3080-3080 (1992) https://doi.org/10.1121/1.402899

Caine, J. S., Evans, J. P., & Forster, C. B. (1996). Fault zone architecture and permeability structure. *Geology*. https://doi.org/10.1130/0091-7613(1996)024<1025:FZAAPS>2.3.CO;2

Cavinato, G. P., Carusi, C., Dall'asta, M., Miccadei, E., & Piacentini, T. (2002). Sedimentary and tectonic evolution of Plio-Pleistocene alluvial and lacustrine deposits of Fucino Basin (central Italy). *Sedimentary Geology*. https://doi.org/10.1016/S0037-0738(01)00209-3

Chopra, S., & Marfurt, K. J. (2009). Interpreting fractures through 3D seismic discontinuity attributes and their visualization. *CSEG Recorder*, *34*(8), 5–14.

Cohen, I., Coult, N., & Vassiliou, A. A. (2006). Detection and extraction of fault surfaces in 3D seismic data. Geophysics. https://doi.org/10.1190/1.2215357

Cowie, P. A., & Scholz, C. H. (1992). Growth of faults by accumulation of seismic slip. Journal of Geophysical Research: Solid Earth, 97(B7), 11085-11095.

Cowie, P. A., Vanneste, C., and Sornette, D. (1993), Statistical physics model for the spatiotemporal evolution of faults, J. Geophys. Res., 98(B12), 21809– 21821, doi:10.1029/93JB02223.

Cowie, P. A., & Shipton, Z. K. (1998). Fault tip displacement gradients and process zone dimensions. Journal of Structural Geology, 20(8), 983-997.

Cunningham, J., Cardozo, N., Townsend, C., Iacopini, D., & Waerum, G. O. (2019). Fault deformation, seismic amplitude and unsupervised fault facies analysis: Snøhvit Field, Barents Sea. Journal of Structural Geology, 118, 165-180.

Davatzes, N. C., & Aydin, A. (2003). Overprinting faulting mechanisms in high porosity sandstones of SE Utah. Journal of Structural Geology, 25(11), 1795-1813.

De Joussineau, G., & Aydin, A. (2007a). The evolution of the damage zone with fault growth in sandstone and its multiscale characteristics. Journal of Geophysical Research: Solid Earth, 112(B12).

De Joussineau, G., Mutlu, O., Aydin, A., & Pollard, D. (2007b). Characterization of fault-splay relationships: Field survey and mechanical modeling. Journal of Structural Geology, 29, 1831-1842.

Dutzer, J. F., Basford, H., & Purves, S. (2010). Investigating fault-sealing potential through fault relative seismic volume analysis. Petroleum Geology Conference Proceedings. https://doi.org/10.1144/0070509

Faulkner, D. R., Mitchell, T. M., Healy, D., & Heap, M. J. (2006). Slip on "weak" faults by the rotation of regional stress in the fracture damage zone. *Nature*. https://doi.org/10.1038/nature05353

Faulkner, D. R., Mitchell, T. M., Jensen, E., & Cembrano, J. (2011). Scaling of fault damage zones with displacement and the implications for fault growth processes. Journal of Geophysical Research: Solid Earth, 116(B5).

Faure Walker, J. P., Roberts, G. P., Sammonds, P. R., and Cowie, P. (2010), Comparison of earthquake strains over 102 and 104 year timescales: Insights into variability in the seismic cycle in the central Apennines, Italy, J. Geophys. Res., 115, B10418, doi:10.1029/2009JB006462.

Ferraro, F., Grieco, D. S., Agosta, F., & Prosser, G. (2018). Space-time evolution of cataclasis in carbonate fault zones. Journal of Structural Geology, 110, 45-64.

Ferraro, F., Agosta, F., Ukar, E., Grieco, D. S., Cavalcante, F., Belviso, C., & Prosser, G. (2019). Structural diagenesis of carbonate fault rocks exhumed from shallow crustal depths: An example from the central-southern Apennines, Italy. Journal of Structural Geology, 122, 58-80.

Ferraro, F., Agosta, F., Prasad, M., Vinciguerra, S., Violay, M., & Giorgioni, M. (2020). Pore space properties in carbonate fault rocks of peninsular Italy. *Journal of Structural Geology*. https://doi.org/10.1016/j.jsg.2019.103913

Filomena, C. M., Hornung, J., & Stollhofen, H. (2014). Assessing accuracy of gas-driven permeability measurements: A comparative study of diverse Hassler-cell and probe permeameter devices. Solid Earth. https://doi.org/10.5194/se-5-1-2014

Fossen, H., & Gabrielsen, R. H. (1996). Experimental modeling of extensional fault systems by use of plaster. Journal of structural geology, 18(5), 673-687.

Gabay, R., Eyal, S., Yoseph, Y., Amir, S., Noam, W., 2014. The permeability of fault zones: a case study of the Dead Sea rift (Middle East). Hydrogeol. J. 22, 425–440.

Galadini, F., Galli, P., 1999. The Holocene paleo-earthquakes on the 1915 Avezzano earthquake faults (central Italy): implications for active tectonics in the central Apennines. Tectonophysics 308, 143e170.

Ghanbarian, B., Perfect, E., & Liu, H. H. (2019). A geometrical aperture–width relationship for rock fractures. Fractals, 27(01), 1940002.

Ghisetti, F., Vezzani, L., (1999). Depth and modes of Pliocene-Pleistocene crustal extension of the Apennines (Italy). Terra Nova 11, 67e72.

Ghisetti F, Kirschner DL, Vezzani L, Agosta F (2001) Stable isotope evidence for contrasting paleofluid circulation in thrust and seismogenic normal faults of central Apennines, Italy. Journal of Geophysical Research, 106, 8811–25.

Ghisetti, F., & Vezzani, L. (2002). Normal faulting, extension and uplift in the outer thrust belt of the central Apennines (Italy): role of the Caramanico fault. Basin Research, 14(2), 225-236.

Giuffrida, A., Agosta, F., Rustichelli, A., Panza, E., La Bruna, V., Eriksson, M., Torrieri, S., & Giorgioni, M. (2020). Fracture stratigraphy and DFN modelling of tight carbonates, the case study of the Lower Cretaceous carbonates exposed at the Monte Alpi (Basilicata, Italy). *Marine and Petroleum Geology*. https://doi.org/10.1016/j.marpetgeo.2019.104045

Giuffrida, A., La Bruna, V., Castelluccio, P., Panza, E., Rustichelli, A., Tondi, E., Giorgioni, M., & Agosta, F. (2019). Fracture simulation parameters of fractured reservoirs: Analogy with outcropping carbonates of the Inner Apulian Platform, southern Italy. *Journal of Structural Geology*. https://doi.org/10.1016/j.jsg.2019.02.007

Grippa, A., Hurst, A., Palladino, G., Iacopini, D., Lecomte, I., & Huuse, M. (2019). Seismic imaging of complex geometry: Forward modeling of sandstone intrusions. *Earth and Planetary Science Letters*. https://doi.org/10.1016/j.epsl.2019.02.011

Gudmundsson, A., Berg, S. S., Lyslo, K. B., & Skurtveit, E. (2001). Fracture networks and fluid transport in active fault zones. *Journal of Structural Geology*. https://doi.org/10.1016/S0191-8141(00)00100-0

Iacopini, D., Butler, R. W. H., Purves, S., McArdle, N., & De Freslon, N. (2016). Exploring the seismic expression of fault zones in 3D seismic volumes. Journal of Structural Geology. https://doi.org/10.1016/j.jsg.2016.05.005

James, M. R., & Robson, S. (2012). Straightforward reconstruction of 3D surfaces and topography with a camera: Accuracy and geoscience application. Journal of Geophysical Research: Earth Surface, 117(F3).

Johri, M., Zoback, M. D., & Hennings, P. (2014). A scaling law to characterize fault-damage zones at reservoir depths. AAPG Bulletin, 98(10), 2057-2079.

Klimczak, C., Schultz, R. A., Parashar, R., & Reeves, D. M. (2010). Cubic law with aperture-length correlation: implications for network scale fluid flow. Hydrogeology Journal, 18(4), 851-862.

Kumar, M., & Han, D. H. (2005). Pore shape effect on elastic properties of carbonate rocks. In SEG Technical Program Expanded Abstracts 2005 (pp. 1477-1480). Society of Exploration Geophysicists.

Lanari, R., Faccenna, C., Benedetti, L., Sembroni, A., Bellier, O., Menichelli, I., et al. (2021). Formation and persistence of extensional internally drained basins: The case of the Fucino basin (Central Apennines, Italy). Tectonics, 40, e2020TC006442. https://doi.org/10.1029/2020TC006442

Lasdon, L. S., Fox, R. L., & Ratner, M. W. (1974). Nonlinear optimization using the generalized reduced gradient method. Revue française d'automatique, informatique, recherche opérationnelle. Recherche opérationnelle, 8(V3), 73-103.

Lecomte, I. (2008). Resolution and illumination analyses in PSDM: A ray-based approach. *Leading Edge (Tulsa, OK)*. https://doi.org/10.1190/1.2919584

Lecomte, I., & Kaschwich, T. (2018). Closer to real earth in reservoir characterization: A 3D isotropic/anisotropic PSDM simulator. *78th Society of Exploration Geophysicists International Exposition and Annual Meeting, SEG 2008*.

Lecomte, I., Lavadera, P. L., Anell, I., Buckley, S. J., Schmid, D. W., & Heeremans, M. (2015). Ray-based seismic modeling of geologic models: Understanding and analyzing seismic images efficiently. *Interpretation*. https://doi.org/10.1190/INT-2015-0061.1

Lecomte, I., Lavadera, P. L., Botter, C., Anell, I., Buckley, S. J., Eide, C. H., Grippa, A., Mascolo, V., & Kjoberg, S. (2016). 2(3)D convolution modelling of complex geological targets beyond – 1D convolution. *First Break*.

Li, F., Zhao, T., Lin, T., & Marfurt, K. J. (2015). Fracture characterization based on attenuation estimation from seismic reflection data using well-log-based localized spectral correction. *Society of Petroleum Engineers - Unconventional Resources Technology Conference, URTeC 2015*. https://doi.org/10.2118/178529-ms

Liao, Z., Liu, H., Carpenter, B. M., Marfurt, K. J., & Reches, Z. (2019). Analysis of fault damage zones using three-dimensional seismic coherence in the Anadarko Basin, Oklahoma. *AAPG Bulletin*. https://doi.org/10.1306/1219181413417207

Lubrano-Lavadera, P., Senger, K., Lecomte, I., Mulrooney, M. J., & Kühn, D. (2019). Seismic modelling of metre-scale normal faults at a reservoir-cap rock interface in central spitsbergen, svalbard: Implications for Co2 storage. *Norsk Geologisk Tidsskrift*. https://doi.org/10.17850/njg003

Mauldon, M., Dunne, W. M., & Rohrbaugh, M. B. (2001). Circular scanlines and circular windows: New tools for characterizing the geometry of fracture traces. *Journal of Structural Geology*. https://doi.org/10.1016/S0191-8141(00)00094-8

Mayolle, S., Soliva, R., Caniven, Y., Wibberley, C., Ballas, G., Dominguez, S., & Milési, G. (2019, September). Scaling of Fault Damage Zones and Implications for Naturally Fractured Reservoirs. In Fifth International Conference on Fault and Top Seals (Vol. 2019, No. 1, pp. 1-5). European Association of Geoscientists & Engineers.

Mayolle, S., Soliva, R., Dominguez, S., Wibberley, C., & Caniven, Y. (2021). Nonlinear fault damage zone scaling revealed through analog modeling. Geology.

Mendez, J. N., Jin, Q., Gonzalez, M., Zhang, X., Lobo, C., Boateng, C. D., & Zambrano, M. (2020). Fracture characterization and modeling of karsted carbonate reservoirs: A case study in Tahe oilfield, Tarim Basin (western China). Marine and Petroleum Geology, 112, 104104.

Mercuri, M., McCaffrey, K. J. W., Smeraglia, L., Mazzanti, P., Collettini, C., & Carminati, E. (2020). Complex geometry and kinematics of subsidiary faults within a carbonate-hosted relay ramp. *Journal of Structural Geology*. https://doi.org/10.1016/j.jsg.2019.103915

Merico, A., Iezzi, G., Pace, B., Ferranti, L., Cremona, M., Scafa, M., ... & Scarlato, P. (2020). Grain size and grain size distribution of a lithified fault core in carbonates rocks using multi-scale image analysis: The example of the San Benedetto-Gioia dei Marsi fault (Central Italy). Journal of Structural Geology, 134, 104017.

Michelena, R. J., Godbey, K. S., Wang, H., Oilman, J. R., & Zahm, C. K. (2013). Estimation of dispersion in orientations of natural fractures from seismic data: Application to DFN modeling and flow simulation. *Leading Edge*. https://doi.org/10.1190/tle32121502.1

Michetti, A. M., Brunamonte, F., Serva, L., & Vittori, E. (1996). Trench investigations of the 1915 Fucino earthquake fault scarps (Abruzzo, Central Italy): geological evidence of large historical events. Journal of Geophysical Research: Solid Earth, 101(B3), 5921-5936.

Miller, S. L. (1992). Well log analysis of Vp and Vs in carbonates. Consurtium for Research in Elastic Wave Exploration Seismology (CREWES) Research Report, 4, 1-12.

Mitchell, T. M., & Faulkner, D. R. (2009). The nature and origin of off-fault damage surrounding strike-slip fault zones with a wide range of displacements: A field study from the Atacama fault system, northern Chile. *Journal of Structural Geology*. https://doi.org/10.1016/j.jsg.2009.05.002

Mizoguchi, K., & Ueta, K. (2013). Microfractures within the fault damage zone record the history of fault activity. Geophysical Research Letters, 40(10), 2023-2027.

Myers, R., & Aydin, A. (2004). The evolution of faults formed by shearing across joint zones in sandstone. Journal of Structural Geology, 26(5), 947-966.

Panza, E., Agosta, F., Rustichelli, A., Zambrano, M., Tondi, E., Prosser, G., ... & Janiseck, J. M. (2016). Fracture stratigraphy and fluid flow properties of shallow-water, tight carbonates: the case study of the Murge Plateau (southern Italy). Marine and Petroleum Geology, 73, 350-370.

Panza, E., Agosta, F., Rustichelli, A., Vinciguerra, S. C., Ougier-Simonin, A., Dobbs, M., & Prosser, G. (2019). Meso-to-microscale fracture porosity in tight limestones, results of an integrated field and laboratory study. *Marine and Petroleum Geology*. https://doi.org/10.1016/j.marpetgeo.2019.01.043

Panza, Elisa, Sessa, E., Agosta, F., & Giorgioni, M. (2018). Discrete Fracture Network modelling of a hydrocarbon-bearing, oblique-slip fault zone: Inferences on fault-controlled fluid storage and migration properties of carbonate fault damage zones. *Marine and Petroleum Geology*. https://doi.org/10.1016/j.marpetgeo.2017.09.009

Piccardi L, Gaudemer Y, Tapponnier P, Boccaletti M (1999) Active oblique extension in the central Apennines (Italy); evidence from the Fucino region. Geophysical Journal International, 2, 499–530.

Pitts, A. D., Casciano, C. I., Patacci, M., Longhitano, S. G., Di Celma, C., & McCaffrey, W. D. (2017). Integrating traditional field methods with emerging digital techniques for enhanced outcrop analysis of deep water channel-fill deposits. *Marine and Petroleum Geology*. https://doi.org/10.1016/j.marpetgeo.2017.05.001

Rabbel, O., Galland, O., Mair, K., Lecomte, I., Senger, K., Spacapan, J. B., & Manceda, R. (2018). From field analogues to realistic seismic modelling: A case study of an oil-producing andesitic sill complex in the Neuquén Basin, Argentina. *Journal of the Geological Society*. https://doi.org/10.1144/jgs2017-116

Riegel, H., Zambrano, M., Balsamo, F., Mattioni, L., & Tondi, E. (2019). Petrophysical properties and microstructural analysis of faulted heterolithic packages: A case study from Miocene turbidite successions, Italy. Geofluids. https://doi.org/10.1155/2019/9582359

Roberts, G. P., & Michetti, A. M. (2004). Spatial and temporal variations in growth rates along active normal fault systems: an example from The Lazio–Abruzzo Apennines, central Italy. Journal of Structural Geology, 26(2), 339-376.

Rohrbaugh, J. B., Dunne, W. M., & Mauldon, M. (2002). Estimating fracture trace intensity, density, and mean length using circular scan lines and windows. *AAPG Bulletin*. https://doi.org/10.1306/61eede0e-173e-11d7-8645000102c1865d

Romano, V., Bigi, S., Carnevale, F., De'Haven Hyman, J., Karra, S., Valocchi, A. J., Tartarello, M. C., & Battaglia, M. (2020). Hydraulic characterization of a fault zone from fracture distribution. *Journal of Structural Geology*. https://doi.org/10.1016/j.jsg.2020.104036

Rotevatn, A., Fossen, H., Hesthammer, J., Aas, T. E., & Howell, J. A. (2007). Are relay ramps conduits for fluid flow? Structural analysis of a relay ramp in Arches National Park, Utah. *Geological Society Special Publication*. https://doi.org/10.1144/GSL.SP.2007.270.01.04

Sagy, A., Reches, Z. E., & Roman, I. (2001). Dynamic fracturing: Field and experimental observations. Journal of Structural Geology, 23(8), 1223-1239.

Savage, H. M., & Brodsky, E. E. (2011). Collateral damage: Evolution with displacement of fracture distribution and secondary fault strands in fault damage zones. *Journal of Geophysical Research: Solid Earth*. https://doi.org/10.1029/2010JB007665

Scholz, C. H. (2019). The mechanics of earthquakes and faulting. Cambridge university press.

Scibek, J. (2020). Multidisciplinary database of permeability of fault zones and surrounding protolith rocks at world-wide sites. Scientific data, 7(1), 1-14.

Shipton, Z. K., & Cowie, P. A. (2003). A conceptual model for the origin of fault damage zone structures in high-porosity sandstone. Journal of Structural Geology. https://doi.org/10.1016/S0191-8141(02)00037-8

Smeraglia, L., Mercuri, M., Tavani, S., Pignalosa, A., Kettermann, M., Billi, A., & Carminati, E. (2021). 3D Discrete Fracture Network (DFN) models of damage zone fluid corridors within a reservoir-scale normal fault in carbonates: Multiscale approach using field data and UAV imagery. Marine and Petroleum Geology, 126, 104902.

Snow, D. T. (1969). Anisotropie permeability of fractured media. Water resources research, 5(6), 1273-1289.

Soliva, R., & Benedicto, A. (2004). A linkage criterion for segmented normal faults. Journal of Structural Geology, 26(12), 2251-2267.

Thiele, S. T., Grose, L., Samsu, A., Micklethwaite, S., Vollgger, S. A., & Cruden, A. R. (2017). Rapid, semi-automatic fracture and contact mapping for point clouds, images and geophysical data. *Solid Earth*. https://doi.org/10.5194/se-8-1241-2017

Tondi, E., Rustichelli, A., Cilona, A., Balsamo, F., Storti, F., Napoli, G., Agosta, F., Renda, P., & Giorgioni, M. (2016). Hydraulic properties of fault zones in porous carbonates, examples from central and southern Italy. Italian Journal of Geosciences. https://doi.org/10.3301/IJG.2015.08

Torabi, A., Ellingsen, T. S. S., Johannessen, M. U., Alaei, B., Rotevatn, A., & Chiarella, D. (2020). Fault zone architecture and its scaling laws: where does the damage zone start and stop?. Geological Society, London, Special Publications, 496(1), 99-124.

Trippetta, F., Carpenter, B.M., Mollo, S., Scuderi, M.M., Scarlato, P., Collettini, C., (2017).Physical and transport property variations within carbonate-bearing fault zones: insights from the Monte Maggio Fault (Central Italy). G-cubed 18 (11), 4027–4042

Vezzani L, Ghisetti F (1998) Carta geologica dell'Abruzzo. S.EL.CA., Firenze.

Vezzani, L., Festa, A., & Ghisetti, F. C. (2010). Geology and tectonic evolution of the Central-Southern Apennines, Italy (Vol. 469). Geological Society of America.

Volatili, T., Zambrano, M., Cilona, A., Huisman, B. A. H., Rustichelli, A., Giorgioni, M., Vittori, S., & Tondi, E. (2019). From fracture analysis to flow simulations in fractured carbonates: The case study of the Roman Valley Quarry (Majella Mountain, Italy). *Marine and Petroleum Geology*, *100*(July 2018), 95–110. https://doi.org/10.1016/j.marpetgeo.2018.10.040

Wilson, J. E., Chester, J. S., & Chester, F. M. (2003). Microfracture analysis of fault growth and wear processes, Punchbowl Fault, San Andreas system, California. *Journal of Structural Geology*. https://doi.org/10.1016/S0191-8141(03)00036-1

Westphal, H., Eberli, G.P., Smith, L.B., Grammer, G.M., Kislak, J., (2004). Reservoir characterization of the Mississippian Madison formation, Wind river basin, Wyoming. AAPG Bull. 88 (4), 405–432.

Wood, A. M., Paton, D. A., & Collier, R. E. L. L. (2015). The missing complexity in seismically imaged normal faults: What are the implications for geometry and production response? In *Geological Society Special Publication*. https://doi.org/10.1144/SP421.12

Wrona, T., Fossen, H., Lecomte, I., Eide, C. H., & Gawthorpe, R. L. (2020). Seismic expression of shear zones: Insights from 2-D point-spread-function based convolution modelling. *Journal of Structural Geology*. https://doi.org/10.1016/j.jsg.2020.104121

Zambrano, M., Tondi, E., Korneva, I., Panza, E., Agosta, F., Janiseck, J. M., & Giorgioni, M. (2016). Fracture properties analysis and discrete fracture network modelling of faulted tight limestones, Murge Plateau, Italy. Italian Journal of Geosciences, 135(1), 55-67.

5. GENERAL CONCLUSIONS

This Doctoral thesis provides details of outcrop-based geological modelling and fluid flow simulations in both porous and tight carbonates. The outcomes of the study can be useful to solve the interpretative problems and uncertainties of subsurface geofluid reservoirs. The effect of both lithological and structural heterogeneities on fluid storage and migration was investigated at different scales by constructing Dual-Porosity/Permeability (DP/P) models, including both matrix and fracture pore systems. At the macroscale, the fracture networks petrophysical properties have been upscaled by means of stochastic DFN approaches. At the pore-scale the X-ray computed microtomography (micro-CT) technique have been combined with Lattice-Boltzmann Method (LBM) for relating pore morphology to permeability. In figure 5.1, the main topics tackled by each chapter are summarized in a schematic representation, relating the obtained achievements to the scale of the studies.

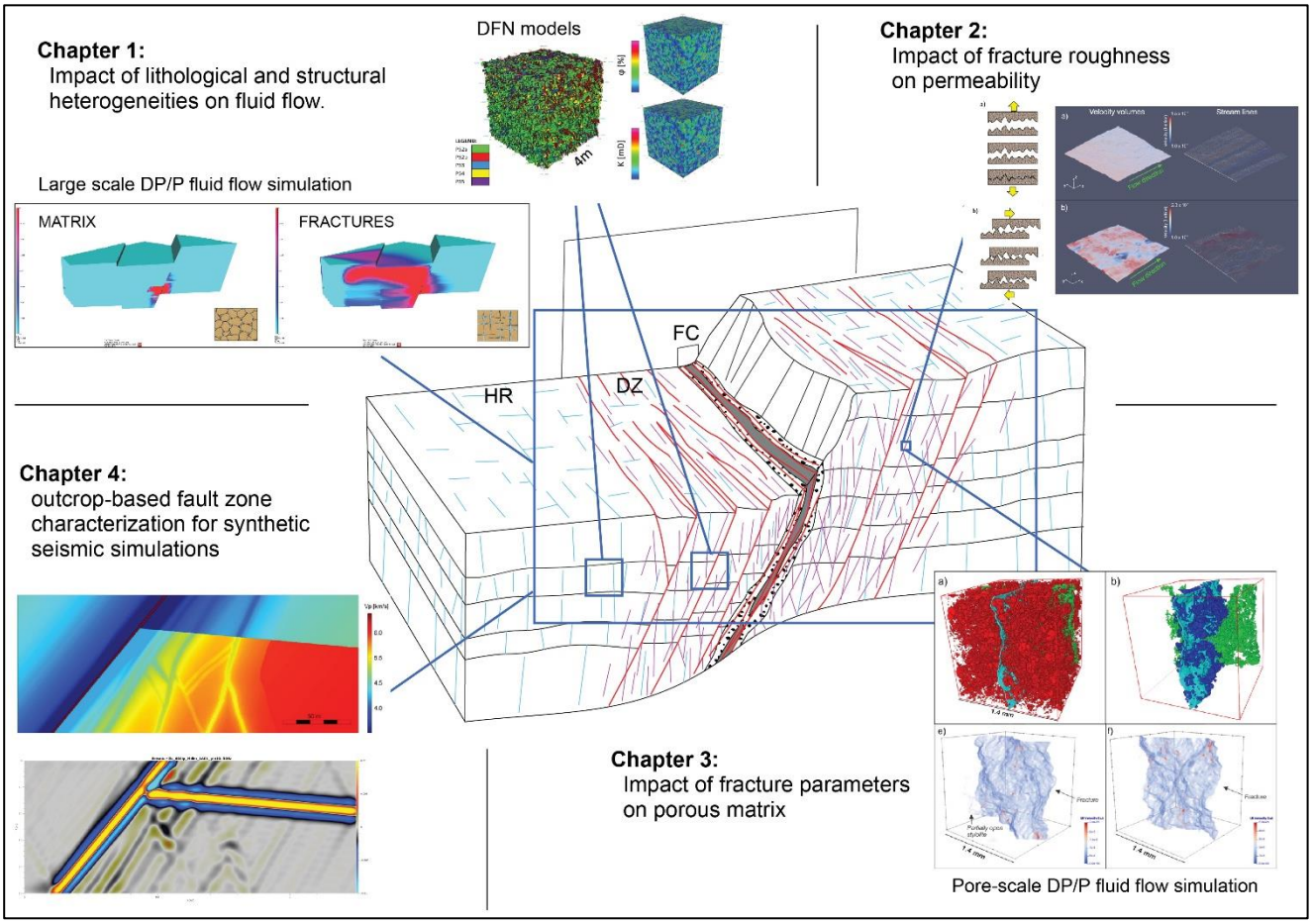

Fig. 5.1. Schematic representation of the chapters associated with the relative scale of study.

In all the presented chapters the SfM photogrammetry technique set the base for the adopted geological modelling. This technique, recently used in geosciences, demonstrated to be a powerful tool due to its versatile application at different scales, offering a cost-effective realization of high-resolution 3D digital outcrop models. Specifically, in the first chapter the SfM technique was used to generate a georeferenced and textured DEM of the study area, where it was possible to identify faults and stratigraphy, subsequently reported in the final DP/P model. In the second and third chapter, the photogrammetry was applied to a close-range setting, achieving accuracy of 0.02 mm to characterize the micro-topography of fracture surfaces. Finally in the fourth chapter the products from photogrammetry aid to further acquire fault measurements from digital outcrops and develop a 2D geological model of the studied fault damage zone.

In the first chapter, the fluid flow simulations of the DP/P model at large scale, demonstrate how the geofluid storage and migration in deformed porous carbonates can be largely affected by lithological and structural heterogeneities. The modelled fault zones denote a dual-hydraulic behavior associated with different fault rocks. Sealing and conduit fault segments have been assigned for cataclasites and fault breccia, respectively. The type and continuity of fault cores have a strong impact on the across-fault fluid migration. Secondly, the fluid migration is strongly affected by the fracture distribution and related permeability anisotropy. The fracture network petrophysical properties derived from DFN modelling increase of a factor 3 within the fault damage zone with respect to the surrounding host rock. Furthermore, the permeability tensor related to the DFN associated with fault damage zones show values three times higher in the components sub-parallel to the fault respect with the across fault one, therefore suggesting an enhanced fluid flow along the fault zones likely related to the presence of fault-related fractures. In this modelling experiment the fracture system seems to play the main role on fluid migration. However, the matrix component rules both fluid storage and migration within the more pervious lithofacies (i.e., grainstones) which are largely invaded by the fluid, resulting in a decreased speed of the fluid front moving in the fracture system. Whereas, in the lithofacies characterized by low permeability (i.e., wackestones and mudstones) the fluid does not flow throw the matrix component of the DP/P model. The presented modelling experiment highlights the importance of accounting for fault-induced permeability anisotropy while producing geofluids from a reservoir.

The fracture hydraulic aperture, which can be indirectly derived by the mechanical aperture and the joint roughness coefficient (JRC), is a crucial parameter for determining the permeability of fracture networks. However, the traditional methods for collecting fracture roughness in the field may lack accuracy to provide valid results. The work presented in chapter two overcomes these field-derived bias by analyzing high-resolution 3D micro-topography of fracture surfaces acquired from SfM photogrammetry and used to realize synthetic fractures. Through numerical modelling, and Lattice-Boltzmann fluid flow simulations the effect of fracture surface features (i.e., roughness, aperture, mismatch) on permeability was investigated. Results from this study allowed to mathematically validate a positive power-law relationship between mechanical aperture and hydraulic aperture, with exponent between 1.6 and 1.8, depending on the considered fractal dimensions of fracture roughness. Fracture roughness was demonstrated to exerts a higher control on permeability at lower apertures. In opening mode fractures the roughness reduce the permeability, whereas in sliding/tearing mode fractures (without surface wearing) higher roughness generate a higher pore space and therefore enhancing fracture porosity and permeability.

In chapter three, the use of DP/P models at the pore-scale allows to decipher the role exerted by the matrix and fracture pore system interplay on permeability, therefore explaining macroscopic phenomena of a reservoir, such as a heterogeneous hydrocarbon distribution. Both porosity and permeability are directly proportional to fracture roughness parameters (i.e., fractal dimension, standard deviation of asperity height). Although the presence of macrofracture enhance the hydraulic properties of the studied rock samples, due to the addition of the fracture porosity, these structures have a dissimilar impact on the pervious (grainstones) and impervious (wackestones and mudstones) lithofacies. The latter show a more significant increment of neo-connected porosity (pores that were originally isolated ad now connected by the intersecting fracture), whereas this increment seems to be negligible in the pervious lithofacies, due to their already well-connected pore system. Similarly, to the macroscale DP/P model previously discussed, also at the pore-scale the permeability increment associated with fractures, in the order of a few hundreds of millidarcy, denote a relevant control of the fracture system on the fluid migration.

Differently from the previous chapters, the study reported in chapter four was carried out in tight carbonates. Here the complexity of the internal architecture of the damage zone associated with a seismic scale (throw ≈ 300

m) normal fault, was investigated from the petrophysical and seismic point of view, with emphasis on the role exerted by subsidiary structures (i.e. 2nd and 3rd order faults). Fracture abundance distribution (i.e., fracture density and fracture intensity) within the studied damage zone does not decrease smoothly away from the main slip surface (MSS). The occurrence of 2nd order faults strongly affects this distribution. The fracture intensity decay has power law contributions from both the MSS and the 2nd order faults. Both fracture porosity and permeability show a decreasing trend moving away from the MSS. Nevertheless, these trends denote a dissimilarity in correspondence of the main subsidiary structures where the fracture porosity increases by a factor 2-3, and the permeability decreases up to 3 orders of magnitude. The presented workflow led to the construction of a field- and digital-based 2D petrophysical model of the fault zone, subsequently populated by elastic properties (i.e., Vp, Vs, density) derived from porosity of both the fracture and matrix components. This model was the input to seismic modelling, performing a sensitivity analysis of geological and geophysical parameters in order to evaluate the seismic signature of the studied fault zone.

Considering the results from the performed seismic simulations, the most important geological parameter affecting the seismic signature of a damage zone hosted in tight carbonates is the fracture aperture. Even in highly deformed tight carbonates if the fracture aperture is narrow enough to yield fracture porosity ranges below 0.5%, the seismic impedance contrasts associated to subsidiary faults cannot be imaged on seismic. Secondly, higher impedance contrasts associated with different surrounding lithologies slightly conceal the reflectors close to the MSS, without drastically compromising the damage zone signal. The illumination angle strongly influences the seismic image, however, a realistic illumination angle of 45° still images the subsidiary structures within the studied damage zone, although most of the reflectors are lost due to the steep nature of the main structures within the damage zone.